The Synthesis and Transport Properties of Conjugated Molecular Wires

MURAT GULCUR

How to cite:

GULCUR, MURAT (2012) The Synthesis and Transport Properties of Conjugated Molecular Wires. Doctoral thesis, Durham University.

The Synthesis and Transport Properties of Conjugated Molecular Wires

Murat Gulcur

Ustinov College

Department of Chemistry

Durham University

A Thesis Submitted for the Degree of Doctor of Philosophy at Durham University

June 2012

STATEMENT OF COPYRIGHT

DECLARATION

The work described in this thesis was carried out in the Department of Chemistry at Durham University between June 2009 and May 2012. All the work was carried out by the author unless otherwise stated and has not previously been submitted for a degree at this or any other university.

Table of Contents

Abstract

The Synthesis and Transport Properties of Conjugated Molecular Wires

Murat Gulcur, Durham University, 2012

Due to the rapid growth in the electronics industry for over the last century, the demand for more advanced materials has been raised. As a result of this, the number of the scientific studies to develop new type of electronic materials has increased and new fields of research such as molecular electronics and nanotechnology are now established. The trend in the advances in electronics follows the miniaturisation of the electrical components and therefore introducing single or a few molecules into electronic devices has become an important topic.

In this work, a summary of the new aspects/developments in the field of single-molecule electronics is presented. Symmetrical tolane compounds with thiol (SH), amino (NH_2), pyridyl (Py) and cyano (CN) anchoring groups were synthesised and single-molecule conductances of those molecules were systematically compared. With the help of density functional theory (DFT) calculations, single-molecular junction formation mechanism is also identified.

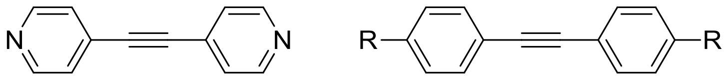

R = NH_2, SAc, CN

Oligoyne molecular wires with different anchoring groups are also synthesised and their electron transport properties at the single-molecule level are studied. The stability of the functional diaryltetrayne compounds is discussed and X-ray molecular structures of the stable tetraynes are presented. The effects of the molecular length and the anchoring group are discussed in detail. Additionally, oligoynes with methyl shielding of the carbon backbone are synthesised and their stability is discussed.

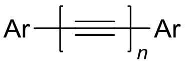

n = 1, 2 and 4

Finally, length-persistent, conjugated OPE and tolane analogues with different molecular lengths and amine anchors were synthesised and their transport properties were investigated in quantum dot sensitised solar cells.

Acknowledgements

Firstly, I would like to thank my supervisor, Prof. Martin R. Bryce for his help, support and guidance. I am grateful to him for giving me the opportunity to work in his research group. Working with him has been a real privilege for me.

I would like to thank to Prof. Thomas Wandlowski and his research group at the University of Bern, Switzerland, especially Pavel Moreno Garcia, who provided all the physical data for Chapters 2 and 3, Wenjing Hong and Bhadra Kaliginedi for their continuous help in the single-molecule measurements of my molecules and welcoming me to their lab to demonstrate the techniques used.

Thanks to Prof. Colin Lambert and his research group at Lancaster University for theoretical calculations.

I also would like to thank to Prof. Dirk M. Guldi from University of Erlangen-Nuremberg for the fruitful scientific discussions and welcoming me to his group. Special thanks to my friend, Andres Ruland Palaia for being a wonderful host and for his irreplaceable contributions to our collaboration.

Many thanks to the European Commission – FP7 research project “FUNMOLS” (Project No. 212942) for the funding, including research visits to collaborator groups and attendance at workshops and meetings. Thanks a lot to FUNMOLS participants Prof. Nazario Martin, Prof.Silvio Decurtins, Prof. Nicolas Agrait and Dr. Michel Calame for the scientific discussions.

Thanks to Prof. Paul J. Low for sharing his valuable comments and opinions about my research.

Special thanks to Dr. Andrei S. Batsanov for X-ray crystal structure elucidation and all analytical services at Durham University, Chemistry Department.

To all past and present members of Bryce group; Katharine, Jose, Luke, Kara, Steven, Ahmed and many others; thank you. Special thanks to Katja and Katy for their help to proof-read this thesis. Many thanks to Byron for his help and for sharing some of his compounds with me. Thanks to Ffion Abraham, for her help to access the microwave reactor. Thanks to my friend Dr. Malek Alsharairi for being a multitasking helper.

Finally, to my beloved parents, Ismail and Necla Gulcur, I very much appreciate your efforts for raising and supporting me so much. Thanks to my brother Mert for his support. I am expecting “Gulcur, M.” publications from him soon.

Dedication

This work is dedicated to my family… My wife Muazzez and daughter Nazli Miray…

Thanks for being the meaning of my life…

Sizi çok seviyorum…

Publications

The following papers are based on work described in this thesis:

- M. Gulcur, P. M. Garcia, A.S. Batsanov, B. Kaliginedi, W. Hong, D.Z. Manrique, C.J. Lambert, T. Wandlowski, M. R. Bryce, “**Synthesis of Oligoyne Molecular Wires with Functionalized End-groups and Their Transport Properties in Single-Molecular Junctions**” *manuscript in preparation*.

- A. Ruland, M. Gulcur, M.R. Bryce, D. M. Guldi, “**Inter-Layer Ligand Effect in Multilayer CdSe Based Photoelectrochemical Cells**” *manuscript in preparation*.

- W. Hong, D.Z. Manrique, P.M. García, M. Gulcur, C.J. Lambert, M.R. Bryce, T. Wandlowski, “**Single Molecular Conductance of Tolanes: Experimental and Theoretical Study on the Junction Evolution Dependent on the Anchoring Group**”, *J. Amer. Chem. Soc.*, **2012**, 134, 2292-2304. “Featured as JACS Spotlights” DOI: 10.1021/ja209844r.

- I.V. Pobelov, G. Mezsaros, K. Yoshida, A. Mischenko, M. Gulcur, M. R. Bryce, T. Wandlowski, “**An approach to measure electromechanical properties of atomic and molecular junctions**”, *J. Phys.: Condens. Mater.*, **2012**, 24, 164210. DOI: 10.1088/0953-8984/24/16/164210.

Presentations and Conferences

- Oral Presentation, FUNMOLS Tutorial Course, 15-18 January 2012, Zurich, Switzerland.
- Poster Presentation, European Conference on Molecular Electronics (ECME’11), 5-9 September 2011, Barcelona, Spain.
- Oral Presentation, FUNMOLS Workshop, 4-5 September 2011, Barcelona, Spain.
- Poster Presentation, RSC Organic Division Northeast Regional Symposium, 13th April 2011, Newcastle, UK.
- Poster Presentation, RSC Chemical Nanoscience Symposium, 30 March 2011, Newcastle, UK.
- Oral Presentation, FUNMOLS Tutorial Course, 9-11 February 2011, Bern, Switzerland.
- Oral Presentation, FUNMOLS Mid-Term Meeting, 12-15 September 2010, Malvern, UK.
- Poster Presentation, 3rd European Chemistry Congress (EuCheMS’ 2010), 29 August – 2 September 2010, Nuremberg, Germany.
- Oral Presentation, FUNMOLS Workshop, 15-18 April 2010, Mueggendorf, Germany.
- International Conference on Molecular Electronics, 5-9 January 2010, Emmetten, Switzerland.
- European Conference on Molecular Electronics (ECME’09), 9-12 September 2009, Copenhagen, Denmark.
- FUNMOLS Workshop, 7-8 September 2009, Copenhagen, Denmark.

List of Abbreviations

A	Acceptor
AC	Alternative current
AcOH	Acetic acid
abs	Absorbance
Ac	Acetyl
AFM	Atomic force microscope
BDT	1,4-benzenedithiol
BDTMS	1,4-bis(trimethylsilyl)buta-1,3-diyne
BJ	Break junction
bp	Boiling point
Cp-AFM	Conducting probe-atomic force microscope
D	Donor
DC	Direct current
DCM	Dichloromethane
DFT	Density functional theory
DMF	*N*,*N*-Dimethylformamide
DMSO	Dimethyl sulfoxide
EBJ	Electromigration break junction
ET	Electron transport
EtOAc	Ethyl acetate
EtOH	Ethanol
FET	Field-Effect Transistor
HOMO	Highest occupied molecular orbital
HR	High resolution
I	Current
LUMO	Lowest unoccupied molecular orbital
M	Molar
Me	Methyl
MeOH	Methanol
MCBJ	Mechanically controllable break junction
mp	Melting point
MS	Mass spectroscopy
NMR	Nuclear magnetic resonance
OAE	Oligo(aryleneethynylene)
OP	Oligophenylene

OPE	Oligo(phenyleneethynylene)
OPV	Oligo(phenylenevinylene)
PE	Petroleum ether (b.p. 40° - 60°C)
SAM	Self-assembled monolayer
SPM	Scanning probe microscopy
STM	Scanning tunelling microscopy
TCNQ	Tetracyanoquinodimethane
TBAF	Tetrabutylammonium fluoride
THF	Tetrahydrofuran
TIPS	Tri*iso*propylsilane
TMB	1,3,5-dimethylbenzene
TMS	Trimethylsilyl
TMSA	Trimethylsilylacetylene
TTF	Tetrathiafulvalene
UV-Vis	Ultraviolet- visible
XPS	X-ray photoelectron spectroscopy

Chapter 1

Introduction to the Molecular-Scale Electronics

1.1 An Overview

In the 20th century, industrialisation of scientific studies in the area of electronics grew rapidly. This growth was the requirement for advances in communication devices such as telephone and radio. At that time the long travel distance of communication signals was the main problem for the industry. The amplification of the signal was achieved by thermionic triodes which led to the growth of the electronic communication industry and the first transcontinental telephone network (1915) relied on signal amplification by triodes.

The first transistor was invented at the Bell Labs by Bardeen and Brattain in 1947. This can be identified as a major breakthrough for electronics because all electronic devices developed afterwards were built on this principle. In 1958, the first integrated circuit was developed by Jack Kilby using junction transistors.[1] Subsequently, junction transistors were replaced by field-effect transistors (FETs). In the late 1950s, the integration of complete circuits (e.g. wires, capacitors, resistors, transistors) was achieved on a single piece of silicon. By developing new techniques, miniaturisation of the components started to boost computing capabilities.

In 1965, the co-founder of the world's largest semiconductor chipset producer[2], Gordon Moore, observed that the number of transistors per integrated circuit chip doubled every year and he predicted that it would be the same for the next decade.[3] A few years later, Moore revised his statement, which is now known as "Moore's law" and stated that the number of the transistors per integrated chip would double every 18-24 months.[4]

Over the past 40 years, the power of computation has doubled approximately every 18 months (Figure 1.1). However, the rapid increase in the number of the transistors will reach its physical limit in the near future. Lithographic techniques, which are currently used for producing integrated circuits, enable the microelectronics industry to produce circuits on silicon wafers. However, these techniques are limited by the wavelength at which they operate.[5] As the components are reduced to the molecular level, some difficulties such as quantum tunnelling and excessive power consumption will arise in the miniaturisation and therefore Moore's Law will not be accurate after reaching its physical limit.[5]

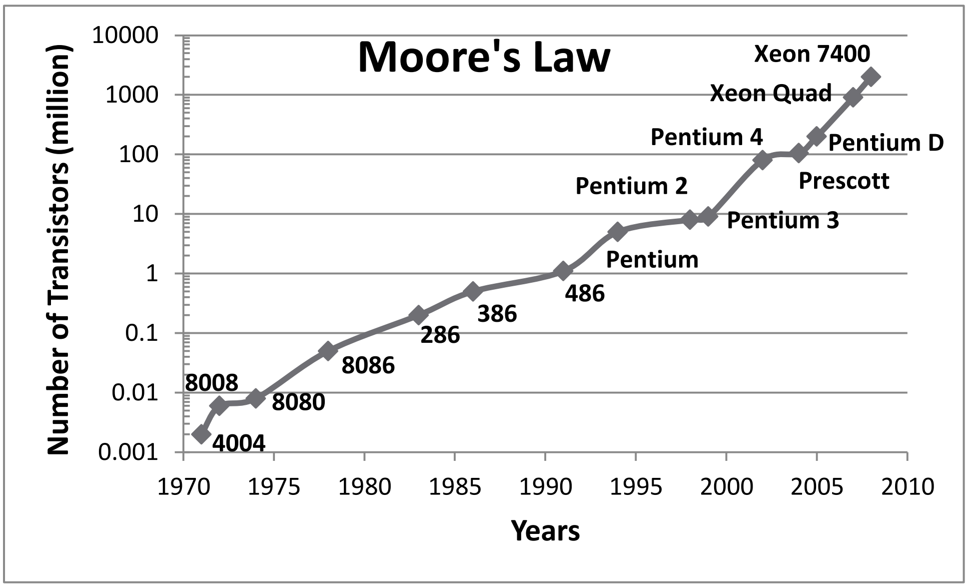

Figure 1.1 The number of the transistors on a chip (Reproduced from reference [6]).

As the silicon wafer era in computing technology approaches the end, new processes will have to be developed in order to produce smaller, faster and more environmentally friendly computing elements. This is a driving force to develop new techniques to introduce single-molecule components into the electronics of the future.

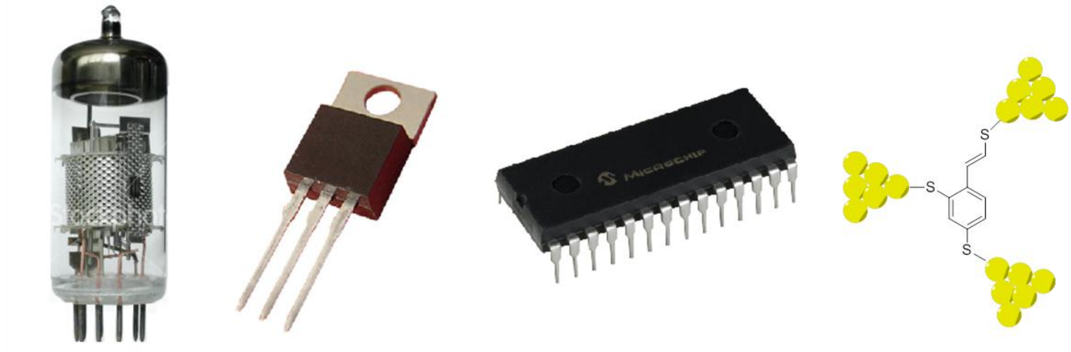

Vacuum tube
~5cm
1900s

Transistor
~5mm
1950s

Integrated circuit
~5 µm
2000s

Molecule
<5 nm
Future?

Figure 1.2 Miniaturisation of transistors over the last century (Reproduced from reference [7]).

In 1959, the physicist Richard Feynman suggested a scenario about the miniaturisation of circuits: [8]

> *"I don't know how to do this on a small scale in a practical way, but I do know that computing machines are very large; they fill rooms. Why can't we make them very small, make them of little wires, little elements–and by little, I mean little. For instance, the wires should be 10 or 100 atoms in diameter, and the circuits should be a few thousand angstroms across... there is plenty of room to make them smaller. There is nothing that I can see in the physical laws that says the computer elements cannot be made enormously smaller than they are now. In fact, there may be certain advantages."*

In 1974, Aviram and Ratner published a landmark theoretical study for the preparation and characterisation of donor-acceptor (D – A) species.[9] They designed a molecule that could act as a molecular rectifier. This molecule used tetrathiafulvalene (TTF) as its donor moiety and was connected by a rigid alkane bridge to tetracyanoquinodimethane (TCNQ), its acceptor moiety, Figure 1.3.

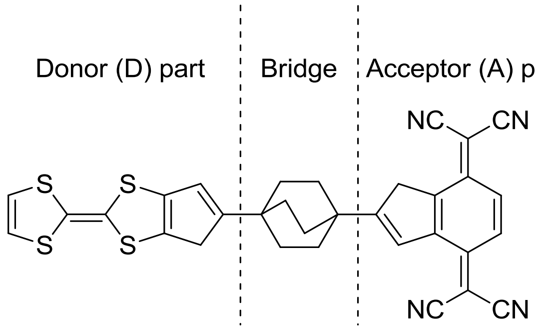

1

Figure 1.3 Molecular rectifier designed by Aviram and Ratner.

Assuming that Aviram and Ratner's work was the starting point for molecular electronics, it is of interest to note the number of published articles which have cited their work. By mid-2012, Aviram and Ratner's publication was cited 1723 times according to the Web of Science®. The distribution chart (Figure 1.4) of the citations by years shows that throughout the 1990's the number of the citations increases steadily and in the early 2000's escalates dramatically. This data reflects the increase in the importance of molecular electronics due to the limitation of conventional methods for the production of integrated circuits.

Molecular electronics deals with a number of integrated chemical structures, whose properties are on the sub-10 nanometer scale and can contain one molecule or a few thousand molecules. These molecular assemblies can be characterised by various methods (e.g. spectroscopic techniques, scanning probe microscopy (SPM), bulk heterojunctions, etc.). One of the earliest electron transport measurements was performed in 1971 by Kuhn and co-workers using organic adlayers on solid substrates.[10] There were many important studies after Kuhn's work, but of paramount significance for single-molecule electronics was the discovery of scanning probe microscopy in 1983. The ability to image at the molecular level brought new developments to molecular electronics. Additionally, the advances in synthetic chemistry of tailor-made molecules widened the horizon of molecular electronics. Thereafter, nearly a decade after the introduction of SPM, theoretical calculations of structure and transport in molecular junctions became a popular subject.

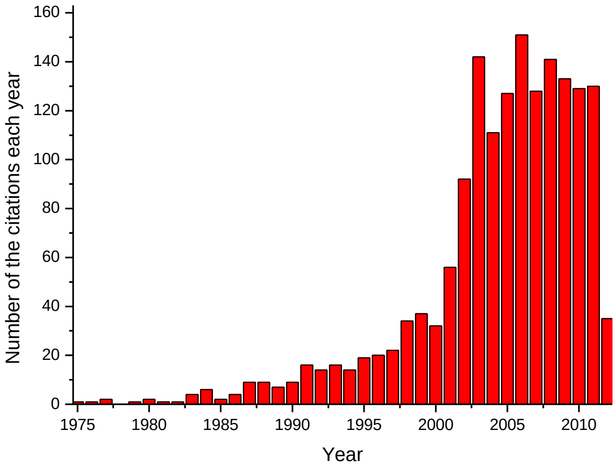

Figure 1.4 Distribution of the number of citations of Aviram and Ratner's work (from Web of Science®) from 1975 to April 2012.

1.2 Molecular Junctions

1.2.1 Introduction

The conductance of macroscopic substances is described by Ohm's law which states that the conductivity (σ) is proportional to the current (I) and the length of the substance (L), where it is inverse proportional to the potential difference between two leads (V) and the cross-sectional area (A) of the substance.

$$\sigma \propto \frac{I}{V} \times \frac{L}{A}$$

However, this equation cannot be applied to a molecular electronic system because as the dimensions of a conductor are reduced to the molecular level, the wave nature of the electrons becomes considerable. It is also not viable to determine the cross-sectional area of a single molecule, and the length can be variable depending on the junction geometry. Therefore, electron transfer through a single molecule, or a group of molecules, can be described by tunnelling or hopping mechanisms.

Molecular junctions are structures that conduct electrical current between two electrodes via a single molecule or a group of molecules. A molecule should be brought into contact with at least two external electrodes in order to measure its single-molecule conductance. For reliable data to be obtained the contacts must be robust, reproducible and provide sufficient flow of current between the electrodes and the molecule.

The length dependence of the electron transport through molecules is another important factor for defining an efficient molecular junction.[11] The electron transport through molecular junctions decreases with the increasing length of the junction. Therefore, this decay factor, the so-called attenuation factor (β) must be low for an efficient electron transfer between the electrodes. Its relevance with the measured conductance (G) is defined by the following equation; [12]

$$G = G_c e^{-\beta L_m}$$

Where G_c is the effective contact conductance and L_m is the molecular length.

The conductance of a molecular junction depends not only on the molecule itself but also on the environment of the molecule (e.g., solvents, vacuum or air) and the contact geometry of the molecule between the electrodes.[13] Measuring the conductance of a metal | molecule |metal junction can be performed via certain delicate techniques, which will be discussed later in this chapter.

1.2.2 Self-Assembled Monolayers (SAMs)

Molecular self-assembly is the spontaneous organisation of functional molecules into well-defined structural aggregates. The strength of the interaction between a molecule and a substrate represents either a minimum-energy structure or an equilibrium phase.

Self-assembled monolayers (SAMs) are ordered molecular structures formed by the adsorption of active molecules on a substrate. In SAM formation none of the molecules are on top of another molecule. A SAM film can be formed on a substrate by exposing the molecules to the surface of the substrate for a certain period of time. This can be achieved by either immersing the substrate in a solution of the molecules or by vapour deposition.

A SAM is formed when molecules are anchored to the surface spontaneously by chemisorption to form an energetically favourable layer.[14] A self-assembly system tries to lower the total free energy and to reach a thermodynamically stable level. Thereby a self-assembly system self-eliminates the faulty-or-impure structures during the assembly process.

Gold-alkylthiolate monolayers and alkylsilane monolayers are the most widely studied SAMs in the literature. Allara and Nuzzo reported the first gold-alkylthiolate monolayer in 1983.[15] They showed that dialkyldisulfides form well-structured monolayers on a gold surface.

Whitesides and co-workers published the first well-defined SAMs in 1989.[16] In this work, SAMs were formed by the adsorption of long-chain alkanethiols onto gold surfaces and the wetting properties of the SAM surfaces were characterised by ellipsometry and X-ray photoelectron spectroscopy (XPS) methods.

Charge transport properties of SAMs have also been widely studied by various techniques, such as cross-wire and mercury droplet techniques. Some of these will be discussed later in this chapter.

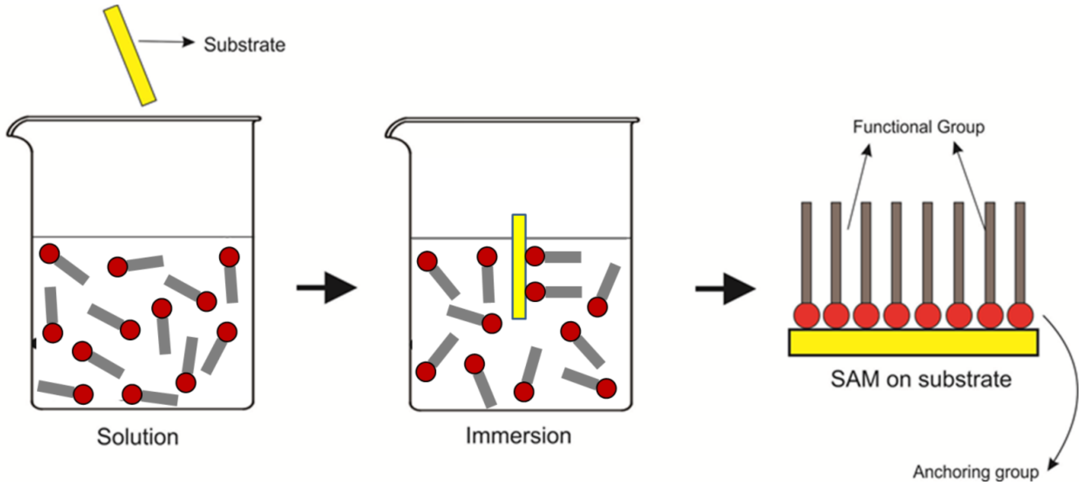

Figure 1.5 SAM formation by immersion of a substrate in a solution of functional molecules

To measure the conductance of a single molecule, it should be self-assembled or chemically bonded between two electrodes. These electrodes can be metal, silicon, graphene etc. depending on the nature of the molecular anchoring group.

1.2.3 Evolution and Interpretation of Single-Molecule Data

Statistical analysis of single-molecule devices is one of the most important factors for understanding the details of metal | molecule | metal junctions. In all repetitive single-molecule conductance measurement techniques the results are statistically analysed in order to determine the conductance characteristics of the molecule (Figure 1.6).

In scanning tunnelling microscopy – break junction (STM-BJ) and mechanically-controlled break-junction (MCBJ) experiments, the current is recorded while the gold-gold contact is broken. When a gold point contact is stretched and broken, its conductance decreases step by step. These steps indicate the quantisation of the gold point contact. Therefore, the cross-section of the point contact is reduced down to a few and finally a single atomic chain of Au atoms. These steps are multiple integers of G_0, which is the conductance of a single chain of gold atoms. G_0 is defined as;

$$G_0 = \frac{2e^2}{h}$$

Where, e is the electron charge and h is the Planck constant.

When an Au|Au contact is broken in the absence of molecules, the conductance exponentially decreases as the distance between Au points increases. If the Au point contact is broken in the presence of molecules, the step (plateau) corresponding to the conductance of a single molecule can be observed.

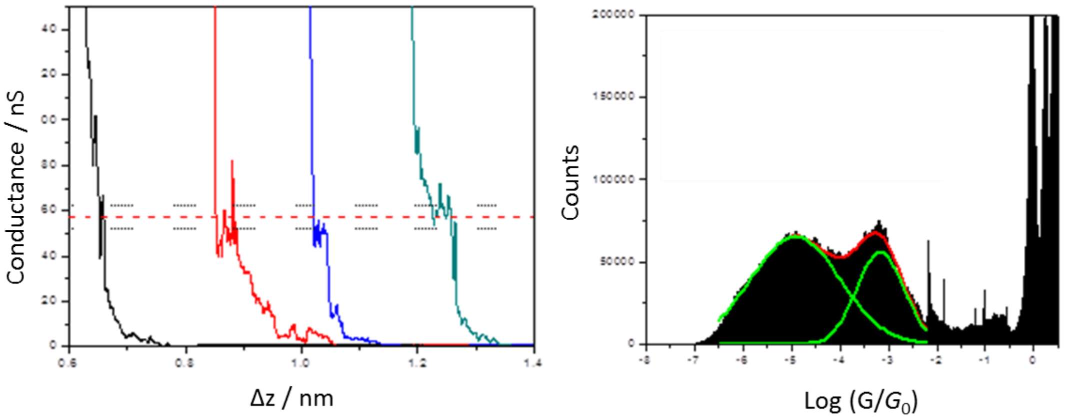

Figure 1.6 Representative conductance-distance traces (left), conductance histogram (right).[17]

In order to determine the most probable conductance data, the results should be statistically analysed after recording a certain number of traces (typically 300-5000 traces). The distribution of the data can then be depicted as 1D conductance histograms and/or 2D conductance-distance diagrams as shown in Figure 1.7.

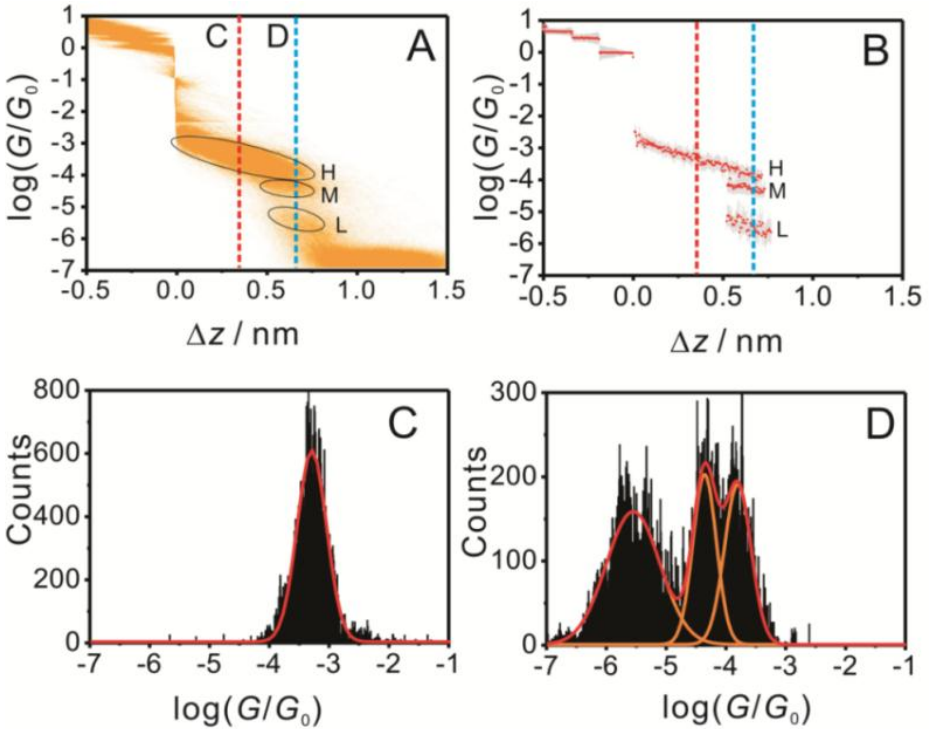

Figure 1.7 (A) Representative 2D histogram constructed from STM-BJ conductance traces. (B) Master traces from the 2D histogram. (C) Conductance distribution and Gaussian fitting at Δ*z* = 0.32 nm (red line). (D) Conductance distribution and Gaussian fitting at Δ*z* = 0.70 nm (blue line). (Reproduced from reference [18])

1.2.4 Mechanically Controllable Break Junction (MCBJ)

Mechanically controllable break junctions (MCBJ) were first reported by Moreland *et al.*[19] and Muller *et al.*[20] This technique depends on a lithographically defined, metallic, free suspended bridge or a notched wire glued on a flexible substrate.[21-23] Due to the very good mechanical properties, phosphor-bronze sheet is often used as the bendable substrate. This substrate is placed in a three point bending system, which is operated by a piezo controlled pushing rod (Figure 1.8).

As the substrate is bent, the wire, which is glued onto it, is elongated until the wire breaks to form two atomically sharp electrodes. Molecular wires can be assembled on the gold wire either with[23] or without a solution.[24,25] By adjusting the gap distance, a single-molecular junction is formed and *I-V* characteristics are recorded for statistical analysis.

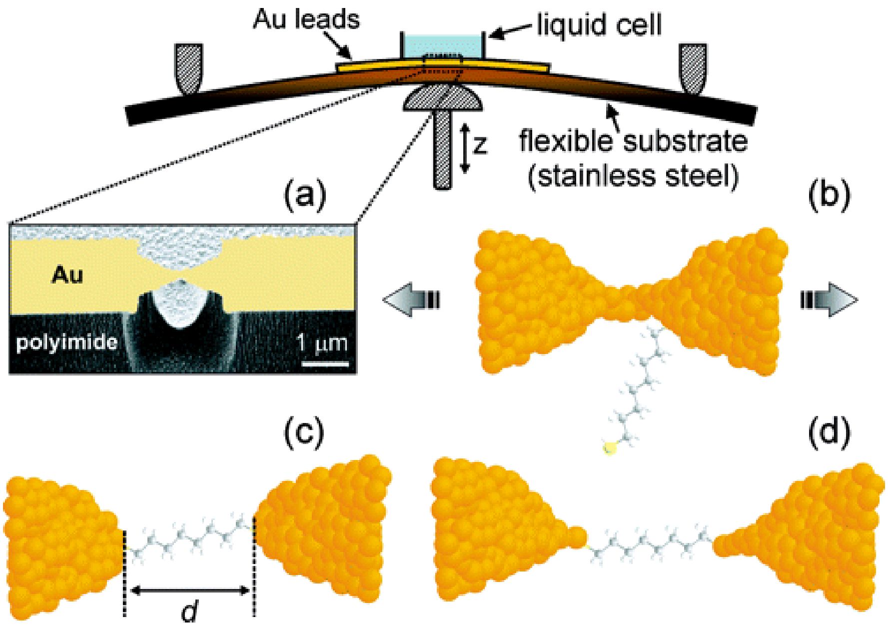

Figure 1.8 (a) Schematics of MCBJ (b) to (d) step-by-step formation of a molecular junction using the MCBJ technique (Reproduced from reference [22]).

The first example of MCBJs for measuring single-molecule junctions was reported by Reed *et al.* in 1997.[23] In this study, a gold wire, which was covered by a self-assembled monolayer of 1,4-benzenedithiol (BDT), was connected between electrodes and elongated until a fracture was induced in the weak notched area by bending the substrate at room temperature. After the breakage, the solvents were removed and the gap between the wires was adjusted until a tunnelling current was observed. Two types of molecular conductance were observed for BDT compounds; the lower was 22.2 megaohm (0.045 μS) and the higher was 13.3 megaohm (0.075 μS). As a control experiment the *I-V* curves were recorded in THF without 1,4-benzenedithiol and a resistance of 1 to 2 gigaohm was observed. The higher vacuum resistance observed without THF led to the conclusion that THF contributes to the conductance.

A modified MCBJ method was developed by Gonzalez *et al.* in 2006.[22] In this study, the conductance of 1,8-octanedithiol was measured in solution at room temperature. While the Au wire was getting thinner, current plateaus were observed due to the quantisation of the gold wire. After the last atomic contact between the electrodes was lost, conductance decreased significantly. When a metal|molecule|metal bridge formed, plateaus in the lower conductance region were observed (Figure 1.9).

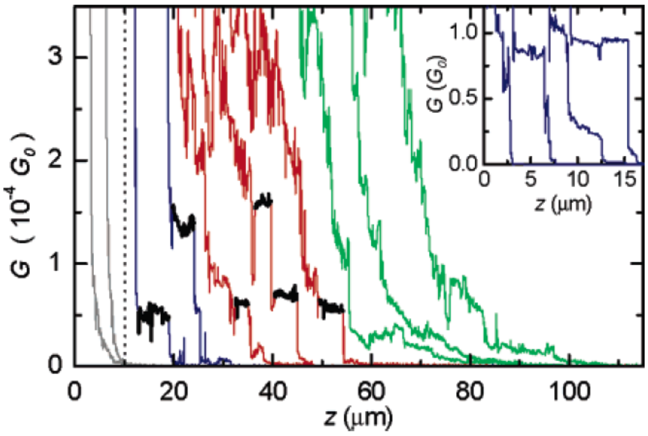

Figure 1.9 The conductance change during the breaking process of a gold wire in mesitylene. Without 1,8-octanedithiol molecules no plateaus were observed (left of the dotted line on the left). In the presence of 1,8-octanedithiol, 50% of the curves present plateaus (Reproduced from reference [22]).

Approximately 100 conductance traces were taken to determine the probability of which particular conductance value was measured. From the conductance histogram the peak corresponding to the conductance of 1,8-octanedithiol was observed at 4.5×10^{-5} G_0 (Figure 1.10).

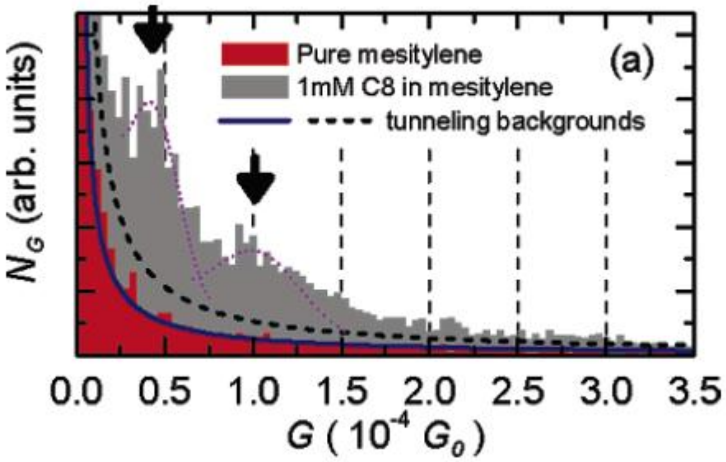

Figure 1.10 Conductance histogram of 1,8-octanedithiol (grey) and blank experiment (red). (Reproduced from reference [22]).

The continuous adjustment of the contact size by the precise control of the piezoelectric component is one of the main advantages of the MCBJs. Moreover, the ability to repeat a back-and-forth bending of the flexible substrate allows a robust statistical analysis by recording a large number of measurements on the desired molecule.[22,25]

1.2.5 Scanning Probe Microscopy Methods

Scanning probe microscopy methods have been widely used to measure the charge transport properties of a single or a group of molecules.[26] Scanning tunnelling microscopy (STM) allows the high resolution imaging of individual molecules adsorbed on a conductive substrate.[27,28] In addition, the STM tip can be used to manipulate atoms or molecules on a conducting substrate.[29] The conducting probe-atomic force microscopy (CP-AFM) method allows measurements of the mechanical properties of a single-molecule junction. STM and CP-AFM are currently the most popular methods to determine molecular conductance.

1.2.5.1 Conducting-Probe Atomic Force Microscopy (CP-AFM)

AFM is a type of scanning probe microscopy, which operates on the principle of detecting the forces between the cantilever tip and the sample. AFM is a powerful device for topographic imaging and by using a conductive probe, it can be applied for measuring the single-molecule conductance and mechanical properties of a molecular junction.[30] In this method, a metal coated conductive tip is brought into contact with the molecules on the conductive substrate. An external circuit is used to measure the current-voltage characteristics. In 2001, a reproducible single-molecule conductance measurement was reported by Lindsay and co-workers.[31] 1,8-Octanedithiol molecules were inserted into an octanethiol monolayer on a Au(111)surface. The octanethiol layer acted as an insulating layer and prevented intermolecular interaction between dithiol molecules on the surface. The free thiol groups (of the octanedithiol) on the top were treated with a suspension of gold nanoparticles and a conducting AFM probe was used to locate these gold nanoparticles floating over an insulating octanethiol layer (Figure 1.11A). $I(V)$ measurements gave only five distinct groups of curves and these groups of curves were integer multiples of a fundamental curve (Figure 1.11B). This fundamental curve was obtained by dividing the $I(V)$ curves by an appropriate integer, (Figure 1.11C). The histogram built from the statistical analysis of 4600 $I(V)$ curves is shown in Figure 1.12D. These five sets were interpreted as the probe tip contacting multiple dithiol molecules or, alternatively, a gold nanoparticle bonded to multiple dithiol molecules at the same time. Consequently, this fundamental curve must be the conductance of a single 1,8-octanedithiol molecule.

Although AFM has a lower resolution than STM, its strength is measuring both the mechanical and electrical properties of a molecule when a conducting probe is used.[32,33]

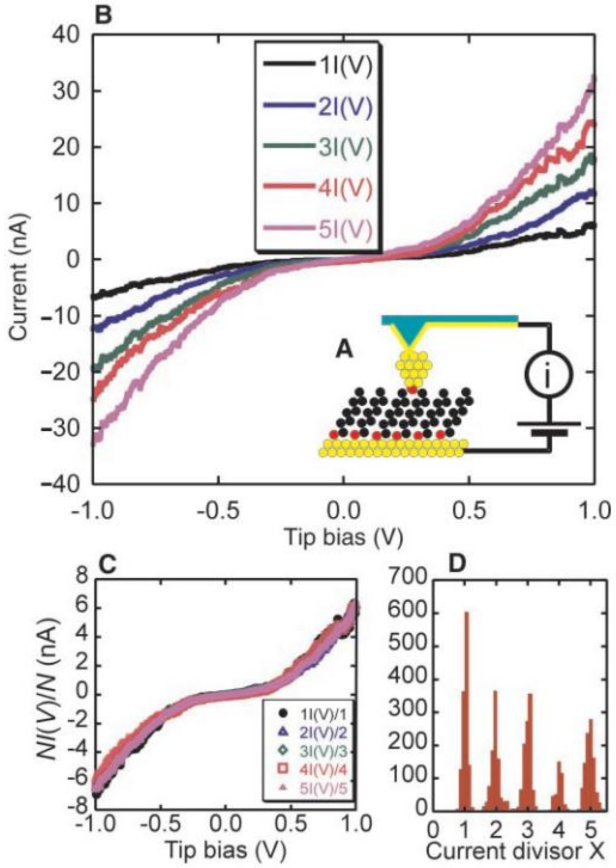

Figure 1.11 (A) Schematic diagram of the experiment (sulfur atoms are shown in red). (B) *I*(*V*) curves measured with the apparatus shown in (A). (C) Curves from (B) divided by an integer (*N*=1, 2, 3, 4 and 5). (D) Histogram of observed curves. Sharp peaks can be seen at integer values (Reproduced from reference [31]).

1.2.5.2 Scanning Tunnelling Microscopy (STM) Methods

STM is a powerful method to measure single-molecule conductance. It was pioneered in the IBM laboratories to image surfaces on an atomic level and the inventors, Gerd Binnig and Heinrich Rohrer, received the Nobel Prize in Physics in 1986 for their discovery. The STM works on the quantum tunnelling concept. An atomically sharp conductive tip is brought very close to the surface to be analysed and a bias voltage is applied between the tip and the surface, which allows electrons to tunnel through the intervening space. The tunnelling current is a function of the applied voltage, the tip-surface distance and the local density of the states. For imaging purposes, the position of the tip is recorded while the current and height of the tip are kept constant. Through the piezoelectric movements of the tip, a surface image is formed (Figure 1.12). Measurements of a single molecule have become possible after the recent advances in STM.

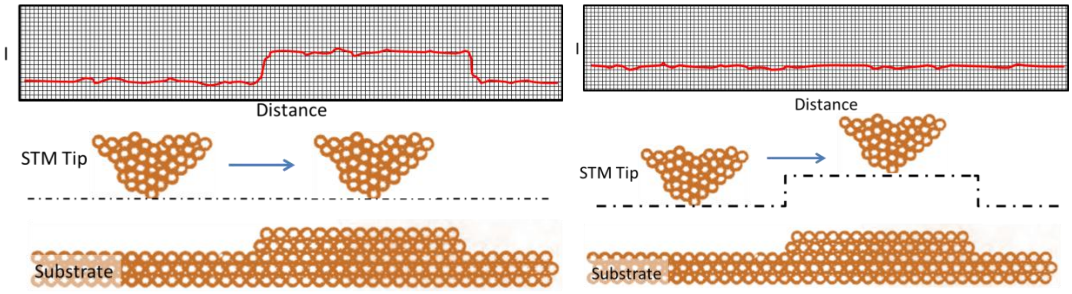

Figure 1.12 (Left) Constant height mode; in this mode the position of the tip is not changed while scanning. The varying current is recorded. (Right) Constant current mode; in this mode the voltage applied to the piezo is recorded (Reproduced from reference [30])

STM-Break Junction

The STM-BJ technique was developed by Tao and Xu.[34] Individual break junctions are formed by repeatedly moving the STM tip into and out of contact with the substrate in the presence of sample molecules (e.g. 4,4’-bipyridine and alkanedithiols). The molecules in this study have anchoring groups on both termini in order to bind to the tip from one end and to the substrate from the other end. An STM-BJ cycle consists of three steps: (a) The tip approaches the substrate until it contacts the sample molecules and subsequently the substrate, (Figure 1.13A). One or more molecules can bind to the tip (Figure 1.13B). (b) The tip is then lifted up from the substrate until the contact between the molecules and the tip is lost (Figure 1.13C). (c) The process is repeated until a considerable number of molecular junctions are formed.

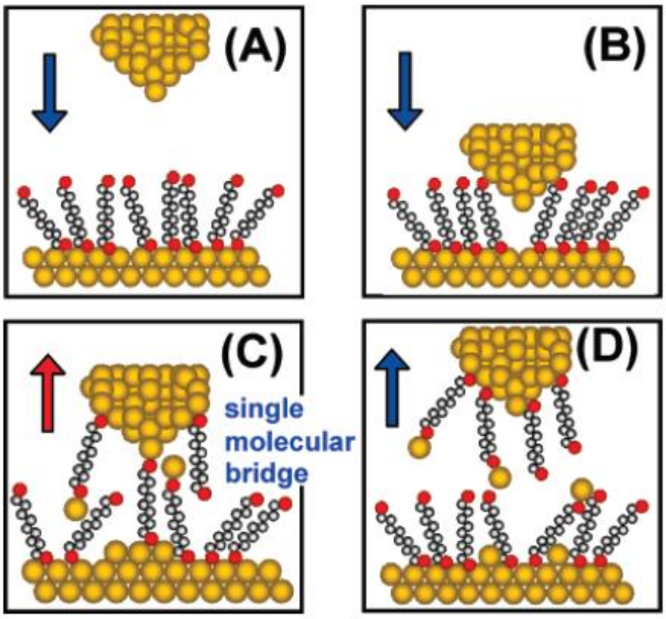

Figure 1.13 Evolution of a STM-BJ measurement cycle (Reproduced from reference [35]).

In the report of Xu and Tao, 4,4'-bipyridine molecules (**2**) bound onto the gold surface by a pyridyl nitrogen atom.[36] While pulling the tip out from the substrate the conductance decreased stepwise, which corresponded to an integer multiple of conductance quantum occurring at each step (Figure 1.14A).[37,38]

After ca. 1000 measurements, conductance curves were statistically analysed and conductance histograms were generated. Conductance quantisation can be observed by the stepwise decrease in conductance. These steps correspond to the multiple integers of G_0. The conductance decreases until the gold contact becomes a chain of gold atoms (Figure 1.14B). When this chain was broken a new sequence of lower conductance was observed (Figure 1.14C). The lower conductance peaks were two orders of a magnitude less than the conductance quantisation, which belonged to the formation of stable molecular junctions between the STM tip and the substrate.

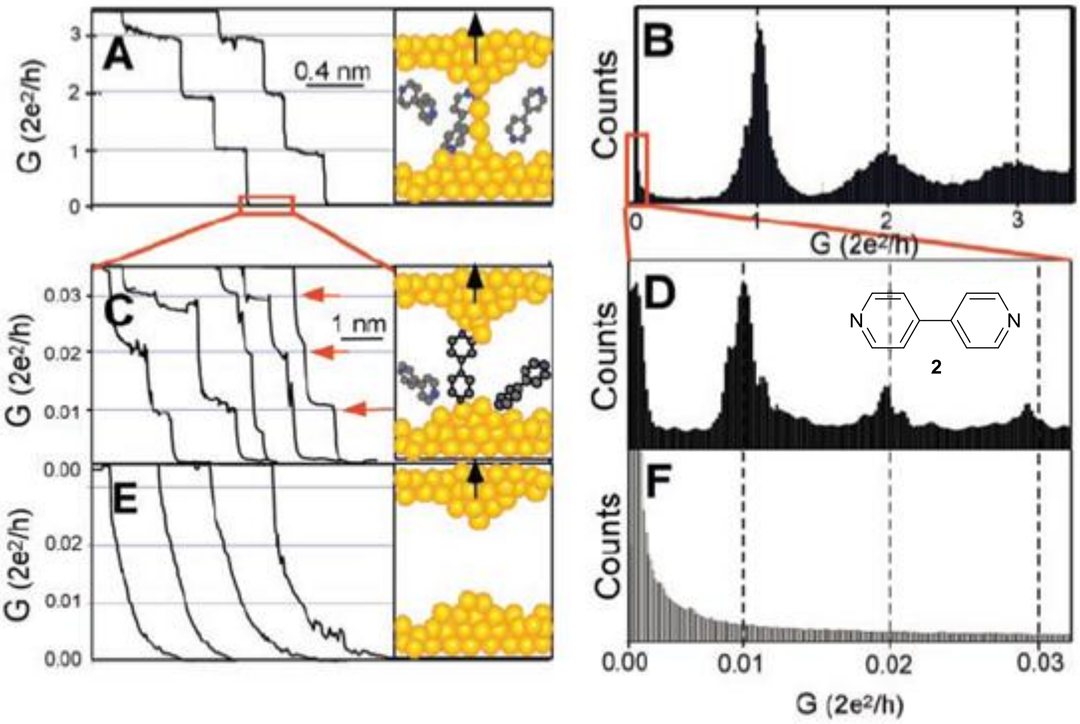

Figure 1.14 (A) Conductance of a gold contact decreases stepwise as the tip pulled out of the substrate. (B) Conductance histogram built by the curves shown in (A) corresponds to well-defined 1 G_0, 2 G_0, and 3 G_0 values. (C) When the contact shown in (A) is completely broken, a new sequence of conductance steps appear. (D) Conductance histogram of the curves shown in (C). (E) and (F) No curves or peaks observed when no molecules are present in the molecular junction (Reproduced from reference [34])

The molecular conductance peaks (Figure 1.14D) near 1x, 2x and 3x 0.01 G_0 are ascribed, respectively to one, two and three molecular junctions formed at the same time. When no molecular junctions were formed, no peaks were observed. To confirm the data, a measurement with 2,2'-bipyridine was performed.[36] As expected no conductance value was observed from **2**, since the nitrogen atoms on the pyridine ring could not bind to the surface because of steric hindrance.

By using the imaging ability of STM, conductance measurements can be performed on the atomically flat areas of the substrate. Additionally, junction length can also be determined by the STM-BJ technique.

I(s) Method

The *I*(*s*) method was first reported by Haiss *et al.* in 2003.[39] The viologen derivative 6-[1'-(6-mercapto-hexyl)-[4,4']bipyridinium]-hexane-1-thiol (**3**) (6V6) was used in the study because of its redox properties which will be explained later in this chapter. Thiol end-groups acted as anchors to bind the molecule to the gold surface and the STM tip. A schematic diagram of the *I*(*s*) method is shown in Figure 1.15.

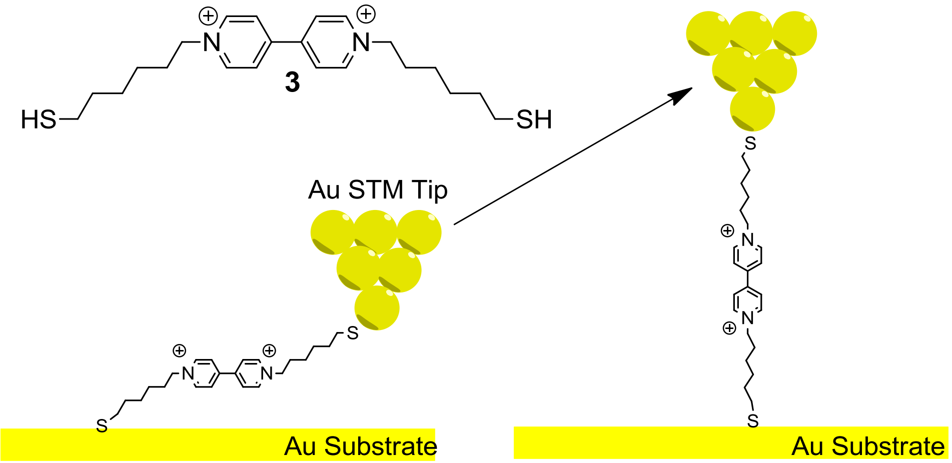

Figure 1.15 Schematic diagram of the *I*(*s*) technique to study conductance of single molecules (Reproduced from reference [39])

Firstly, **3** formed a low-coverage adsorption on a Au(111) surface and yielded flat-lying molecules. This process increases the probability of forming single-molecule junctions between the STM tip and the substrate. To form a molecular junction, the tunnelling current (I_0) was fixed to relatively high values and the STM tip was lowered towards the surface without touching. When the tip was close enough to the Au surface, stable molecular junctions were formed spontaneously. While keeping the *x*–*y* position constant, the tip was then lifted and current-distance curves were recorded.

Two types of current decay (*I*(*s*) scans) curves were observed. The first one showed an exponential decrease of the tunnelling current between the gold substrate and gold STM tip (Curve 1 in Figure 1.16). The second one showed a less sharp decrease of the current followed by a characteristic plateau (Curve 2 in Figure 1.16). The authors proposed that the plateau is the conductance value of a single molecule bonded between the substrate and the STM tip. The plateau was followed by another exponential current decay for a longer distance.

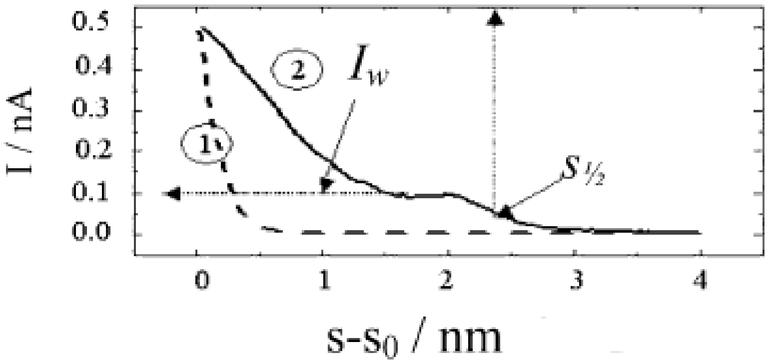

Figure 1.16 Current decay curves [*I*(*s*) scans] for a 6V6 molecule (3) on a gold surface in air (Reproduced from reference [39]).

I(t) Method

The *I*(*t*) method[40] is very similar to the *I*(*s*) method in terms of experimental preparation. In the *I*(*s*) method alkanedithiols were adsorbed onto a gold surface by immersion of the substrate into low concentration of alkanedithiol molecules which formed a flat-lying phase on the gold surface. With the *I*(*t*) technique, molecular junction formation was monitored in time domain. A gold STM tip was lowered onto the substrate without contacting it and molecular junctions were observed. A schematic diagram of the *I*(*t*) experiment is shown in Figure 1.17.

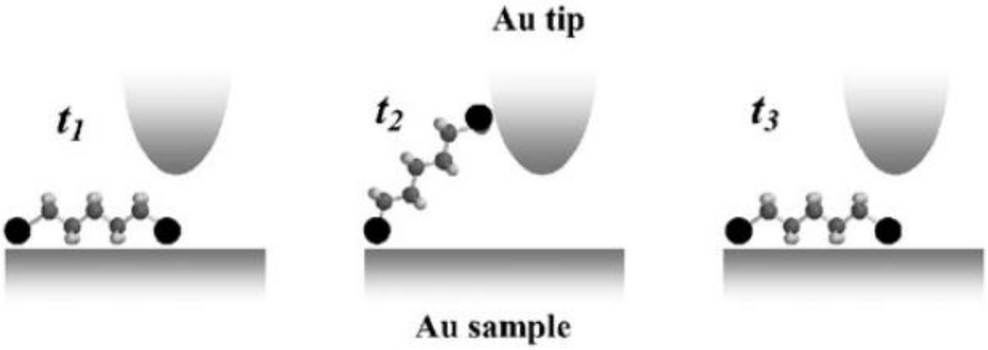

Figure 1.17 Schematic diagram of *I*(*t*) experiment (Reproduced from reference [40]).

Characteristic current jumps were not observed on a blank gold substrate or on monothiol covered gold substrates. When a single molecule was chemically bonded between the tip and the substrate, a significant current jump was monitored (Figure 1.18).

The difference between the tunnelling current before the observation of a current jump and the final current gives the single-molecule conductance value.

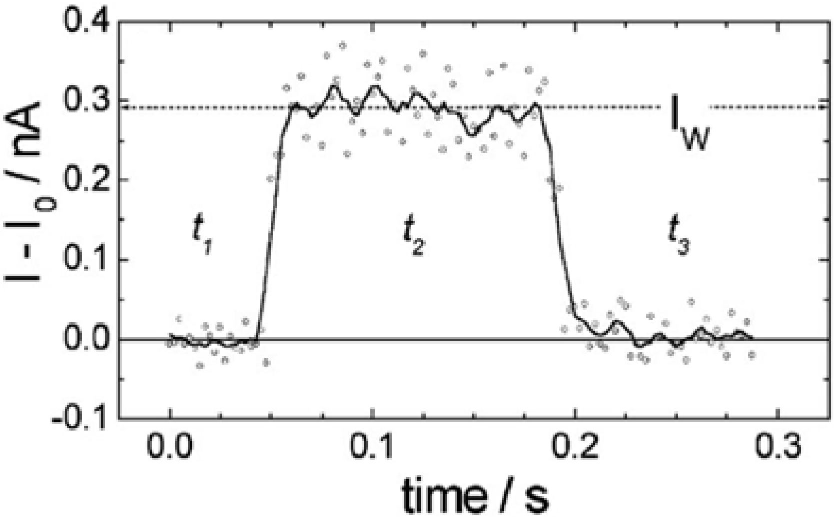

Figure 1.18. Typical current jump recorded on a gold surface with a small concentration of 1,8-octanedithiol (Reproduced from reference [40]).

1.2.6 Hg Droplet Method

Rampi, Whitesides and co-workers developed the Hg-droplet method to measure electron transport rates through organic thin films.[41] In this method, a drop of Hg, supporting a SAM of alkanethiol molecules, is brought into contact with another SAM supported by a second metal (Ag, Cu, Hg, Au) and *I*(*V*) characteristics of the thin films are studied (Figure 1.19).[42]

The SAM coated Hg electrode is the key element of this method, since the alkane thiol molecules form a SAM on the Hg surface easily and liquid Hg adapts to the topography of the surface when it is brought in contact with the other SAM. This feature minimises the chance of short-circuit occurrence and mechanical damage to the SAM.

This method is a simple and reproducible way to measure the electron transport properties of SAMs. However, the presence of a second SAM in the junction formation should be considered for the data analysis and this technique cannot be performed in cryogenic temperatures. Also it should be noted that the presence of two different electrode materials complicates data analysis.

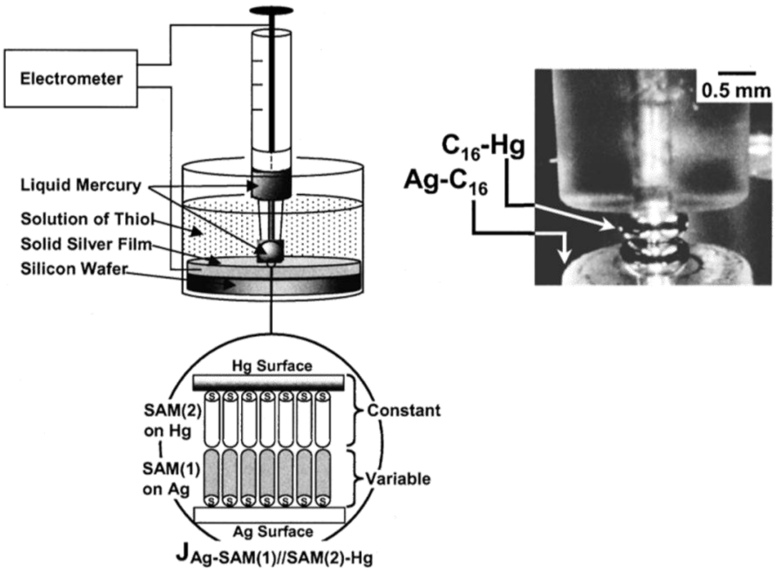

Figure 1.19 (Left) Schematic illustration of a Ag-SAM(1)//SAM(2)-Hg junction. (Right) The photographic image of a Ag-C_{16}||C_{16}-Hg junction (reproduced from reference [41]).

1.2.7 Cross-wire Method

In the cross-wire method, 10 µm diameter wires, one modified with a self-assembled monolayer of molecules, were mounted to the electrical connectors.[43] The distance between two wires was controlled by bending the deflection wire with the Lorentz force: the dc current in one of the wires deflects in the magnetic field. This deflection current is increased slowly to bring the wires together with a contact point (Figure 1.20). It was calculated that there were approximately 10^3 molecules in the junction. The *I(V)* characteristics of the molecular wires can be determined by this method.

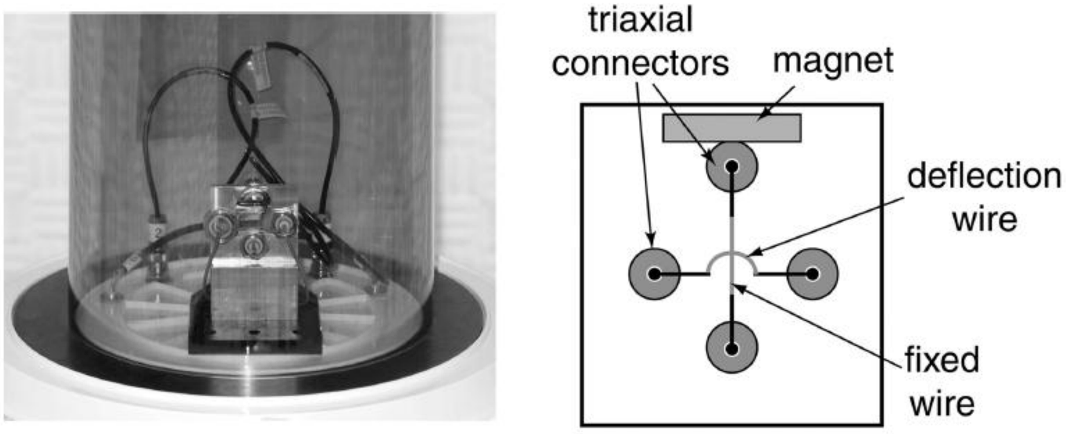

Figure 1.20 Picture and schematic illustration of a cross-wire tunnelling junction (Reproduced from reference [43]).

1.2.8 Electromigration Break Junction (EBJ)

Electromigration break junctions (EBJs) were developed by Park *et al.* in 1999.[44] A thin metal wire, created by electron beam lithography, was exposed to the vapour or a solution of the target molecules and then placed under vacuum at cryogenic temperatures to adsorb molecules in the area, where a gap is formed. When a high current is applied to the sample, a separate electrode pair can be created, which the molecule will bridge.[45] EBJs are advantageous for building three-terminal devices. However, due to the poor reproducibility of the nanogap junctions and the requirement of a large number of device fabrications for statistical analysis of the results, this method is not commonly used to determine single-molecule characteristics.

1.2.9 Fixed Electrodes

One of the simplest methods to measure a single-molecule conductance is to arrange a pair of electrodes to face each other on a solid substrate and then link the molecule to the electrodes by appropriate anchoring groups. However, it is often not easy to fabricate electrodes with such a small gap. Most of the molecules which are used as molecular wires are often a few nanometers long. To produce a device with such a small gap between the electrodes is beyond the capacity of conventional nano-fabrication methods. Therefore, new fabrication techniques have been developed to produce electrodes with a nanometer-scale gap (i.e. electromigration [44,45], electrochemical deposition[46] etc.).

In earlier work, metal nanoparticles were used as bridges between the electrodes and molecules to avoid fabrication of a molecular-scale gap between the electrodes (Figure 1.21b). In this technique, the distance between the electrodes is much larger than the length of the molecules. The electrodes are covered by a layer of molecules and a metal nanoparticle, whose diameter is greater than the gap, bridges two electrodes by using dielectrophoresis[47] or a magnetic field[48] when Au-coated Ni particles are used. In this process, a metal|molecule|metal|molecule|metal junction is formed. A similar technique was reported by Dadosh *et al.*[49] using dithiolate molecules as bridges between two gold nanoparticles and electrostatically trapping the bridged dimer between two metal electrodes (Figure 1.21c).

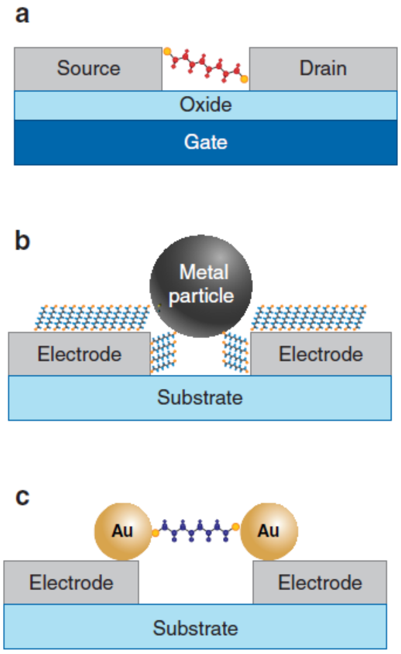

Figure 1.21. (a) Anchoring a molecule between electrodes. (b) Using metal nanoparticles as bridges. (c)Trapping Au|molecule|Au systems between electrodes (Reproduced from reference [50]).

A recent study[51] from our research group and collaborators established the bridging of a fixed length molecular wire into a fabricated silicon nanogap.

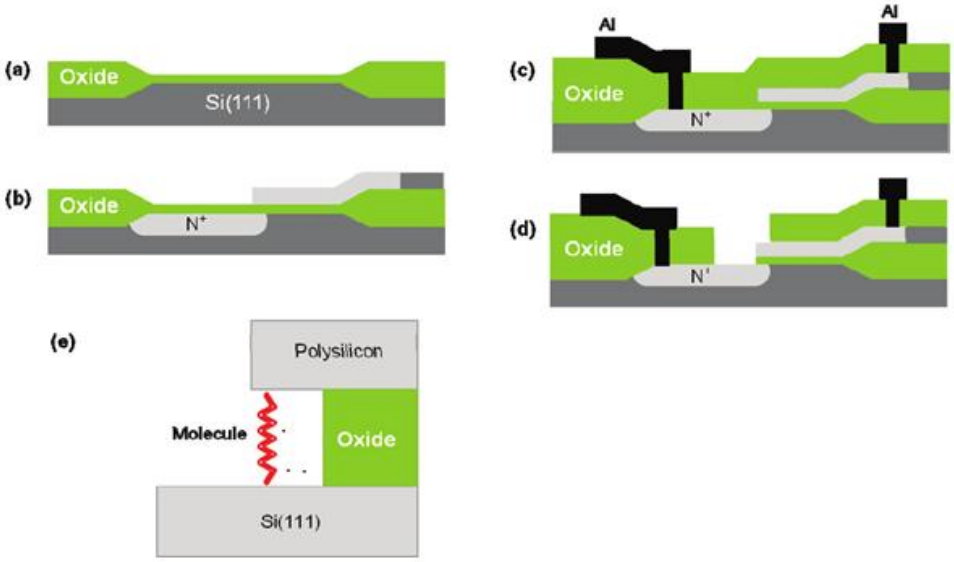

Figure 1.22. Microfabrication of a silicon nanogap structure (Reproduced from reference [51]).

The nanogap electrode was fabricated as depicted in Figure 1.22. Firstly, on an n-type Si (111) surface a 7 nm thick oxide layer was grown (Figure 1.22a), which was followed by arsenic implantation to provide a highly doped N^+ channel in the substrate (Figure 1.22b). Then, a low temperature oxide (LTO) layer was deposited for patterning the contact holes (Figure 1.22c). The micro-fabrication of a silicon nano-gap was finalised by patterning and etching of the LTO to expose and hydrogenate the silicon surface which was then reacted with the diethylacetal derivative of 4-ethynylbenzaldehyde to protect the surface from oxidation (Figure 1.22d-e). The device was rinsed with chloroform and acidified solution, respectively, to generate aldehyde functions on the surface. Surface characterisation by solid-state Fourier-Transformed infra-red spectroscopy confirmed the presence of aldehyde functions on the surface.

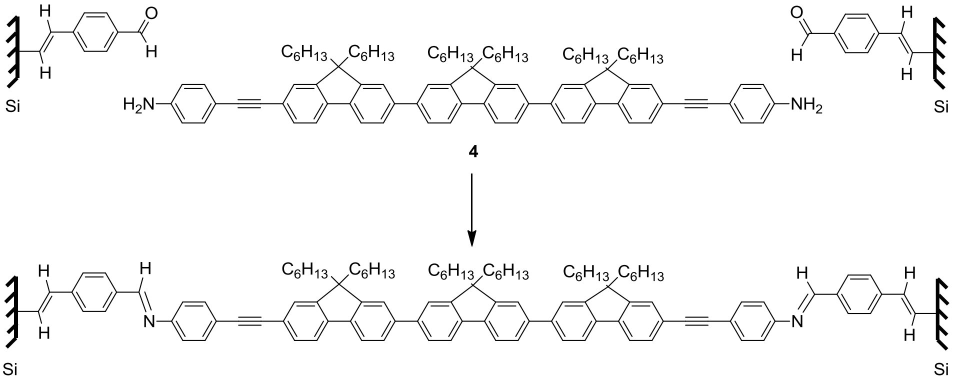

Scheme 1.1 Coupling of a 4 nm long diamino terminated molecule into the nanogap (Reproduced from reference [51])

The 4 nm long compound **4** was tailored to bridge the electrodes by imine formation at both ends of the molecule with the surface bound aldehyde functionalities. Solutions of **4** were exposed for 5 to 53 minutes to achieve bridging. From the changes in the electrical properties, molecular bridging was apparent, (Figure 1.23) (Note the y axis scale is µA on the left and nA on the right). When the imine bonds were hydrolysed, the electrical properties reverted to the same as before mounting the molecules in the gap. It was also possible to reproduce the experiment by hydrolysing and re-forming the imine bonds.

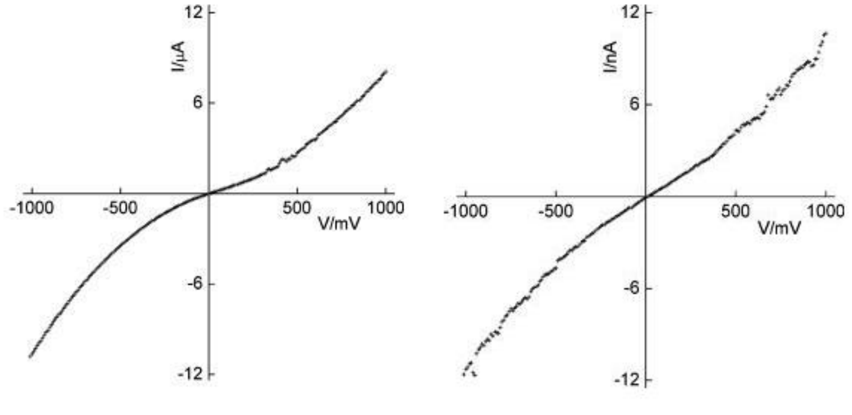

Figure 1.23 *I-V* characteristics of bridged silicon nanogap devices (left) when multiple molecules bridge the nanogap after 53 h of immersing the device in a solution of the amino compound; (right) the lower limit obtained from 5 min of immersion (Note the y axis scale is µA on the left and nA on the right) (Reproduced from reference [51]).

In summary, the molecular junctions are mechanically stable because the fixed electrodes are supported on a solid substrate, which makes this method ideal for studying the electron transport through a molecule as a function of external parameters such as temperature, magnetic field etc. Another advantage of using the fixed electrode method is that the substrate can be used as a gate electrode to control the electron transport through the molecule.

1.3 Molecules as Components of a Nanocircuit

1.3.1 Introduction

The concept of single-molecule electronics was developed as the limitations of using bulk materials in electronics became clear. The molecules used in single-molecule electronics have the properties of conventional electronic circuit components such as rectifiers, transistors, wires, switches etc.

1.3.2 Molecular Rectifiers

In macroelectronics, a rectifier is an electrical component which converts alternating current (AC) to direct current (DC) allowing electron flow in only one direction. The first idea of a molecular rectifier was published by Aviram and Ratner in 1974.[9] They designed a molecule to rectify electron flow from the electron rich (TTF) moiety to the electron poor (TCNQ) moiety (Figure 1.3). The rectification was envisaged by tunnelling over the sigma bridge. If the molecule was fully conjugated, the D and A moieties of the molecule would interact and form a single donor level, which would prevent the rectification. When a unimolecular rectifier is placed between two electrodes, electric current will pass at a lower voltage from the acceptor to the donor than in the opposite direction. This is because the potential energy of the highest occupied molecular orbital (HOMO) of the donor is higher than the lowest unoccupied molecular orbital (LUMO) of the acceptor (Figure 1.24).[52] Therefore, an electron tunnels inelastically (releasing energy) through the σ bridge from the higher energy level LUMO of the acceptor, to the lower energy HOMO of the donor moiety (Figure 1.24). Between the metal electrodes (M_d and M_a) the rectifier is formed as $M_d|D$ – bridge – $A|M_a$ with easy electron transfer from M_a to M_d because of the down-hill tunnelling from the excited state D^+-bridge-A^- to the ground state D^0-bridge-A^0.

The specific unimolecular rectifier molecule **1** has not yet been synthesised. This *"Gedankenmolecule"* (never synthesised molecule) has a very strong donor-acceptor interaction, which prevents covalent coupling reactions of donor and acceptor moieties by forming a D^+A^- salt of two sub-units of the molecule.[7]

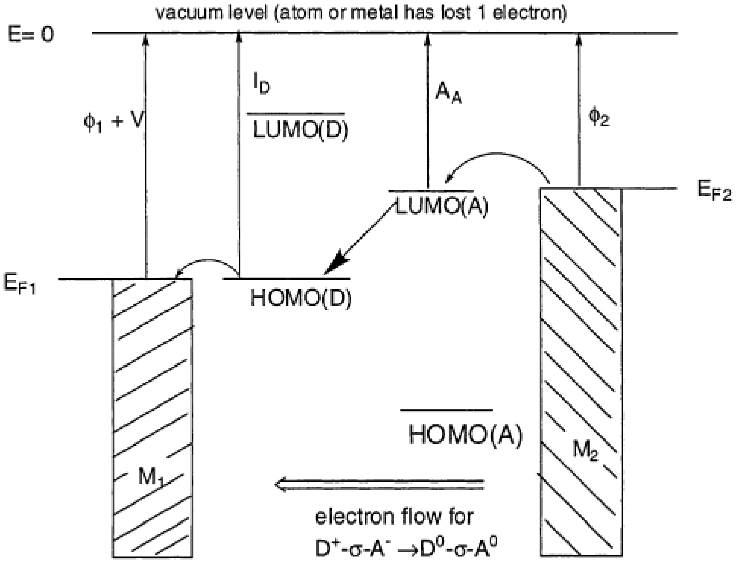

Figure 1.24 Rectification mechanism in a molecule (Reproduced from reference [52]).

An unambiguously characterised TTF-σ-TCNQ compound (**5**) was reported by our group.[53] Studies of a TTF-based molecular rectifier (**6**)[54,55] were reported by Bryce, Heath, Perepichka and co-workers in 2005.[56] The rectification ratio in Langmuir-Blodgett monolayer of compound **6** was found to be 18:1.

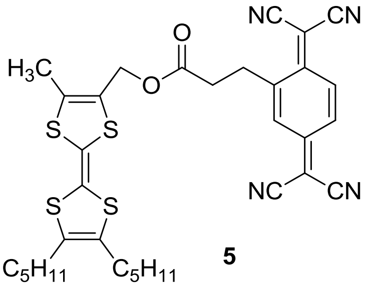

5

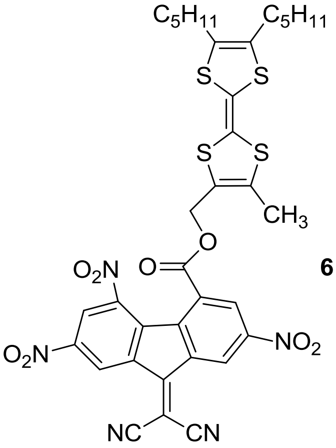

6

Many alternative molecular rectifiers have been studied. Ashwell, Metzger *et al.* in 1997 [57] reported that the zwitterionic molecule **7** showed a rectification ratio of up to 26:1 in Langmuir-Blodgett films. However, the device had very limited stability.

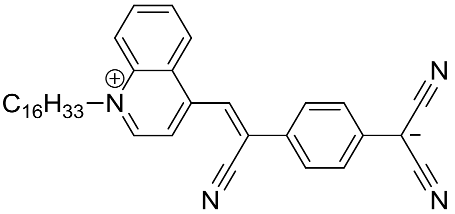

7

Kushmerick *et al.* synthesised tolane and oligophenylene-ethynylene (OPE) molecules with different anchoring groups on both ends[58] which showed asymmetric current-voltage (*I-V*) curves. They demonstrated that the current rectification of a molecular junction could be controlled while keeping the metal-molecule (Au-S) contact constant and tuning the metal-molecule coupling at the other end of the molecule. In the same report, current-induced rectification was observed, when an OPE molecule was anchored at only one end (**10**).[58]

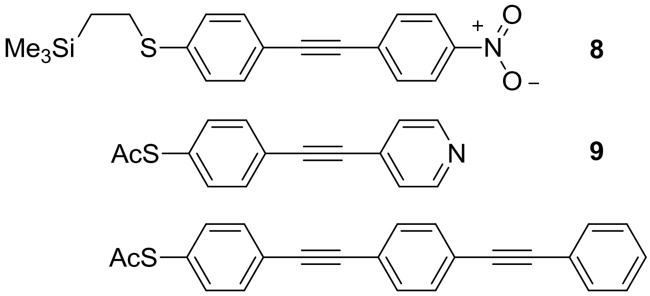

8

9

10

Figure 1.25 Unsymmetrical tolane and OPE systems showing rectification properties.[58]

1.3.3 Molecular Switches

A switch is a device for making and breaking the connection in an electrical circuit. Either in a macroscopic or nanometer scale environment a switch should perform a reversible action to turn “on” and “off” an electrical circuit. One of the key requirements is high stability of both “on” and “off” states. A molecular switch should respond reversibly to changes in an external stimulus, e.g. pH, temperature, light or interaction with another molecule. To switch the properties of a molecule between two states STM, chemical or electrochemical reactions, or an electrical field are often used.

Molecular switches have attracted considerable attention because of the potential applications in molecular-scale electronics. In this context mainly light-induced and redox-active molecular systems have been reported in the recent literature.[59]

A light-induced molecular switch usually changes its conformation upon irradiation, which leads to a spectral change between the “on” and “off” stages. One of the most popular photoswitches are dithienylethene derivatives, which were first reported by Irie.[60] These molecules have bistable isomers which can be switched by light irradiation (Scheme

1.2). In order to prevent *cis* to *trans* photoisomerisation side reactions, the ethene bond of the molecule is often locked into a cyclopentene ring.

11 requires UV light to be converted to **12** which can be converted back to **11** by exposure to visible light. The isomer **12** ("on" state) absorbs longer wavelengths of light because the π-electrons are more delocalised than in **11** ("off state"). In **11** the π-electrons are less delocalised due to the cross-conjugation and the non-coplanarity of the thiophene rings, induced by the methyl substituents. Therefore, two structural isomers, which have different optical spectra, provide ideal properties for a molecular switch in an electrical circuit.

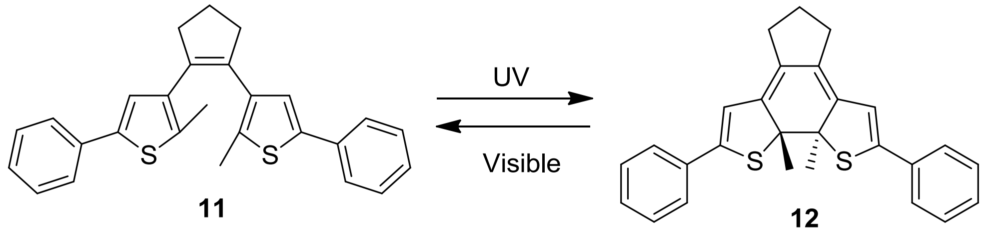

Scheme 1.2 The open-ring and closed-ring isomers of dithienylethene in solution.

The dithienylethene derivative **13** was self-assembled on a gold surface and single-molecule switching properties were studied by Dulic *et al.* [24] The molecular junction was formed by MCBJ techniques with **13** in the "on" state followed by illumination of the junction with visible light while monitoring the resistance of the system. After 20 seconds the resistance sharply increased, which was attributed to the switching off the junction. The open-ring ("off" state) isomer **14** was illuminated with UV light in attempts to switch to the "on" state but this was unsuccessful. The switching process from the "off" to "on" state has a very high quantum yield in solution. However, when the molecule was connected between the gold electrodes it was not possible to induce the switching. This result was explained by theoretical calculations as the excited state of the open form is quenched by the Fermi level of the gold electrode, which inhibits the ring closure reaction.

The successful reversible switching of an analogue of **11** was reported by Schoenenberger and co-workers.[61] Instead of assembling the switch molecule between the electrodes, the authors fabricated two-dimensional lattices of gold nanoparticles which were bridged by compound **15** (Figure 1.27). By irradiation of the device by UV and visible lights, **15** was cycled between "on" and "off" states many times.

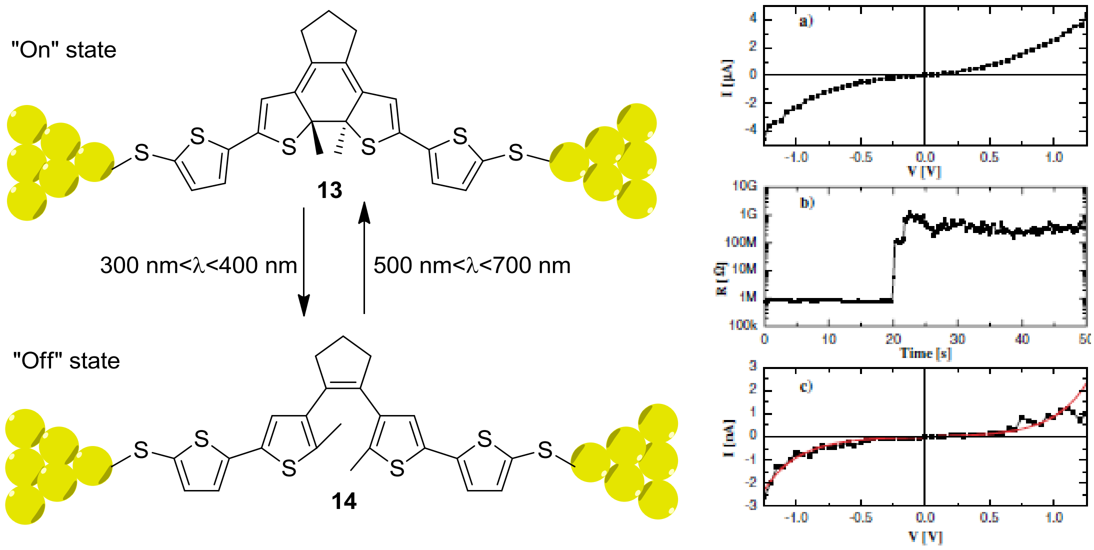

Figure 1.26(Left) Photochromic molecular switch between Au electrodes. Conversion from "on" to "off" state was not possible when the molecule was connected to Au electrodes. (Right) (a) A typical *I-V* curve of the "on" state (b) resistance vs time trace (c) typical *I-V* curve of the "off" state (Reproduced from reference [24]).

A molecular switch can also be turned on and off electrochemically. One of the first examples was studied by Gittins *et et al.*[62] They investigated the dialkylviologen unit **17** with terminal thiol anchor groups. The molecules were assembled on a gold surface and subsequently gold nanoparticles were placed on the monolayer and anchored by the other thiol group. The current passing through the junction (STM tip | nanoparticle| molecule | substrate) was measured while the redox state of the viologen moiety was controlled electrochemically. An increased conductivity was observed for the reduced radical cation of the viologen moiety compared to its dicationic state (Figure 1.28).

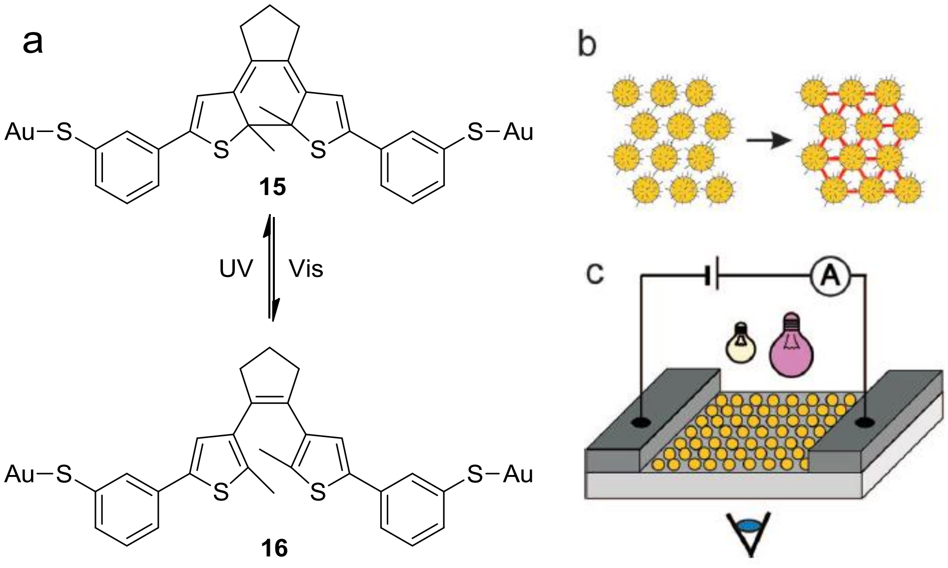

Figure 1.27 (a) Switchable diarylethene molecules (b) Schematic representation of two-dimensional network (c) schematic device structure (Reproduced from reference [61]).

Leary *et al*. reported the comparison of single molecular switching behaviour of dialkylviologen and dialkylpyrrolo-tetrathiafulvalene molecules.[63] They showed that well-defined redox switching can be obtained from Au|6PTTF6|Au single molecular junctions.

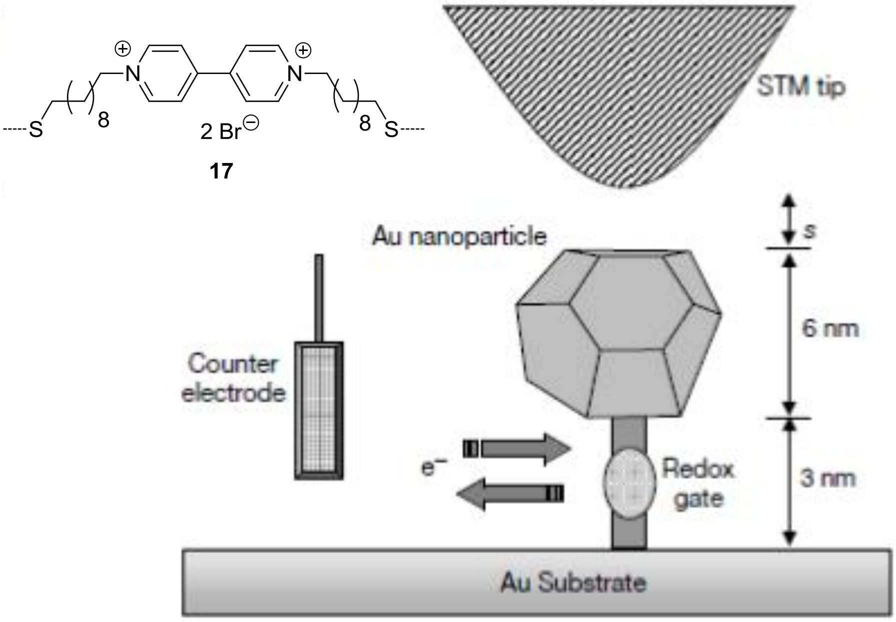

17

Figure 1.28 Schematic representation of the device (Reproduced from reference [62]).

Another electrochemically controlled molecular switch was synthesised by Hummelen and co-workers.[64] The OPE derivative **18** has an anthraquinone moiety in the centre and acetyl protected thiol anchors (Scheme 1.3). The electron delocalisation on this molecule is interrupted by the anthraquinone part; reduction to the aromatic anthracene **19** turns the molecule into a fully conjugated system. This switching process is supported by theoretical calculations. Recent studies by Wandlowski *et al*. reported the electrochemical switching behaviour of **18** to the dihydroxy derivative of **19** in single molecular junctions.[65]

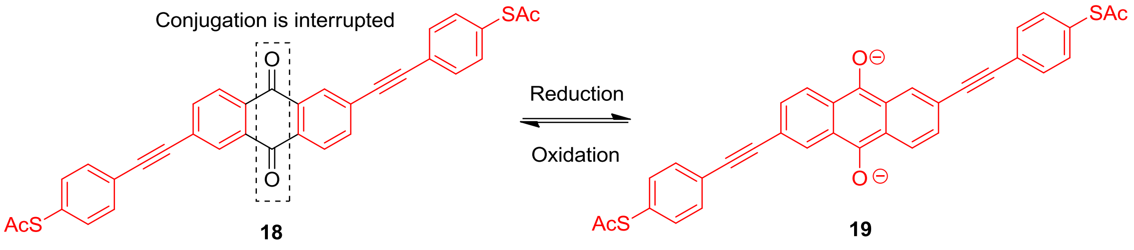

18 **19**

Scheme 1.3 "On" and "off" states of anthraquinone centred OPE molecules with sulfur anchoring groups.

1.3.4 Molecular Wires

"Molecular wires" are candidates for being the simplest components of future electronic systems and have been suggested as the interconnectors for a nanometer scale electronic circuit. They are essentially organic or inorganic molecules carrying electrons which are either injected from external electrodes or generated in situ by a donor (D) moiety bonded to the backbone. Organic molecular wires are usually conjugated π systems and constructed from three parts: an anchoring group (or atom), a spacer and a functional core.[66,67]

The most fundamental requirement for molecular wires is that they are electron or hole conducting in order to transport charge from one side to another (Figure 1.29). It is obvious that conductivity is not the only requirement for a functioning molecular wire. Some of those properties have been approached in different ways, which mainly depends on the technique used to investigate the wire properties.

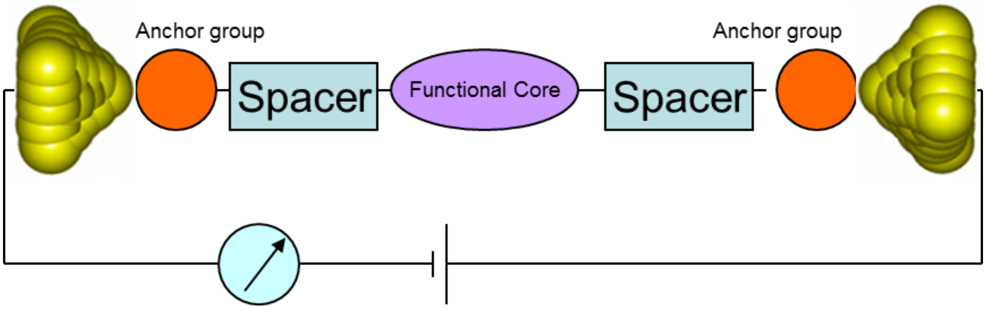

Figure 1.29 Schematic representation of a molecular wire in a nanocircuit.

In the past, the attachment of a wire into a circuit was the main problem because there was not a reliable technique to address individual molecules. Therefore, introducing various redox groups at either end of the wire molecules is one approach to address this problem. The redox centres behave as donor and acceptor moieties and the charge is carried over the wire "bridge".

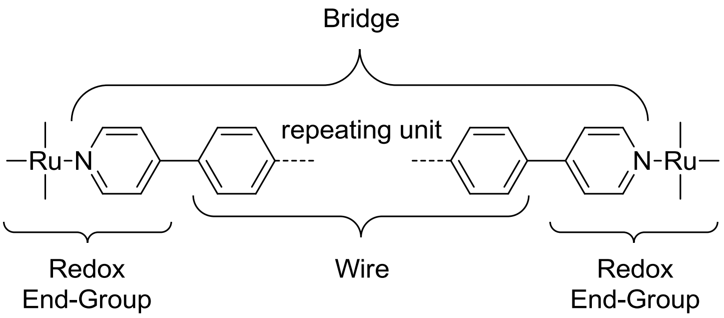

Figure 1.30 General structure of mixed-valence systems.[68]

These systems have the advantage of generating the charge carriers internally without the need to attach the molecules to a circuit. The wire properties of the molecule can be studied by spectrophotometric techniques as a means of assessing the conductivity of the wire.[68] On the other hand, there are some disadvantages, for example, the overlap between the orbitals of the redox centre can contribute to the charge transfer, therefore, it may not be possible to measure the conductance of the molecular wire. Also, the wire provides the electron transfer but at the same time the redox centres contribute to the conductance of the wire.

It is debatable, therefore, whether or not donor-acceptor systems are good models of a real electrical circuit. This issue has been solved by introducing alligator clips to molecular wires and by using scanning probe microscopy techniques. The molecular wire can be attached to two electrodes by these alligator clips so that a real circuit is built to observe single-molecule wire properties. [69]

The effect of different anchoring group on molecular conductance will be discussed in Chapter 2.

1.3.4.1 Saturated Chains

Saturated carbon chains, especially alkanes, end-capped with terminal anchoring groups have been widely studied for the last decade. Even though these systems are not conjugated, in other words they have a very large HOMO-LUMO gap, they have been used as model systems testing both experimental techniques and computational methods.

Previously in this chapter, the developments of CP-AFM, STM-BJ, *I(s)* and *I(t)* methods by using saturated alkane molecules have been explained. Additionally, alkane chains comprising different anchoring groups such as amine,[70] thiol[71] or phosphine derivatives [72] were widely studied to investigate either the attenuation factor or the effect of anchoring groups.

Measuring very low conductance of non-conjugated, saturated molecular wires helped scientists to build very strong data analysis and measurement techniques. Nowadays, these techniques are widely used to understand the details of conjugated and more highly conducting molecular wires.

1.3.4.2 Oligophenylenes (OPs)

Oligophenylenes are well-known π-conjugated systems. An oligophenylene derivative with an anchoring group at each ends is a good model for a molecular wire.[73]

When the torsion angle between two phenyl rings is ca. 90° degrees, *π-π* coupling between the two rings cannot dominate the electron transport through the system (Figure 1.31). Mayor and co-workers studied the influence of molecular structure on electronic transport.[74] In this study, a series of oligophenylene rods were synthesised and methyl groups were attached to the phenyl rings to decrease the *π* overlapping along the molecular backbone. The electron transport properties of those molecules were studied by MCBJ. The authors reported that the conjugation along the molecule is reduced by methyl substitution, but not fully interrupted since the conductances of **21**-**23** were not significantly lower compared to **20**.

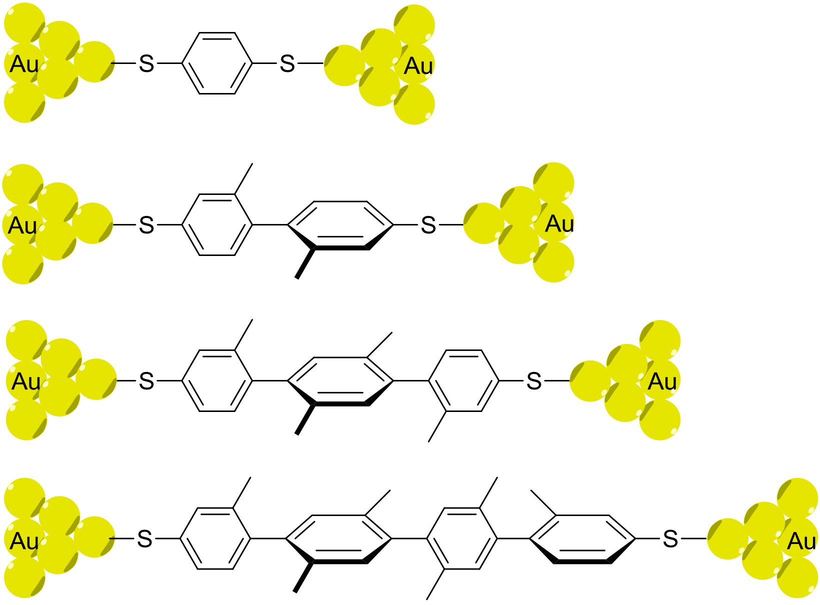

Figure 1.31 Oligophenylene compounds with interrupted conjugation studied in reference[74].

The conductivity of oligophenylenes can be tuned by substituting or bridging phenyl rings.[75] A recent study by Wandlowski and co-workers showed that the conductivity of dithiol substituted biphenyls is a function of the torsion angle between the phenyl rings (Table 1.1). Phenyl rings were either substituted by methyl groups on the 2,2' positions or bridged by alkyl groups and single-molecular conductance was measured by the STM-BJ method.

Table 1.1 Experimental and computational results for the torsion angle and conductance[75]

Structure	Torsion angle φ X-ray	G / G_0 Experimental	G / G_0 DFT Atop-atop	G / G_0 DFT Bridge-bridge
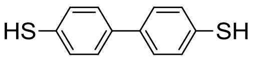 **24**	36.4	$1.7\text{x}10^{-4}$	$5.0\ \text{x}10^{-2}$	$1.3\ \text{x}10^{-1}$
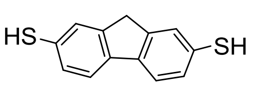 **25**	1.1	$1.4\ \text{x}10^{-4}$	$9.9\ \text{x}10^{-2}$	$1.4\ \text{x}10^{-1}$
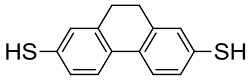 **26**	16.8	$2.2\ \text{x}10^{-4}$	$8.9\ \text{x}10^{-2}$	$1.2\ \text{x}10^{-1}$
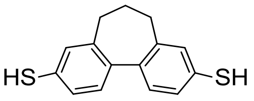 **27**	44.7	$1.3\ \text{x}10^{-4}$	$4.6\ \text{x}10^{-2}$	$7.4\ \text{x}10^{-2}$
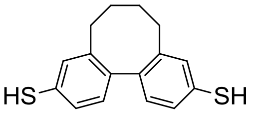 **28**	57.8	$7.0\ \text{x}10^{-5}$	$1.8\ \text{x}10^{-2}$	$3.8\ \text{x}10^{-2}$
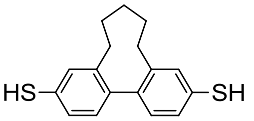 **29**	71.5	$1.7\ \text{x}10^{-5}$	$8.2\ \text{x}10^{-3}$	$1.6\ \text{x}10^{-2}$
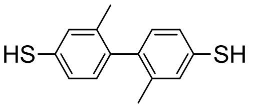 **21**	79.7	$1.3\ \text{x}10^{-5}$	$8.4\ \text{x}10^{-4}$	$4.1\ \text{x}10^{-2}$
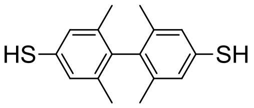 **30**	89.0	$9.0\ \text{x}10^{-6}$	$4.7\ \text{x}10^{-4}$	$5.0\ \text{x}10^{-4}$

Atop-atop and bridge-bridge junction geometries of the molecules were taken into account in the computational studies (Figure 1.32). Almost the full range of torsion angles between the phenyl rings was studied and it was observed that the junction conductance increases by the factor of $\cos^2\varphi$ (φ is the torsion angle between phenyl rings determined by X-ray analysis).

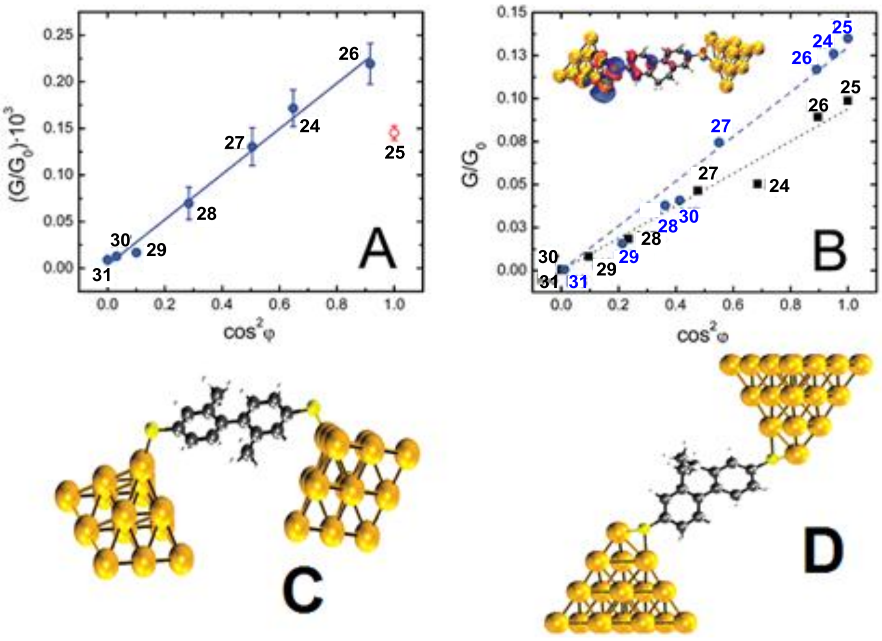

Figure 1.32 (A) Experimentally determined conductance of biphenyl molecules vs cos$^2\varphi$, where φ is the torsion angle between phenyl rings determined by X-ray crystallography. 25 excluded from the linear fit. (B) Conductance obtained from DFT calculations as a function of cos$^2\varphi$ (Dotted line represents atop-atop, dashed line represents bridge-bridge bonding between the STM tip and substrate. (C) Atop-atop bonded molecule to gold pyramid (D) Bridge-Bridge bonded molecule to a gold pyramid (Reproduced from reference [75])

1.3.4.3 Oligo(arylene)ethylenes (OAEs)

Oligo(aryleneethylenes) (OAEs) are widely studied in molecular electronics. OAEs possess a –(C≡C-aryl)$_n$- structure, where aryl groups can be phenyl, fluorenyl, thienyl or pyridyl.[76] OAEs have cylindrical structures and they are most stable in the co-planar conformation (Figure 1.33).[77] Unlike oligo(phenylenevinylenes (OPVs), oligo(phenylene-ethynylenes) (OPEs) cannot undergo *cis-trans* isomerism and are, therefore length-persistent molecules. This property and their scope for extensive functionalisation, makes OAEs good candidates for molecular wires.

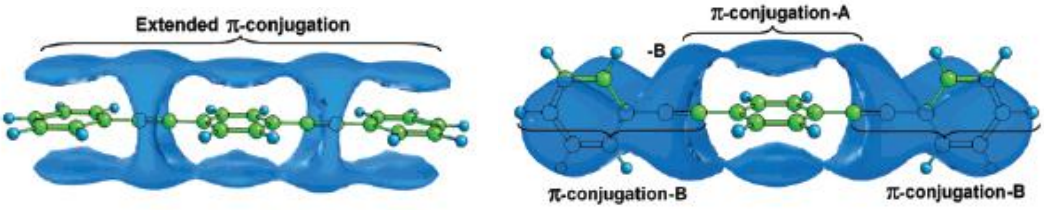

Figure 1.33 π- Conjugation features for OPE in different conformations (Reproduced from reference [77])

The single-molecule conductance of OPV derivative **32** and the OPEs **33-35** with thiol anchoring groups was studied by Huber *et al*. in 2008 using MCBJ methods.[21] (Figure 1.34)

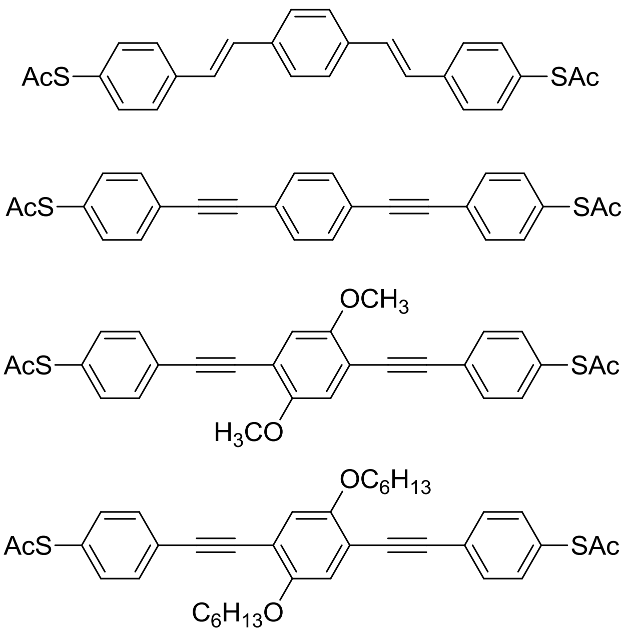

31

32

33

34

Figure 1.34 OPE and OPV molecules studied in reference.[21]

The results showed that the conductance of **32** was slightly higher than that of OPEs and solubilising alkyl groups on **34** and **35** did not have any influence on either the conductance or the thiolate binding to the gold surface. This is an important observation for subsequent studies on longer OPE / OPV systems where side-chains are essential for solubility.

1.3.4.4 Mono Anchored Molecular Wires

In 2008, Wu et al. reported the electron transport through aromatic π-π stacking of two oligo(phenyleneethylene) molecules.[78] In this study, mono-thiolated OPE systems were studied by the MCBJ technique (Figure 1.35).

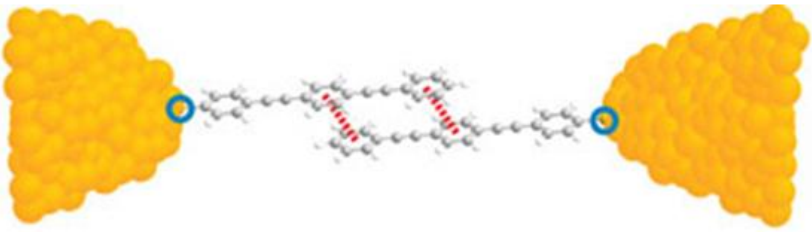

Figure 1.35 The proposed staggered π-π stacking of a pair of mono-thiolated OPE molecules between gold electrodes (Reproduced from reference [78])

When an OPE-dithiol molecule was placed between two gold electrodes of a MCBJ cell, a sudden current decay followed by a plateau for single-molecular conductance was observed. When OPE-monothiol solution was placed in a MCBJ cell, one OPE molecule bonded to one electrode and another molecule bonded to the other electrode with individual thiol groups: a current plateau was observed if the gap between the electrodes was sufficient for *π*-*π* stacking between the two (mono-anchored) OPEs. The current value of the *π*-*π* stacked pair of OPEs is not as high as that for single-molecule conductance of a di-anchored OPE (Figure 1.36). Another proof for electron transport via *π*-*π* stacking is the distance between the electrodes, which was larger than the length of single OPE molecule.

In subsequent work, a Durham-Liverpool-Lancaster collaboration showed that similar *π*-*π* stacking in mono-thiolated OPEs could be observed in STM-BJ studies. Furthermore, this work established that bulky *t*-butyl substituents on the central ring prevented *π*-*π* stacking in the junction.[79]

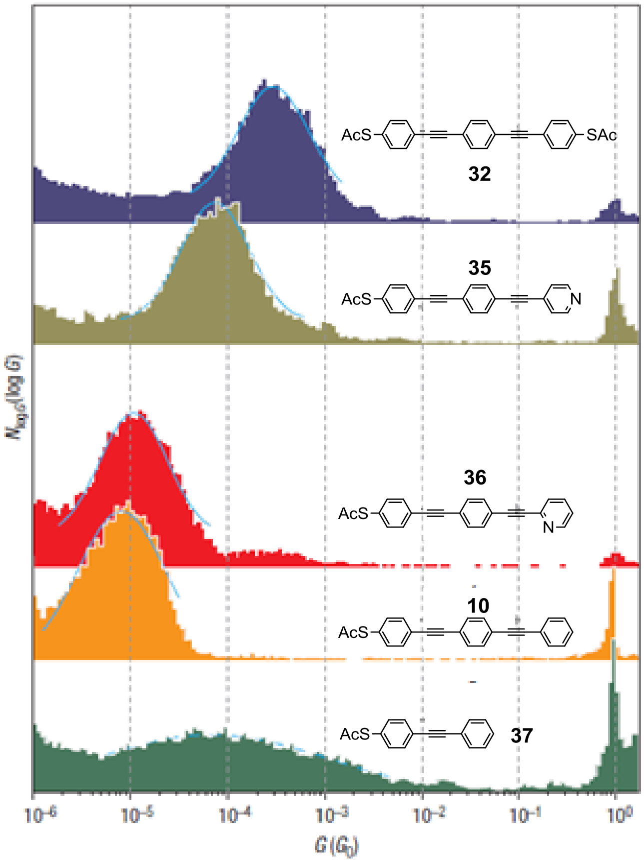

Figure 1.36 Conductance histograms for the molecules studied by the Schönenberger group from reference [78].

Chapter 2

The Effect of the Anchoring Group on the Single Molecular Conductance of Tolanes

2.1 Introduction

The efficient formation of molecular junctions is a prerequisite for addressing charge transport in molecular components and devices.[23,34,76] As briefly explained in Chapter 1, several approaches have been developed to monitor and to characterise charge transport in molecular junctions. A critical issue in all single-molecule experimental techniques is the electrical contact between the single and/or the small ensembles of the molecular wires and the macroscopic leads. Tour and co-workers addressed this problem by introducing thiol anchoring groups on both termini of the molecular wires.[69] Generally, the ideal molecular anchoring group should form reproducible and mechanically stable contacts with well-defined binding sites. To optimise charge transport, a second essential property is the strong electronic coupling between the ends of the molecule and the macroscopic (metal) electrodes.[80,81] Chemical synthesis offers unique possibilities to tailor anchoring groups to specific contact sites.

Conjugated molecules which possess delocalized π–systems have been utilized extensively as molecular wires in metal-molecule-metal junctions.[7,76] In this context, oligo(phenyleneethynylene) (OPE) derivatives with three or more [phenyl–C≡C–] units end-capped with thiol anchor groups are a prototype family of compounds which have been integrated into device structures for studies of their electronic transport properties, including single-molecule conductance.[21,82-85]

It is notable that the simpler, shorter, tolane (diarylethyne) analogues functionalized with terminal anchor groups have been less well studied.[81,86,87] Tolanes, like OPEs, are length-persistent, rigid-rod molecules,[88] i.e. they cannot be stretched, in contrast to molecules with saturated alkane linkers. Also there is no possibility of *Z/E* isomerism in tolanes, in contrast to their diarylenevinylene counterparts. However, the barrier to rotation about the phenyl–ethynyl bond is low, so the conformations of tolanes in molecular junctions can involve a range of dihedral angles between the planes of the phenyl rings. *Ab initio* calculations for OPEs have shown that these different conformations can have a significant effect on the transport properties, with coplanar phenyl rings giving rise to maximum conjugation and the highest conductivity values.[77,89]

In this chapter, our aim is to synthesise tolane derivatives with different anchoring groups and investigate the effect of these anchor groups on the charge transport properties. We identified tolane derivatives with different anchoring groups suitable for assembly between two gold electrodes to enable the role of different anchor groups on the transport properties to be quantitatively assessed at the single-molecule level because they possess a conjugated rod-like backbone, their synthesis is straightforward and their molecular length (ca. 1.1-1.6 nm, including the anchors) is ideally suited to both MCBJ and STM-BJ experiments.

2.1.1 Common Anchor Groups Used in Molecular Electronics

Amino (NH_2), pyridyl (PY) and thiol (SH) groups are the most frequently used “chemical” anchoring groups in charge transport studies of single-molecule junctions because of their stable binding to metals (often gold electrodes) as well as their reasonable electrical coupling in nanoscale hetero-junctions with contact to macroscopic leads.

Thiol is the first and most widely studied anchor group due to its strong binding affinity to many metals such as gold, copper and silver.[23,34,90] Charge transport through S-bound molecular junctions is dominated by hole transport through the HOMO because this is the closest level to the metal Fermi level.[73,91] Several research groups have demonstrated that the thiol anchoring group binds to different sites on metal surfaces, such as gold, which leads to a wide spread in experimentally measured conductances.[35,90] Furthermore, the strong covalent bond between S and gold surfaces leads to distinct changes in the surface crystallography, such as lengthening the Au-Au spacing between the first and the second layers[92] which may affect the conductance characteristics of a single-molecule junction. The strong interaction between SH and the metal electrodes often leads to rather high conductance values. On the other hand the SH moiety attached to an aromatic system is not stable in the presence of oxygen; thus requires a protection group and in situ deprotection under an inert atmosphere, prior to the junction formation.

The amine group has been exploited as an alternative to thiol due to its relatively uniform binding geometry. Venkataraman and co-workers showed in a series of recent papers that the conductance of the amine – gold bond does not significantly change from junction to junction because of the interaction of the N lone pair electrons to gold electrodes.[70,93] The conductance of NH_2- anchored metal | molecule | metal junctions is HOMO controlled.[94]

Experimental studies with 4,4′-bipyridine (**2**) suggested that the PY anchoring group can form stable and reproducible molecular junctions.[34] However, the surface coordination sites and binding configurations of pyridyl anchors may change upon stretching of a molecular junction.[95] It was shown that the charge transport through pyridyl anchored molecules is predominantly controlled by the LUMO.[95,96] This data is also supported by a study of a single-molecule transport with pyridyl anchored oligoynes by our research group in the collaboration with Liverpool and Lancaster Universities.[86]

The contact characteristics of biphenyl derivatives with nitrile (CN) anchoring groups was studied by Wandlowski and co-workers.[97] According to the DFT calculations, the charge transport through these molecules is controlled by the LUMO of the molecule.[97]

Other anchoring groups explored include nitro,[81] isonitriles (NC),[80,98] carboxylic acid,[99] trimethyltin[100] and fullerene.[101,102]

Tao *et al*. compared conductances of aliphatic molecular wires with COOH, SH, and NH_2 anchoring groups. They reported that the junction conductances decrease in the following sequence: SH > NH_2 > COOH.[99] Kushmerick *et al*. showed in experiments with SH-, PY-, and NO_2-terminated OPE derivatives that the nature of the anchoring group has a distinct effect on the current rectification.[58] These conclusions are supported by DFT calculations for SH, CN, NO_2, and NH_2 anchoring groups performed by Erbe and co-workers[81] and another experimental report by Loertscher *et al*. with NC and SH substituted molecular rods.[80] Both publications[80,81] are based on an analysis of current (I)−bias voltage (V_{bias}) traces acquired in an MCBJ setup under vacuum conditions. In particular, the electronic coupling at the respective molecule−metal interfaces was investigated.

As discussed in Chapter 1, MCBJ and STM-BJ experiments provide a unique platform for exploring the evolution of molecular contacts during the formation and breaking processes under controlled conditions. Many junction configurations can be sampled and characterised quantitatively on the basis of a statistical analysis of current−distance and/or current−voltage traces. Comparison with *ab initio* calculations enables identification of the most probable junction geometries as well as structural changes during the pulling and/or breaking processes.[103,104] Besides the conductance characteristics, the plateau length in current−distance traces provides additional information about the stability and evolution of molecular junctions. At room temperature, the plateau length and stability are dominated by the binding strength of the anchoring group and competition with thermal vibrations. Tao *et al*. found, on the basis of room temperature STM-BJ studies in toluene, that NH_2-terminated aliphatic wires form longer plateaus, i.e. more stable molecular junctions, than COOH-terminated wires.[99] Venkataraman *et al*. compared amines with dimethylphosphine (PMe_2) and methyl sulfide (SMe) anchoring groups.[105,106] These authors reported the stability sequence: PMe_2 > SMe > NH_2. A narrow distribution of both binding sites and conformations is an ideal platform to explore molecular details of the evolution of junction structure and conductance during the stretching process. This strategy was explicitly addressed in comparative experimental work with benzene derivatives having SH-, NH_2-, and NC termini.[70]

Most experimental reports to date have focused on establishing conductance values for specific systems and the comparison of measurements and predictions by different research groups. However, the evolution of a molecular junction during the stretching process has rarely been investigated.[95,105,107,108] The analysis of entire stretching traces is essential for in-depth understanding of contact geometries, binding configurations, molecular-junction evolution, the most probable junction characteristics and their spread, and differences between the data from various experimental approaches. Kruger *et al*. reported *ab initio* molecular dynamics (MD) simulations of gold nanowires formed in the presence of chemisorbed thiolates.[107] They demonstrated the formation of monatomic gold nanowires leading to the preferential breaking of Au−Au instead of Au−S bonds during a simulated rupture event. This approach also established the formation of gold clusters during the stretching process.[107] The result is in agreement with an earlier proposal.[109] Konopka *et al*. showed for the copper−alkylthiolate interface that mechanical stress, as typically applied in a molecular junction, stabilises selectively the S−C bond due to the suppression of fluctuations and undercoordination of the sulfur atom as a result of a strongly uniaxial stress upon pulling.[110] Very recently, Kim *et al*. reported in a combined experimental and theoretical study of SH- and NH_2-terminated octanes, bound at low temperatures to gold electrodes, that the SH-terminated molecules cause large deformations of the Au electrode.[111] This effect is much weaker for amine-terminated molecular wires. However, the full simulation of the evolution of molecular configuration changes during the stretching process remains a major challenge.

In this chapter, we present studies of charge transport during the evolution of single-molecular junctions of tolane derivatives with four terminal end groups, PY, SH, NH_2, and CN, attached to gold leads. We report complementary experiments in STM-BJ and MCBJ techniques, both in solution and under environmentally controlled conditions. On the basis of a statistical analysis of conductance–distance traces, we have explored the evolution of the single molecular junctions during the stretching process. Conductances have been determined for different junction geometries and their stability and their probability of formation has been addressed. Our aim was to develop an understanding of the entire stretching process in an attempt to evaluate the specific features of the anchoring groups in promoting efficient electronic and mechanical coupling to metal electrodes. DFT-based calculations performed by David Manrique and Colin Lambert (Lancaster University) reveal the nature of the transport channels involved for selected stable binding geometries. These computations have been extended to provide a simulation of entire conductance versus displacement traces.

2.2 Synthesis and Experimental Setup

Compound **41** was synthesised according to the literature route.[112] Commercially available 4-iodopyridine **38** was reacted with trimethylsilyl acetylene under standard Sonogashira cross-coupling conditions to give **39** in 92% yield. The TMS protecting group was removed in high yield by using tetrabutylammonium fluoride (TBAF) and a subsequent Sonogashira cross-coupling between 4-ethynylpyridine **40** and 4-iodopyridine **38** gave **41** in 91% yield (Scheme 2.1).

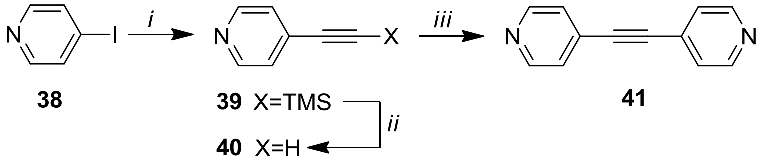

Reagents and conditions: (i) TMSA, Pd[$(PPh_3)_4$], Et_3N, CuI, 3h, rt, 92%; (ii) TBAF, THF, 30 mins, rt, 85%; (iii) **38**, Pd[$(PPh_3)_4$], (i-Pr)$_2$NH, CuI, 5h, rt, 91%.

Scheme 2.1 Synthesis of compound 41.

The terminal alkyne **46** is the key building block for thiol anchored OPEs and oligoyne molecules. The first 7-step synthesis of **46** was developed by Dr Wang in our laboratory.[113] With modification of the deprotection of the TMS group, compound **46** was synthesised in four steps. The commercially available 4-bromothiophenol **42** was protected by using *t*-BuCl. Then compound **43** was lithiated and reacted with I_2. The *t*-butyl group was transformed to the acetyl group using BBr_3 and acetyl chloride without further purification to give **44** in 81% yield. 4-Iodothioacetate **44** was coupled with TMSA under Sonogashira conditions. The deprotection of the alkyne by TBAF gave the terminal alkyne **46**. Finally, Sonogashira coupling with **44** gave desired bis(thioacetate) protected tolane **47** (Scheme 2.2).

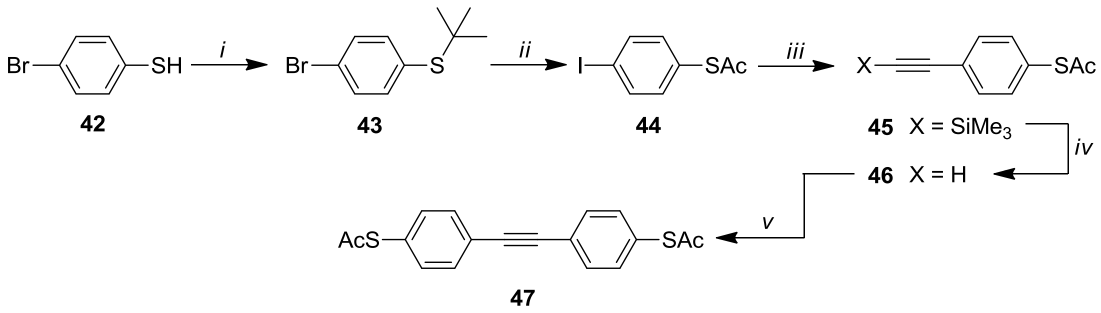

Reagents and conditions: (i) *t*-BuCl, $AlCl_3$, overnight, rt, 88%; (ii) (1) *n*-BuLi, I_2, THF, -78°C, 7h, (2) BBr_3, AcCl, DCM_1, 5h, rt, 81% (one pot); (iii) TMSA, $Pd[(PPh_3)_4]$, $(i\text{-Pr})_2NH$, CuI, 3h, rt, 92%; (iv) TBAF, THF, then AcOAc, rt, 67%; (v) **44**, $Pd[(PPh_3)_4]$, $(i\text{-Pr})_2NH$, CuI, overnight, rt, 79%.

Scheme 2.2 Synthesis of thioacetate anchored tolane (47).

Amine (**50**)[114] and nitrile (**53**)[115] analogues were synthesised by Sonogashira coupling reactions between commercially available iodo and ethynyl compounds in 47% and 55% yields, respectively (Scheme 2.3).

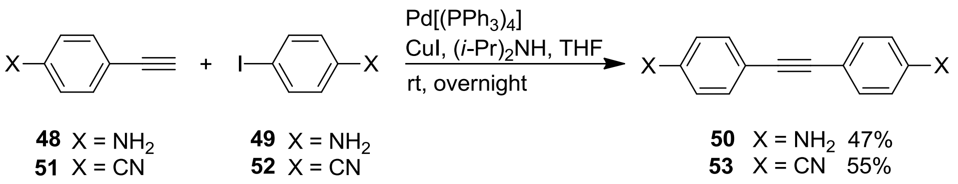

Scheme 2.3 Synthesis of amino (50) and nitrile (53) anchored tolane compounds.

The single-molecule conductance experiments were carried out in the group of Prof Wandlowski at the University of Bern, primarily by Wenjing Hong, Pavel Moreno Garcia and Artem Mischenko. The present author contributed to the experimental work and data analysis during visits to Bern.

The transport characteristics were studied using both STM-BJ and MCBJ measurements, in solution, at room temperature, and in an argon-protected environment. Typically, a freshly prepared solution containing a 0.1 mM concentration of the sample molecule in a mixture of 1,3,5-trimethylbenzene (TMB) (mesitylene) and tetrahydrofuran (THF) (ratio 4:1 v/v), was placed in the liquid cell. Deprotection of the diacetyl derivative of **47** was performed in situ by adding four equiv of tetrabutylammonium hydroxide.

The STM-BJ measurements were performed with a modified Molecular Imaging Pico-SPM housed in an all-glass argon-filled chamber. The conductance (*G*)– distance measurements were performed by applying a constant bias voltage V_{bias} between the tip and substrate and recording the corresponding current signal through a linear amplifier stage. The MCBJ experiments are based on the formation and breaking of molecular junctions between a notched, freely suspended 0.1 mm thick gold wire, supported on spring steel sheets and fixed with glue. The sample sheet was bent with a pushing rod controlled by the combination of a stepper motor and a piezo stack. The bending was initialised by the stepper motor. Once the measured current reached a value corresponding to 15 G_0, the stepper motor paused and the piezo stack was activated. This strategy could reduce significantly noise contributions from the operation of the stepper motor. After the junction was completely broken, the piezo stack was reset and the rod pushed down by the stepper motor.

2.3 Results and Discussion

Figure 2.1 displays typical conductance−distance stretching traces (on a logarithmic scale) for the PY derivative **41** in the STM-BJ (Figure 2.1C) and MCBJ (Figure 2.1D) setups at a bias potential V_{bias} = 0.10 V. Characteristic quantised conductance steps occur at integer multiples of $G_0 = 2e^2/h$, the fundamental quantum conductance. Opening the gap results in an elongation of the gold−gold junction and decreases the number of gold atoms in the constriction, which causes the conductance to change by up to ~1 G_0, where the contact between the tip and Au(111) substrate of the STM-BJ, or between the two gold leads of the MCBJ, consists of only one gold atom. Subsequently, an abrupt decrease of the current over several orders of magnitude occurs, which is assigned to the "jump out of atomic contact",[95] and additional features are observed at $G < 10^{-3}$ G_0. The curves show well-developed plateaus in the range from 10^{-3} to 10^{-4} G_0 characterised by a small, but distinct, monotonic decrease in the conductance with stretching distance. This pronounced high-conductance plateau region (H) is followed by up to two additional, less extended step-like features in the conductance traces, labelled M and L, until the noise level is reached. The transitions are not always sequential. We observed traces with plateaus in the H region with either a sharp drop directly into the L regime or a drop via the M stage. The H, M, and L features are assigned to molecular junctions bridging the gap between the two gold electrodes. The noise level is different in the STM-BJ ($G \le 10^{-6}$ G_0) and MCBJ ($G \le 10^{-7}$ G_0) measurements because of the different pre-amplification stages used. Furthermore, due to thermal fluctuations at room temperature, the molecular plateau regions H, M, and L vary from one trace to another in both experimental configurations, which might reflect different binding geometries and/or switching events between different molecular configurations in the individual stretching traces.

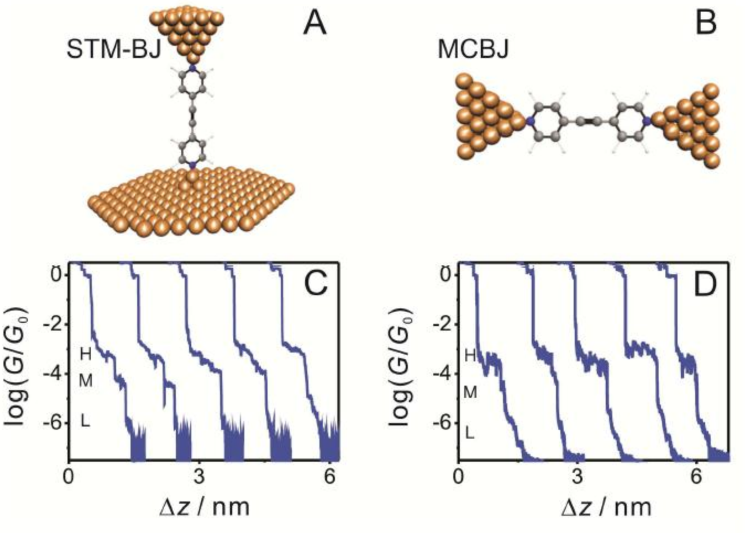

Figure 2.1 (A, B) Schematics of the STM-BJ (A) and MCBJ (B) configurations. (C, D) Typical conductance–distance traces of 0.1 mM 41 (PY) in THF/TMB (1:4, v/v) recorded in the STM-BJ (C) and MCBJ (D) configurations. H, M, and L refer to high, medium, and low conductances, respectively.

Several thousand individual traces were recorded and subsequently analysed by constructing all-data-point histograms, without any data selection, to extract statistically significant results from the different junction configurations. Figure 2.2 displays the corresponding one-dimensional (1D) histograms for the four derivatives, constructed from both the STM-BJ (black) and the MCBJ (red) measurements. A clear peak around 1 G_0 is observed, which represents the breaking of the last gold–gold atomic contact, and there is a prominent molecular conductance feature H at $10^{-3.3}$ G_0 (PY), $10^{-2.7}$ G_0 (SH), $10^{-3.1}$ G_0 (NH_2), and $10^{-4.6}$ G_0 (CN). Except for the CN derivative **53**, a second low-conductance peak (L) is clearly resolved for **41** (PY, $10^{-6.0}$ G_0) and **50** (NH_2, $10^{-4.8}$ G_0); there is a more shallow peak for the dithiol derivative **47**. Here, the data scatter between 10^{-4} and 10^{-6} G_0. STM-BJ experiments (black trace in Figure 2.2B) revealed a broad, single, second conductance feature around $10^{-4.7}$ G_0, while two broad maxima are resolved in the MCBJ data (red trace) at ca. $10^{-4.2}$ and $10^{-5.8}$ G_0, respectively. A unique characteristic of **41** is a third molecular conductance feature M which is visible between the H and L regions. For the MCBJ data, the M feature is much less pronounced in the conductance histogram (Figure 2.2A). Limitations in extracting the properties of the L region, in particular in the STM-BJ setup with **41**, could be overcome by complementary MCBJ experiments, which were carried out with a preamplifier stage of higher current sensitivity.

Table 2.1 Most Probable Conductance Values of 41, 47, 50 and 53 from Both MCBJ and STM-BJ Measurements

	H (STM-BJ) log (G_H/G_0)	H (MCBJ) log (G_H/G_0)	L (STM-BJ) log (G_L/G_0)	L (MCBJ) log (G_L/G_0)
PY (41)	-3.3	-3.3	-6.0	-6.0
SH (47)	-2.7	-2.7	-4.7	-4.2/-5.8
NH_2 (50)	-3.1	-3.1	-4.8	-4.9
CN (53)	-4.6	-4.6	-	-

The statistically most probable conductance states of the single-molecule junctions formed by **41**, **47**, **50** and **53** were obtained by fitting Gaussians to the characteristic maxima in the conductance histograms. All conductance values (H and L) are summarised in Table 2.1. They demonstrate excellent agreement between STM-BJ and MCBJ experiments. The most probable main conductances H decrease in the following sequence: SH > NH_2 > PY ≫ CN. While the values for these three molecules are rather similar, the CN anchors lead to a significantly lower junction conductance for **53**. The same sequence was observed in recent single-molecule junction conductance studies of substituted biphenyls.[75,97,116] The accessible L data in the tolanes show a similar trend, i.e., SH > NH_2 > PY. However, their values spread over nearly two orders of magnitude between 10^{-4} and 10^{-6} G_0. A low-conductance feature for the CN-substituted compound **53**, if present, could not be resolved due to masking by instrumental noise.

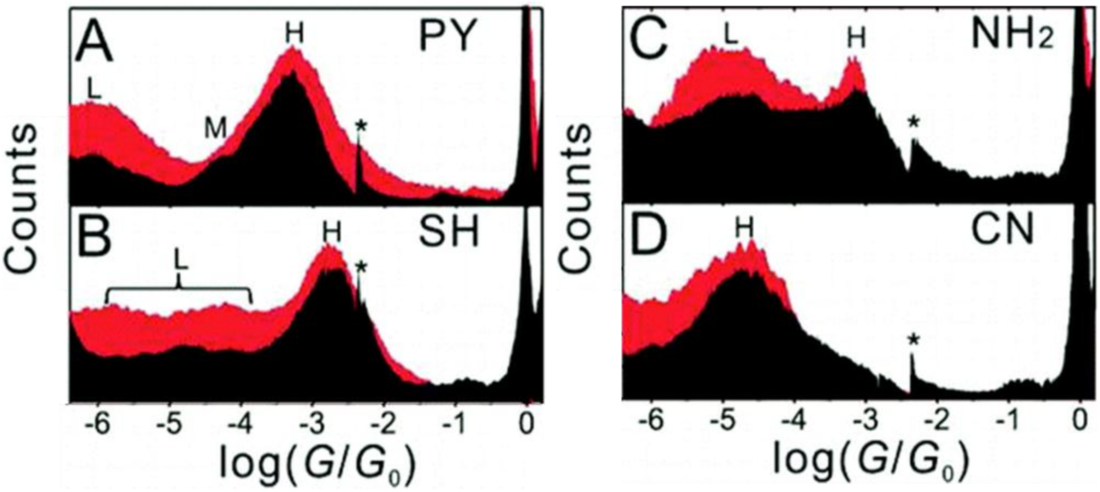

Figure 2.2 Conductance histograms of (A) PY, (B) SH, (C) NH_2, and (D) CN terminated molecules 41, 47, 50 and 53 obtained from 2000 curves recorded in the STM-BJ (black) or the MCBJ (red) setup. H = high-conductance feature, M = medium-conductance feature, and L = low-conductance feature. The asterisk indicates an experimental artifact originating from switching ranges in the linear amplifier in the STM-BJ setup.

The data analysis was extended by constructing two-dimensional (2D) conductance vs. displacement histograms.[101] This strategy provides direct access to the evolution of molecular junctions during the formation, stretching, and breakdown steps. The precise calibration of the distance scale in the STM-BJ and MCBJ measurements was carried out by tunnelling experiments in the clean solvent.

Panels A−D of Figure 2.3 display the 2D conductance versus displacement histograms[101] of the four tolane derivatives as constructed from 2000 individual STM-BJ traces. To assign a common scale to each conductance−distance trace, a relative displacement was introduced with Δz, defined so that $\Delta z = 0$ at 0.1 G_0.[97] This procedure leads to an accurate alignment of the conductance−distance curves because of the sharp drop in conductance at $G < G_0$. Figure 2.3A−D shows features in the upper part of the histograms which are attributed to the quantum conductance of gold−gold atomic contacts.

Once the gold−gold contact breaks ($\Delta z = 0$), the gold atoms snap back quickly by an amount Δz_{corr} estimated as ~0.5 nm to create a nanogap between the two gold electrodes.[117] After adding this correction to the relative displacement, an absolute displacement $z = \Delta z + \Delta z_{corr}$ was obtained which we attribute to the electrode separation. The junctions with molecules trapped between the adjacent leads undergo several structural changes during the stretching process (i.e. with increasing displacement Δz), leading to the evolution of distinct data density clouds until the noise level is reached. All the tolanes studied reveal clear high-conductance clouds, indicated by the H regions in Figure 2.3A−D.

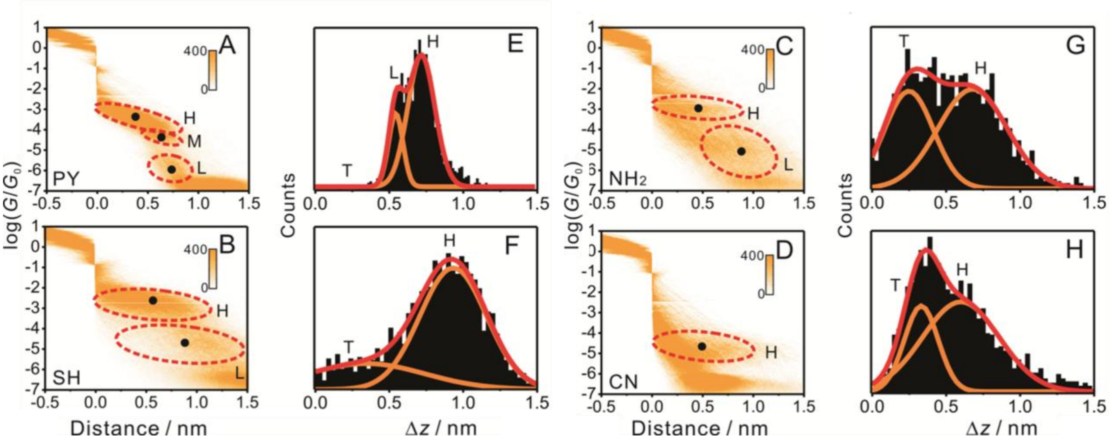

Figure 2.3 (A−D) 2D conductance−relative displacement histograms from STM-BJ experiments. (E−H) Relative displacement (Δz) distribution from STM-BJ experiments. The relative displacement histograms are obtained from conductance traces between 0.1 and $10^{-3.7}$ G_0 (SH), $10^{-4.0}$ G_0 (NH_2), and $10^{-5.6}$ G_0 (CN). In the case of PY, we consider medium conductances as a sub-feature of high conductances and construct relative displacement histograms from conductance traces between 0.1 and $10^{-5.0}$ G_0.

In particular, the pyridyl and thiol derivatives **41** and **47** show well-defined high-conductance clouds centred on the most probable conductances $10^{-3.3}$ and $10^{-2.7}$ G_0, respectively. The boundaries of the density clouds of the NH_2 ($10^{-2.2}$ to $10^{-4.2}$ G_0) and CN ($10^{-4.2}$ to $10^{-5.5}$ G_0) derivatives **50** and **53** are less clearly resolved, illustrating that, for these junctions, a significantly larger percentage of traces do not lead to junction formation. The "smearing out" effect results from the corresponding tunnelling-through-solvent traces. As indicated in the 1D histograms of Figure 2.2, we also observed clear L features for **41** (10^{-5} to 10^{-6} G_0), **47** (10^{-4} to 10^{-6} G_0), and **50** ($10^{-4.5}$ to 10^{-6} G_0) which have not been reported previously for these molecules. No L region was detectable for the CN-derivative **53**, again most probably due to sensitivity limitations of both setups. A medium conductance region (M) for **41** observed in the 1D histograms of Figure 2.2A appears in Figure 2.3A as a small but distinct data density cloud between the H and L states ranging from $\sim 10^{-4}$ to $\sim 10^{-5}$ G_0. Regarding the evolution of the two M and H regions for **47** (SH) and **50** (NH_2) and the M, H, and L regions for **41** (PY), the analysis of the 2D histograms of Figure 2.3 shows clearly that the H state evolves immediately after breaking of the gold–gold contact, while M and L states develop at a later stage during the displacement, at a relative displacement Δz. Molecular junctions of **41** trapped between two gold electrodes were explored by Wang *et al.*[86] and Velizhanin *et al.*[118] using an STM-BJ approach. The literature data ($10^{-4.0}$ to $10^{-3.3}$ G_0 and $10^{-3.7}$ to $10^{-3.5}$ G_0) agree within half an order of magnitude with our findings for the M and H states, respectively. However, no evidence was found previously[86,118] for the L region. In this context, two conductance states were also found by Quek *et al.*[95] for 4,4′-bipyridine. In a comparative study of dithiolate and carbodithioate linkers, Xing *et al.*[119] reported a conductance value for **47** of $10^{-3.6}$ G_0. No suggestion of this value was found in the present work. On the other hand, the most probable conductance values, $10^{-3.1}$ and $10^{-3.2}$ G_0, as reported by Widowsky *et al.*[87] and Hybertsen *et al.*[120] for **50** in 1,2,4-trichlorobenzene are in good agreement with our data for the H state. Finally, it is noted that Zotti *et al.*[81] presented I–V_{bias} curves from an MCBJ experiment with **53**, from which we estimate a low bias junction conductance of $10^{-4.6}$ G_0.

Further analysis of the relative-displacement histograms of Figure 2.3E–H is now presented. The conductance histograms of Figure 2.2 are obtained by projecting the 2D data of Figure 2.3A–D onto the vertical axis. Calculation of the displacement from the relative zero position (0.1 G_0) to the end of the high conductance feature [$10^{-3.7}$ G_0 (SH), $10^{-4.0}$ G_0 (NH_2), and $10^{-5.6}$ G_0 (CN)] of each individual trace yields the relative displacement distribution histograms of Figure 2.3E–H. The PY derivative **41** develops no stretching traces shorter than 0.3 nm, and the 2D histogram (Figure 2.3A) shows no features attributed to direct tunnelling (T). On this basis we conclude that 100% of the stretching traces lead to the successful formation of a single-molecule junction. Further displacement, Δz, leads to a partial transformation into the M and L states (Figure 2.3E). In contrast, the relative-displacement distributions of the SH, NH_2 and CN analogues reveal clear peaks labelled with T around 0.2−0.3 nm which represent contributions from direct tunnelling traces. The peaks marked with L (and H) in Figure 2.3E−H represent the contribution of true molecular junctions.

Taking the area ratio between the molecular contributions of the H, M, and L states and the total data density in Figure 2.3E−H leads to a junction formation probability of the H state of 90% for **47** (SH) 60% for **50** (NH_2) and 70% for **53** (CN). After the high-conductance junctions break, a transformation occurs to the low-conductance state. Extending the analysis of the relative displacement to the entire accessible conductance range between 10^{-1} and 10^{-6} G_0 yields an estimation of the most probable relative displacements Δz_L* in the L regions. The trend is similar to that of the H regions, with the longest value of Δz_L* for **47**, (1.2 nm) followed by **50** (1.0 nm) and **41** (0.9 nm).

For **41** (PY), as shown in Figure 2.3E, most of the molecular junctions break at a relative displacement Δz_L* of ca. 0.7 nm. A detailed analysis reveals that 24% of the junctions break from the H state and transform to the L state at ca. 0.5 nm, 22% have the transformation at ca. 0.7 nm, and 54% transform from the H state via the M state into the L state at ca. 0.7 nm. All the traces ruptured subsequently at ca. 0.8 nm from the L state. A similar analysis for **47**, **50**, **53** (Figure 2.4) demonstrates that the majority of molecular junctions [(91% (SH), 59% (NH_2), and 70% (CN)] break in the H state with a smaller contribution from the respective L state [9% (SH), 41% (NH_2), or 30% (bare tunnelling, CN)] without formation of the H state.

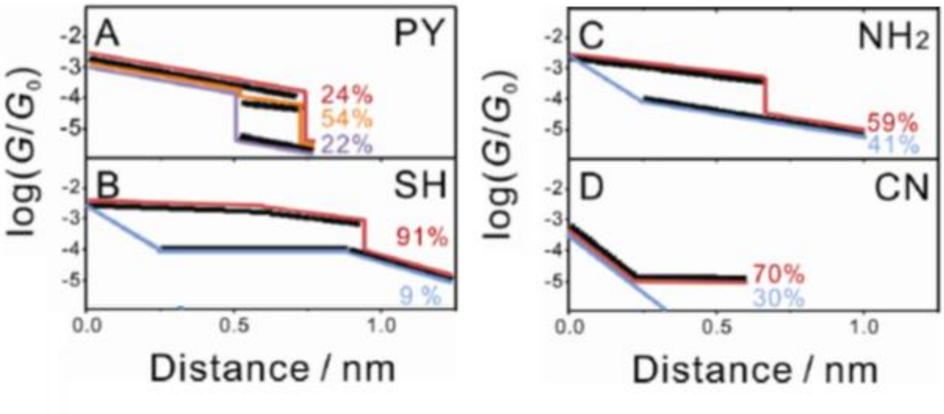

Figure 2. 4 Evolution of the different conductance states of (A): 41 PY (B): 47 SH (C): 50 NH_2 (D): 53 CN. The black traces were obtained from the analysis of the experimental data displayed in Figure 2.2.

Adding the snapback distance Δz_{corr} to the relative displacement Δz yields the absolute displacement $z^* = \Delta z + \Delta z_{corr}$, which is a measure of the electrode-electrode separation. The values of the most probable absolute displacements z_H^* for the H states match the molecular lengths of **41** (PY) and **47** (SH) which suggests that the most probable breaking of the junction occurs when the molecule is in an upright orientation with respect to the surface normal. The other two derivatives, **50** (NH_2) and **53** (CN) possess values of z_H^* which are lower than their molecular lengths, suggesting breakage in a tilted orientation. Examination of the junction displacement into the M-(PY) and L-conductance (PY, SH, and NH_2) regions reveals most probable absolute displacements z_L^* which are longer than the molecular length. This suggests, in particular for **41** (PY) and **47** (SH) the pulling out of gold adatoms[107,109,112] and/or the formation of inter-molecular π-stacking assemblies.[78,79]

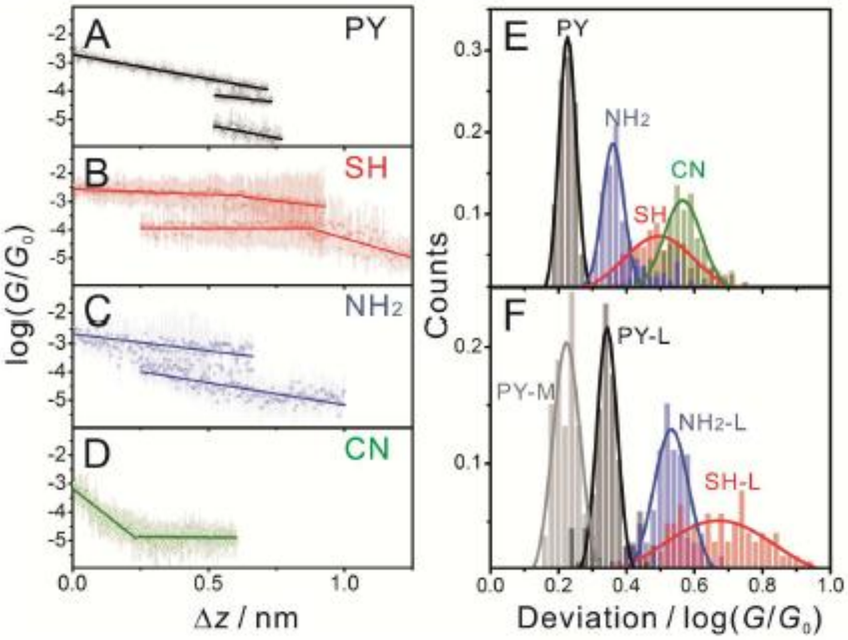

Figure 2.5 (A–D) Statistically averaged conductance–distance traces (circles) with variation indicated by the standard deviation (bar) and fitting of the traces (line) of 41 PY (A), 47 SH (B), 50 NH_2 (C), and 53 CN (D). (E, F) Distribution of variations in different positions in the (E) H range and (F) M/L range during stretching.

The analysis of the 2D histograms and the displacement characteristics provide important information about the evolution of molecular junctions in the H plateau regions and their transition into the M and L configurations. Venkataraman *et al.* used the width of the conductance peak to evaluate variations of the binding geometries of SH and NH_2 anchoring groups on saturated alkyl chains.[93] However, the peak width also contains contributions from the conductance decay during the stretching process as caused by changes of the tilt and/or torsion angles of the molecules[121] and evolution of the binding sites. In an attempt to exclude the influence of the conductance decay, the most probable conductance values were calculated, as well as the standard derivations, from Gaussian fits to cross-sections of the 2D histograms at different displacement positions Δz (Figure 2.5). Compared to the rather constant plateau conductances observed when breaking monatomic metal contacts,[122] the plateaus of molecular junctions extend over much longer distances, with conductance changes during the stretching process of up to 2−3 orders of magnitude. This feature reflects the evolution of different molecular orientations and junction configurations during the stretching until breakage occurs. As illustrated in Figure 2.5, **41** (PY) and **50** (NH_2) show a linear conductance decay during the stretching in the H region with slopes of 1.9 and 1.2 $\log(G/G_0)$/nm, respectively. Our stretching simulations suggest that this trend partly reflects the sliding of molecular rods along the electrode surfaces.[93] For derivate **47** (SH) a linear dependence of the conductance on displacement Δz is also seen in the H region. At longer displacements, the slope of $|\log(G/\ G_0)|$ versus Δz increases significantly, which may reflect changes in the Au−S coordination geometry. The CN derivative **53** also shows an inflection point. However, its position at ca. 0.3 nm primarily reflects contributions of “through-space” tunnelling at the beginning of the stretching process, which interferes with the molecular junction conductance in this displacement range. The statistically averaged conductance−distance traces (Figure 2.5A−D) show different conductance decays for the four anchor groups. This is assigned to differences in the evolution of the respective molecular junction configurations during the stretching process.

The distributions of conductance-variation histograms shown in Figure 2.5E were obtained by decomposing the 2D histograms shown in Figure 2.3 into 1D histograms at different relative displacements Δz. Subsequently the main features in the H and L regions were fitted with Gaussians to extract the local maximum value of the respective conductance and its variation (i.e., standard deviation) at each relative displacement Δz. The resulting distributions of the variation for all four derivatives in the H region are plotted in Figure 2.5E. The widths of the distributions of the variations decrease according to the following sequence: PY < NH_2 < SH < CN. Attempts to analyse the L regions in a similar way yielded a rather large distribution in the variation of the respective conductance values (Figure 2.5F), which correlates with the weaker interaction between the different molecules in these junctions and a larger variation in possible binding geometries. Moreover, the conductance deviation of the M feature of **41** (PY) is close to that of the H feature and clearly represents the characteristics of a single-molecule junction.

2.4 Conclusions

In this chapter four symmetrical tolane derivatives with different anchoring groups have been synthesised and systematically compared and the following trends have been observed. First, from the conductance measurements in both MCBJ and STMBJ configurations, the PY (**41**), SH (**47**), and NH_2 (**50**) derivatives showed relatively high conductances, whereas for the CN (**53**) the conductance is significantly lower. Second, on the basis of an analysis of the conductance−displacement traces, PY and SH revealed statistically higher junction formation probabilities as well as higher molecular junction stabilities. This result is attributed to variability in the binding geometries and the higher binding energy. Third, PY and NH_2 showed the smallest conductance fluctuations over the entire stretching process.

The chemical inertness of the PY and CN anchors is attractive, since they are stable under ambient conditions and no deprotection step is needed. The SH moiety attached to an aromatic backbone is not stable in the presence of oxygen and thus requires a protecting group and in situ deprotection in an inert atmosphere before the start of the conductance measurements.[123] Furthermore, it is well-known that aromatic amines are often used as antioxidants, because these compounds act as H atom donors in radical reactions due to their relatively labile N−H bonds. Aromatic amines have low ionisation potentials and rather weak N−H bonds. They can undergo oxidation reactions and hydrogen atom transfer reactions rather easily.[124,125] Moreover, the NH_2 group is sensitive to light.

Comparable results for conductance−displacement measurements were obtained for both STM-BJ and MCBJ setups, which strengthens the experimental reliability of these single-molecule conductance measurements. According to the analysis of the conductance−displacement traces from the STM-BJ setup, PY exhibits the best anchoring performance of the four tolane derivatives analysed, with high conductance and 100% molecular junctions formed. This conclusion is also strongly supported by the theoretical calculations of the binding energy and binding geometry. Furthermore, current−voltage curves constructed for the most probable MCBJ molecular geometries allowed an estimate of the relative positions of the molecular levels with respect to the Fermi level, which facilitated the simulation of the dynamic stretching curves. Comparison between experiment and theory has yielded good agreement in the decays of the molecular conductance plateaus. This work highlights the underlying atomic-scale complexity of the stretching curves, and reveals crucial the role of the anchoring group in the evolution of the configuration of the single molecular junctions.

Chapter 3

Synthesis of Oligoyne Molecular Wires with Functionalised End-Groups and Their Transport Properties in Single-Molecule Junctions

3.1 Introduction

Conjugated polyyne molecules are of great interest as a family of carbon rich backbones.[126-128] They comprise an array of *sp*-hybridised carbon atoms with alternating single and triple bonds and almost cylindrical electron delocalisation in a one-dimensional chain.[128-130] Both shorter *sp* oligomers (oligoynes) and polyynes have been proposed for molecular electronics applications (wires, switches, non-linear optics etc.).[131,132] Their study is, therefore, of both fundamental and economic interest. Unlike oligo(phenylenevinylene)s (OPVs)[21] and oligo(phenyleneethylene)s (OPEs),[77,89] the extent of conjugation through the oligo/polyyne carbon backbone is not interrupted by phenyl rings or by bond rotations. Theoretical studies have predicted that polyynes should have excellent intramolecular electron- and charge-transport properties, exhibiting efficient molecular wire behaviour.[133,134] In this regard, experimental studies are very much an open issue.

Polyynes exhibit reduced stability with increasing length of the *sp* chain. The main strategies to stabilise longer derivatives are to terminate the chains with bulky aryl or organometallic groups[135-138] or to shield the polyyne backbone.[139,140] Without such stabilising groups, polyynes which are longer than eight acetylenic carbons (i.e. tetrayne derivatives) tend to decompose or polymerise rapidly at room temperature.[141,142] The stability of oligoynes will be discussed in Chapter 4.

As discussed in Chapter 1, in order to study the electronic properties of the metal | molecule | metal junction by STM or MCBJ methods[7,50,76,77,143-145] molecules need to be terminated by functional groups which have relatively high binding strengths to gold, e.g.

thiol,[99] pyridyl[34,146] and amino.[70] However, functional groups at the terminal positions can react with the oligoyne *sp*-backbone to form polymer-like structures,[147] and the bulky terminal groups which are known to stabilise longer polyynes are not suitable for anchoring the molecules onto metal surfaces. Consequently, it remains a challenge to synthesise polyynes with end-groups which will anchor the molecule to gold, yet will not react (inter- or intra-molecularly) with the *sp* backbone.

In previous studies, cumulenes, which are made of double bonded chain of carbon atoms, were proposed as ideal molecular wires by several research groups.[148,149] Lang and Avouris reported one of the first theoretical studies on the electron transport properties of cumulenes.[150] It was shown that the conductance oscillates as a function of the wire length, with odd-number carbon atom chains showing higher conductance than even-number carbon chains. This result is due to the HOMO of the odd-number carbon chains being located near the average Fermi level. Following on from reports of the electronic properties of graphene and graphene nanoribbons interest in cumulenes increased due to the possibility of carving a cumulenic carbon chain from graphene.[151,152]

A theoretical study from Crljen and Baranovic predicted that oligoyne chains end-capped with thiol moieties [$HS{-}(C{\equiv}C{-})_nSH$] show almost metallic-like conductance characteristics.[133] This series of molecules are expected to be highly unstable; therefore, experimental cross-checking of the theoretical results was not possible. Oligoynes and polyynes show higher conductance than cumulenes, due to the cylindrical π electron systems along the backbone. Garcia-Suarez and Lambert calculated the electron transport properties of oligoyne chains (2 to 12 atoms) end-capped by either 4-mercaptophenyl or 4-pyridyl groups.[134] It was shown that the conductance of thiol anchored oligoynes was much higher than their pyridyl analogues and that conductance was almost independent of length.

In this context, the first synthetic examples were stable 4-pyridyl (PY) end-capped derivatives containing up to a C8 (tetrayne) chain length [$PY{-}(C{\equiv}C)_n{-}PY$] (n =1, 2, 4) and their electronic properties at the single-molecular level were studied in STM-BJ experiments.[86] In this particular study, multiple series of peaks were observed from the conductance histograms which were explained by theoretical simulations as arising from different contact geometries between the pyridyl anchoring group and the gold electrodes. The experimental results, supported by theoretical calculations demonstrated that the high coordination (ie., step edges or alongside gold atoms) of the pyridyl anchoring group resulted in high conductance values. Another remarkable finding from this work was very low β values, implying the conductance of oligoyne compounds is weakly dependant on the molecular length.

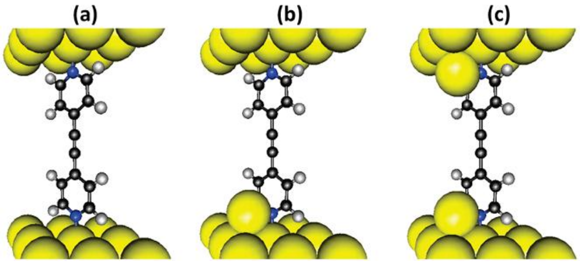

Figure 3.1 Illustration of 41 in different adsorption positions between two gold surfaces (a) Both pyridyl anchoring groups adsorbed on a flat gold surface, (b) one pyridyl anchoring group located alongside a gold surface adatom, (c) both pyridyl groups located alongside a gold adatom. Calculated conductance increases from (a) to (c) (Reproduced from reference [86]).

Subsequently, a molecule with a C8 chain between two bulky triarylphosphine-Pt(II) centres bearing thiol end groups has been studied in MCBJ experiments.[153]

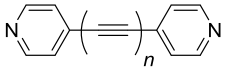

n = 0 **2**
n = 1 **41**
n = 2 **54**
n = 4 **55**

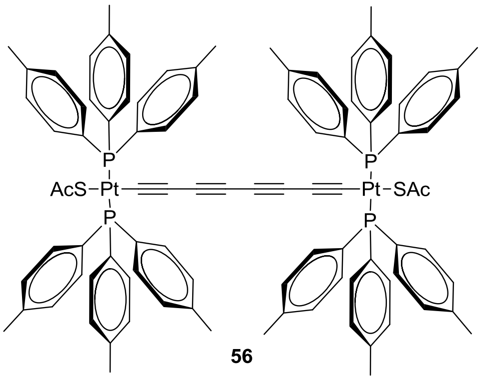

56

The aim of the work in this chapter is to explore analogues of **41**, **54** and **55** with terminal functionality which could facilitate assembly of the molecules onto gold for incorporation into electrical junctions. Earlier work showed that primary amines readily react with oligoyne chains,[147] which precludes the use of NH_2 as an end-group for stable polyynes. It is also known that 2-aminophenyl end-capped tetraynes react intra-molecularly to form indole derivatives in high yields in the presence of a copper salt.[154] *N,N*-Dimethylaminophenyl end-capped tetraynes are sufficiently stable for spectroscopic characterisation.[155] However, *N,N*-dimethylaniline is not effective as an anchoring group on a gold surface because of the steric hindrance of the methyl groups (see below). The synthesis and X-ray crystal structure of a bis(*N,N*-diisopropylaminophenyl) end-capped hexayne was reported.[156] However, the increased steric hindrance of the isopropyl groups means that *N,N*-diisopropylaminophenyl is not attractive as an anchor group.

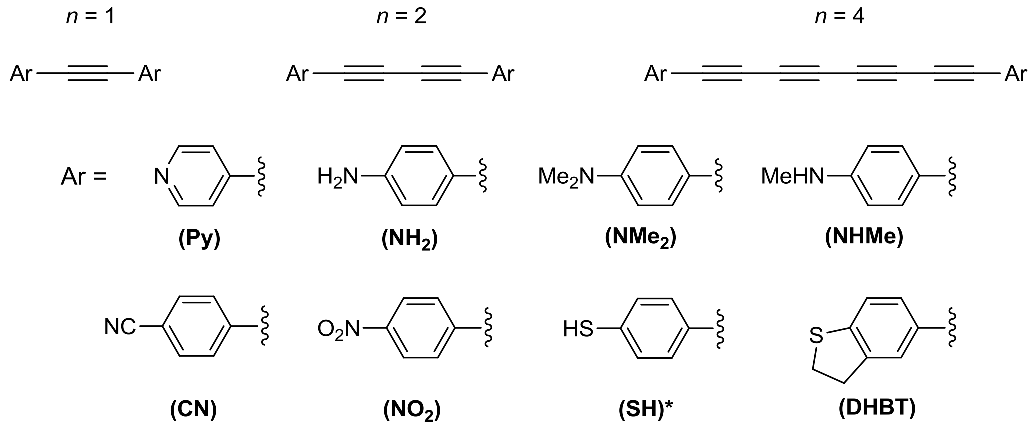

* Isolated as thioacetate

Scheme 3.1 Anchoring groups and backbones of the molecules which are studied in this chapter.

In this chapter, we focus on the synthesis and properties of diaryloligoynes (*n* = 1 to 4) with terminal thiol, amino, cyano, *N*-methylamino, *N,N*-dimethylamino, nitro and 2,3-dihydrobenzo[*b*]thiophen-5-yl (DHBT) end-groups and assess their stability under standard laboratory conditions. Comparisons are made with the corresponding diarylacetylene (tolane) derivatives (*n* = 1) in previous chapter.[18] Single-molecule transport measurements in gold-molecule-gold junctions are reported for the stable derivatives using complementary STM-BJ and MCBJ techniques, and we address the effect of increasing length of the molecules on the transport characteristics of eight series of oligoyne compounds (Scheme 3.1).

3.2 Synthesis

3.2.1 Synthesis of Pyridyl End-Capped Oligoynes

The syntheses and single-molecule conductance properties of pyridyl oligoynes were reported in 2009 by a collaboration of the Bryce Group (Durham), the Lambert Group (Lancaster) and the Nichols Group (Liverpool).[86] To benchmark the new measurements, **41** and **54** were re-synthesised by the previously-reported methods (Scheme 3.2).[112,157]

A new method was developed for the synthesis of tetrayne compound (**55**) which is one step shorter than the previously reported procedure.[86] 1,3-Butadiynetrimethylsilane (BDTMS) (**58**)[158] was prepared by the deprotection of one TMS groups of 1,4-bis(trimethylsilyl)buta-1,3-diyne (**57**) in the presence of MeLi.LiBr complex solution, in a 58% yield. Subsequently, the Sonogashira cross-coupling reaction of **38** and **58** gave **59** in a 98% yield. The synthesis of **55** was performed via Eglington-Galbraith coupling conditions [$Cu(OAc)_2.H_2O$, pyridine, methanol] in a 59% yield,[154] almost twice that previously reported.[86]

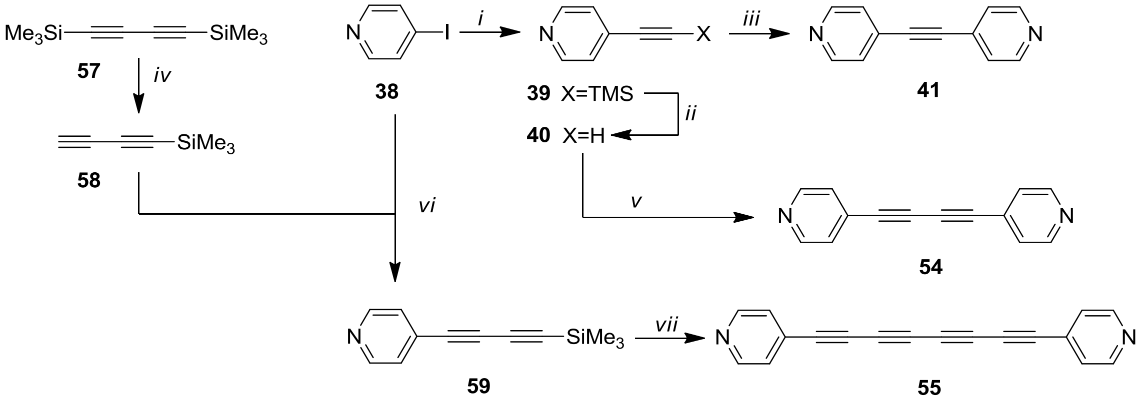

Reagents and conditions: (i) TMSA, Pd[$(PPh_3)_4$], Et_3N, CuI, 3h, rt, 92%; (ii) TBAF, THF, 30 mins, rt, 85%; (iii) **38**, Pd[$(PPh_3)_4$], (*i*-Pr)$_2$NH, CuI, 5h, rt, 91%; (iv) MeLi.LiBr, Et_2O, overnight, rt, 58%; (v) $PdCl_2[(PPh_3)_2]$, CuI, Et_3N, O_2, rt, 12h, 94%; (vi) HC≡C-C≡C-$SiMe_3$ (**58**), Pd[$(PPh_3)_4$], (*i*-Pr)$_2$NH, CuI, 3h, rt, 98%; (vii) $Cu(OAc)_2.H_2O$, Pyridine / MeOH, overnight, rt, 59%.

Scheme 3.2 Synthesis of pyridyl end-capped oligoynes.

In addition to the known pyridyl oligoyne series, extending the oligoyne backbone could aid in the understanding of the electronic properties of longer oligoynes through single-molecule conductance measurements.

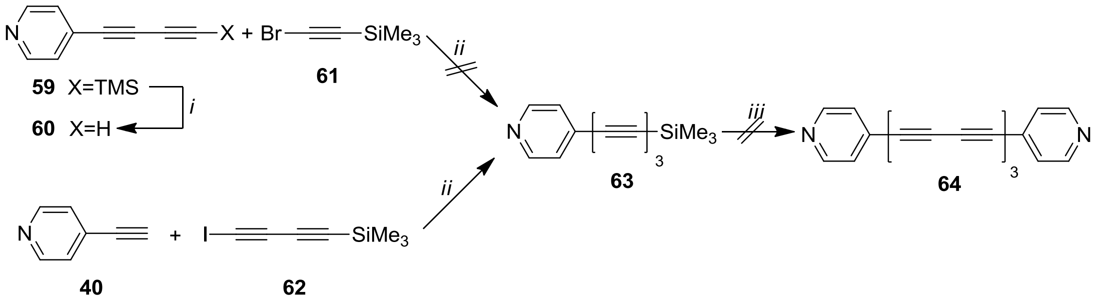

Reagents and conditions: (i) TBAF, THF, 30 mins, rt, 78%; (ii) Pd[$(PPh_3)_4$], Et_3N, CuI, 6h, rt, 42%; (iii) $Cu(OAc)_2.H_2O$, Pyridine / MeOH, overnight, rt, neither product nor the starting material could be obtained.

Scheme 3.3 Attempted synthesis of pyridyl end-capped hexayne.

The synthesis of the precursor compound (**63**) of hexayne (**64**) was attempted via two different routes (Scheme 3.3). At first, **59** was treated with TBAF to deprotect the TMS group giving the pyridyl terminated butadiyne **60** in a 78% yield. The cross-coupling reaction between **60** and **61**[159] was attempted but the desired compound **63** could not be isolated, possibly due to the low reactivity of the alkynyl bromide (**61**). Consequently, an alternative route was developed. The cross-coupling reaction between 4-ethynylpyridine (**40**) and 1-iodo-1,3-butadiynetrimethylsilane (**62**)[160,161] gave **63** in a 42% yield which was identified by ^1H and ^{13}C NMR spectroscopy. Rapid decomposition of the product was observed as a white-yellow to black colour change both in solid and solution state. Subsequently, the attempted homo-coupling reaction of **63** failed due to either its decomposition or the instability of the hexayne compound **64**, in which an insoluble black material was isolated from the reaction mixture.

3.2.2 Synthesis of Aniline End-Capped Oligoynes

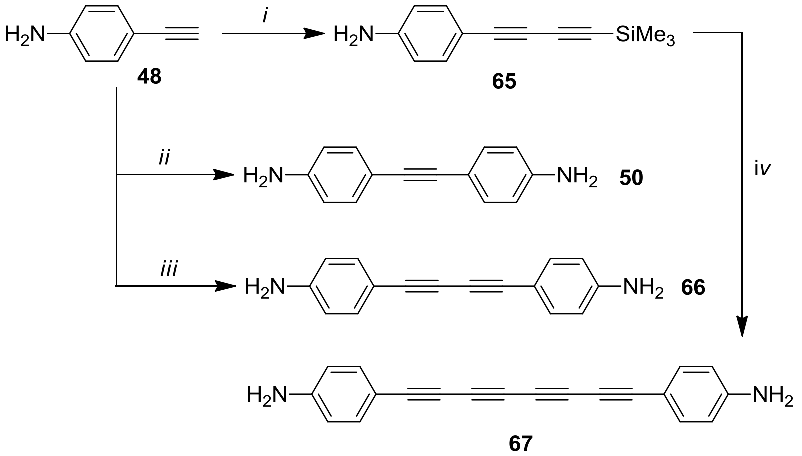

Reagents and conditions: (*i*) TMSA (excess), $PdCl_2[(PPh_3)_2]$, Et_3N, CuI, O_2, 5h, rt, 57%; (ii) 4-iodoaniline (**49**), $Pd[(PPh_3)_{4]}$, CuI, Et_3N, 3h, rt, 47%; (iii) $PdCl_2[(PPh_3)_2]$, Et_3N, CuI, O_2, 5h, rt, 65%; (iv) $Cu(OAc)_{2.}H_2O$, Pyridine / MeOH, 12h, rt, 82%.

Scheme 3.4 Synthesis of aniline end-capped oligoynes.

Compounds **50**[114] and **66**[162] were synthesised according to the literature routes. The precursor **65** was obtained by the Pd-catalysed oxidative cross-coupling reaction of 4-ethynylaniline **48** with an excess of TMSA in 57% yield. Homo-coupling of **65** under Eglington-Galbraith coupling conditions gave compound **67** in 82% yield (Scheme 3.4).

The tolane **50** and diyne **66** derivatives are stable to storage, when kept in the dark at room temperature. However tetrayne **67** was observed to be highly unstable under ambient conditions. Both in solution and solid state, upon isolation of **67** almost immediate decomposition was observed by the precipitation of a brown insoluble solid and a colour change. Despite the instability of **67**, characterisation by ^1H and ^{13}C-NMR (Figure 3.2), UV-Vis and MS techniques established its structure. It was not possible to detect the decomposition product(s) by NMR, due to their insolubility.

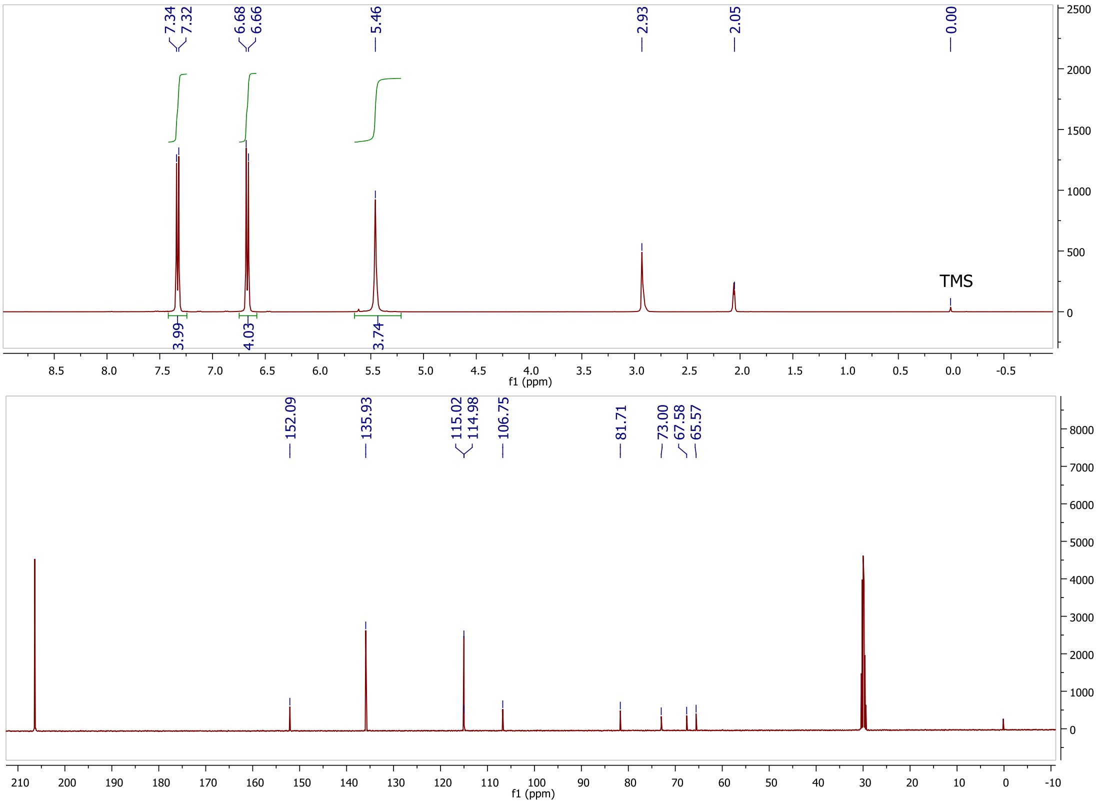

Figure 3.2 ^{1}H and ^{13}C NMR spectra of 67 in acetone-d$_6$ at 400 Mhz and 100 MHz.

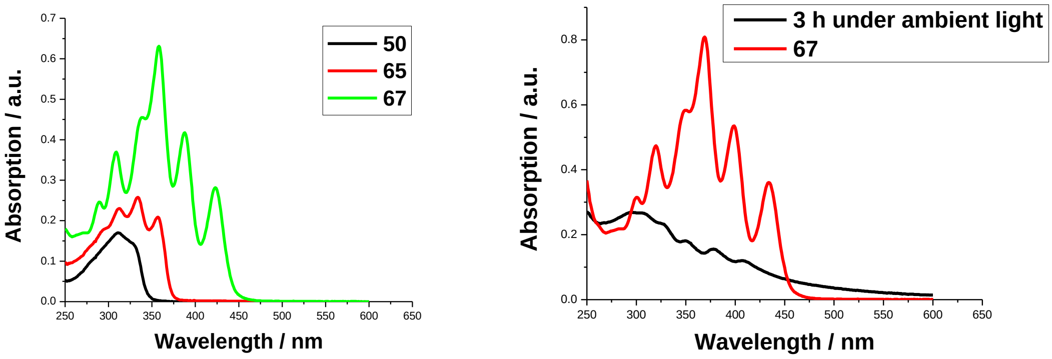

Figure 3.3 (Left) UV-Vis absorption spectra of aniline end-capped oligoynes, 50, 65 (5 x 10^{-6} M) and 67 (normalised) in CHCl$_3$; (Right) UV-Vis absorption spectra of 67, 5 minutes after the isolation (red) and after leaving under ambient laboratory light for 3 hours at ambient temperature(black).

UV-Vis absorption spectra of compounds **50**, **66** and **67** show the extension of conjugation upon increasing the oligoyne chain length by a progressive red shift of increasing absorption and increased vibronic features for longer analogues **66** and **67** (Figure 3.3, left). These are consistent with the previously reported oligoyne spectra.[86,137,141] The comparison of the absorption spectra of **67** 5 minutes after the isolation with that after leaving the same sample under ambient laboratory light for 3 hours (Figure 3.3, right) clearly shows the decomposition by a decreasing of absorption intensity and scattering due to aggregation. The probable decomposition route of **67** involves an amine moiety reacting with the *sp*-chain to form a polymeric product which is insoluble in common laboratory solvents.

As increasing the length of the oligoyne chain reduces the stability, it was anticipated that a triyne compound should have sufficient stability for the single-molecule conductance measurements.

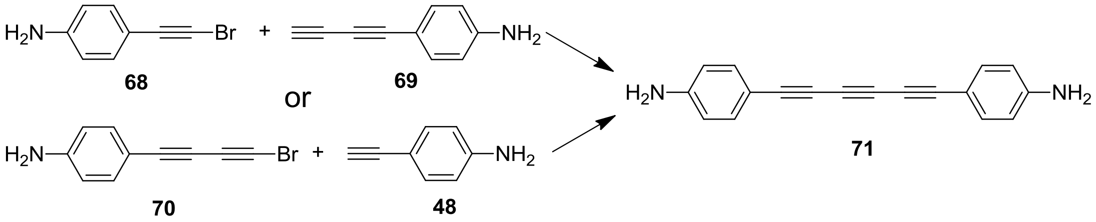

Scheme 3.5 Proposed syntheses of triyne 71.

Initially, two different routes were proposed for the synthesis of an aniline end-capped triyne compound. The first route was the Pd-catalysed *sp*-cross coupling of terminal butadiyne **69** with the alkynyl bromide **68**. This route was favourable because of our interest in the isolation of the terminal butadiyne derivative to build on studies involving terminal butadiynes by our research group.[163,164] However, neither terminal butadiyne **69** nor alkynyl bromide **68** could be isolated. This failure may be attributed to the instability of the products since the starting materials were consumed during the reaction. Protection of the amine moiety by trifluoroacetate **72** did not enable isolation of the terminal butadiyne derivative **73**. Only insoluble decomposition products were observed, which could not be characterised.

After the failure of the initial route to synthesise the triyne **71**, the synthesis of the butadiynylbromide derivative **70** was attempted in order to cross-couple with 4-ethynylaniline **48**. Unfortunately, **70** was also observed to be unstable; hence triyne compound **71** could not be synthesised. Due to the experimental problems synthesising triynes, it was decided to focus further on tetrayne derivatives. To this end, *N,N*-dimethyl and *N*-methyl substituted analogues of diaryltetraynes were synthesised.

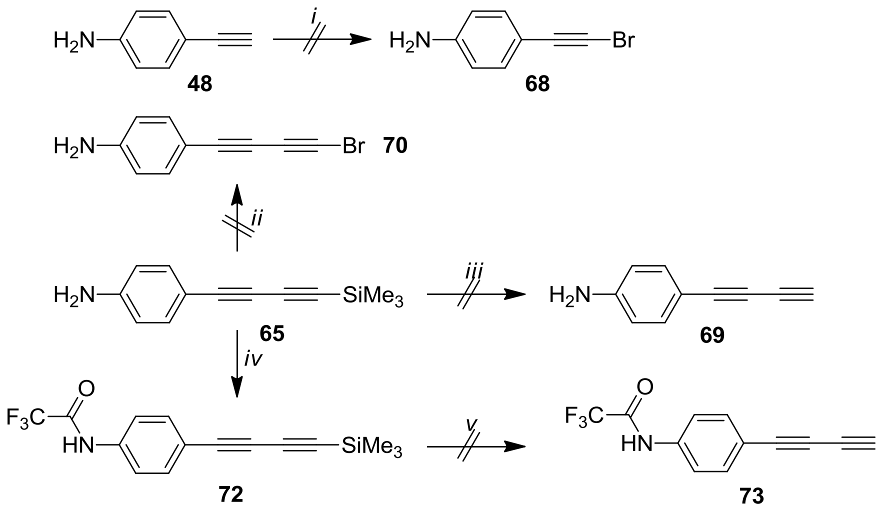

Reagents and conditions: (*i*) NBS, $AgNO_3$, Acetone, 4h, rt; (ii) NBS, AgF, Acetonitrile, 4h, rt ; (iii) K_2CO_3, THF/MeOH, 4h, rt; (iv) Trifluoroacetic anhydride, THF, 0°C, 1h, 96%; (v) K_2CO_3, MeOH/THF, rt, 4h.

Scheme 3.6 Synthesis of precursor compounds to synthesise 71.

In order to increase the stability by reducing the reactivity of the amine moiety, the 4-(*N,N*-dimethylamino)phenyl derivative **80** was synthesised.[155]

The methylation of 4-iodoaniline (**49**)[165] was performed by methyliodide in a 55% yield, the subsequent Sonogashira cross-coupling reaction with TMSA gave **75**[166] in a 95% yield and deprotection of TMS gave **76**[166] in a 90% yield. Tolane (**77**)[165], diacetylene (**78**)[165] and tetrayne (**80**)[155] derivatives were synthesised by methods analogous to those discussed previously. However, we observed that this molecule was not suitable for assembly onto a gold surface presumably due to the bulk of the methyl groups, which will be discussed in more detail later in this chapter.

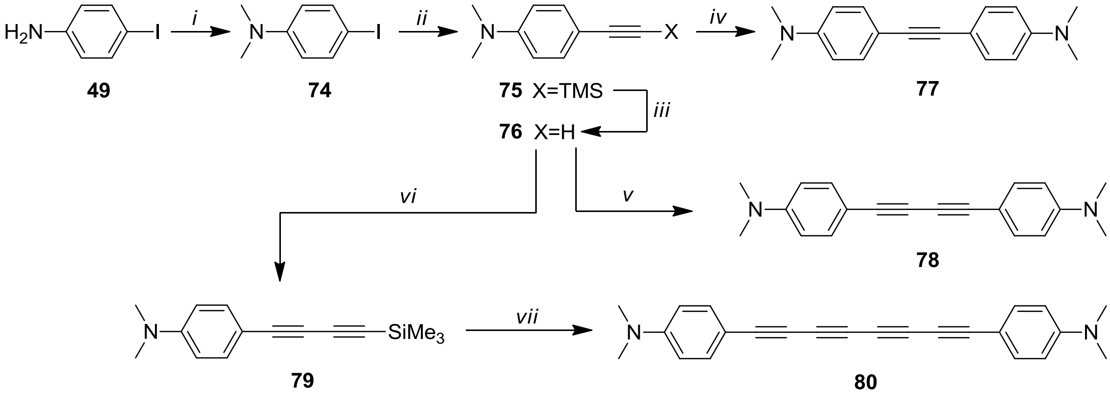

Reagents and Conditions: (i) MeI, $NaHCO_3$, DMF, 24h, rt, 55%; (ii) TMSA, $Pd[(PPh_3)_4]$, CuI, $(i\text{-}Pr)_2NH$, 5h, rt, 95%; (iii) K_2CO_3, MeOH, rt, 12h, 90%; (iv) **74**, $Pd[(PPh_3)_4]$, CuI, $(i\text{-}Pr)_2NH$, THF, 4h, rt, 38% (v) $PdCl_2[(PPh_3)_2]$, Et_3N, CuI, O_2, 3h, rt, 45%; (vi) TMSA (excess), $PdCl_2[(PPh_3)_2]$, Et_3N, CuI, O_2, 5h, rt, 74%; (vii) $Cu(OAc)_2.H_2O$, Pyridine / MeOH, 12h, rt, 79%.

Scheme 3.7 Synthesis of *N,N*-dimethylaniline end-capped oligoynes.

Additionally, *N*-methylaminophenyl end-capped oligoynes, which have less steric bulk on the nitrogen atoms, were also synthesised. 4-iodo-*N*-methylaniline (**81**)[167] and 4-ethynyl-*N*-methylaniline (**82**)[167] were obtained by literature methods, using paraformaldehyde, sodium methoxide and sodium borohydride in 60% and 65% yields, respectively. In order to investigate the effect of the methyl groups on amine anchors, tolane and diacetylene analogues were also synthesised. Tolane (**83**), diacetylene (**84**) and tetrayne (**86**) analogues of this series were synthesised by analogy with the previous syntheses.

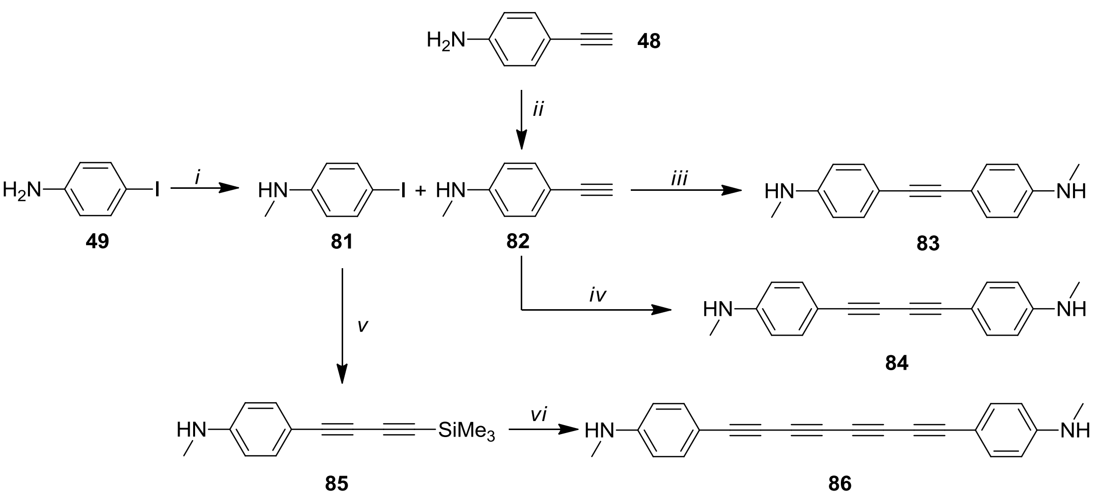

Reagents and conditions: (i) Paraformaldehyde, NaOMe, $NaBH_4$, MeOH, 4h, reflux, 60%; (ii) Paraformaldehyde, NaOMe, $NaBH_4$, MeOH, 4h, reflux, 65%; (iii) $Pd[(PPh_3)_4]$, $(i\text{-}Pr)_2NH$, CuI, 3h, rt, 62%; (iv) $PdCl_2[(PPh_3)_2]$, CuI, Et_3N, O_2, rt, 12h, 88%; (v) HC≡C-C≡C-$SiMe_3$ (**58**), $Pd[(PPh_3)_4]$, $(i\text{-}Pr)_2NH$, CuI, 3h, rt, 92%; (vi) $Cu(OAc)_2.H_2O$, Pyridine / MeOH, 12h, rt, 81%.

Scheme 3.8 Synthesis of *N*-methylaniline end-capped oligoynes.

In comparison to the aniline end-capped tetrayne **67**, increased stability was observed for *N*-methylaniline end-capped tetrayne **86**. However, traces of similar decomposition products were seen and only limited stability under ambient conditions was observed for the tetrayne **86**, which was characterised by ^1H, ^{13}C NMR (Figure 3.4), and mass spectroscopy. Single crystals of **86** were grown in the dark and an X-ray single crystal molecular structure was obtained (Figure 3.5).

The molecular structure of **86** has no crystallographic symmetry and its carbon chain shows a C-shaped bend where the terminal C(4)-C(7) bond inclined to the other terminal C(14)-C(15) bond by 18.6°. The phenyl head groups are not in the same plane and there is 43.2° twist angle. There is 15.9° and 13.0° torsion angle between the C(1)-N(1)-C(21) and C(22)-N(2)-C(8) planes between the corresponding phenyl rings, respectively. The hydrogen bonds between the molecules form a continuous chain of molecules of **86** in the crystal structure. The stacks are slanted and arranged in a herring-bone motif.

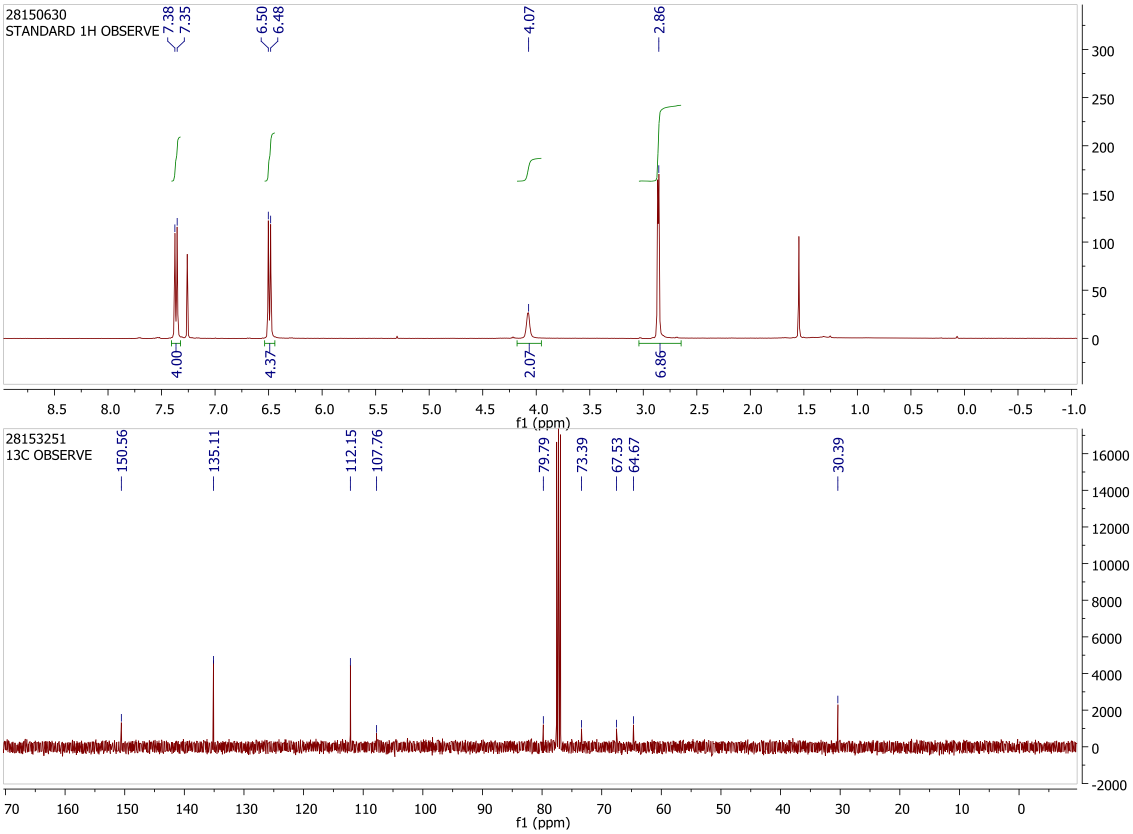

Figure 3.4 ^{1}H-NMR and ^{13}C-NMR spectra of 86 in CDCl$_3$ at 400 Mhz and 100 MHz.

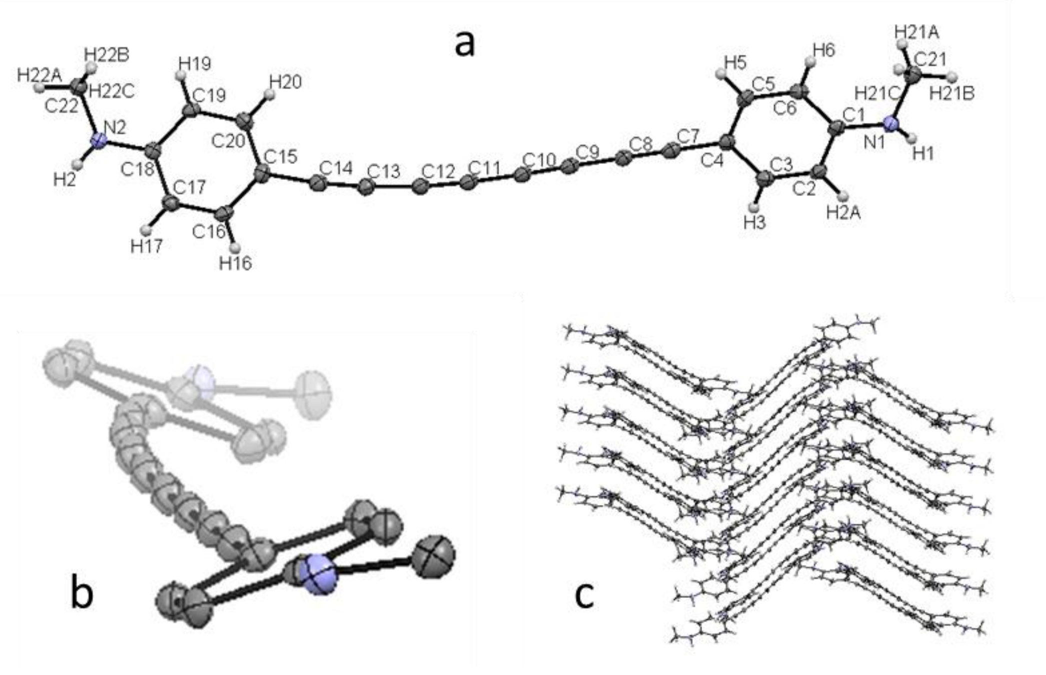

Figure 3.5 X-ray molecular structure (a and b) and crystal packing diagram (c) of 86, hydrogen atoms are omitted in b for clarity.

3.2.3 Synthesis of Benzonitrile End-Capped Oligoynes

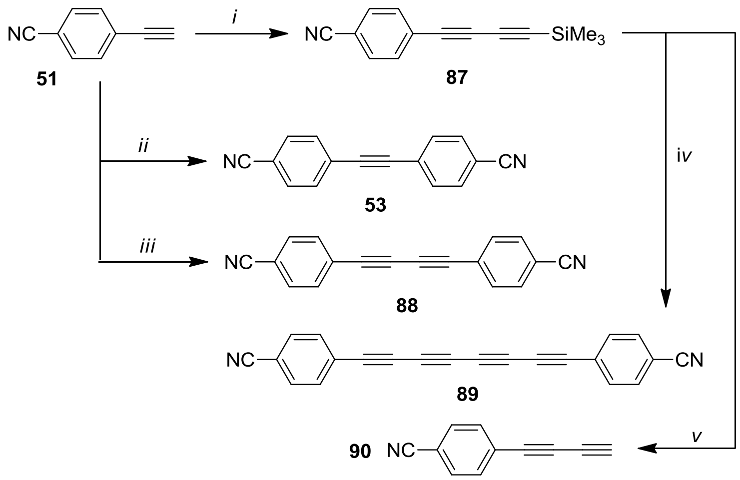

Reagents and conditions: (*i*) TMSA (excess), $PdCl_2[(PPh_3)_2]$, Et_3N, CuI, O_2, 5h, rt, 40%; (ii) 4-iodobenzonitrile (**52**), $Pd[(PPh_3)_4]$, CuI, $(i\text{-}Pr)_2NH$, overnight, rt, 52%; (iii) $PdCl_2[(PPh_3)_2]$, Et_3N, CuI, O_2, overnight, rt, 82%; (iv) $Cu(OAc)_2.H_2O$, Pyridine / MeOH, 12h, overnight, 63%; (v) K_2CO_3, THF, overnight, rt, 85%.

Scheme 3.9 Synthesis of benzonitrile end-capped oligoynes.

Benzonitrile end-capped oligoynes were synthesised by analogy with previous syntheses (Scheme 3.9).[115,168] Tetrayne **89** was observed to be stable under ambient conditions; indeed, it was stable enough to recrystallise from boiling acetic acid (ca. 120°C). On the other hand, low solubility was observed with increasing oligoyne chain length. ^1H and ^{13}C NMR spectra of the tetrayne **89** were recorded in $CDCl_3$/TFA-d mixture since it was not soluble in more common NMR solvents (Figure 3.6).

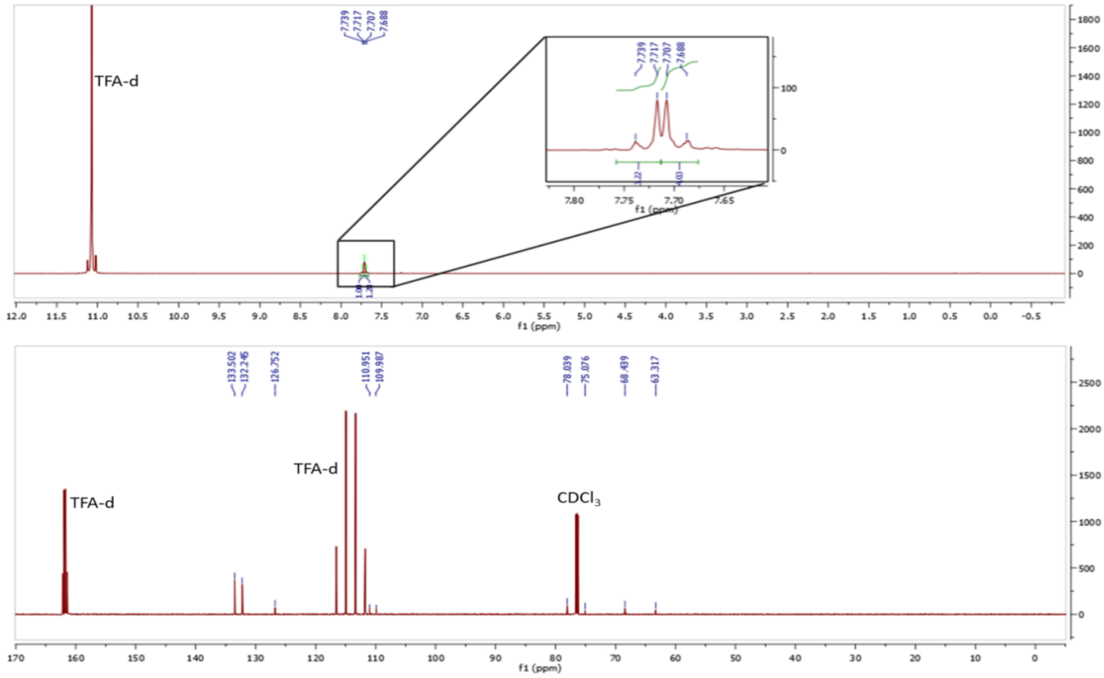

Figure 3.6 ^1H-NMR and ^{13}C-NMR spectra of 89 in TFA-d/$CDCl_3$ mixture at 400 Mhz and 100 MHz.

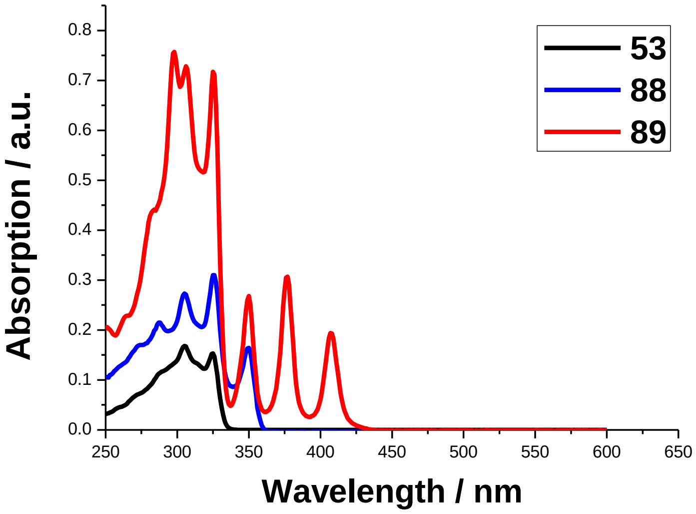

Figure 3.7 UV-Vis absorption spectra of benzonitrile end-capped oligoynes 53, 88 and 89 in CHCl$_3$ (5 x 10^{-6} M).

The UV-Vis absorbance spectrum shows the increase of conjugation with increasing chain length. The red-shift in absorption and vibronic features are consistent with previously reported oligoyne spectra (Figure 3.7).

The X-ray crystal structure of the tetrayne **89** shows an inversion centre (Figure 3.8). **89** is almost completely linear and the phenyl head groups are co-planar. However, the oligoyne chain shows a slight S-shaped bend. In the triclinic structures, the stacks are slanted and parallel.

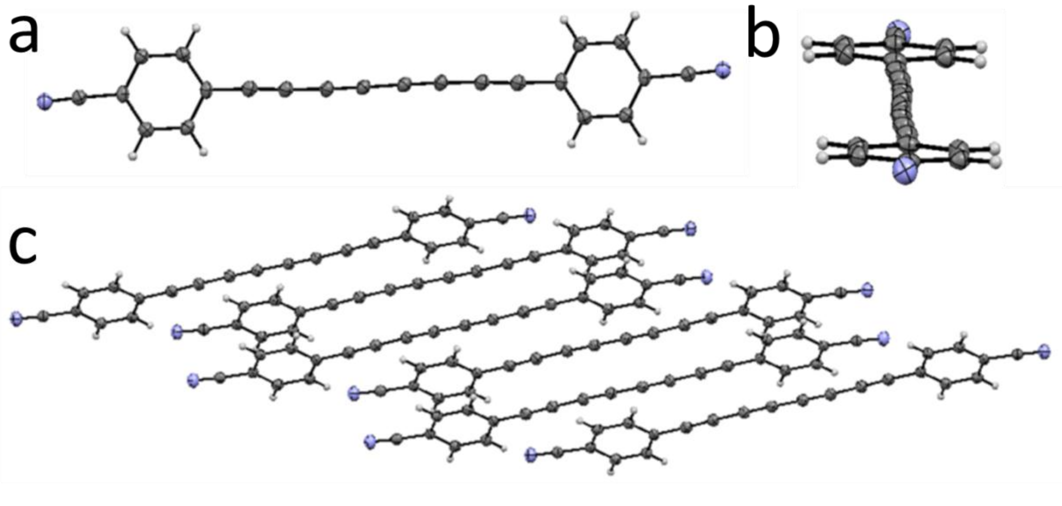

Figure 3.8 X-ray molecular structure (a, b) and crystal packing diagram (c) of 89.

During the synthesis of the benzonitrile derivatives, a terminal butadiyne[169] **90** was isolated, which was observed to be stable under ambient conditions. **90** was characterised by ^{1}H, ^{13}C NMR (Figure 3.8) and mass spectroscopy, and X-ray crystallography.

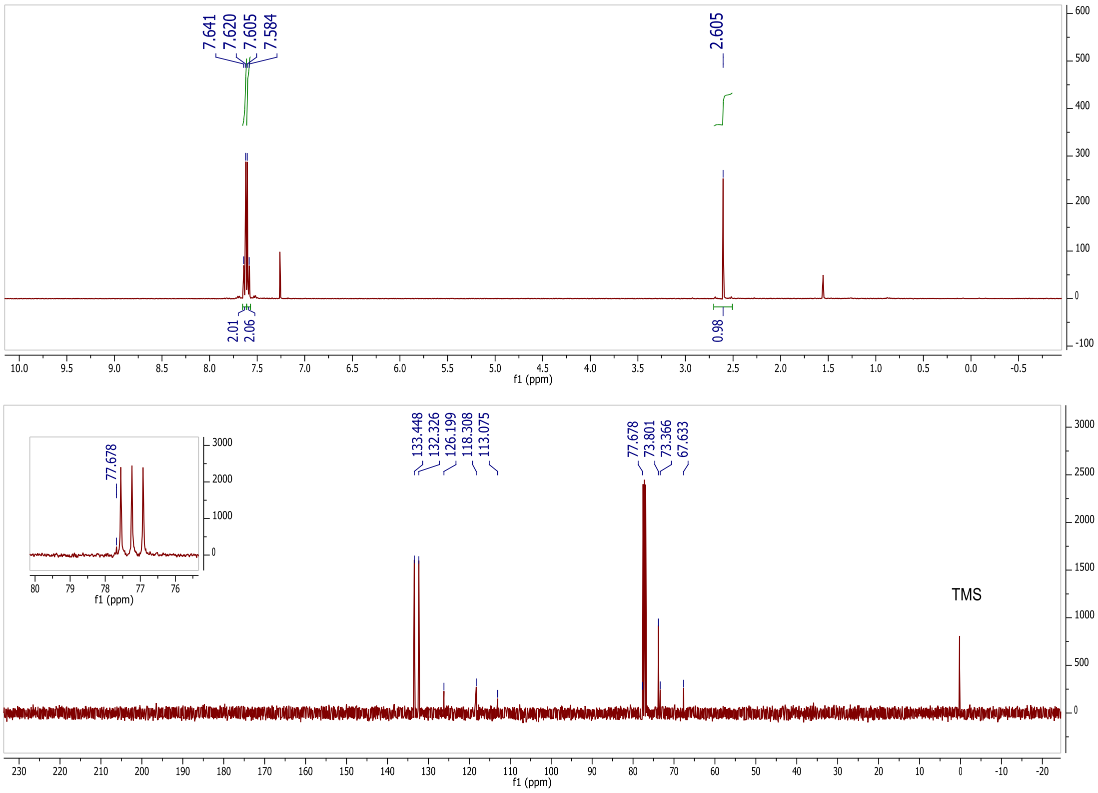

Figure 3.9 ^{1}H-NMR and ^{13}C-NMR spectra of 90 in $CDCl_3$ at 400 Mhz and 100 MHz.

The crystal structure of **90** (Figure 3.9) shows ≡C-H…N hydrogen bonds which link the molecules together in an infinite chain. Due to the distance and orientation between the triple bonds in the crystal structure, solid state polymerisation of terminal butadiyne **90** was possible[170] and, this was performed by keeping the crystals under daylight for one month. Although solid state polymerisation was observed, the crystallinity was lost and no structural data were obtained on the polymer.

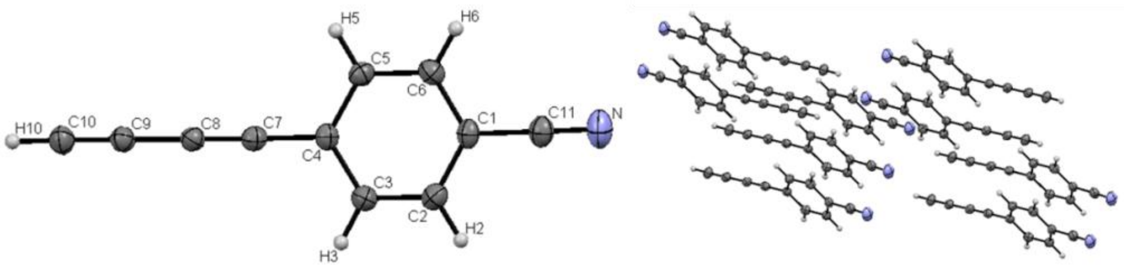

Figure 3.10 X-ray molecular structure (left) and crystal packing diagram (right) of 90.

3.2.4 Synthesis of Nitrobenzene End-Capped Oligoynes

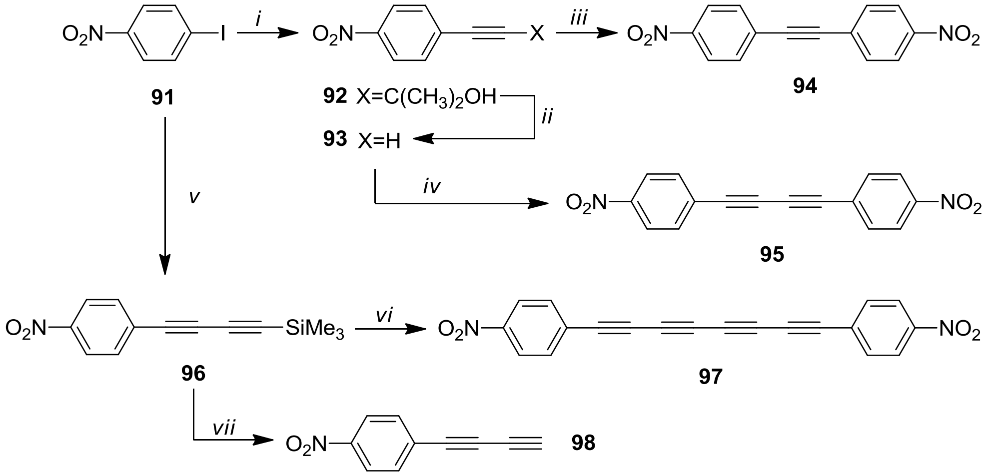

Reagents and conditions: (i) HC≡CC$(CH_3)_2$OH, Pd[$(PPh_3)_4$], Et_3N, CuI, 5h, rt, 94%; (ii) NaOH, toluene, 45 mins, reflux, 70%; (iii) **41**, Pd[$(PPh_3)_4$], (*i*-Pr)$_2$NH, CuI, overnight, rt, 50%; (iv) $PdCl_2[(PPh_3)_2]$, CuI, Et_3N, O_2, rt, overnight, 75%; (v) HC≡C-C≡C-$SiMe_3$ (**76**), Pd[$(PPh_3)_4$], (*i*-Pr)$_2$NH, CuI, 3h, rt, 77%; (vi) $Cu(OAc)_2.H_2O$, Pyridine / MeOH, overnight, rt, 86%; (vii) TBAF, THF, rt, 30 mins, 95%.

Scheme 3.10 Synthesis of nitrobenzene end-capped oligoynes.

Nitrobenzene end-capped oligoynes were synthesised by similar methods to those discussed previously (Scheme 3.10).[171,172] Tetrayne **97**[173] was also observed to be stable under ambient conditions. However, its solubility was even lower than that of the benzonitrile analogue **89**. Hence no clear NMR spectra could be obtained for **97**. However, the structure was unambiguously established by a combination of high-resolution MS (Figure 3.11), UV-Vis spectroscopy (Figure 3.12) and X-ray crystallography (Figure 3.13). The UV-Vis absorbance spectrum shows an increase of extinction co-efficient with increasing conjugation through the molecules. The red-shift in the absorption and vibronic features are consistent with previously reported oligoyne spectra.

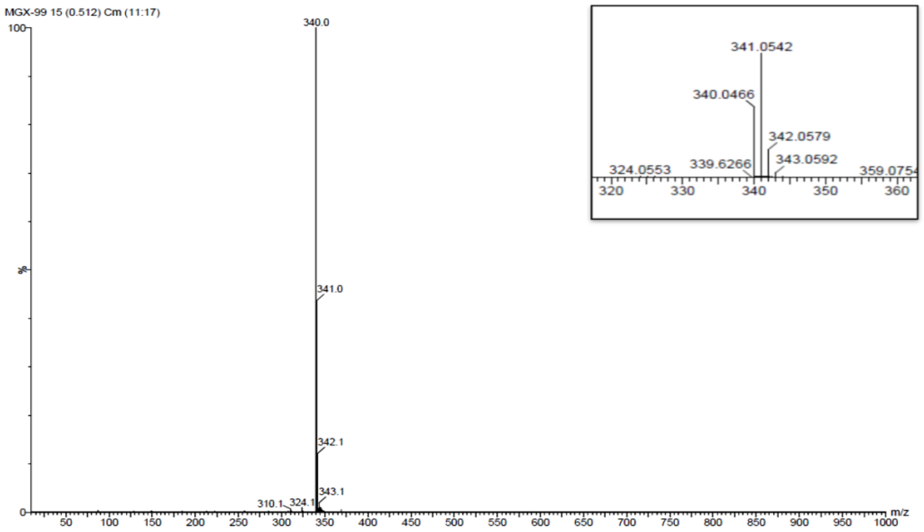

Figure 3.11 Low resolution and high resolution (inset) ASAP-MS spectrum of the tetrayne 97.

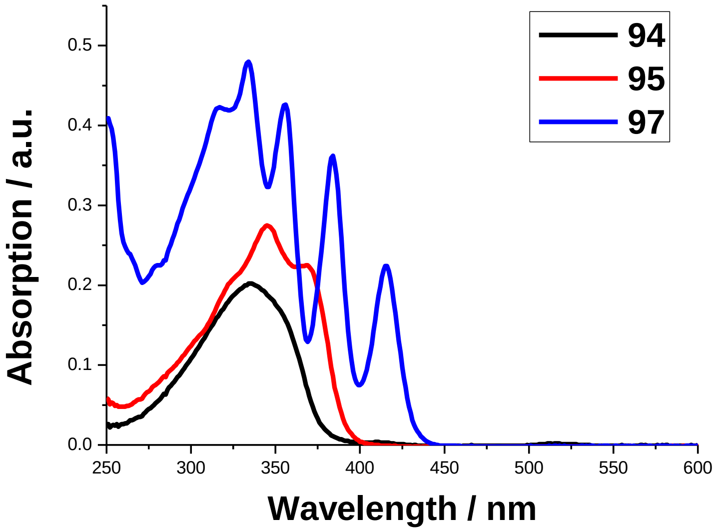

Figure 3.12 UV-Vis absorption spectra of nitrobenzene end-capped oligoynes 94, 95 and 97 in $CHCl_3$ (5×10^{-6}M).

The X-ray crystal structure of tetrayne **97** shows an inversion centre and the two aryl rings are coplanar. However there is a 10° twist between the arene ring and the nitro-group the oligoyne chain shows a slightly S-shaped bend. The stacks are slanted and arranged in a herring-bone motif.

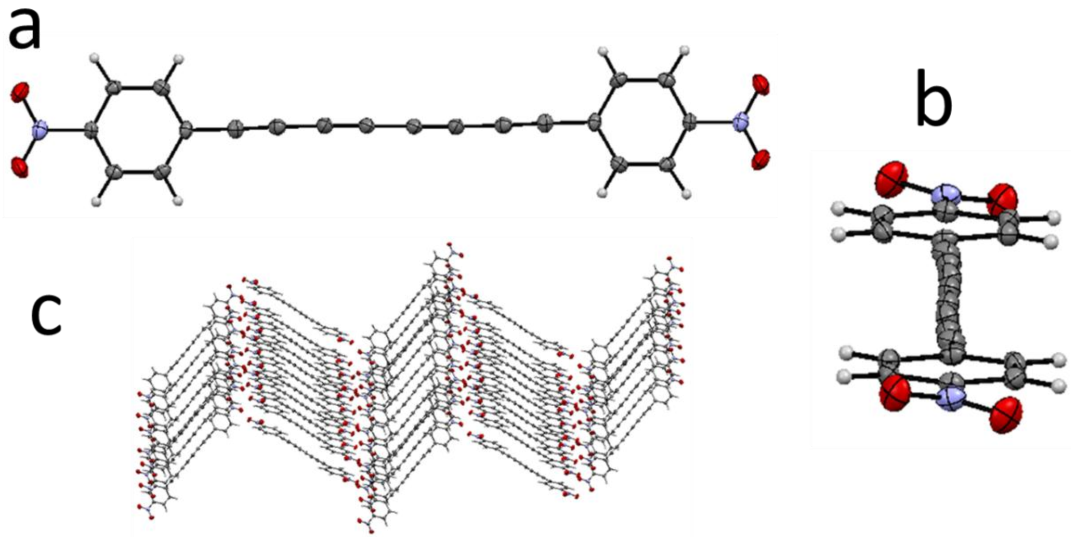

Figure 3.13 X-ray molecular structure (a, b) and crystal packing diagram (c) of 97.

3.2.5 Synthesis of Thiophenol End-Capped Oligoynes

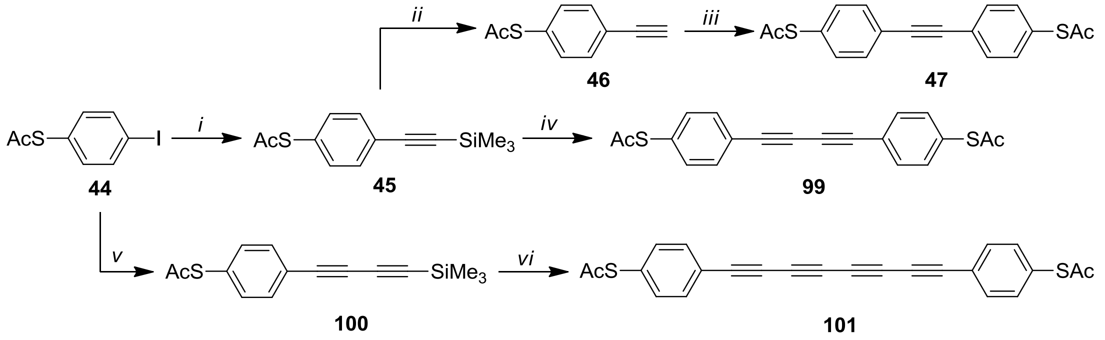

Reagents and conditions: (i) TMSA, Pd[(PPh$_3$)$_4$], Et$_3$N, CuI, 3h, rt, 92%; (ii) TBAF, THF, rt, 87%; (iii) **44**, Pd[(PPh$_3$)$_4$], Et$_3$N, CuI, overnight, rt, 95% (iv) Cu(OAc)$_2$.H$_2$O , Pyridine / MeOH, overnight, rt, 76%; (v) HC≡C-C≡C-SiMe$_3$ (**58**), Pd[(PPh$_3$)$_4$], (*i*-Pr)$_2$NH, CuI, 3h, rt, 94%; (vi) Cu(OAc)$_2$.H$_2$O , Pyridine / MeOH, 12h, rt, no stable product.

Scheme 3.11 Synthesis of thiphenol end-capped oligoynes.

The syntheses of compounds **44** and **47** were described in Chapter 2. The diyne derivative **99**[174] was synthesised by the standard homo-coupling of **45** under Eglington-Galbraith conditions in 76% yield. The tetrayne **101** could not be isolated after the attempted homo-coupling reaction of **100** under the same conditions, due to the instability of **101**. However, the UV-Vis absorption spectrum was recorded following the filtration of the reaction mixture through a small silica pad (Figure 3.14). The significant red shift and the vibronic features in the absorption spectra are consistent with the formation of **101**.

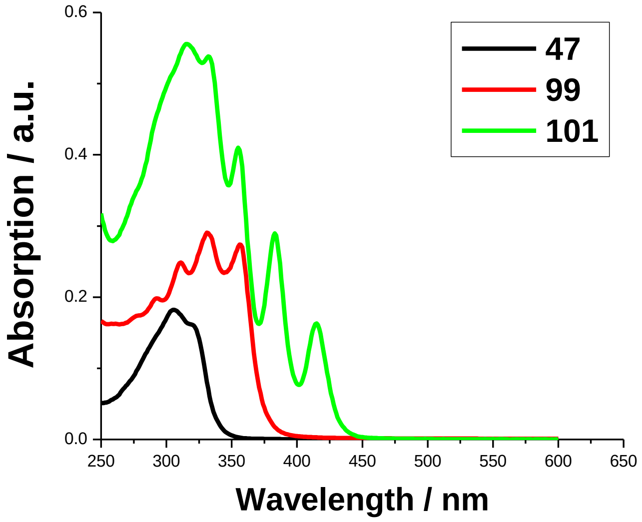

Figure 3.14 UV-Vis absorption spectra of mercaptophenyl end-capped oligoynes 47, 99 (5 x 10^{-6} M) and 101 (normalised) in CHCl$_3$.

3.2.6 Synthesis of Dihydrobenzothiophene (DHBT) End-capped Oligoynes

Due to the instability of **101**, new alternative anchoring groups bearing sulfur atom were needed. Venkataraman and co-workers[175] reported the comparison of the single-molecule transport properties of benzene derivatives with thioether (**102**) and 2,3-dihydrobenzo[*b*]thiophene (DHBT) (**103**) anchoring groups.

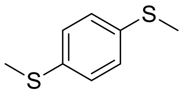

102

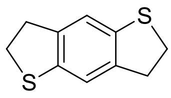

103

They showed that the orientation of the Au-S bond relative to the aromatic ring controls the electron transport through these molecules. Hence locking the sulfur with an alkyl linkage to the aromatic ring in **103** prevents the rotation of the flexible thioether moiety of **102**. This stabilises the position of the lone pair electrons of sulfur, thus increasing the chance of the single-molecule junction formation and enhancing the single-molecule conductance.

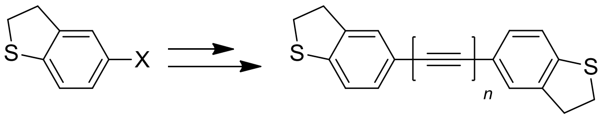

104 X = Br
105 X = I

n = 1 to 4

Scheme 3.12 The route for the synthesis of DHBT end-capped oligoynes.

Inspired by Venkataraman's work, we decided to investigate the use of DHBT as an anchoring group for an oligoyne series. The initial route to synthesise the bromo derivative (**104**)[176] which would be the key building block for the synthesis of DHBT end-capped oligoynes, starting from 4-bromothiophenol (**42**) unfortunately failed in the last step, due to the instability of the compound **108**.[177] An alternative route involving the cross-coupling of **108** with TMSA also failed due to instability of either reactant **108** or product **109**, for which a black residue was obtained (Scheme 3.13).

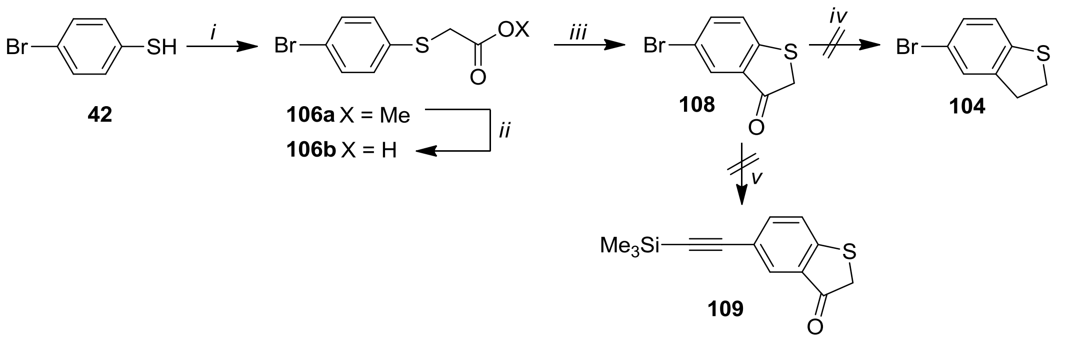

42 106a 106b 108 104 109

Reagents and conditions: (i) Methyl bromoacetate, benzene, reflux, 2h, 97%; (ii) NaOH, MeOH, reflux, 2h, 81%; (iii) (a) $SOCl_2$, reflux, 1h; (b) $AlCl_3$, $(ClCH_2)_2$, 0 to rt, 1h (iv) Hydrazine monohydrate, MeOH, NaOEt, reflux, 6-18 h; (v) TMSA, $Pd[(PPh_3)_4]$, Et_3N, CuI, 4h, rt.

Scheme 3.13 First route for the attempted synthesis of 104 and 109.

Another route (Scheme 3.14) to synthesise **104** was developed similar to the literature route.[178] Commercially available benzo[*b*]thiophene (**110**) was oxidised to give the corresponding sulfone (**111**) in 98% yield, which was hydrogenated using H_2 and Pd/C catalyst to give 2,3-dihydrobenzo[*b*]thiophene 1,1-dioxide (**112**) also in 98% yield. Reduction of **112** by $LiAlH_4$ gave the desired 2,3-dihydrobenzo[*b*]thiophene **113** in 77% yield.[178] The bromination of **113** under mild conditions gave 5-bromo-2,3-dihydrobenzo[*b*]thiophene (**104**) in 89% yield.[176]

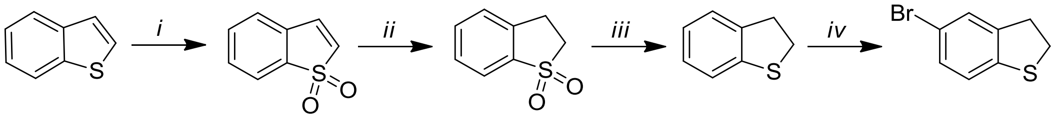

110 111 112 113 104

Reagents and conditions: (i) mCPBA, CH_2Cl_2, rt, overnight, 98%; (ii) H_2, Pd/C, EtOH, 5h, 98%; (iii) $LiAlH_4$, Et_2O, reflux, 4h, 77%; (iv) Br_2, DCM, 1h, 89%.

Scheme 3.14 Synthesis of 104.

For the synthesis of tolane derivative **114**, **104** was cross-coupled with TMSA to give **107a** in a 95% yield. The deprotection of the TMS group was followed by a Sonogashira cross-coupling with **104**. Initially, the yield of this step was around 20-25%; this was increased to 30-35% by rigorous purification of **104** via sublimation. However, this problem was resolved by synthesising the iodo derivative (**105**), which has higher reactivity for Sonogashira cross-couplings. This was achieved via the lithiation of **104** and quenching with I_2 to give **105** in 89% yield. The Sonogashira cross-coupling reaction between **105** and **107b** gave tolane derivative **114** in 67% yield (Scheme 3.15).

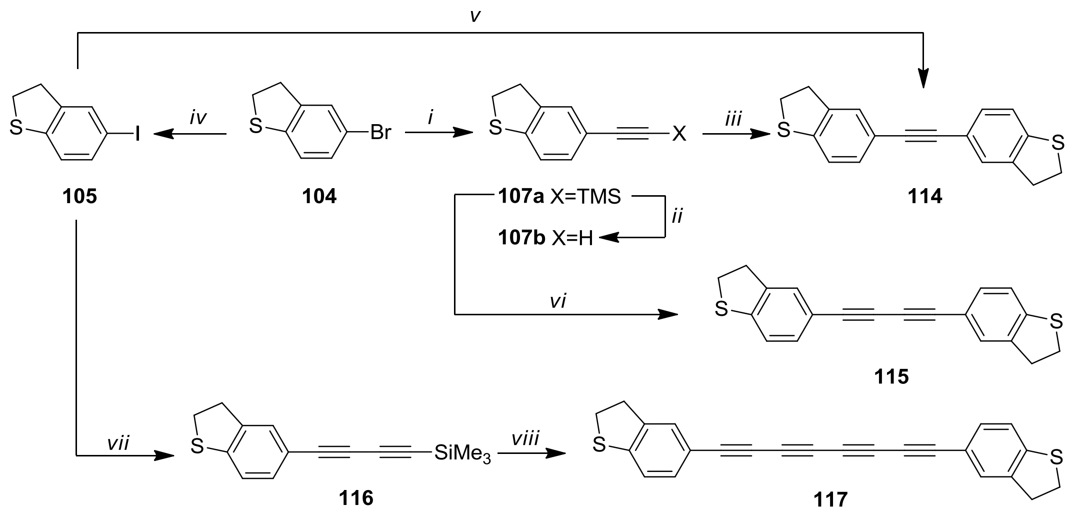

Reagents and conditions: (i) TMSA, Pd[(PPh$_3$)$_4$], (*i*-Pr)$_2$NH, CuI, 4h, rt, 95%; (ii) TBAF, THF, 30 mins, rt, 92%; (iii) **104**, Pd[(PPh$_3$)$_4$], (*i*-Pr)$_2$NH, CuI, overnight, rt; (iv) *n*-BuLi, I$_2$, THF, 3h, 89%; (v) **106**, Pd[(PPh$_3$)$_4$], Et$_3$N, CuI, 4h, rt, 67%; (vi) Cu(OAc)$_2$.H$_2$O , Pyridine / MeOH, 12h, rt, 86%; (vii)HC≡C-C≡C-SiMe$_3$ (**58**), Pd[(PPh$_3$)$_4$], (*i*-Pr)$_2$NH, CuI, 3h, rt, 78%; (viii) Cu(OAc)$_2$.H$_2$O , Pyridine / MeOH, 12h, rt, 77%.

Scheme 3.15 Synthesis of DHBT end-capped oligoynes.

The DHBT end-capped diyne (**115**) and tetrayne (**117**) compounds were synthesised by analogy with the previous syntheses (Scheme 3.15). Tetrayne **117** was found to be stable under ambient conditions. Unlike benzonitrile (**89**) and nitrobenzene (**97**) end-capped tetraynes, the solubility of **117** is very good in common laboratory solvents.

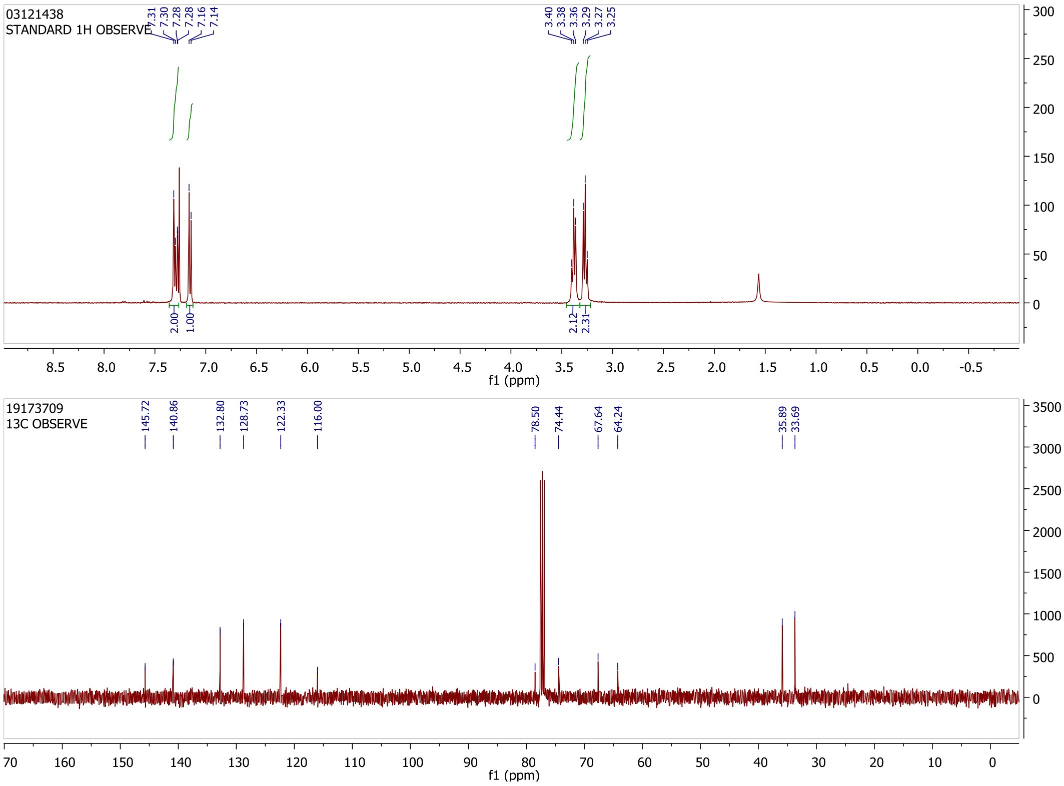

Figure 3.15 ^{1}H-NMR and ^{13}C-NMR spectra of 117 in CDCl$_3$ at 400 Mhz and 100 MHz.

The ^1H and ^{13}C NMR spectra (Figure 3.15) show the formation of **117** and the red shift in absorption and vibronic features in the UV-Vis spectra (Figure 3.16) are consistent with the previous oligoyne data.

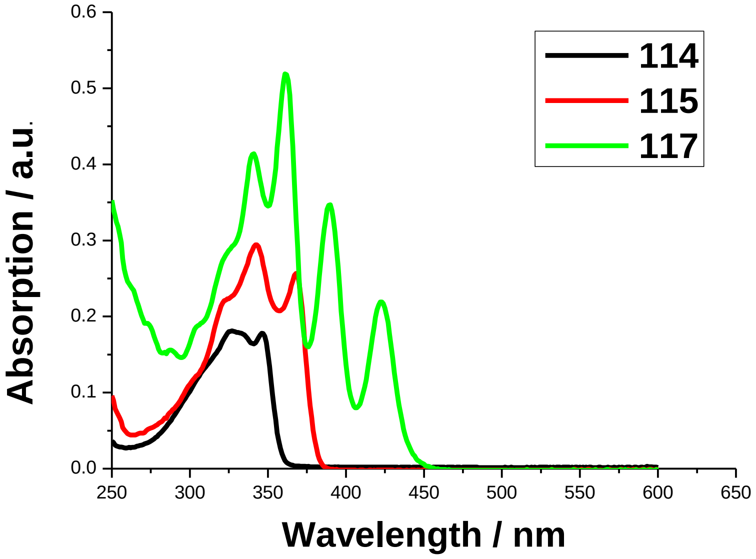

Figure 3.16 UV-Vis absorption spectra of DHBT end-capped oligoynes in $CHCl_3$ (5 x 10^{-6} M).

The X-ray molecular structure of diyne **115** (Figure 3.17) contains two crystallographically non-equivalent molecules: one at an inversion centre and the other in a general position. The centro-symmetric molecule has a linear diyne chain and coplanar dihydrobenzothiophene moieties; the other molecule has a 39.9° angle and a C-shaped bend of 9.5° in the diyne chain. The single/triple bond length alternations in the oligoyne chains are as expected.

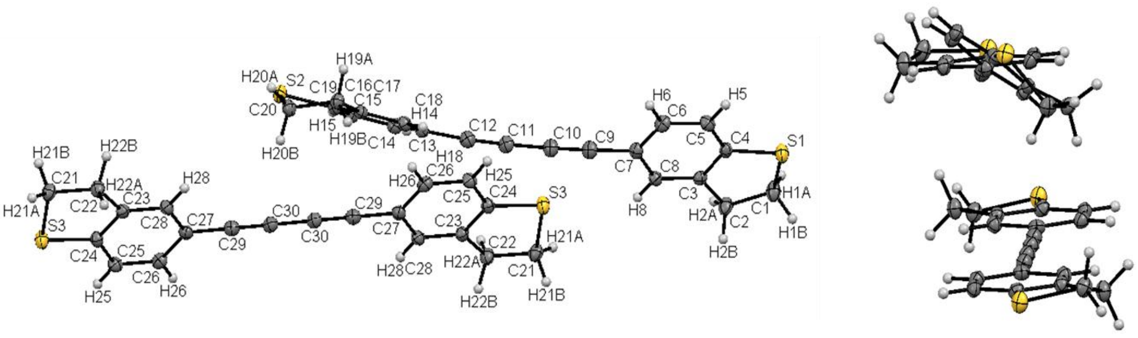

Figure 3.17 X-ray molecular structure of 115.

Tetrayne **117** has no crystallographic symmetry (Figure 3.18) and its carbon chain shows an appreciable S-shaped bend: the central C(12)-C(13) bond is inclined to the terminal C(7)-C(9) and C(16)-C(17) bonds by 9.4° and 13.4°, respectively, while the angle between the latter bonds is only 4.2°. Both DHBT moieties are planar, with the exception of the C(1) and C(24). In tetrayne **117**, each arene ring forms one face-to-face intermolecular contact with its inversion equivalent and one herring-bone type contact with a symmetrically independent ring (interplanar angle 34.4°).

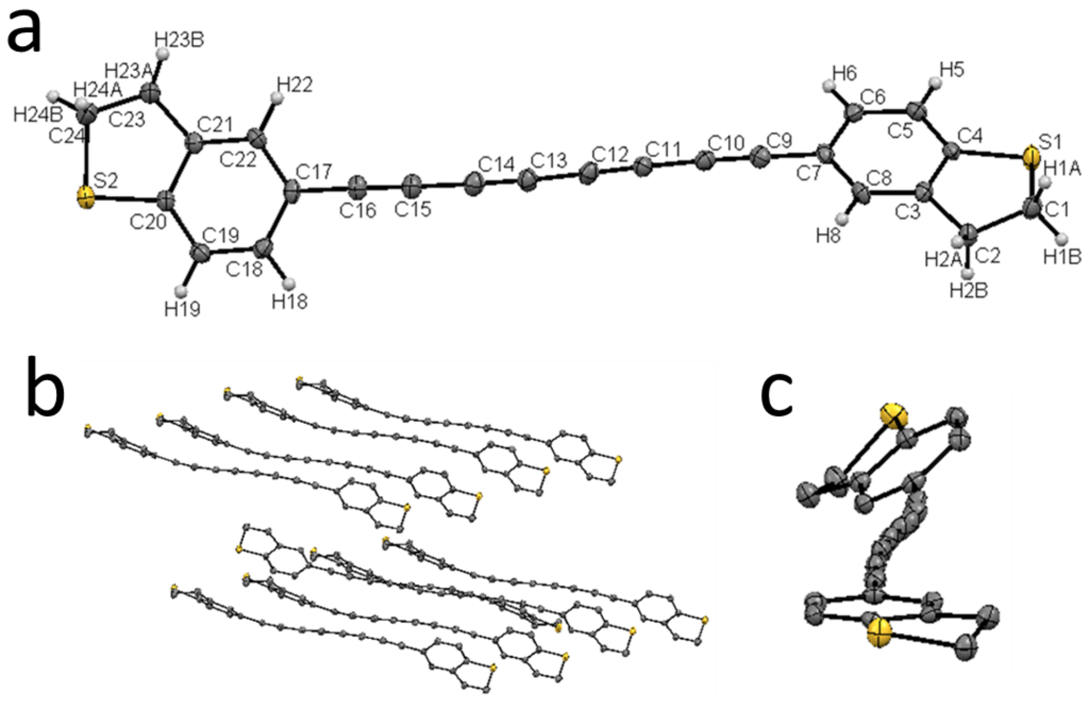

Figure 3.18 X-ray molecular structure (a, c) and crystal packing diagram (b) of 117.

3.2.7 Comparison of the Alternating Bond lengths of Tetrayne Crystal Structures

The bond lengths of the tetrayne compounds studied in this chapter are summarised in Table 3.1, which are obtained from X-ray molecular structures. In summary, the alternating single-triple bond lengths in the oligoyne backbone are consistent with the literature data.[179] From the comparison of different end-capped tetrayne's bond-lengths, it can be seen that the bond lengths are not affected by the head-groups.

Phenyl,[179] pyridyl (**55**), benzonitrile (**89**) and nitrophenyl (**97**) end-capped tetraynes carbon chains show a slight S-shape bend; DHBT end-capped tetrayne (**117**) shows a strong S-shape bend. However, *N*-methylaniline end-capped tetrayne (**86**) shows C-shape bends.

From these findings, it is hard to correlate the shape and the end-cap of the tetrayne chains.

Table 3.1 The summary of the bond lengths of the tetraynes studies in this chapter, determined by X-ray molecular structures.

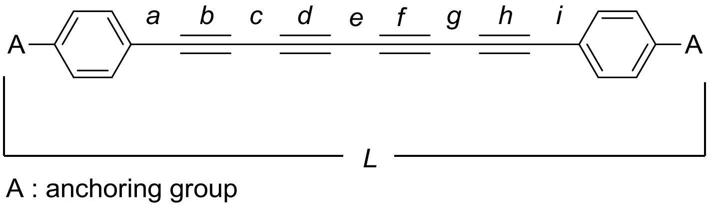

End-Cap	Length (Å)									
	a	***b***	***c***	***d***	***e***	***f***	***g***	***h***	***i***	***L***
Phenyl[179]	1.41	1.19	1.36	1.22	1.32	1.22	1.36	1.19	1.41	N/A
Pyridyl	1.433	1.207	1.363	1.213	1.359	1.213	1.363	1.207	1.433	17.3
N-methylaniline	1.431	1.209	1.362	1.214	1.365	1.210	1.366	1.217	1.422	19.9
Benzonitrile	1.426	1.209	1.366	1.210	1.363	1.210	1.366	1.209	1.426	22.4
Nitrophenyl	1.432	1.201	1.368	1.210	1.360	1.210	1.368	1.201	1.432	21.3
DHBT	1.431	1.195	1.375	1.204	1.367	1.208	1.369	1.202	1.430	20.7

3.3 Conductance-Distance Measurements

The transport characteristics of the oligoynes were studied at the single-molecule level by complementary STM-BJ and MCBJ measurements in trimethylbenzene (TMB) / tetrahydrofuran (THF) (1:4, v/v) solution, at room temperature and under argon atmosphere. The STM-BJ and MCBJ setups and experimental details are described in Chapter 2.

Deprotection of compounds **47** and **99** was carried out *in situ* by adding four equivalents of tetrabutylammonium hydroxide just before the beginning of the stretching experiment.

3.3.1 Single-Molecule Conductance Measurements of DHBT End-capped Oligoyne Series

The DHBT series **114**, **115** and **117** are taken as a model for this study since these compounds have the highest conductance values and more uniform junction formation compared to the other oligoyne series studied herein. Figure 3.19A displays three typical sample sets of conductance-distance *G*-Δ*z* stretching traces, plotted on a semi-logarithmic scale, for molecules **114**, **115** and **117** (blue, red and black curves respectively) in TMB/THF using STM-BJ approach upon application of a bias voltage V_{bias} = 0.35 mV between STM tip and Au(111) substrate. All curves are displaced horizontally for clarity. The plots show stepwise conductance features at multiple values of the fundamental quantum of conductance $G_0 = 2e^2/h$ = 77.5 µS. These short, nearly flat steps emerge as the tip is being retracted out of contact with the substrate, and a gold chain of decreasing diameter forms until eventually only two gold atoms from each electrode are in contact. With further tip retraction, the constriction collapses and an instantaneous gap emerges. This so-called snapback distance has been investigated and determined to be approximately 0.5 nm by STM measurements in clean solvent.

The conductance range where these plateaus appear extends from 10^{-2} G_0 to 10^{-4} G_0 (high conductance region, H in panel A). For a relatively large number of cycles the plateaus are followed by a drastic decrease of the conductance until the limitation of the measurement 10^{-6} G_0 (noise level) is reached. Some cycles, however, show additional molecular features in a lower conductance range, between 10^{-4} G_0 and the noise level (low conductance region, L). The existence and variation of more than one molecular state is related to different structural changes of the single-molecular junctions (SMJs) as they evolve through different pulling stages: formation, conformational rearrangements and breakage.[18] For each applied V_{bias} conductance-distance measurement cycles are repeated over 2000 times in order to have solid statistical analysis. Without any data selection protocol and for experiments under identical conditions, one-dimensional (1D) conductance histograms of the logarithmic conductance $\log(G/G_0)$[22] were constructed for **114**, **115** and **117** with all data points of 2232 traces each (V_{bias} = 0.35 mV).

Figure 3.19 B displays sharp peaks in the conductance histogram, positioned in the conductance scale at 0 that represent the conductance through a single atom gold-gold contact.[122] In a lower conductance range (region H), three pronounced peak-shaped distributions were observed for each molecule whose maximum G_{H} is positioned at a lower conductance range for longer molecules. By using Gaussian fits the most probable conductance values were extracted for **114** ($G_{\text{H}} = 10^{-2.44}$ G_0, 276.50 nS), **115** ($G_{\text{H}} = 10^{-3.09}$ G_0, 62.13 nS) and **117** ($G_{\text{H}} = 10^{-3.72}$ G_0, 14.60 nS). In region L, a shallow shoulder is observed for **114** and **115** and the extracted conductance values G_{L} from Gaussian fits are 0.62 nS ($10^{-5.09}$ G_0) and 0.23 nS ($10^{-5.52}$ G_0), respectively. We assign these two molecular conductance features G_{H} (high) and G_{L} (low) to the most probable conductance states of single molecules bound to the two gold leads promoted as the molecular junction is being stretched. We did not observe a low conductance state G_{L} for **117** most probably because its position in the conductance scale overlaps with, or is below, the noise level of the STM setup.

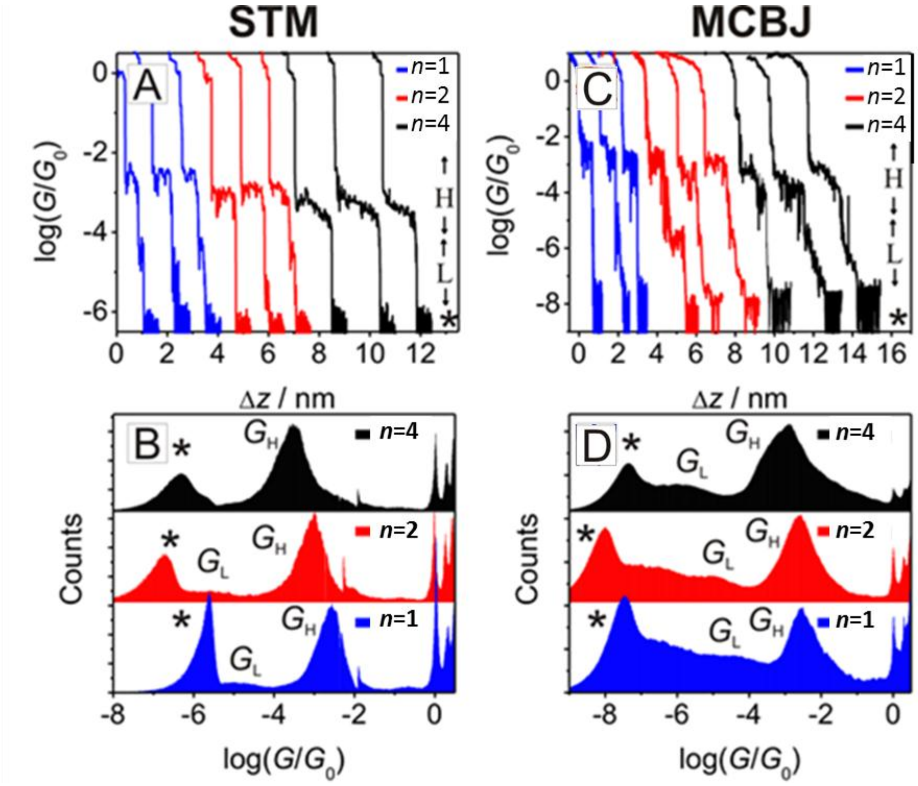

Figure 3.19 (A, B) Conductance measurements of 114, 115 and 117 employing the STM-BJ approach. (A) Typical conductance distance traces recorded at V_{bias} = 0.035 V. (B) 1D conductance histograms and (C, D) Conductance measurements, employing the MCBJ approach. (C) Typical conductance distance traces measured at V_{bias} = 0.1 V. (D) 1D conductance histograms and (F) 2D conductance histograms for 114 generated from 2000 curves each. The noise level peaks are labeled with an asterisk (*).

In Figure 3.20 (A-C), two-dimensional (2D) representations[101] of all the individual traces recorded for **114, 115,** and **117** are shown which further support the assignment of distinct conductance states at different stretching stages. For the construction of these 2D traces, a common origin 0.7 G_0 was assigned to accurately align all individual conductance-distance traces in the distance scale.[97] This strategy is justified because of the sharp decrease of conductance when the last atomic gold-gold contact breaks.[117] The plots in Figure 3.20 show quantised conductance features at distances Δz < 0 corresponding to gold-gold contacts and two well resolved clouds of high data point density in regions H and L at positions that allow us to trace back the evolution of the junctions. In region L for **114** (Figure 3.20 A), a feature at [$10^{-3.5}$ $G_0 \leq G_H \leq 10^{-2}$ G_0] and centered around $10^{-2.50}$ G_0 (245 nS) was observed that extends and slightly tilts from 0 to 1 nm. A second molecular feature of lower intensity develops at [10^{-6} $G_0 \leq G_L \leq 10^{-4.5}$ G_0], centered around 10^{-5} G_0 in a shorter distance range [0.8 – 1.2 nm]. From this observation, it is clear that there are structural transitions of the extended molecule with the evolution of the stretching process.

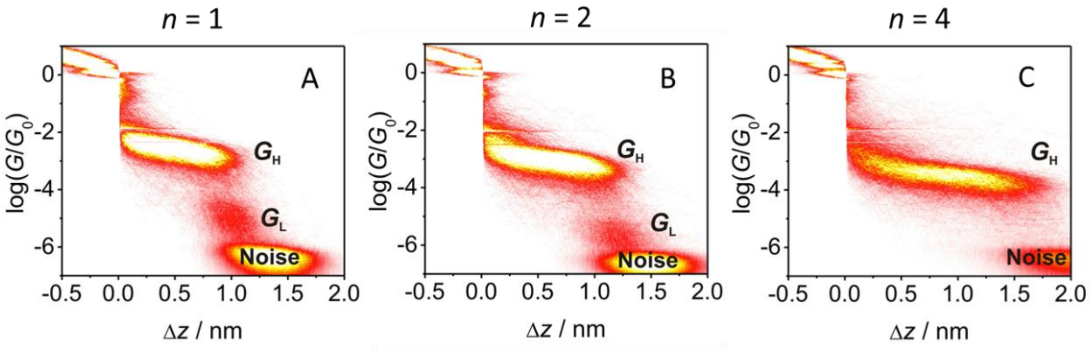

Figure 3.20 2D conductance histograms generated from 2232 individual curves for 114 (A), 115 (B) and 117 (C).

Complementary G-Δz measurements were carried out with the MCBJ technique. The corresponding sample traces and conductance histograms are displayed in Figure 3.19 B, D and Figure 3.20, respectively. The extracted most probable conductance values from the MCBJ experiments are quoted in Table 3.2. The extended conductance window of this setup enables us to resolve the low conductance feature $G_L = 10^{-6.06}\ G_0$ (0.067 nS) of **117** and at the same time allows us to distinguish the features for **114** and **115** more clearly. Identical trends are extracted from both experimental approaches which supports the reliability of the results. Since this series is studied in single-molecule conductance measurements for the first time, there are no reference results to compare with. However, the conductance values are significantly larger than the conductance observed for conjugated compounds of similar lengths, such as OPE3 molecules, with different anchoring groups and different functional groups in the middle phenyl ring.[116,119,180-182]

3.3.2 Effect of the Anchoring Groups on the Single-Molecule Conductance Values

Following the experimental approaches and data analysis strategies introduced for the DHBT series, we explored the transport characteristics and single-molecule junction (SMJ) evolution of five different end-capped oligoyne series. All molecules were studied by an STM-BJ approach and selected compounds were additionally measured using the MCBJ set up (Table 3.2).

For the PY series, we observed three molecular states G_H, G_M and G_L which are stable at different stretching stages. Due to the minimum detection limit of our measurements, all of those three stages are resolved for molecule **41**, two stages for molecule **54** (G_H and G_M) and only the G_H state for **55**. Previously, these three states were assigned to distinct junction configurations.[18]

In the high conductance state, we hypothesise that in the beginning of the cycle the molecule is not fully stretched between the leads and one or two pyridyl rings can lie adjacent to gold adatoms, enhancing the electronic coupling between the gold leads and the π electron cloud of the molecule.[18,86,95] Upon further retraction of the tip, the configuration of the molecule is changed from a tilted configuration to a fully extended upright configuration and the conductance undergoes an abrupt transition to the G_M state. Finally, the G_L state appears only after the molecule has been completely stretched and pulling out of gold atoms can occur or the formation of π-stacks can take place.[78,79] This is also supported by the increasing and stepwise length of the plateaus when analysing the H, M and L ranges. Comparing the conductance values [G_H = 33.52 nS = $10^{-3.36}$ G_0, G_M = 5.8 nS = $10^{-4.12}$ G_0 and G_L = 0.11 nS = $10^{-5.84}$ G_0] with literature data, compound **41** has been trapped between gold electrodes by Wang *et al.*[86] and Velizhanin *et al.*[118] Their data ($10^{-4.0}$ G_0 to $10^{-3.3}$ G_0 and $10^{-3.7}$ G_0 to $10^{-3.5}$ G_0, respectively) agree to within half an order of magnitude with the present results for the M and H states, respectively. Diyne (**54**) and tetrayne (**55**) compounds were also reported by Wang *et al.*[86] In that work, three sets of conductance values were assigned to different coordination arrangements of the pyridyl groups by gold atoms. Our new results for **54** (G_H = $10^{-3.76}$ G_0 and G_M =$10^{-4.48}$ G_0) agree to within less than half an order of magnitude with the previous middle (G_M = $10^{-3.53}$ G_0) and low (G_L = $10^{-4.29}$ G_0) values. The previous high ($10^{-2.6}$ G_0) and middle and high ($10^{-3.61}$ G_0; $10^{-2.66}$ G_0) conductance values for **54** and **55,** respectively, were not observed in this work.

Due to synthetic difficulties already mentioned in the synthesis section, the whole SH and NH_2 series could not be studied. The study of compound **67** was attempted but prior to break junction measurement we observed a colour change and precipitation of the freshly prepared solution. Contrary to the experiments conducted with compounds **50** and **66**, once the gold substrate was reached with the STM tip we observed that the surface was blocked, indicating decomposition of **67**. No defined conductance-distance feature could be obtained, besides the fundamental quantum of conductance G_0 in the 1D-conductance histograms. On the other hand, for the compounds **77** and **78** no conductance data was observed, presumably because of the steric bulk of the methyl groups. We did not attempt to measure tetrayne **80**.

Compounds **50** and **66** each showed two molecular features (G_H = 45.22 nS = $10^{-3.23}$ G_0 and G_L = 1.13 nS = $10^{-4.83}$ G_0) and (G_H = 26.26 nS = $10^{-3.47}$ G_0 and G_L = 0.88 nS = $10^{-4.94}$ G_0) respectively. The reported values for **50** are $10^{-3.25}$ $G_{0,}$ [182,183] and $10^{-3.1}$ G_0,[87] which correlate perfectly with our G_H state; no low conductance state had previously been reported. For the *N*-methylaniline end-capped compounds **83** and **84**, we obtained exactly the same conductance values as their analogues without methyl groups. However, attempts were not made to measure *N*-methylaniline end-capped tetrayne **86** because of difficulty of handling as a result of its light sensitivity.

Thiol end-capped oligoynes **47** and **99**, showed two conductance states that differ by more than one order of magnitude (G_H = 117.3 nS = $10^{-2.82}$ G_0; G_L = 2.11 nS = $10^{-4.56}$ G_0) and (G_H = 56.14 nS = $10^{-3.14}$ G_0; G_L = 1.72 nS = $10^{-4.65}$ G_0) respectively. Employing STM-BJ and *I*(t) and *I*(s) approaches, Xing *et al.*[119] and Sedghi *et al.*[184] reported, respectively, single conductance values that lie between our two conductance states (20 nS = $10^{-3.58}$ G_0) for **47** and (3.1 nS = $10^{-4.39}$ G_0)for **99**.

For the CN series a unique feature at a lower conductance range was found. To the best of our knowledge, only molecule **53** has been studied previously using MCBJ-based *I*-V_{bias} measurements.[81] By fitting the experimental current–voltage characteristics to a single-level tunneling model the authors determined a conductance $G = 10^{-1.88}$ G_0 which is much larger than our finding ($10^{-4.8}$ G_0). However, we note that Zotti *et al*. presented I–V_{bias} curves[18] of an MCBJ experiment with **53**, from which we estimate a low bias junction conductance of $10^{-4.6}$ G_0.

The range of molecular conductance for the NO_2 series **94**, **95** and **97** fell below the noise level of the STM setup, but were accessible with the MCBJ setup. The results were extracted only by using a heavy data selection procedure that removed all the pure tunnelling conductance traces (~95 %) from the recorded data sets. This is indicative of either weak interaction of nitro anchoring group with gold surfaces or selective directionality of the Au-NO_2 bond. Further analysis of the remaining curves gave one conductance feature (G_H) for **94**, **95** and **97** (0.54 nS = $10^{-5.15}$ G_0, 0.16 nS = $10^{-5.69}$ G_0 and 0.01 nS ≈ $10^{-7.0}$ G_0) respectively.

3.3.3 Effect of the Molecular Length on the Single-Molecule Conductance

From analysis of the conductance-distance traces, the conductances of three compounds (*n* = 1, 2 and 4) in each series decrease in the expected order $G_{n=1} > G_{n=2} > G_{n=4}$ for both high and low conductance features. The decrease of the high *G* state follows an exponential dependence with the length of the molecules according to the formula below, where G_C is an effective contact conductance defined by the specific interaction at the molecule-electrode interfaces; β is a decay pre-factor that depends on the nature of electronic communication in the molecular backbone and L_m is the molecular length.[185]

$$G = G_c e^{-\beta L_m}$$

The length dependence of the conductance is a direct consequence of the mechanism that governs the electron transport through the molecular wire and for short conjugated molecules (< 3 nm) following this exponential dependence with the length it is well accepted that the mechanism involved in the electron transport is direct (non-resonant) tunneling. In the semi-logarithmic plot of the high conductance state G_H versus molecular length L_m (Figure 3.21 A), each data point represents the most probable G_H value extracted from 2232 individual G-Δz measurements.

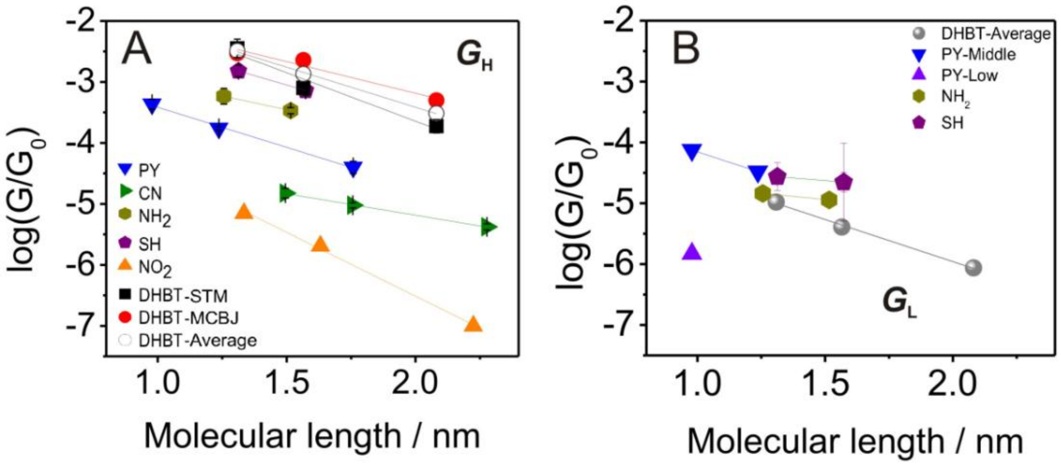

Figure 3.21 Experimental conductances as a function of molecular length of all oligoyne series for (A) the G_H and (B) the G_L states. Each data point represents the average value of measurements carried out using at least three different V_{bias} (0.25-0.17 V) and the error bars are their standard deviations. The straight lines are linear fits from which we calculated the decay pre-factors. Since CN and NO_2 series only have one conductance state, they are not included in panel B.

Using a linear fit and extrapolation to L_m = 0, a decay parameter for the high conductance band of the oligoyne series was determined. The summary of the most probable single-molecule conductance data, single-molecule junction formation probabilities (SMJ FP), β values, and resistances of all molecules measured in this chapter are shown in Table 3.2.

Table 3.2 Most probable conductance values of oligoyne series from both STM and MCBJ measurements

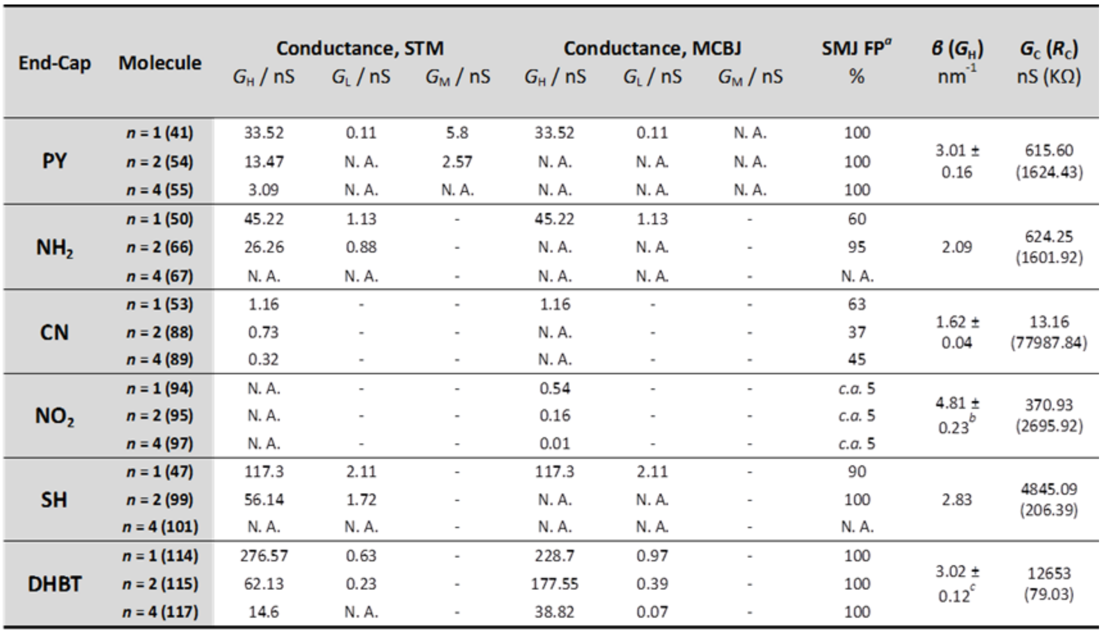

End-Cap	Molecule	Conductance, STM			Conductance, MCBJ			SMJ FP[a]	β (G_H)	G_c (R_c)
		G_H / nS	G_L / nS	G_M / nS	G_H / nS	G_L / nS	G_M / nS	%	nm^{-1}	nS (KΩ)
PY	***n* = 1 (41)**	33.52	0.11	5.8	33.52	0.11	N. A.	100	3.01 ± 0.16	615.60 (1624.43)
	***n* = 2 (54)**	13.47	N. A.	2.57	N. A.	N. A.	N. A.	100		
	***n* = 4 (55)**	3.09	N. A.	N. A.	N. A.	N. A.	N. A.	100		
NH_2	***n* = 1 (50)**	45.22	1.13	-	45.22	1.13	-	60	2.09	624.25 (1601.92)
	***n* = 2 (66)**	26.26	0.88	-	N. A.	N. A.	-	95		
	***n* = 4 (67)**	N. A.	N. A.	-	N. A.	N. A.	-	N. A.		
CN	***n* = 1 (53)**	1.16	-	-	1.16	-	-	63	1.62 ± 0.04	13.16 (77987.84)
	***n* = 2 (88)**	0.73	-	-	N. A.	-	-	37		
	***n* = 4 (89)**	0.32	-	-	N. A.	-	-	45		
NO_2	***n* = 1 (94)**	N. A.	-	-	0.54	-	-	*c.a.* 5	4.81 ± 0.23[b]	370.93 (2695.92)
	***n* = 2 (95)**	N. A.	-	-	0.16	-	-	*c.a.* 5		
	***n* = 4 (97)**	N. A.	-	-	0.01	-	-	*c.a.* 5		
SH	***n* = 1 (47)**	117.3	2.11	-	117.3	2.11	-	90	2.83	4845.09 (206.39)
	***n* = 2 (99)**	56.14	1.72	-	N. A.	N. A.	-	100		
	***n* = 4 (101)**	N. A.	N. A.	-	N. A.	N. A.	-	N. A.		
DHBT	***n* = 1 (114)**	276.57	0.63	-	228.7	0.97	-	100	3.02 ± 0.12[c]	12653 (79.03)
	***n* = 2 (115)**	62.13	0.23	-	177.55	0.39	-	100		
	***n* = 4 (117)**	14.6	N. A.	-	38.82	0.07	-	100		

Figure 3.21 and Table 3.2 summarise the dependence of the most probable conductance states G_H and G_L (G_M) versus molecular length L_m for all oligoyne series. The G_H state follows an exponential decrease with the molecular length and for the series comprising three data points we calculated tunnelling decay pre-factors (β) and contact conductances (G_c) by using linear fits of the semi-logarithmic plots. The β values range from 1.6 to 4.8 nm^{-1} following the trend $\beta_{CN} < \beta_{DHBT} = \beta_{PY} < \beta_{NO2}$. For completion and with due precaution we also extracted decay factors for SH (2.83 nm^{-1}) and NH_2 (2.09 nm^{-1}). It is clear then that the different anchor groups control not only the strength of the coupling to the metal but also the position of the relevant energy levels which in turn determine the electron transport in SMJ.[81]

In the low conductance range, we could only obtain one decay factor for the DHBT series 3.17 ± 0.17 nm^{-1}, which is in good agreement with the value for the G_H states. The low conductance values of **114**, **115,** and **117** for this calculation were the average conductances from both STM-BJ and MCBJ. Figure 3.21 B illustrates that the low conductance state also decreases with the molecular length but these are insufficient data points to extract conclusive quantitative information.

The existence of more than one conductance state and its origin coming from stability to elongation are evidence of strong and stable contacts upon elongation for DHBT, PY, SH and NH_2 anchoring groups. The most probable absolute displacement for high and low conductance states and the results are summarised in Figure 3.22. From the analysis of the high conductance range [0.7 $G_0 < G < 0.1\ G_H$], we see that the elongation that can stabilise the junction in the high state scales almost linearly with the molecular length (Figure 3.23 A, dash line). The individual conductance-distance traces and the 2D histograms in Figure 3.20 clearly display that the conductance decreases slightly during the evolution of each conductance state. We thus conclude that for the same four series of molecules the high conductance state starts from the formation of the junction, when the molecule has a tilted configuration, and prevails and slightly decreases upon stretching until it is in an upright position. Extension of this analysis to lower conductance ranges [0.7 $G_0 < G < 10^{-6}\ G_0$] indicates that the junctions sustain elongation beyond complete extension (data points above the dash line) and this would suggest two possibilities. On the one hand, if the interaction between molecule and gold leads is stronger than the Au-Au linkage, there could then be rearrangements (Figure 3.22 B) of the gold electrodes after the SMJ is completely stretched. On the other, formation of longer π-stacked junctions could explain why the junction can be elongated beyond the actual molecular length. These four groups of molecules also showed rather high yield of successful junction formation probability (Table 3.2).

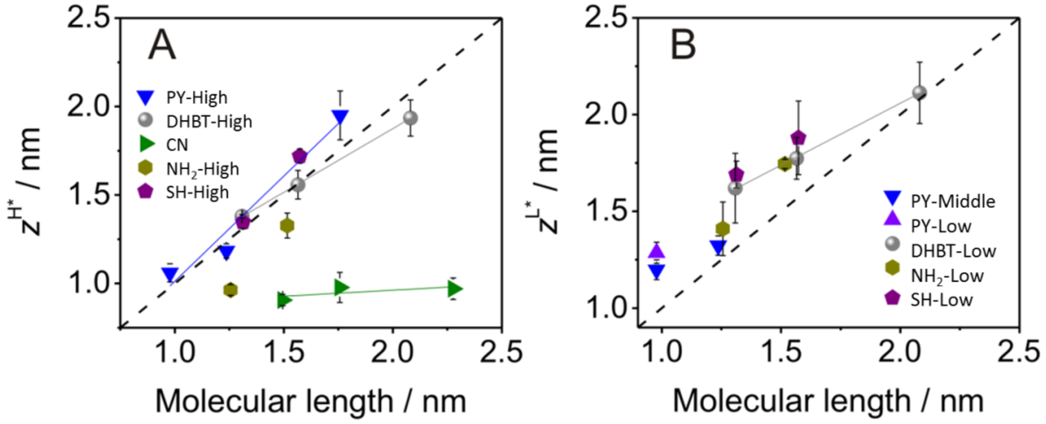

Figure 3.22 Most probable characteristic length z^* of molecular junctions in (A) the high conductance range 0.7 $G_0 < G < 0.1\ G_H$ and in (B) the low conductance range 0.7 $G_0 < G < 0.1\ G_L$. Each data point represents the average value of measurements carried out using at least three different V_{bias} values (0.25-0.17 V) and the error bars are their standard deviations.

Conversely, the CN and NO_2 series behave differently. For those molecules the formation junction probability was rather low, 37-63% for CN and ≤ 5% for NO_2 series. Figure 3.22 A shows that the length of the plateaus (relative elongation of trapped molecule between leads) for the CN series is rather independent of the molecular length and much lower than the actual length of the molecule. This leads to the conclusion that junctions from the cyano and nitro series, if formed, break typically in a tilted orientation, because they do not survive total extension, presumably due to thermal vibrations. We hypothesise that these two groups interact weakly with the gold surfaces compared to the other anchors. This could explain why more than one conductance state was not observed, in contrast to molecules with more robust metal-molecule interactions.

3.4 Conclusions

In conclusion, we have synthesised and characterised functional oligoyne compounds for single-molecule transport experiments. Some known and some novel stable tetrayne derivatives comprising six different anchoring groups have been synthesised and their conductance characteristics and junction stabilities addressed at the single-molecule level by using both STM-BJ and MCBJ approaches. Their conductances and length dependences (decaying parameter β) indicate that this new series of conjugated molecules are promising candidates for molecular wires, in comparison to both OPEs and OPVs. Notably the DHBT anchoring group shows great promise.

These results encourage further extension of this work towards the synthesis of longer functional oligoyne compounds, which could be introduced into single-molecule devices. Our initial studies in this direction are described in Chapter 4.

Chapter 4

Shielding Strategy Towards more Stable Functional Oligoynes

4.1 Introduction

After the discovery of fullerene (C_{60}) in 1985, carbon-rich compounds became a popular research subject.[186] The sp^3 (diamond) and sp^2 hybridised carbon systems (eg., graphene, nanotubes, fullerene) have been widely investigated due to their outstanding electronic and optical properties.[131,132] However, *sp* hybridised carbon allotrope –so called carbyne- is the least known among the carbon allotropes.

According to the computational studies by the Lambert Group, after reaching a certain number of contiguous carbon atoms (ca. 28) in the backbone, the single-molecule conductance of oligoynes would be independent of the chain length. The synthesis of longer analogues is, therefore, an important synthetic challenge.[134,187]

As briefly explained in the previous chapter, oligoynes/polyynes have very attractive electron transport properties. However, the synthesis of the longer derivatives encounters problems as the stability decreases with the increasing number of the triple bonds in the *sp*-backbone. The main strategies to stabilise longer analogues are to terminate the oligoyne chains with bulky head groups[135-138] or to shield the oligoyne backbone.[139,140] The purpose of both methodologies is to prevent the reactive oligoyne core from cross-linking or being oxidised by keeping the reactive backbones apart from each other.[141,142] In the recent literature, there are numerous examples of stable oligoynes/polyynes.

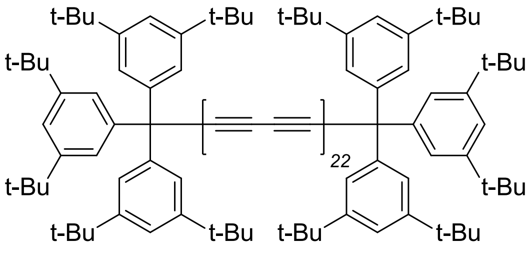

118

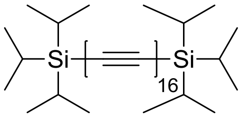

119

Various bulky head groups stabilise oligoynes such as, alkyl, aryl, trialkylsilyl or organometallic groups. An important example was recently reported by Tykwinski and Chalifoux.[188] They synthesised the longest known polyyne (**118**) to date which has 44 contiguous carbon atoms between very bulky tris(3,5-di-tert-butylphenyl)methyl (Tr) head groups. Previously, Tykwinski and co-workers also synthesised up to 16 triple bonds between two triisopropylsilyl (TIPS) end-groups (**119**).[189] The X-ray crystal structures of hexayne derivatives show the dramatic difference in size between Tr and TIPS groups (Figure 4.1).

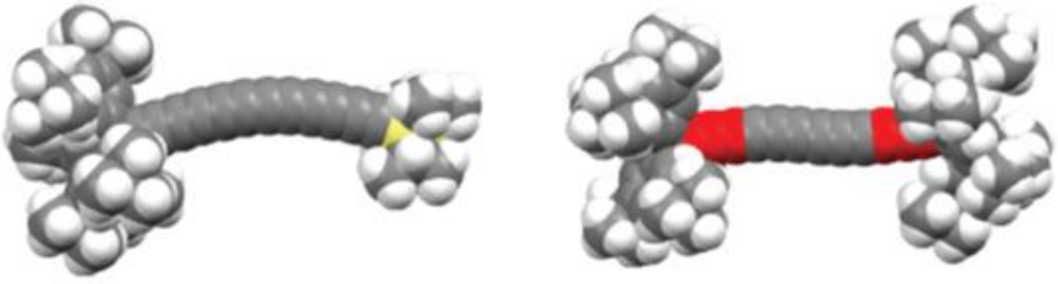

Figure 4.1 X-ray molecular structures of hexaynes (left: Tr – TIPS end-capped, right: Tr-Tr end-capped) as space filling models (Reproduced from reference [188]).

Another hexayne stabilised by bulky head groups **120** was synthesised in our laboratory by Dr.Wang.[138] *N*-phenylcarbazole was also shown to stabilise the more reactive terminal hexatriyne. Organometallic end-capped oligoynes are also known, and Hirsch and co-workers reported 28 contiguous carbon atoms between bulky Pd centres surrounded by triarylphosphines (**121**).[137]

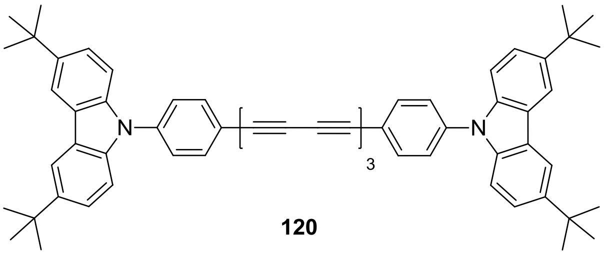

120

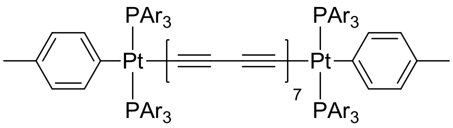

121

Shielding the reactive oligoyne backbone is another method to stabilise longer oligoyne analogues. However, due to the difficulty of the synthesis of the precursors, shielding is not as common method in this topic. Hirsch and co-workers reported the improved stability of octayne (**122**) with a long alkyl group shielding the core.[139] Sugiyama and Tomita also stabilised of a phenanthryl end-capped octayne with rotaxane formation by a cyclodextrin macrocycle (**123**).[140]

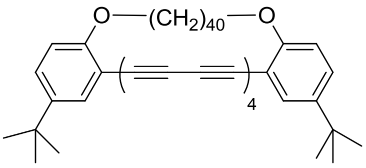

122

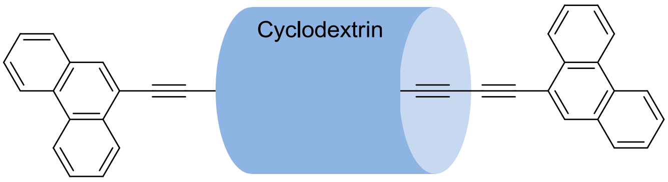

123

All the stable oligoynes mentioned above were made to demonstrate enhanced stability. None of them has any functionality suitable for self-assembly on a metal surface or to use in an electron transport application. In this context, we have designed new functionalised oligoynes, in which the backbone is shielded by two methyl groups. We chose pyridyl and amino anchoring groups for our initial studies (Figure 4.2), because of their uniform junction formation and rather high conductance values (Chapter 2 and 3).

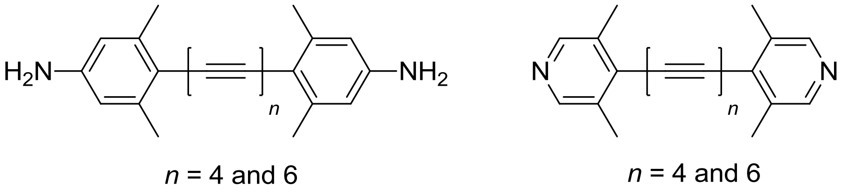

Figure 4.2 Functional oligoynes with methyl shielded backbones.

4.2 Synthesis

4.2.1 Synthesis of 3,5-Dimethylaniline End-Capped Oligoynes

We developed the following route for the synthesis of 3,5-dimethylamino end-capped oligoynes (Scheme 4.1). Initially, our target was tetrayne **127** in order to judge the contribution of the methyl groups to the stability of the tetrayne, by comparison with **67**. The key iodo derivative **125** was synthesised in 67% yield by the iodination of commercially available 3,5-dimethylaniline (**124**) under mild conditions.[190,191] The Sonogashira cross-coupling reaction between **125** and TMSA was previously reported by Nielsen and co-workers.[192] However, by using exactly the conditions they reported, we could not reproduce that reaction either with TMSA or BDTMS (**58**). In our hands, we isolated unreacted **125** and homo-coupled TMSA from this reaction.

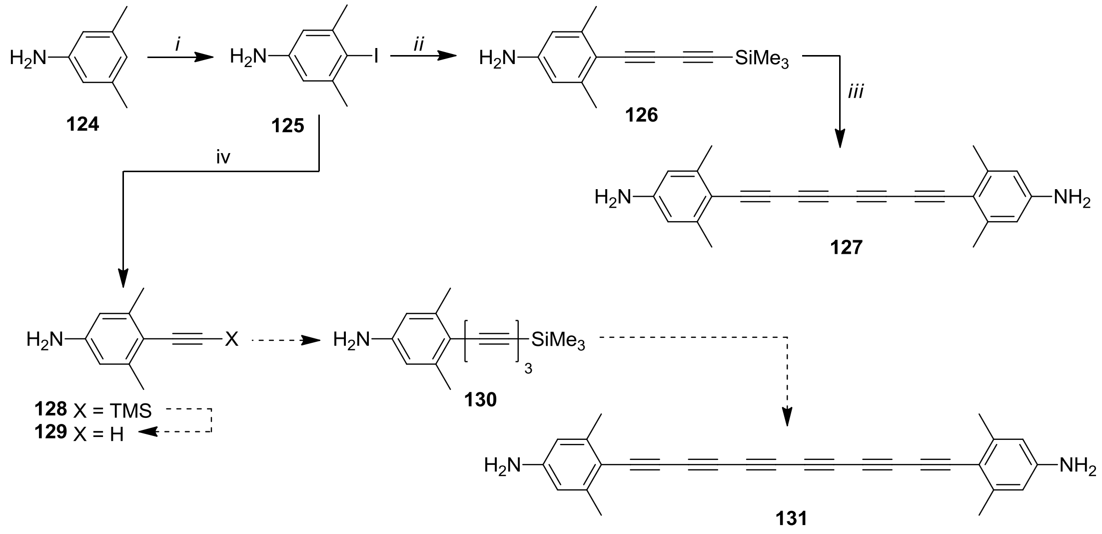

Reagents and conditions: (*i*) *N*-iodosuccinimide, acetonitrile, overnight, rt, 67%; (ii) HC≡C-C≡C-SiMe$_3$ (**58**), Pd[(PPh$_3$)$_4$], (*i*-Pr)$_2$NH, CuI, 20 mins, MW, 100°C, 13%; (iii) Cu(OAc)$_2$.H$_2$O , Pyridine / MeOH, 12h, overnight, 65%; (iv) TMSA (excess), Pd[(PPh$_3$)$_4$], (*i*-Pr)$_2$NH, CuI, 20 mins, MW, 100°C, 72%.

Scheme 4.1 Synthesis of methyl shielded tetrayne (127) and hexayne (131).

Therefore, an alternative route was developed (Scheme 4.2). Commercially available 4-hydroxy-3,5-dimethylnitrobenzene (**132**) was reacted with triflic anhydride to give **133** and following a Sonogashira cross-coupling with TMSA gave **134**[192] in a 78% yield. At this stage we tried to reduce the nitro moiety to amine, but obtained only 15-25% yields of **128** and **129** from the reduction reactions of either **134** or **135**. Compound **129** was not purified, but ^{1}H NMR data are consistent with its structure.

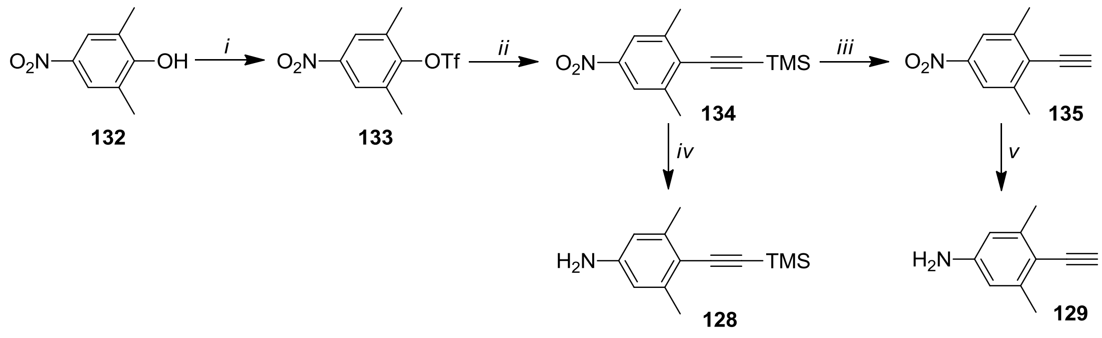

Reagents and conditions: (*i*) Tf$_2$O, DCM/Pyridine, 1h, 0°C to rt, 88%; (ii) TMSA, Pd[(PPh$_3$)$_4$], CuI, Et$_3$N, overnight, rt, 78%; (iii) TBAF, THF, 30 mins, rt, 85%; (iv) SnCl$_2$.2H$_2$O, DMF, overnight, 80°C, 15%; (v) SnCl$_2$.2H$_2$O, DMF, overnight, 80°C, 25%;.

Scheme 4.2 Alternative synthesis of 128 and 129.

The Sonogashira cross-coupling reaction between **133** and TMSA proves that the failure of the previous Sonogashira cross-coupling between **125** and corresponding alkyne was not due to steric hindrance from the methyl groups adjacent to the iodo position.

After trying various conditions (eg., various bases, catalysts etc.) to obtain **126** and **128,** microwave irradiation of the reaction mixture afforded **128** in a 72% yield. However, under the same microwave conditions, the cross-coupling between **125** and BDTMS (**58**) gave desired product **126** in only a 13% yield. The low yield is presumably due to the decomposition of either alkyne **58** or **126** under microwave conditions.

The synthesis of the tetrayne **127** was achieved in a 65% yield by the same methods as discussed in chapter 3. Comparing the stability of aniline end-capped tetrayne (**67**) with *N*-methylaniline end-capped tetrayne (**127**), showed a significantly improved stability for **127**. However, due to the light sensitivity of **127**, decomposition as seen for compound **67** was observed. **127** was unambiguously characterised by ^{1}H and ^{13}C NMR spectroscopy (Figure 4.3 and 4.4), mass spectrometry and X-ray crystallography, using single crystals which were grown in the dark. NMR spectra of **127** provided no evidence for decomposition upon storage in $CDCl_3$, in the NMR tube for 6 days in the dark after isolation. No precipitation or colour change in the NMR tube was observed when it was kept in the dark. After these 6 days storage, the NMR solution was exposed to ambient laboratory light. Subsequently, the formation of a brown-black precipitate was observed in the tube, after 2h under light. However, the decomposition product(s) was not soluble in the NMR solvent and could not be observed in the spectrum.

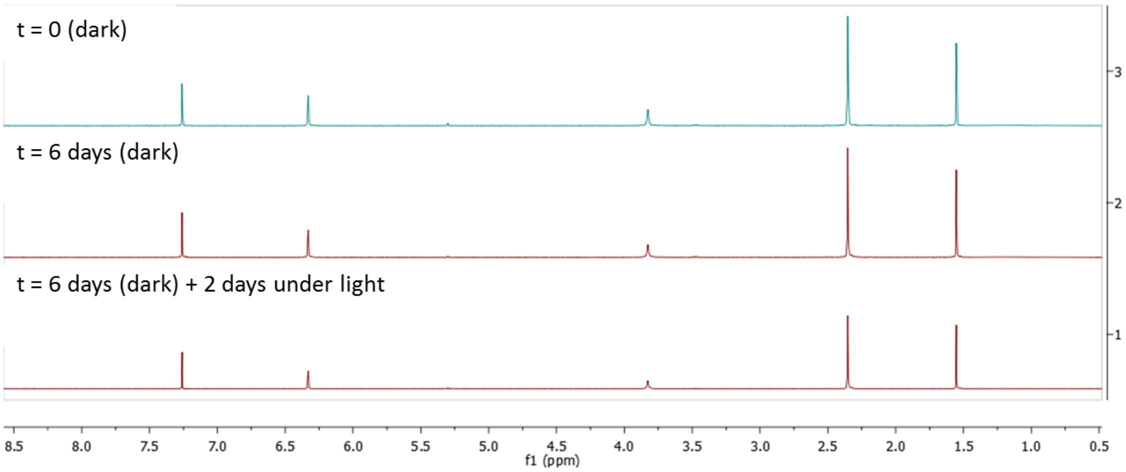

Figure 4.3 Comparison of ^{1}H NMR spectra of 127 in $CDCl_3$ at 400 Mhz in different times frames.

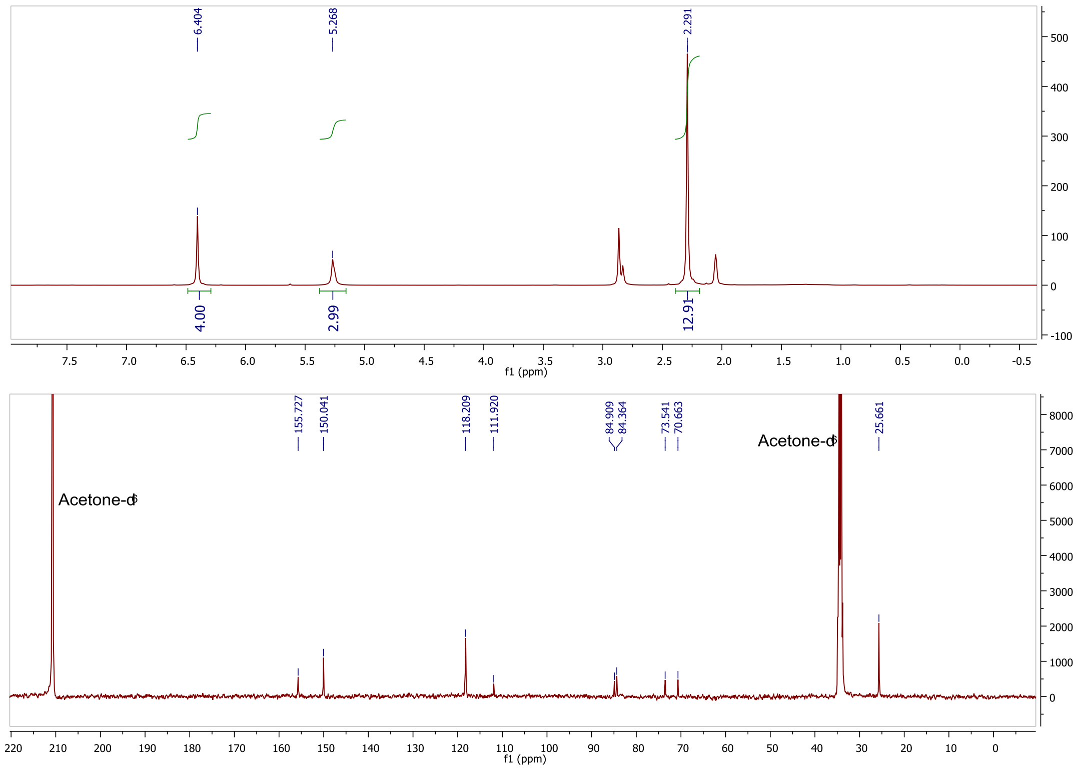

Figure 4.4 ^{1}H and ^{13}C NMR spectra of 127 in acetone-d_6 at 400 Mhz and 100 MHz.

The X-ray molecular structure of **127** has two crystallographically equivalent molecules, in which amine moieties are hydrogen bonded to solvent acetone carbonyls (Figure 4.5). The phenyl rings are co-planar and the carbon chain is linear.

The planned synthesis of hexayne compound (**131**) as depicted in scheme 4.1 is still in progress.

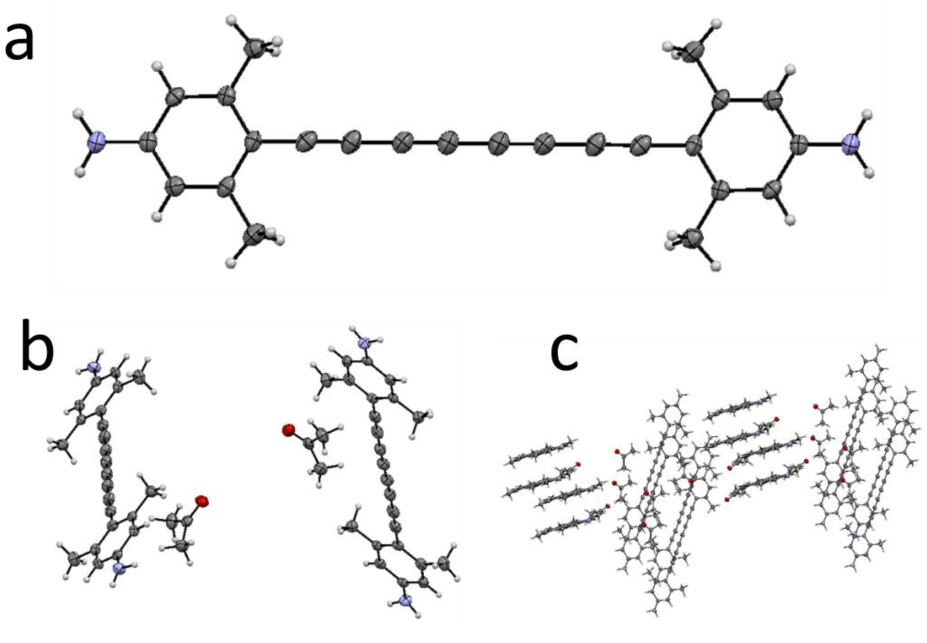

Figure 4.3 X-ray molecular structure (a, b) and crystal packing diagram (c) of 127.

4.2.2 Synthesis of 3,5-Dimethylpyridine End-Capped Oligoynes

As mentioned in chapter 3, pyridyl end-capped hexayne (**64**) could not be isolated, presumably because of its instability. Therefore, in order to test methyl shielding on the stability, hexayne **140** is a target (Scheme 4.3).

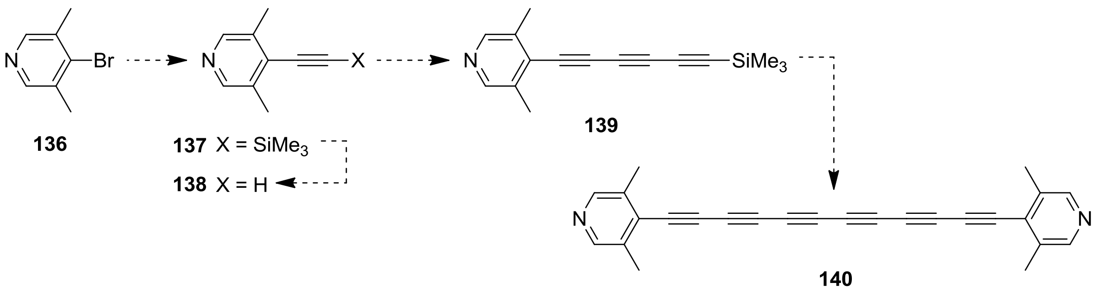

Scheme 4.3 Planned route to the synthesis of hexayne 140.

The synthesis of the key building block **136** for the synthesis of 3,5-dimethylpyridyl end-capped oligoynes was performed according to the literature route (Scheme 4.4).[193] Commercially available 3,5-lutidine (**141**) was oxidised to *N*-oxide (**142**) by using *m*-chloroperbenzoic acid to activate the 4-position of the pyridyl ring. Direct bromination of pyridine *N*-oxides using bromine in acetic acid and thallium acetate was reported by Saito and Hamana.[194] However, the 3-step literature route was preferred due to the financial and safety concerns. Nitration of **142** was followed by a reaction with acetyl bromide to give **144** in high yield. The following reduction step of the *N*-oxide unit by $LiAlH_4$ gave desired bromo product (**136**) in a 65% yield.

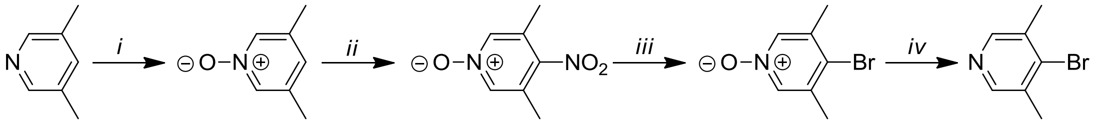

141 **142** **143** **144** **136**

Reagents and conditions: (*i*) mCPBA, 2h, rt, 73%; (ii) H_2SO_4/HNO_3, 90°C, 3h, 71%; (iii) AcBr, AcOH, 80°C, 3h, 96%; (iv) $TiCl_4$, $LiAlH_4$, THF, 0°C to rt, 2h, 65%.

Scheme 4.4 Synthesis of 4-bromo-3,5-luditine 136.

The rest of the synthesis of hexayne **140** is still under investigation.

4.3 Conclusions and Future Work

The improved stability of 3,5-dimethylaniline end-capped tetrayne (**127**), compared to the aniline end-capped analogue **67**, is an encouraging result which proves that methyl groups adjacent to the oligoyne chain can improve the stability of oligoynes. However, these are initial studies and due to time constraints it has not been possible to establish if this strategy will stabilise the longer or different end-capped derivatives. In the future, after synthesising and assessing the stability of **127**, **131** and **140** single-molecule transport studies will be performed.

Chapter 5

Inter-Layer Ligand Effect in Multilayer CdSe Based Photoelectrochemical Cells

5.1 Introduction

Semi-conductor quantum dots (QDs) have been of interest since the early 1980's.[195] Their diameters are between 1 and 10 nm and they consist of hundreds to a few thousand atoms. Their electronic properties are between those of bulk solid semi-conductors and molecules[196] and their optoelectronic properties can be tuned by varying the particle size (Figure 5.1).[197] In semi-conducting QDs the charge carriers (electrons and holes) are confined by potential barriers which give rise to unique quantisation effects.[198] QDs are sometimes referred as nanocrystals but that term covers a range of shapes, not only the spherical particles but nanowires, nanotubes, nanorods and nanoribbons.[198]

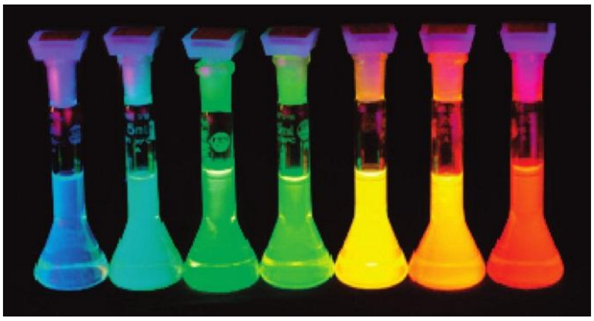

Figure 5.1 Size-dependent luminescence of colloidal semiconductor QDs (Reproduced from reference [198])

The semi-conducting properties of QDs are the result of periodic arrangements of atoms in a crystal lattice. The overlap of atomic orbitals leads to the formation of new bands of allowed electron and hole states separated by a band gap (Figure 5.2).[196,199]

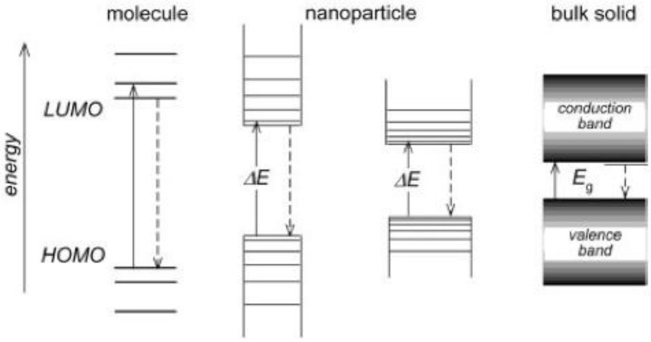

Figure 5.2 Schematic energy diagrams of a molecule, nanoparticle and bulk semiconductor.[196]

Inorganic semiconductors possess superior charge carrier mobility, light absorption and stability properties which make them favourable for electronics and optoelectronics applications in comparison with organic semiconductors.[200] However, the synthesis of inorganic semiconductors is rather expensive (e.g high vacuum, high temperature). In this context, QDs are attractive because nanometer size crystals can be produced and processed inexpensively.[201] They can be synthesised in large scales and can be solution processed by spin-coating, dip-coating and ink-jet printing processes. Hence, the fabrication costs of QD-based electronic and optoelectronic devices could be reduced.

5.1.1 Synthesis of Quantum Dots

Semiconducting QDs can be synthesised by the combination of different groups within the periodic table, such as II-VI (eg. CdSe), III-V (eg. GaAs), IV-VI (eg. PbSe) and V-VI (eg. Bi_2S_3).[197] In addition to secondary QDs, ternary (eg. $CuInS_2$) and quarternary (eg. $ZnCuInS_2$) QDs can also be synthesised.[197] The combination of different groups yields different band-gap energies.[199] The colloidal synthesis of monodisperse spherical QDs has been a popular research subject.[202] Many research groups are working on more sophisticated methods to optimise the size, shape and the connectivity between the particles to tune the band gap of a QD. The colloidal QDs can be synthesised from metal precursors (eg. inorganic salts) in a process which involves several steps. These are classified as nucleation, growth of the preformed nuclei and the isolation of the QDs.[202-204] Ideal QD particles should have narrow size distribution. This can be achieved by the hot-injection technique, which is the injection of the precursors (containing the M^{-2} precursor) into a hot solvent containing an organic ligand and the M^{+2} precursor with a subsequent temperature drop.[202,204,205] QDs can also be synthesised by various methods such as sol-gel,[206,207] vapour deposition[208] and *in situ* (eg. chemical bath deposition).[209]

Organic ligands bind onto the growing QD particles during the nucleation and growth steps in solution.[201,210] The ligands, which are usually long-chain carboxylic acid (eg. oleic acid), phosphonic acids (eg., *n*-octadecylphosphonic acid), alkanethiols (eg., dodecanethiol), alkyl phosphines or alkylphosphine oxides (eg., trioctylphosphine [TOP], trioctylphosphine oxide[TOPO]), can vary depending on the components of the QD (eg., CdSe or CdTe, etc.).[211,212]

The ligands control the kinetics of nucleation and growth steps.[202,204] Therefore, these steps should be balanced because if the nucleation rate is too slow or too fast, either bulk crystals or molecular clusters can be obtained from the reaction. The optimisation of the combination of molecular precursors, ligands, reaction conditions yields QDs with tailored monodisperse size, shape and surface morphology.

The ligands play a critical role in the synthesis and processing stages of QDs. Some ligands, for example carboxylate groups, provide colloidal stability due to the electronic repulsion between charged QDs.[213] The presence of ligands prevents the aggregation of the particles and prevents precipitation. The ligand can affect the optoelectronic properties of the isolated QDs. For example, CdSe nanoparticles do not show fluorescence when thiol ligands are used due to the hole trapping effect of the thiol moiety.[214] Hence, depending on the specific QD application, appropriate ligand selection is crucial for the QD synthesis and post-functionalisation.

Surface ligands also control the reactivity of QDs with other supramolecular systems by using bi-functional linkers. Considering QD thin films, surface ligands play a crucial role in the film morphology and conductivity – which is of special interest in the field of optoelectronics. Up to now, very little attention has been given to the interparticle coupling between QDs. Most of the ligands utilized are bulky and insulating, which prevent efficient charge transport between the particles, thereby limiting the potential of QDs in the field of optoelectronic applications (e.g. solar cells or FETs). The common ligands are summarised in Table 5.1.

Most surface ligands have an anchoring group which has high affinity for the nanoparticle and an aliphatic tail which provides steric stabilisation of a colloidal solution in nonpolar solvents.

Bulky ligands, which are suitable for the colloidal synthesis of QDs, can be replaced by other functional ligands by ligand exchange procedures[202,215] involving exposure of colloidal QDs to a larger excess of the competitive ligand to give partial or complete exchange of surface functionality of the QDs.[216] The degree of ligand exchange is usually determined by NMR, FTIR and XPS methods.

Table 5.1 Different Types of Surface Ligands Used in Nanocrystals and Nanocrystal Solids [198]

Ligand Type	Molecular Structure	Interparticle Spacing	Functions, Characteristics, Examples
Molecules with single anchoring group and long hydrocarbon chain	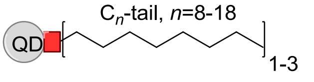 🟥 = HS-, HOOC-, H_2N-, $(OH)_2P(O)$- etc.	>1.5 nm	- Most common ligands for QD synthesis - Form stable colloidal solutions - Hydrophobic surface - Form highly insulating QD solids
Short-chain molecules with single anchoring group	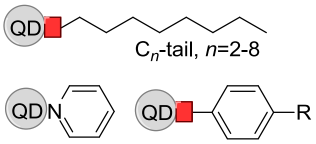 🟥 = HS-, HOOC-, H_2N-	0.3-1 nm	- Treatment of QD solids or ligand-exchang in solutions - Decreased colloidal stability - Improved electronic transport compared tc long-chain ligands - Higher conductivity
Cross-linking molecules with two end groups	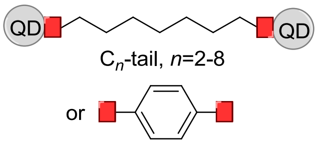 🟥 = HS-, H_2N-	0.3-1 nm	- Mainly prepared by treating QDs - Solar cells based on PbS and PbSe QDs showed power conversion efficincies upto 2.1%

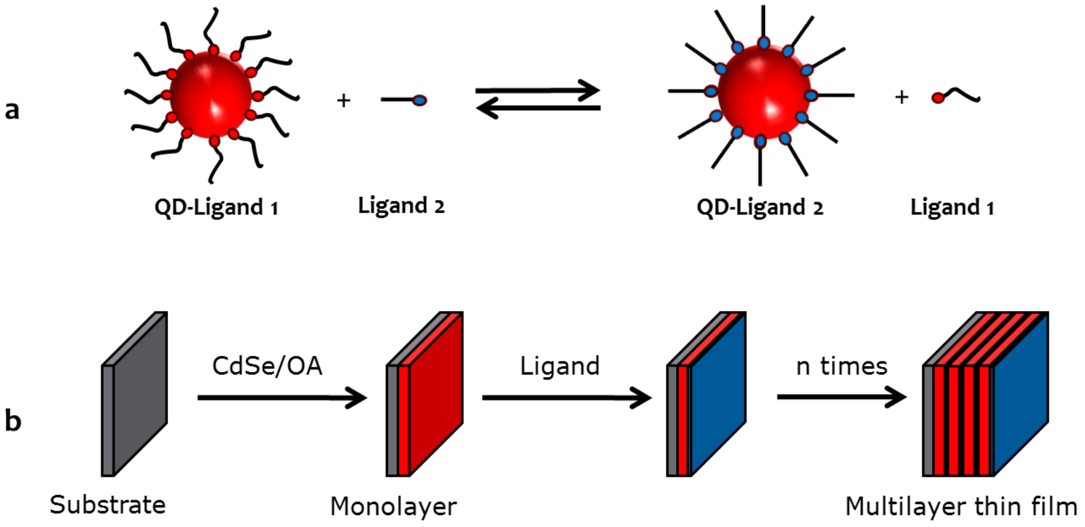

Figure 5.3 Illustration of ligand exchange process (a) in solution (b) on a solid substrate

Bifunctional ligands can be used to cross-link nanoparticles which provide reduced interparticle separation and improved electronic coupling between the particles, or to assemble them onto a surface. Guyot-Sionnes and co-workers have shown a significant ten-fold increase in the conductivity of TOP/TOPO end-capped CdSe nanoparticles by treating them with 1,7-diaminoheptane.[217] Subsequently, by using 1,4-phenylenediamine a further 1000 times increased conductivity was observed.

5.1.2 Quantum Dot Sensitised Solar Cells (QDSSCs)

Due to their favourable (opto)electronic properties and their solution processability, QDs are being used in many applications, such as solar cells, light emitting diodes (LEDs), photodetectors, field-effect transistors (FETs) and memory elements.[197]

QD-sensitised solar cells (QDSSCs) are popular due to their ability to harvest sunlight and inject electrons into TiO_2, low cost and ease of fabrication.[197,218] One of the potential advantages of QDSSCs is the phenomenon of multiple exciton generation, which is known as the inverse Auger effect.[219] Theoretically, this property leads to better power conversion efficiencies (η) which can reach up to 44%.[220] However, at present most of the QDSSCs provide conversion efficiencies around 4.0%.[221,222] This is because of the electron loss through charge recombination processes at the electrolyte-electrode interfaces (Figure 5.4).

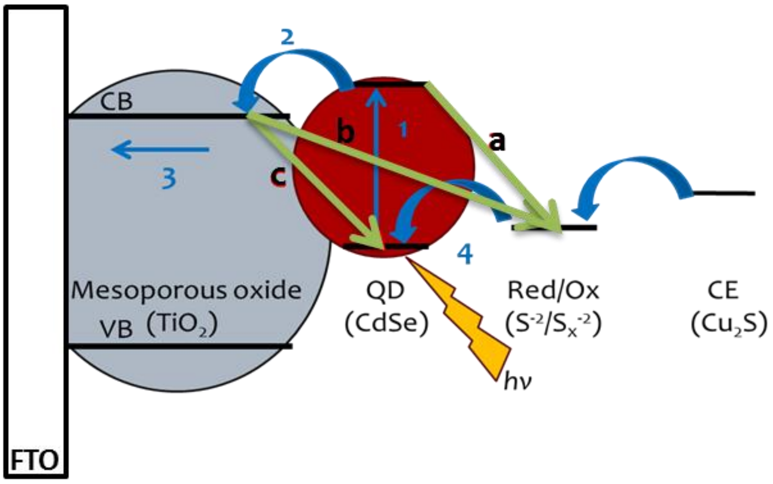

Figure 5.4 Operating principle (steps 1-4 in blue) and loss mechanism (steps a-c in green) of a typical CdSe QDSSC.

The working principles of a QDSSC are shown in Figure 5.4. Upon light absorption electron/hole pairs form in the QDs (step 1), leading to electron injection (step 2) into the conduction band of TiO_2 due to the energy level mismatch between the QD-TiO_2 conduction bands. This is followed by electron transport to the transparent conductive oxide (TCO) electrode (step 3), which is widely called fluorine doped tin oxide (FTO). The original electronic state of the QDs is restored by the electrolyte (step 4) which will reduce QD^+ to QD and the electrolyte will be regenerated by electron diffusion from the counter electrode (CE). The main loss mechanism of QDSSCs is also explained in Figure 5.4. If the electron transfer (step 2) to the CB of TiO_2 is too slow, electrons may be injected back into the electrolyte (step a) or the electrons can be transferred either to the redox layer (step b) or to the QD layer to fill the electron holes in the ground level (step c). The main factor which dominates the back-electron transfer is the low surface coverage of the QD-TiO_2 interface.[223]

The efficiency (η) of a QDSSC can be calculated from the formula in Figure 5.5, where I_{max} is the current at maximum power point, V_{max} voltage at maximum power point and P_{light} is the intensity of the illuminated light. The efficiencies of the absorption (η_{Abs}), charge separation (η_{Sep}) and charge collection (η_{Coll}) determine the overall efficiency of a solar cell. Additionally, the quality of a photovoltaic cell can be defined by fill factor (*FF*), which is the ratio of the maximum obtainable power (V_{max} x I_{max}) to the open circuit voltage and the short circuit current (I_{sc}). Typical FF values for QDSSC are in the range of 50%, as a result of the relatively large TiO_2-electrolyte recombination.

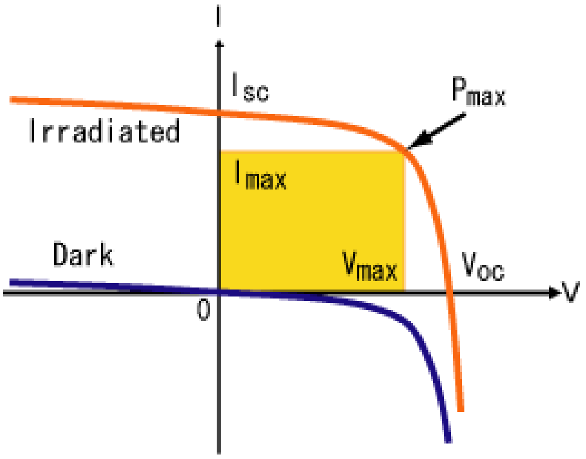

$$\eta = \frac{I_{max}\, V_{max}}{P_{light}}$$

$$FF = \frac{Vmax\, Imax}{I_{sc}\, Voc}$$

$$\eta = \eta_{Abs}\eta_{Sep}\eta_{Coll}$$

Figure 5.5 An illustrative I-V diagram of a solar cell.

Nowadays, key strategies involve increasing the values of η by improving the electron transport rate,[224-226] light harvesting ability[227,228] and decreasing the degree of charge recombination.[229-231]

In this chapter, our aim was to investigate the effects of linking the QD nanoparticles into solar cells via better conductor linkers than the original ligands with systematically varying the length of the molecular bridge and different anchor groups (amine, thiol, pyridyl) on the efficiencies of QD-based photoelectrochemical cells.

5.2 Synthesis and Device Fabrication

The syntheses of compounds **41**, **47**, **54**, **66**, **50** and **99** are described in Chapter 3.

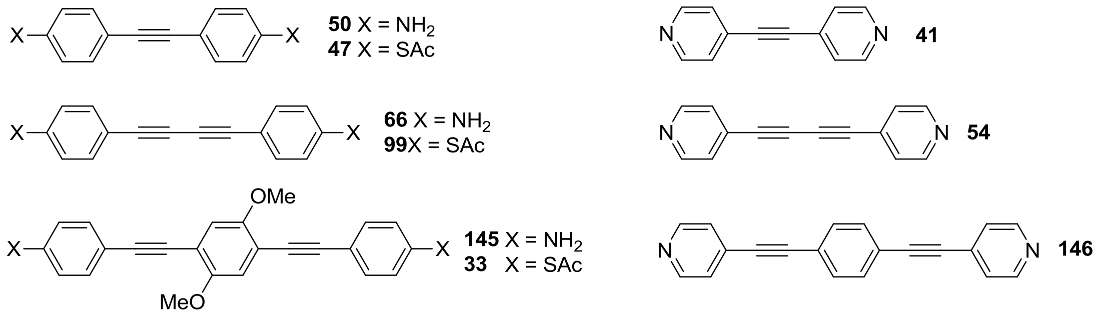

Figure 5.6 Rigid molecular wire ligands.

Due to some concerns about the limited solubility of OPE derivatives the middle ring of **145** and **33** was substituted with methoxy substituents. Longer side-chains could be detrimental by limiting the coverage which could be obtained for self-assembly on the QDs. For the synthesis of **145** 1,4-diiodo-2,5-dimethoxybenzene (**148**) was synthesised from commercially available 1,4-dimethoxybenzene (**147**) in 77% yield. Subsequently, the Sonogashira cross-coupling between **148** and commercially available 4-ethynylaniline (**48**) afforded OPE derivative **145** in 73% yield (Scheme 5.1).

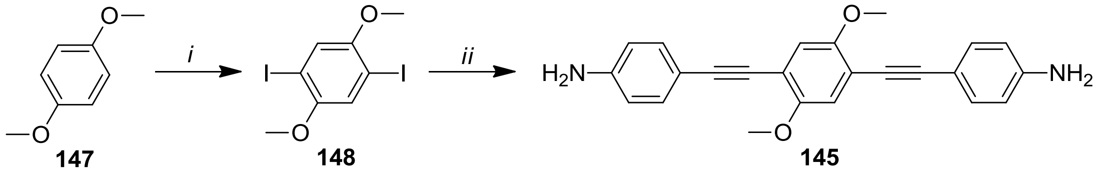

Reagents and Conditions: (i) KIO_3, I_2, AcOH, H_2SO_4, H_2O, 100°C, 18h, 63%; (ii) 4-ethynylaniline (**48**), $Pd[(PPh_3)_4]$, $(i\text{-Pr})_2NH$, CuI, 4h, rt, 73%;

Scheme 5.1 Synthesis of 145.

Another novel amine terminated OPE molecule was also synthesised in a similar route. 4-ethynylaniline (**48**) was cross-coupled with 1,4-diiodotetrafluorobenzene (**149**) to give **150** in a 56% yield. The structure of **150** was characterised by ^1H, ^{13}C NMR, MS and X-ray crystallography.

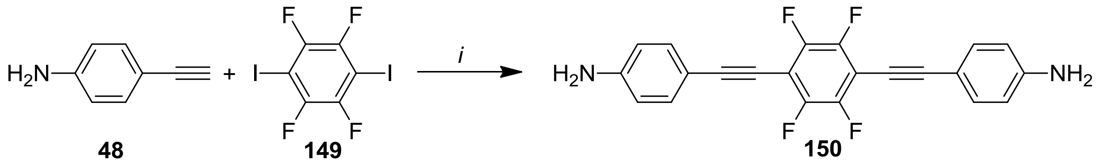

Reagents and Conditions: (i) $Pd[(PPh_3)_4]$, $(i\text{-Pr})_2NH$, CuI, 4h, rt, 56%.

Scheme 5.2 Synthesis of 150.

The X-ray crystal structure of the OPE **150** shows an inversion centre. Amine moieties in the ends of the molecule hydrogen bonded to the oxygen atom of the acetone, which was used for growing the crystals. The phenyl rings are coplanar except the middle ring which has a torsion angle of 12.4°. The molecules pack in a herringbone motif.

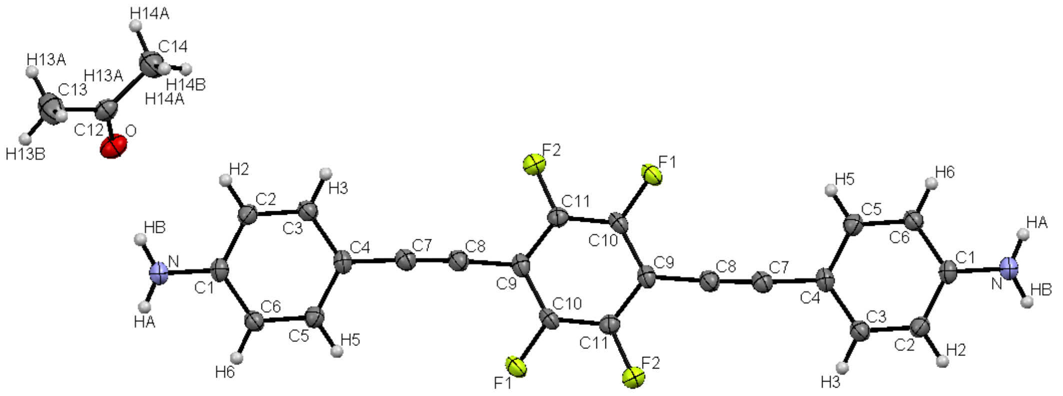

Figure 5.7 X-ray molecular structure of 150 and a molecule of solvent acetone.

The synthesis of thioacetate anchored OPE compound **33** was performed by a similar method (Scheme 5.3). Compound **148** was coupled with TMSA, followed by a deprotection by TBAF gave **152** in high yield. The Sonogashira cross-coupling reaction between **152** and **44** afforded thioacetate anchored OPE compound **33** in a 95% yield.

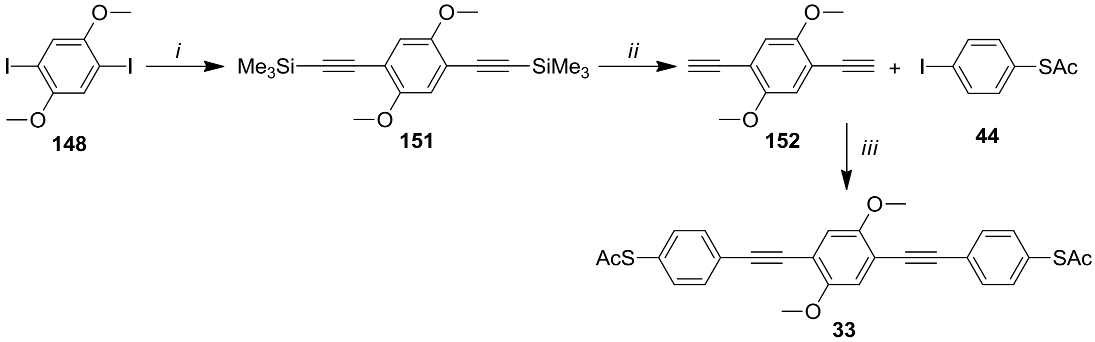

Reagents and Conditions: (i) TMSA, Pd[(PPh$_3$)$_4$], (*i*-Pr)$_2$NH, CuI, 4h, rt, 95%; (ii) TBAF, THF, rt, 30 mins, 95%; (iii) Pd[(PPh$_3$)$_4$], (*i*-Pr)$_2$NH, CuI, 4h, rt, 95%

Scheme 5.3 Synthesis of OPE 33.

The same OPE compound **33** was synthesised in our group previously by a different route in four steps (Scheme 5.4). By using the new route the synthesis is shortened two steps and the overall yield is increased.

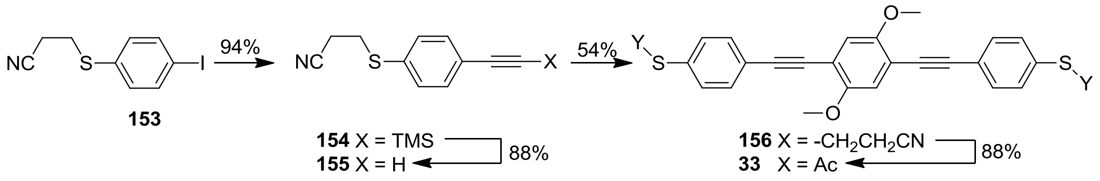

Scheme 5.4 Another route for the synthesis of 33 developed by our research group previously.

Compound **146** was synthesised in two steps starting from 1,4-dibromobenzene (**157**) (Scheme 5.5). The Sonogashira coupling between 1,4-dibromobenzene (**157**) and TMSA gave **158** in 88% yield. Even though the deprotection of TMS groups on compound **158** is straightforward, in order to skip one step and shorten the total reaction time and costs, **158** was cross-coupled with 4-iodopyridine (**38**) by using Sila-Sonogashira cross-coupling conditions, which were reported by Mori *et al.*[232], to give **146** in a 49% yield (Scheme 5.5).

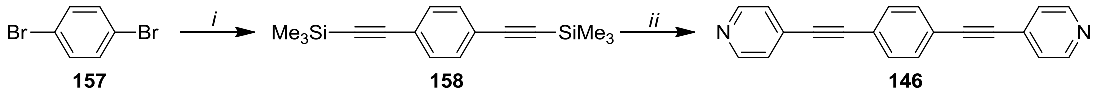

Reagents and Conditions: *i*) TMSA, $[Pd(PPh_3)_4]$, THF, $(i\text{-Pr})_2NH$, rt, 12h, 88%; *ii*) 4-iodopyridine (**38**), Ag_2O, $[Pd(PPh_3)_4]$, THF, reflux, 36h, 49%.

Scheme 5.5 Synthesis of 146.

The synthesis of CdSe QDs, fabrication and characterisation of the devices were carried out in the group of Prof.Dr.Dirk M. Guldi at the University of Erlangen-Nuremberg by Andres Ruland Palaia. The present author contributed to the experimental work and data analysis during visits to Erlangen.

CdSe-Oleic acid synthesis was performed following the hot injection method[233] by reacting TOP-Se with CdO in presence of OA and 1-octadecene (ODE). TiO_2 mesoporous films were obtained by following procedures reported elsewhere.[234] Adsorption of CdSe QDs onto the TiO_2 films was carried out by immersing the glass slides in a solution of CdSe-OA in hexane (concentration approx. 15 mg/ml) at room temperature for 8 h then rinsing with hexane. For assembly of the respective ligands onto the TiO_2-CdSe electrodes, the slides were immersed in 0.01 M ligand solutions in DMF, at 70 °C for 30 min, and rinsed first with DMF, then with acetonitrile to remove excess ligand and DMF, respectively. The second layer of CdSe was obtained by immersion of the TiO_2-CdSe-ligand electrode into the CdSe-Oleic acid solution for 30 min, followed by rinsing in hexane. A final addition of ligands was performed to crosslink the pre-assembled layer of CdSe, following the conditions described above. A similar approach was performed for the optical characterization of CdSe

QDs on glass slides. In the case of thiol molecules, 1 µM solutions were utilised. The deposition of the CdSe QDs onto glass slides was performed by spin coating techniques, using the same QD concentration as stated above (1000 rpm, 30 sec).

$$\text{TOP-Se} + \text{CdO} \xrightarrow[\text{285°C to rt}]{\text{OA / ODE}} \text{CdSe-OA}$$

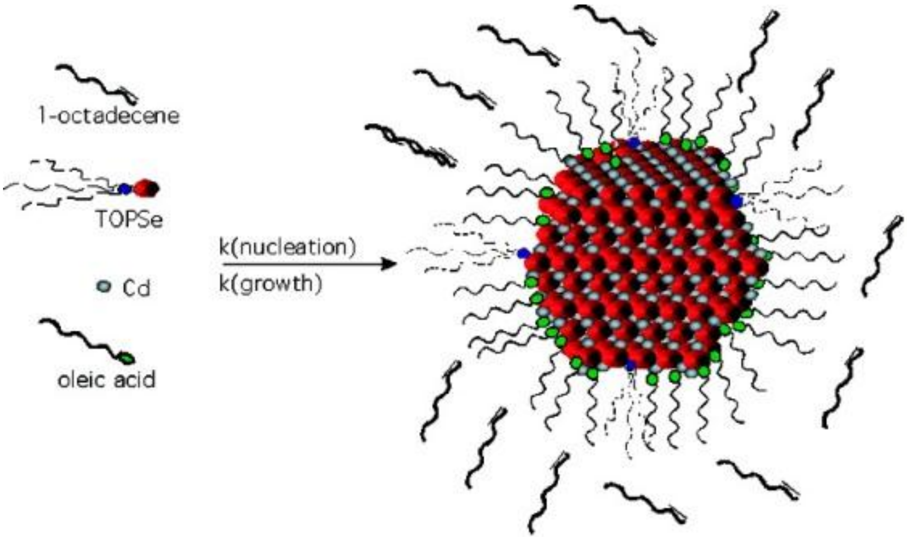

Figure 5.8 Representation of the synthesis of CdSe QDs (Reproduced from reference [233]).

Prior to photocurrent measurements, all the cells (CdSe double layer and single layer) were passivated by ZnS, by successive dipping of the electrode in ZnAc 0.1 M solution, followed by Na_2S 0.1 M solution, with washing and drying between each step. The process was repeated twice to obtain a thin ZnS layer.

The final photoelectrochemical cell consisted of the TiO_2-CdSe-ligand-CdSe-ligand electrode, a polysulfide electrolyte (1 M Na_2S and 1 M S), and a Cu_2S electrode. The Cu_2S was deposited onto a brass slide, by immersing the brass slide into a 0.1 M HCl solution of Cu_2S at 70 °C for 15 min, followed by immersion into the polysulfide solution at room temperature for 1 h. A piece of scotch tape in which there is a pre-cut hole of circumference of 0.28 cm^2 was placed in between the two electrodes, in which a drop of the electrolyte was deposited. Finally, the two electrodes were held together with the aid of 2 crocodile clamps. The photocurrent measurements were performed at room temperature under the standard 1.5 AM illumination (0.1 W/cm^2).

5.3 Results and Discussion

5.3.1 Optical characterisation of QD-Ligand assemblies on glass slides

The effect of the amino and thiol surface ligands on CdSe QDs was studied by absorption and emission spectroscopy. For the measurements, CdSe oleic acid (OA) capped QDs were spin-coated on glass slides as reference samples, and analogous samples were treated with amino and thiol bidentate ligands such as 1,2-ethanedithiol (EDT) and 1,2-ethylenediamine (EDA).

Figure 5.9 shows the absorption (left) and emission (right) spectra of spin-coated films of the original sample (CdSe OA, black line) and after treatment by EDT (red line) and EDA (blue line). The spectra have been normalised in order to clarify the positions of the first excitonic peaks. It can be observed that replacement of the original OA ligands by EDA resulted in a 7 nm blue shift and replacement by EDT yielded a 4 nm red shift in the absorption spectra. The same blue shift was observed for the emission spectrum for the EDA sample. In the case of EDT, the replacement leads to a complete quenching of the photoluminescence. The partial emission quenching upon addition of large excess of amines has also been previously reported.[235]

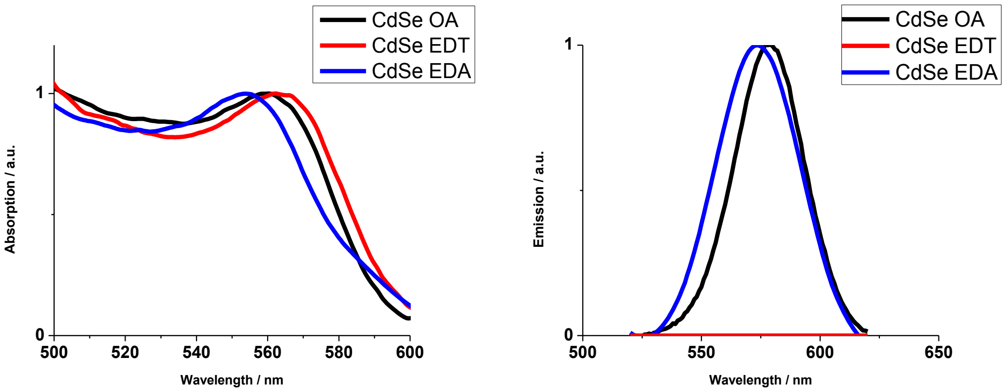

Figure 5.9 Absorbance (left) and emission (right) spectra of QD-Ligand assemblies on glass slide excited at 420 nm (both spectra are normalised for clarity).

The observed changes can be explained if we consider the excitonic state of a QD, where holes are located in the valence band, and electrons in the conduction band, both confined over the QD core and surface. Additionally, the high surface / volume ratio of a relatively small QD should be taken into account (e.g. 56 % of the atoms in a 3 nm particle size are present on the surface). Therefore, a change of the QD environment (e.g., surface ligands) will create drastic changes in the exciton delocalisation (optical shifts) and photoluminescence quenching (charge trapping by surface ligands).

Comparing OA, EDA and EDT molecules, the main difference is the electronegativity of the binding atoms onto the QD (e.g., 3.44 oxygen, 3.04 nitrogen, 2.5 sulfur). Considering molecular orbital theory, introduction of thiol groups will increase the delocalisation of the excitonic state by strong electron donation to the QD, leading to a red shift. Following the same theory, introduction of amino groups should have caused a red shift. However, the introduction of EDA ligands leads to blue shift. We can explain this effect assuming that the QD surface is not fully saturated by OA, and the EDA molecules graft to the QD areas where there is OA deficiency and by partial displacement of OA. Direct evidence for this hypothesis was observed previously by Knowles *et al.*[236] who performed a DFT study of a series of aniline derivatives, which were functionalised by various electron donating and withdrawing moieties at the *para* positions, and correlated the substituent with the emission quenching when implemented on CdSe QD.

The photoluminescence quenching of CdSe after EDT treatment can be explained by the hole trapping effect of thiol ligands. This effect can be understood by the positions of the CdSe energetic levels. If the HOMO level of a thiol ligand is situated at higher energies than the valence band of a QD, hole trapping or electron donation from the thiol to the QD becomes energetically favourable during photoexcitation. During relaxation, the radiative recombination is hindered, and photoluminescence quenching occurs. Moreover the trapped holes by thiol molecules yield the formation of thiyl radicals, which rapidly dimerise into disulfides. As a consequence, the CdSe surface becomes unpassivated and exposed to oxidation.[237] The comparison of the energy levels of bulk CdSe and CdTe is depicted in Figure 5.10. Hole trapping can occur by a ligand which has a higher redox energy level than the QD valence band. Because of this reason, thiols are not suitable for charge transport in CdSe-Ligand assemblies. However, they can be used for another type of QDs such as CdTe, where the thiol HOMO level is below the valance band of the QD, which does not allow the hole trapping. This is an essential requirement for constructing a multilayer film of CdSe QDs, where the ligand acts only as a linker between layers and does not interfere in charge transport through a CdSe film. In the case of thiol ligands as linkers, free movement of holes through the film is blocked.

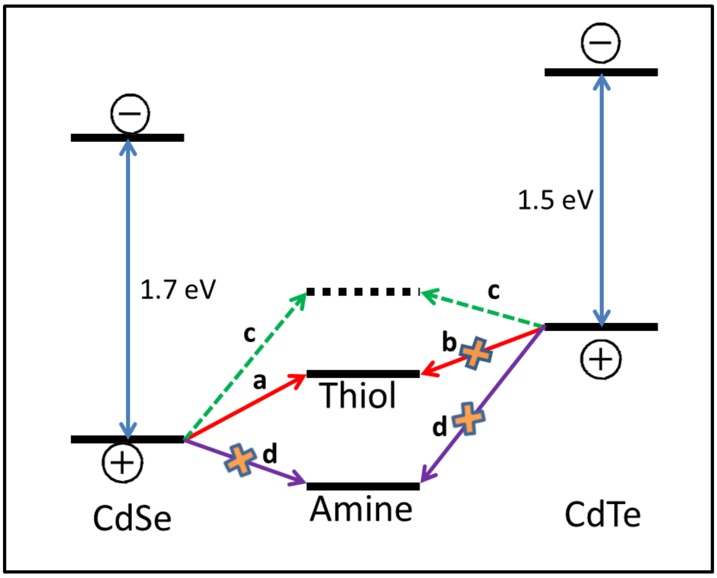

Figure 5.10 Illustration of the energy diagrams of bulk CdSe and bulk CdTe. Hole trapping is possible from CdSe to thiol ligand (a) but not from CdTe to thiol (b); hole trapping is not possible for amine (d). The dashed line indicates the assumed energy level of a thiol (c) molecule which quenches the luminescence of both CdSe and CdTe.

5.3.2 Optical Characterisation of QD-Amino Ligands Assemblies on Glass Slides

After confirmation that amino based linkers are more suitable than thiol analogues for CdSe QDs, we carried out the optical characterisation of several amino based ligands in combination with CdSe OA QDs. For the measurements, CdSe OA coated glass slides were prepared and treated with amino based conjugated ligands. Figure 5.9 (a) summarises the blue shift in the absorption spectrum (at the first excitonic peak) of the QD-amino ligand assemblies with respect to the original CdSe-OA samples, measured on glass slides comparing to the reference which is prepared with original CdSe-OA assemblies without any cross-linking ligands. The differences of the blue shift in this series arise from the different conjugation levels of the backbone. As the conjugation increases, the nitrogen electron donating ability might be reduced. Therefore, we observed a slightly increased blue shift for the alkyl ligand in comparison with aromatic ligands, and a constant value for all of the aromatic backbones.

Emission spectra of QD-amino ligands on glass slides upon excitation at 420 nm are shown in Figure 5.11 (Right). In all the cases, the emission peak values shifted consistently with the absorption spectra. As can be seen from Figure 5.11, introduction of amino groups partially quenches the PL depending on the ligand utilised. In the case of thiol ligands, the PL quenching arose from the hole trapping due to the respective band positions of the QD valence band and ligand HOMO. For the amino ligands, the observed trend from lower to higher quenching follows: **50**>BDA>**66**>**145**>EDA, for ligand lengths of 1.4 nm, 0.57 nm, 1.52 nm, 1.93 nm and 0.38 nm, respectively. Therefore, there are several aspects to consider in explaining the PL quenching, such as the length, the HOMO and LUMO levels of the ligands, and the combination of the two factors.

Compound	Hypsochromic Shift (nm)
EDA	5
BDA	3
50	3
145	3
66	3

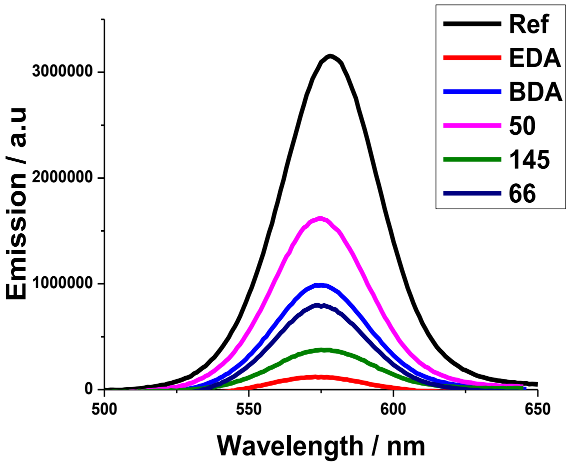

Figure 5.11 (Left Table) Blue shift in the absorption spectra in respect to the reference and (right) Emission spectra of QD-amino ligands on glass slides. (Reference samples are prepared without any crosslinking ligands).

Introduction of ligands shorter than 1 nm, such as EDA, causes a significant change in the CdSe film morphology, as the original interparticle distance for a CdSe OA film is about 1 nm. The shrinkage of the film causes PL quenching upon photoexcitation, through self-quenching.[238]

For molecules with similar length to the CdSe OA interparticle spacing (ie., **50**), the trend in the PL quenching can be explained by the MO theory for the ligands and the respective positions of HOMO and LUMO levels relative to the QD bandgap. Grafting of the ligand onto the QD introduces mid-gap states inside the QD, which interfere in the QD radiative recombination. Greater quenching can be observed if the mid-gap state is located in the bandgap. For example, the DFT calculated LUMO energies (-0.48 and -0.77 eV for **50** and **66**, respectively), clearly explain the observed trend in the PL quenching when comparing **50** and **66**.

A combination of both effects is needed to explain the PL quenching of BDA and OPE. For instance, the short distance of 0.57 nm might be within the limit of the optimum length prior to morphology shrinkage, but due to the lower LUMO level compared to **50** (-1.63 and -0.48 eV, respectively), a higher quenching is observed. The OPE **145**, which is the longest ligand studied, does not follow any of the other trends and shows an anomalously high PL quenching.

In summary, ligands with lengths similar to the inter-QD spacing of the original CdSe network, and with LUMO energies not deep inside the bandgap, are ideal candidates as efficient charge transporters and interlayer linkers in CdSe multilayer assemblies.

5.3.3 Photoelectrochemical Measurements

After the optical characterisation of the CdSe-amino assemblies on glass slides which showed significant differences in photoluminescence intensities, we pursued the study of interlayer ligand effects in CdSe photoelectrochemical cells. In this case the CdSe-amino ligands assemblies were integrated onto mesoporous TiO_2 electrodes. SEM images of blank TiO_2 and after formation of the CdSe bilayer (bearing amino ligand **50** as interlayer linkers) are represented in Figure 5.12 (a-c). The cross-section SEM image (Figure 5.12 c), reveals that the CdSe double layer does not penetrate into the mesoporous film. This is attributed to the use of DMF solutions, which have a rather high viscosity, decreasing the penetration of the ligands inside the film.

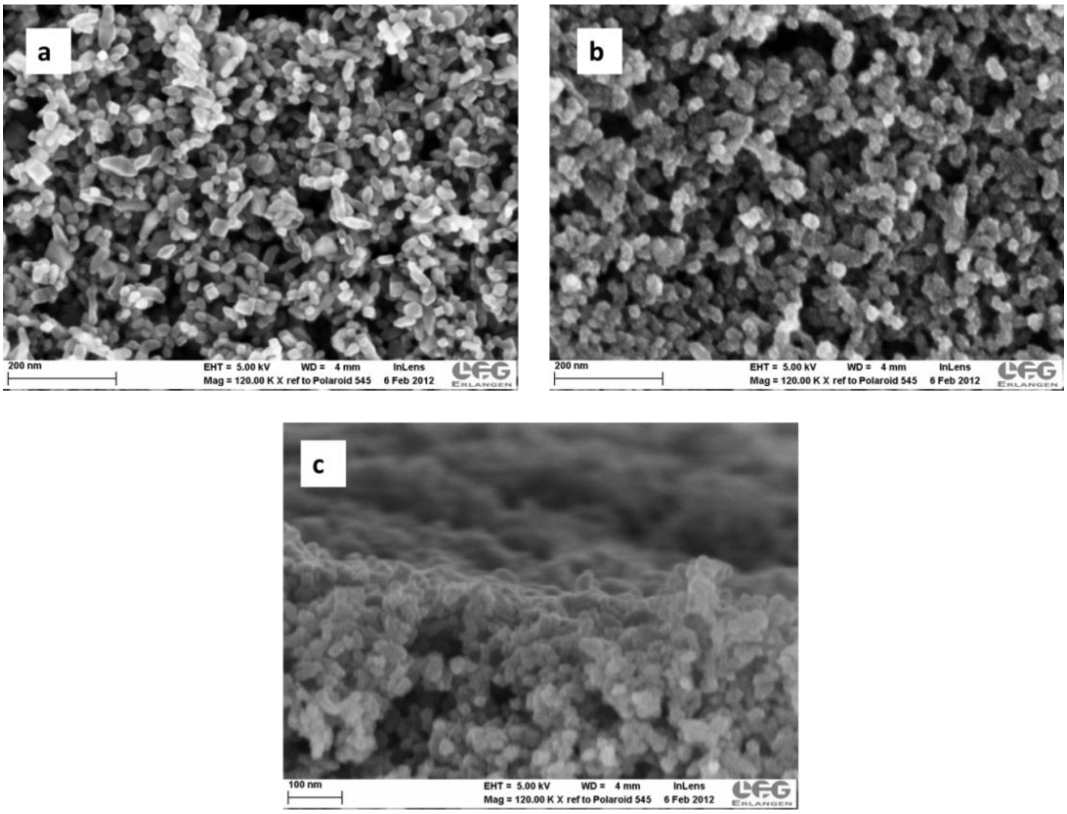

Figure 5.12 SEM top-view images of TiO_2 before (a) and after (b) CdSe QD deposition. Cross-section images of TiO_2 after (c) CdSe QD deposition (Scale bars (a) 200 nm, (b) 200 nm, (c) 100 nm).

Photocurrent characterisation of the CdSe based photoelectrochemical cells showed significant changes in performance as a function of the specific amino ligand present in between the CdSe bilayers, in terms of current-voltage data, despite the similar optical density of the photoelectrodes (Figure 5.13 a) comparing to the reference cells, which are prepared with the original CdSe-OA without any cross-linking ligands.

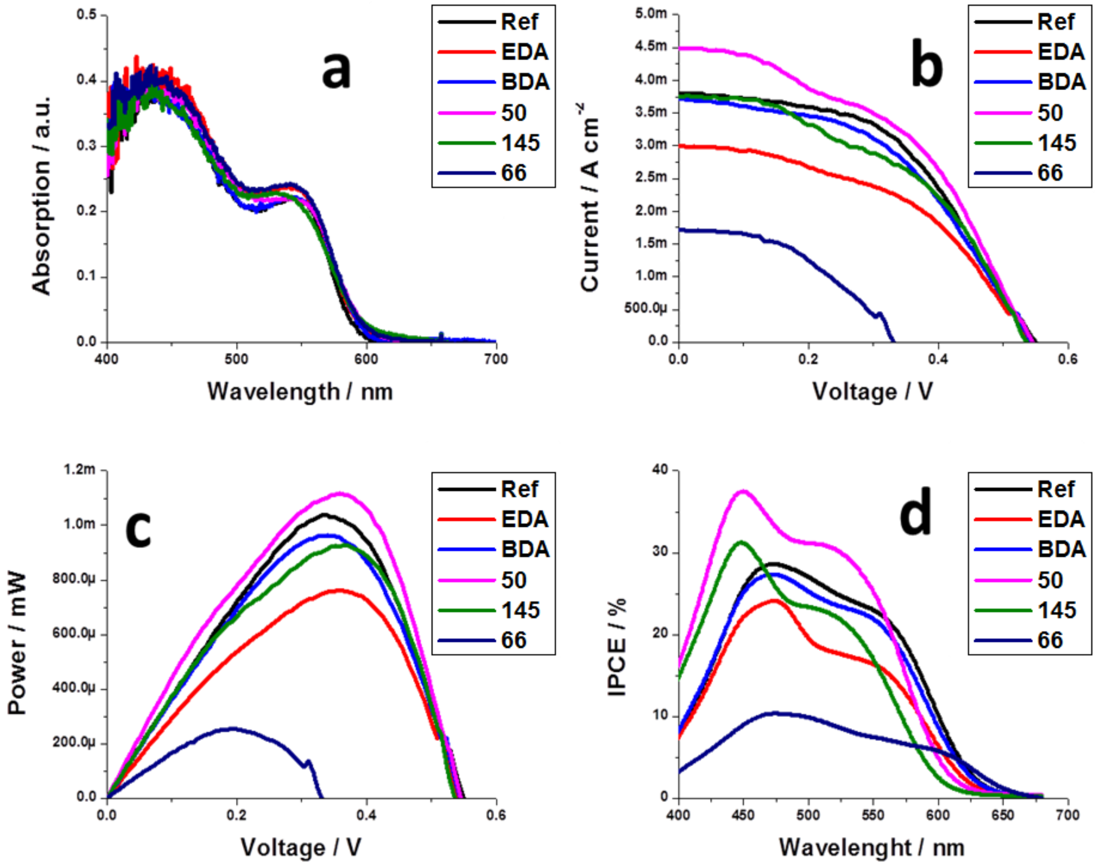

Figure 5.13 (a) Absorption spectra (b) *I-V* curves, (c) power – voltage graph and (d) IPCE measurements of CdSe based photoelectrochemical cells. (Reference cells are prepared without any crosslinking ligands).

From the monochromatic response, we conclude that the presence of the conjugated organic molecules does not contribute to the photocurrent generation, since no particular changes in the IPCEs are observed when comparing with the reference sample. From that, we also conclude that the charge transport process occurs by tunnelling, and not by super-exchange, as the ligand cannot be excited in the IPCE measured interval. We also found a clear trend in the solar cell efficiency as the amino ligand changed (Figure 5.14). Interestingly, the same trend was observed in the quenching of the PL in the CdSe-amino ligand assemblies, where the samples with the lowest quenching (favourable level alignment) resulted in the best performing device. For instance, in respect to the reference sample (single layer CdSe), upon introduction of EDA, which is a short aliphatic ligand, the performance dropped drastically.

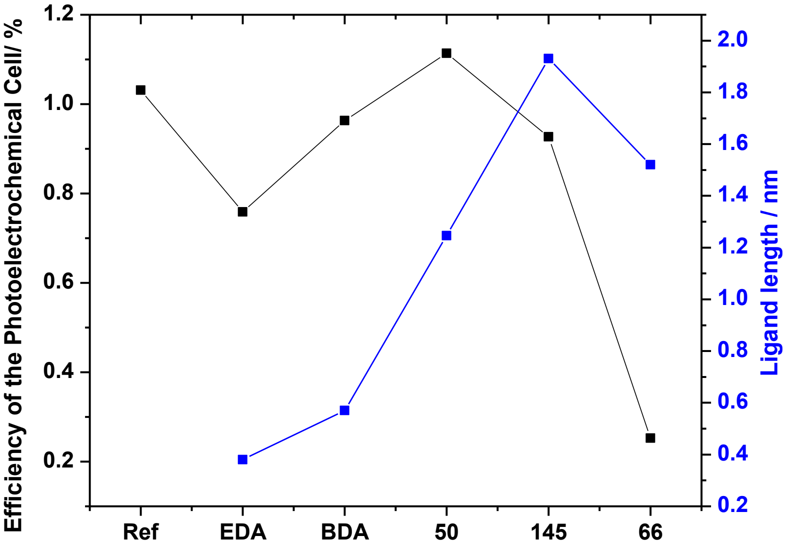

Figure 5.14 Efficiency of the photoelectrochemical cells and ligand lengths.

Contrary to EDA, by introducing a conjugated ligand, the performance increased consistently with the ligand length (Table 5.2), with a maximum ligand length / performance of 1.4 nm, corresponding to the ligand **50**. The longer OPE ligand **145** resulted in a decreased efficiency.

Table 5.2 The summary of the results.

	V_{OC} (V)	I_{SC} (mA)	FF (%)	η (%)
Reference	0.55	3.8	49.4	1.03
EDA	0.54	3	46.9	0.76
BDA	0.54	3.7	47.8	0.96
50	0.54	4.5	45.4	1.11
145	0.53	3.76	46	0.92
66	0.33	1.7	44.6	0.25

5.4 Conclusions and Future Work

In this chapter, length-persistent, conjugated OPE and tolane analogues with different molecular lengths and amine anchors were synthesised and their transport properties were investigated in quantum dot sensitised solar cells. The preliminary results show that introducing conjugated cross-linking ligands (wires) between the QDs improves the performance of a solar cell. Moreover, the performance of the QD-ligand-based solar cell cannot be correlated only with the single-molecule conductance value of the ligand; rather there is a more complex balance between conductances, band alignment and ligand lengths.

To date, pyridyl anchored OPE and tolane analogues have not been fully characterised in QDSSCs. According to the (very) preliminary results, increased solar cell performance is observed with the pyridyl anchored ligands comparing to aniline anchored ones.

In order to investigate the performance of thiol-anchored ligands, similar measurements will be done on CdTe QDs. Thiol and pyridyl ligands will also be used in CdTe QDSSCs for a comprehensive study.

Chapter 6

Experimental

6.1 General Experimental Procedures

All reactions were conducted under a blanket of argon which was dried by passage through a column of phosphorus pentoxide unless otherwise stated. All commercial chemicals were used without further purification. Anhydrous toluene, tetrahydrofuran (THF), dichloromethane (DCM) and diethyl ether (Et_2O) were dried through an HPLC column on an Innovative Technology Inc. solvent purification system. Petroleum ether (PE) used for column chromatography is bp. 40-60 °C fractions and used as received. Column chromatography was carried out using 40-60 µm mesh silica. Analytical thin layer chromatography was performed on 20 mm pre-coated plates of silica gel (Merck, silica gel $60F_{254}$), visualization was made using ultraviolet light (254 nm).

NMR spectra were recorded on: Bruker Avance-400, Varian VNMRS 700, Varian Inova 500 or Mercury 200 spectrometers. Chemical shifts are reported in ppm relative to $CDCl_3$ (7.26 ppm), acetone-d_6 (2.09 ppm), DMSO-d_6 (2.50 ppm) or tetramethylsilane (0.00 ppm). Melting points were determined in open-ended capillaries using a Stuart Scientific SMP40 melting point apparatus at a ramping rate of 2 °C/min. Mass spectra were measured on a Waters Xevo OTofMS with an ASAP probe. Electron ionisation (EI) mass spectra were recorded on a Thermoquest Trace or a Thermo-Finnigan DSQ. Ion analyses were performed on a Dionex 120 Ion Chromatography detector. Elemental analyses were performed on a CE-400 Elemental Analyzer.

CAUTION! We attempted to measure the melting point of tetrayne molecule **89** on a very small scale and under satisfactory safety conditions. At ca. 190 ^{o}C, **89** was observed to explode. Due to this result, we did not attempt to check the melting points and elemental analysis of the other tetrayne and terminal butadiyne compounds.

6.2 Experimental Procedures

General Procedure (I) for Sonogashira Cross-Couplings: Iodoarene (1 eq), [$Pd(PPh_3)_4$](5% mmol) and CuI (2% mmol) were placed in a flame-dried flask and dissolved in THF (7 ml per mmol) and $(i\text{-}Pr)_2NH$ or Et_3N (1 ml per 1 mmol) to which alkyne was added in small portions in 15 mins. The mixture was stirred under argon at rt until the reaction was complete (judged by TLC). Solvents were removed and the crude product was purified either by column chromatography or recrystallisation.

General Procedure (II) for Deprotection of TMS: The corresponding protected aryl alkynes were dissolved in wet THF (5 ml per mmol). A solution of tetrabutylammonium fluoride (TBAF) in THF (2 ml per mmol, 1M) was added and the solution was stirred for 15-30 mins at rt. Water was added to the solution until it became colourless. The mixture was diluted with Et_2O (20 ml per mmol), washed with saturated aqueous NH_4Cl and NaCl solutions, dried with $MgSO_4$ and solvents were removed under reduced pressure. The crude product was purified by either column chromatography or sublimation.

General Procedure (III) for Oxidative Couplings: Arylalkyne (if TMSA used excess), CuI (5% mmol) and $[PdCl_2(PPh_3)]_2$ (5% mmol) were placed in a round bottomed flask and dissolved in THF/Et_3N (1:3) mixture (10 ml per mmol). The reaction mixture was stirred for 2 h whilst air bubbling through the solution. If after this time the reaction was not complete (as judged by TLC), stirring was continued until the starting material disappear in the reaction mixture at rt. Solvents were removed under reduced pressure and the residue was purified by column chromatography.

General Procedure (IV) for Oxidative Homo-Couplings of TMS-Alkynes: TMS-alkyne was dissolved in MeOH/pyridine (1:1, v/v) mixture (10 ml per mmol) and $Cu(OAc)_2.H_2O$ (2 equiv., 0.400 g per mmol) was added to the mixture in one portion and stirred until the reaction is complete (judged by TLC). The reaction was quenched by adding saturated aqueous NH_4Cl solution (5 ml per mmol) and diluted with DCM (25 ml per mmol), organic layer was separated, dried over $MgSO_4$ and solvents were removed under reduced pressure. The crude product was purified either by column chromatography or recrystallisation.

4-((Trimethylsilyl)ethynyl)pyridine; 39

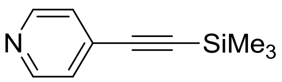

To a solution of 4-iodopyridine (1.00 g, 4.88 mmol), [Pd(PPh$_3$)$_4$] (0.171 g) and CuI (46 mg) in THF/Et$_3$N (50 ml) (3:1 v/v) mixture was added TMSA (0.575 g, 5.85 mmol) and the mixture was stirred under argon for 4 h at rt. Solvents were removed under reduced pressure and the resulting residue was purified by column chromatography using DCM/Et$_2$O (1:1 v/v) as eluent to give **39** as a pale yellow oil (0.78 g, 92%). ^{1}H NMR (400 MHz, CDCl$_3$) δ 8.49 (d, *J* = 6.0 Hz, 2H), 7.23 (d, *J* = 6.0 Hz, 2H), 0.21 (s, 9H). ^{13}C NMR (101 MHz, CDCl$_3$) δ 149.86, 131.33, 125.96, 102.14, 100.06, 0.12. MS (ES$^+$) *m/z* (%) : 175.1 ([M]$^+$, 100). The data are consistent with the literature.[239]

4-Ethynylpyridine; 40

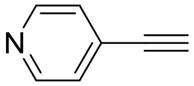

General Procedure (II): 4-((trimethylsilyl)ethynyl)pyridine **39** (0.750 g, 4.27 mmol), 9 ml 1M TBAF solution in THF, 30 min, rt. The resulting solid was purified by sublimation (1 x 10^{-2} mbar, 60 °C) to give **40** as a white powder (0.37 g, 85%). The sample was stored in a freezer under argon. ^{1}H NMR (400 MHz, CDCl$_3$) δ 8.56 (d, *J* = 6.0 Hz, 2H), 7.31 (d, *J* = 6.0 Hz, 2H), 3.28 (s, 1H). ^{13}C NMR (101 MHz, CDCl$_3$) δ 149.95, 130.57, 126.31, 82.15, 81.18. MS (ES$^+$) *m/z* (%) : 103.0 ([M]$^+$, 100). The data are consistent with the literature.[147]

1,2-Di(pyridin-4-yl)ethyne; 41

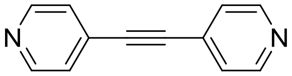

General Procedure (I): 4-iodopyridine (**38**) (0.198 g, 1.92 mmol), [Pd(PPh$_3$)$_4$] (111 mg), CuI (7 mg), (*i*-Pr)$_2$NH and 4-ethynylpyridine (**40**) (0.393 g, 1.92 mmol), 5 h, rt. Purified by column chromatography using DCM/Et$_2$O (1:1 v/v) as eluent and then recrystallisation from EtOAc to give 1,2-di(pyridin-4-yl)ethyne (**41**) as white crystals (0.31 g, 91 %). mp: 162 – 164 °C. ^{1}H NMR (400 MHz, CDCl$_3$) δ 8.65 (dd, *J* = 4.4, 1.6 Hz, 4H), 7.40 (dd, *J* = 4.4, 1.6 Hz, 4H). ^{13}C NMR (101 MHz, CDCl$_3$) δ 150.18, 130.40, 125.79, 90.82. MS (ES$^+$) *m/z* (%): 181.2 ([M]$^+$, 100). Anal. Calcd. for $C_{12}H_8N_2$: C, 79.98; H, 4.47; N, 15.55. Found: C, 80.12; H, 4.65; N, 14.96. The data are consistent with the literature.[112]

1-Bromo-4-(*t*-butylsulfanyl)benzene; 43

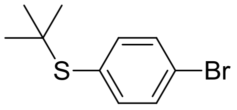

4-Bromothiophenol (**42**) (4.0 g, 21.2 mmol) was dissolved in *t*-butyl chloride (19 ml). To the stirred solution at rt $AlCl_3$ powder (4.2 g) was added slowly in small fractions to afford an orange slurry. The mixture was stirred overnight then poured onto ice. The organic layer was extracted with Et_2O then washed with brine and dried over $MgSO_4$. The solvent was evaporated under vacuum, then purified by column chromatography using hexane as eluent to yield **43** as a pale yellow oil (4.45 g, 88%). ^1H NMR ($CDCl_3$, 300 MHz) δ 7.45 (d, *J*=8.5 Hz, 2H) 7.38 (d, *J*=8.5 Hz, 2H), 1.27 (s, 9H). The data are consistent with the literature.[240]

4-Thioacetyl-iodobenzene; 44

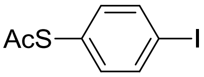

Under Ar, to a solution of 1-bromo-4-(*t*-butylsulfanyl)benzene (**43**) (4.2 g, 17 mmol) in dry THF (40 ml) cooled in a dry-ice-acetone bath was added dropwise *n*-butyllithium solution (2.5 M in hexane) (7.5 ml, 18.7 mmol). The solution was stirred for 2 h at -78 °C followed by the addition of solid iodine (5.2 g, 20.4 mmol). The mixture was stirred for 5 h while the temperature was allowed to rise to rt. The solvents were removed by vacuum evaporation. Diethyl ether (10 ml) was added to the oily residue and the mixture was washed twice with saturated Na_2SO_3 solution. The ether layer was separated and dried over anhydrous $MgSO_4$. Removal of the solution under vacuum yielded a white solid.

The crude product was dissolved in dry DCM (30 ml) and added dropwise into a solution of BBr_3 in DCM (1.0 M, 20 ml). The resultant brownish solution was stirred for 2 h then acetyl chloride (13 ml) was added dropwise and the mixture was stirred for 1.5 h at rt. The resulting mixture was poured onto ice and the DCM layer was separated then washed with water, dried over anhydrous $MgSO_4$, filtered and solvents removed. The solid residue was further purified by column chromatography using DCM-hexane (1:1, v/v) as eluent to afford compound **44** as an off-white solid (3.72 g, 81% overall yield for the two steps). mp: 57.0 – 58.0 °C. ^1H NMR ($CDCl_3$, 300 MHz): δ 2.43 (s, 3H), 7.13 (d, *J* = 8.4 Hz, 2H), 7.74 (d, *J* = 8.4 Hz, 2H). ^{13}C NMR ($CDCl_3$, 75 MHz): δ 30.2, 95.9, 127.7, 135.9, 138.3, 193.1. MS (EI^+) *m/z* (%): 278 ($[M]^+$, 24). The data are consistent with the literature.[121]

1-Thioacetyl-4-[(trimethylsilyl)ethynyl]benzene; 45

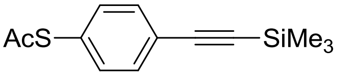

General Procedure (I): **44** (0.50 g, 1.8 mmol), [Pd(PPh_3)$_4$] (0.104 g), CuI (7 mg), TMSA (0.230, 2.34 mmol), (*i*-Pr)$_2$NH, 3 h, rt. Purified by column chromatography using DCM/PE (1:1, v/v) as eluent to give **45** as an off white solid (0.41 g, 92%). mp: 43.4 – 45.6 °C. ^{1}H NMR (400 MHz, $CDCl_3$) δ 7.48 (d, *J* = 8.1 Hz, 2H), 7.34 (d, *J* = 8.1 Hz, 2H), 2.41 (s, 3H), 0.25 (s, 9H). ^{13}C NMR (101 MHz, $CDCl_3$) δ 193.58, 134.29, 132.73, 128.52, 124.57, 104.37, 96.43, 30.50, 0.12. The data are consistent with the literature.[241]

4-Ethynyl-1-thioacetylbenzene; 46

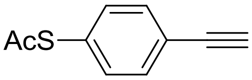

To a solution of **45** (0.35 g, 1.41 mmol) in THF (5 mL) at 0 °C were added acetic acid (0.04 mL) and acetic anhydride (0.04 ml) then 1 M TBAF solution in THF (2.8 ml, 2.8 mmol) was dropwise added to the solution and stirred for 15 mins at rt. The crude was passed through a 5 cm silica pad and the solvent was removed under vacuum to afford **46** as a yellow-orange solid. The crude product was pure enough for further synthesis (0.165 g, 67%). ^{1}H NMR (400 MHz, $CDCl_3$) δ 7.55 (d, *J* = 8.1 Hz, 2H), 7.42 (d, *J* = 8.1 Hz, 2H), 3.17 (s, 1H), 2.48 (s, 3H). The data are consistent with the literature.[241]

Bis[4-(2-acetylsulfanyl)-phenyl]ethyne; 47

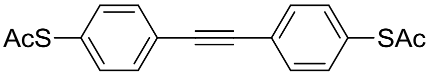

General Procedure (I): **46** (0.100 g, 0.56 mmol), **44** (0.174 g, 0.62 mmol), [Pd(PPh_3)$_4$] (33 mg), CuI (2 mg), (*i*-Pr)$_2$NH, overnight, rt. Purified by column chromatography using DCM as eluent and then recrystallisation from ethanol to give **47** as a white solid (0.145 g, 79%). mp: 144 - 145°C. ^{1}H NMR (400 MHz, $CDCl_3$) δ 7.56 (d, *J* = 8.0 Hz, 4H), 7.40 (d, *J* = 8.0 Hz, 4H), 2.43 (s, 6H). ^{13}C NMR (101 MHz, $CDCl_3$) δ 193.56, 134.48, 132.48, 128.67, 124.35, 90.51, 30.56. HR-MS (ASAP$^+$) Calcd for $C_{18}H_{14}O_2S_2$ $[M+H]^+$ 327.0508 found *m/z* : $[M+H]^+$ 327.0529. Anal. Calcd. for $C_{18}H_{14}O_2S_2$: C, 66.23; H, 4.32. Found: C, 66.10; H, 4.45. The data are consistent with the literature.[181]

4-(2-(4-Aminophenyl)ethynyl)aniline; 50

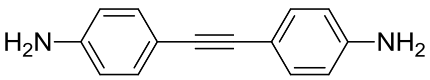

4-iodoaniline (**49**) (0.75 g, 3.42 mmol), [Pd(PPh_3)$_4$] (0.217 g) and CuI (19 mg) were dissolved in anhydrous THF (25 ml) at room temperature under argon atmosphere. 4-ethynylaniline (**48**) (0.44 g, 3.76 mmol) was added to the solution and 0.5 M aqueous ammonia solution (20 ml) added dropwise to the reaction mixture at room temperature. The mixture stirred under argon overnight. Solvents removed under reduced pressure and the residue was dissolved in diethyl ether (40 ml) and washed with water (2 x 100 ml). The organic layers were combined and dried over anhydrous $MgSO_4$. Solvent removed under vacuum and the resulting crude product was purified by column chromatography using hexane/ethyl acetate (3:2, v/v) as eluent to afford **50** which recrystallised from ethanol to give yellow-orange needle crystals. (0.37 g, 47% yield). mp: 232 - 234 °C. ^{1}H NMR (400 MHz, $CDCl_3$) δ 7.30 (d, *J* = 8.8 Hz, 4H), 6.62 (d, *J* = 8.8 Hz, 4H), 3.77 (s, 4H). ^{13}C NMR (101 MHz, $CDCl_3$) δ 146.34, 132.90, 115.00, 113.59, 87.96. MS (ES$^+$) *m/z* (%): 209.1 ([M+H]$^+$, 100). Anal. Calcd. for $C_{14}H_{12}N_2$: C, 80.74; H, 5.81; N, 13.45. Found: C, 80.22; H, 5.88; N, 13.17. The data are consistent with the literature.[114]

4-(2-(4-Benzonitrile)ethynyl)benzonitrile; 53

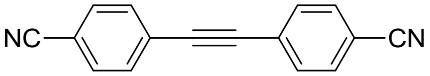

General Procedure (I): 4-ethynylbenzonitrile (**51**) (1.00 g, 7.87 mmol), 4-iodobenzonitrile (**52**) (1.98 g, 8.65 mmol), [Pd(PPh_3)$_4$] (0.454 g), CuI (15 mg) and (*i*-Pr)$_2$NH, overnight, rt. The precipitated solid was filtered and recrystallised from EtOAc to give **53** as white needle crystals (0.97 g, 55% yield). mp: 256.5-257 °C. ^{1}H NMR (400 MHz, $CDCl_3$) δ 7.67 (d, *J* = 8.7 Hz, 4H), 7.62 (d, *J* = 8.7 Hz, 4H). ^{13}C NMR (101 MHz, $CDCl_3$) δ 132.50, 132.41, 127.29, 118.50, 112.62, 91.78. HR-MS (ASAP$^+$) Calcd for $C_{16}H_8N_2$ [M+H]$^+$ 229.0760 found *m/z* : [M+H]$^+$ 229.0729. Anal. Calcd. for $C_{16}H_8N_2$: C, 84.19; H, 3.53; N, 12.27. Found: C, 83.77; H, 3.54; N, 12.06. The data are consistent with the literature.[115]

1,4-Di(pyridin-4-yl)buta-1,3-diyne; 54

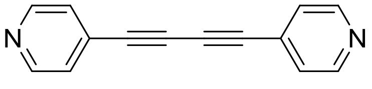

General procedure (III): 4-ethynylpyridine (74 mg, 0.71 mmol) [$PdCl_2(PPh_3)_2$] (10 mg), CuI (3 mg), 12 h, rt. Purified by column chromatography using DCM/acetone (1:1, v/v) and then recrystallisation from EtOAc to give **54** (70 mg, 94% yield) as pale yellow needles. mp: 200.0 – 201.0 °C. ^{1}H NMR (400 MHz, $CDCl_3$) δ 8.63 (d, J = 5.7 Hz, 4H), 7.37 (d, J = 5.7 Hz, 4H). ^{13}C NMR (101 MHz, $CDCl_3$) δ 150.19, 129.57, 126.27, 80.41, 77.38. MS (ES$^+$) *m/z* (%): 204.07 ([M]$^+$, 100). Anal. Calcd. for $C_{14}H_8N_2$: C, 82.33; H, 3.95; N, 13.72. Found: C, 81.88; H, 3.99; N, 13.61. The data are consistent with the literature.[157]

1,8-Di(pyridin-4-yl)octa-1,3,5,7-tetrayne; 55

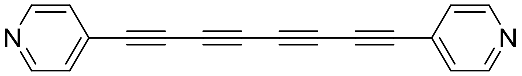

General procedure (IV): **59** (0.150g, 0.75 mmol), $Cu(OAc)_2.H_2O$ (0.331 g, 1.66 mmol), 12 h, rt. Purified by column chromatography using DCM/acetone (1:1, v/v) as eluent and recrystallisation from EtOAc to give **55** (56 mg, 59% yield) as yellow-orange needle crystals. ^{1}H NMR (400 MHz, $CDCl_3$) δ 8.63 (d, J = 6.1 Hz, 4H), 7.37 (d, J = 6.1 Hz, 4H). ^{13}C NMR (101 MHz, $CDCl_3$) δ 150.22, 128.85, 126.63, 78.22, 75.02, 68.69, 63.80. MS (ES$^+$) *m/z* (%): 253.2 ([M+H]$^+$, 100). Anal. Calcd for $C_{18}H_8N_2$: C, 85.70; H, 3.20; N, 11.10. Found: C, 85.64; H, 3.26; N, 11.22. The data are consistent with the literature.[86]

Buta-1,3-diyn-1-yltrimethylsilane; 58

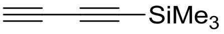

Into a flame-dried flask, Me_3Si-C≡C-C≡C-SiMe (**57**) (0.5 g, 2.6 mmol) was placed and dissolved in dry Et_20 (25 ml) under argon. MeLi.LiBr complex solution (3.8 ml, 1.5 M in Et_2O, 2.6 mmol) was added in one portion to the reaction mixture at rt. The mixture was stirred at rt overnight and MeOH (0.12 ml) was added and the solution was washed successively with saturated aqueous NH_4Cl and brine solutions and the organic layer was dried over $MgSO_4$. The solvent was removed under vacuum without heating and the crude product was vacuum distilled without heating to give **58** as a clear oil (0.190 g, 58%). ^{1}H NMR (400 MHz, $CDCl_3$) δ 2.10 (s, 1H), 0.20 (s, 9H). ^{13}C NMR (101 MHz, $CDCl_3$) δ 90.04, 88.05, 74.23, 70.69, -0.24. The data are consistent with the literature.[158]

4-((Trimethylsilyl)buta-1,3-diyn-1-yl)pyridine; 59

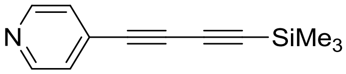

General procedure (I): 4-iodopyridine (**38**) (0.300 g, 1.463 mmol), BDTMS (**58**) (0.286 g, 1.75 mmol), [Pd(PPh$_3$)$_4$] (84 mg), CuI (9 mg), (*i*-Pr)$_2$NH, 3 h, rt. Purified by column chromatography using Et$_2$O/DCM (1:1, v/v) to give **59** (0.284 g, 97% yield) as yellowish oil, which solidified in a fridge. ^{1}H NMR (400 MHz, CDCl$_3$) δ 8.58 (dd, *J* = 4.4, 1.6 Hz, 2H), 7.31 (dd, *J* = 4.4, 1.6 Hz, 2H), 0.23 (s, 9H). ^{13}C NMR (101 MHz, CDCl$_3$) δ 150.05, 129.96, 126.40, 93.80, 87.06, 78.54, 73.60, -0.31. HR-MS (ASAP$^+$) Calcd for $C_{12}H_{13}NSi$ 199.0817 found *m/z* : [M]$^+$ 199.0818.

4-(Buta-1,3-diyn-1-yl)pyridine; 60

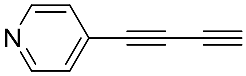

General Procedure (II): **59** (0.250 g, 1.35 mmol), TBAF (2.70 ml, 2.70 mmol), 30 mins, rt. Purified by column chromatography using Et$_2$O/DCM (1:1, v/v) to give **60** as a white solid (0.135 g, 78%). ^{1}H NMR (400 MHz, CDCl$_3$) δ 8.57 (d, *J* = 6.7 Hz, 2H), 7.32 (d, *J* = 6.7 Hz, 2H), 2.60 (s, 1H). ^{13}C NMR (101 MHz, CDCl$_3$) δ 150.06, 129.51, 126.50, 77.85, 73.81, 72.37, 67.52. GC-MS (EI$^+$) *m/z* (%): 128.2 ([M+H]$^+$, 100). The data are consistent with the literature.[164]

(Iodobuta-1,3-diyn-1-yl)trimethylsilane; 62

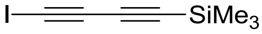

Me$_3$Si-C≡C-C≡C-SiMe (**57**) (1.94 g, 10 mmol) was dissolved in dry Et$_2$O (40 ml). MeLi-LiBr complex solution (1.5 M, 8.3 ml/12 mmol, 1.25 equiv) was added at rt and the mixture was stirred for 4 h to yield a greenish pale-brown solution. Iodine (3.17 g, 12 mmol) solid was added in portions until the brownish colour was stable. Sodium metabisulfite solution was added to decolourise the solution. The ether layer was partitioned, dried over MgSO$_4$, solvent removed under vacuum and the resulting yellow oil was purified by column chromatography using hexane to afford a pale-yellow oil which crystallised upon slow evaporation of the solvent (1.56 g, 63%). ^{1}H NMR (400 MHz, CDCl$_3$) δ 0.19 (s, 9H). ^{13}C NMR (101 MHz, CDCl$_3$) δ 88.74, 83.20, 78.94, 77.36, -0.46. The data are consistent with the literature.[138]

4-((Trimethylsilyl)hexa-1,3,5-triyn-1-yl)pyridine; 63

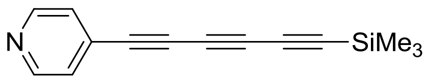

To the degassed (argon bubbled for 20 mins) solution of **62** (0.289 g, 1,16 mmol) in Et_3N (10 ml) was added $[Pd(PPh_3)_4]$ (56 mg), CuI (9 mg) and **40** (0.100 g, 0.96 mmol) and the mixture was stirred at rt for 6 h under argon. Then the mixture was filtered through a 5 cm silica pad and solvents removed under vacuum. The resulting brown residue was purified by column chromatography by using DCM/Et_2O (1:1, v/v) to give **63** as a white powder (90 mg, 42%) which turned to brown-black after 5 mins and could only be characterised by ^{1}H NMR spectroscopy. ^{1}H NMR (400 MHz, $CDCl_3$) δ 8.41 (d, *J*=6.4 Hz, 2H), 7.16 (d, *J*=6.4 Hz, 2H), 0.21 (s, 9H).

4-((Trimethylsilyl)buta-1,3-diyn-1-yl)aniline; 65

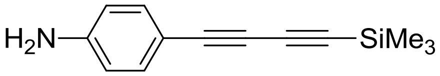

General procedure (III): 4-ethynylaniline (**48**) (0.5g, 4.27 mmol), CuI (40 mg) and $[PdCl_2(PPh_3)_2]$ (0.150 g), TMSA (2.10 g, excess), 5 h, rt. Purified by column chromatography using DCM / hexane (2:3, v/v) as eluent and then recrystallisation from cyclohexane to give **65** as orange-brown needles (0.52 g, 57% yield). mp: 78.0 - 78.5 °C. ^{1}H NMR (400 MHz, $CDCl_3$) δ 7.28 (dd, *J* = 8.8, 2.0 Hz, 2H), 6.56 (dd, *J* = 8.8, 2.0 Hz, 2H), 3.88 (s, 2H), 0.22 (s, 9H). ^{13}C NMR (101 MHz, $CDCl_3$) δ 147.84, 134.49, 114.81, 110.32, 89.68, 88.67, 78.28, 72.57, 0.06. HR-MS (ASAP$^+$) *m/z* : Calcd for $C_{13}H_{15}NSi$ 213.0973, found *m/z* : $[M]^+$ 213.0992. Anal. Calcd. For $C_{13}H_{15}NSi$: C, 73.18; H, 7.09; N, 6.57. Found: C, 72.87; H,7.18, N, 6.86.

4,4’-(Buta-1,3-diyne-1,4-diyl)dianiline; 66

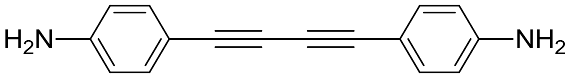

General procedure (III): 4-ethynylaniline (**48**) (0.5 g, 4.3 mmol), $[PdCl_2(PPh_3)_2]$ (60 mg) and CuI (20 mg), 5 h, rt. Purified by column chromatography using DCM as eluent and then recrystallisation from EtOH to give **66** as orange crystals (0.32 g, 65% yield). mp: 183.0 – 184.0 °C. ^{1}H NMR (400 MHz, Acetone-d_6) δ 7.25 (d, *J* = 8.6 Hz, 4H), 6.65 (d, *J* = 8.6 Hz, 4H), 5.16 (s, 4H). ^{13}C NMR (101 MHz, Acetone-d_6) δ 149.97, 133.81, 114.24, 108.81, 82.37, 72.24. MS (ES$^+$) *m/z* (%): 232.1 ($[M]^+$, 100). Anal. Calcd. For $C_{16}H_{12}N_2$: C, 82.73; H, 5.21; N, 12.06. Found: C, 82.47; H, 5.38, N, 11.86. The data are consistent with the literature.[162]

4,4'-(Octa-1,3,5,7-tetrayne-1,8-diyl)dianiline; 67

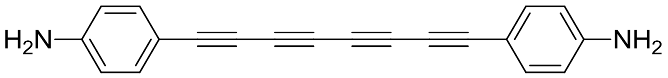

General procedure (IV): **65** (0.200 g, 0.93 mmol), $Cu(OAc)_2.H_2O$ (0.375g), overnight, rt. Purified by column chromatography using DCM as eluent to give **67** as orange solid (0.108 g, 82% yield). ^1H NMR (400 MHz, Acetone-d_6) δ 7.33 (d, *J* = 8.6 Hz, 4H), 6.67 (d, *J* = 8.6 Hz, 4H), 5.46 (s, 4H). ^{13}C NMR (101 MHz, Acetone-d_6) δ 152.06, 135.93, 115.00, 106.75, 81.71, 73.00, 67.58, 65.57. MS (ES$^+$) *m/z* (%): 280.2 ([M]$^+$, 100). High resolution mass spectrum could not be obtained because of the instability.

***N*-(4-Ethynylphenyl)-2,2,2-trifluoroacetamide; 72**

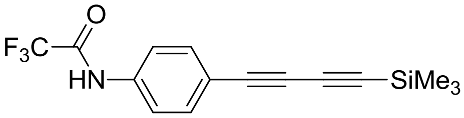

Trifluoroacetic anhydride (0.98 g, 4.69 mmol) was added slowly to a solution of **65** (0.50 g, 2.34 mmol) in dry THF (25 ml) at 0 °C. The mixture stirred for 1 h at this temperature and solvents were then removed under vacuum to give a dark brown oil which was dissolved in diethyl ether and then washed with water. The organic phase dried over $MgSO_4$ and concentrated under reduced pressure. The crude product was purified by column chromatography using EtOAc / hexane (1:20, v/v) as eluent to give **72** as a yellow-brown solid (0.69 g, 96%). mp: 148.0 - 149.5 °C. ^1H NMR (400 MHz, DMSO-d_6) δ 11.41 (s, 1H), 7.71 (d, *J* = 8.6 Hz, 2H), 7.53 (d, *J* = 8.6 Hz, 2H), -0.05 (s, 9H). ^{13}C NMR (101 MHz, DMSO-d_6) 155.10, 138.22, 130.94, 124.41, 116.87, 115.73, 90.48, 88.05, 77.37, 74.39, 1.23. MS (ES$^+$) *m/z* (%): 309.0 ([M]$^+$, 100).

4-Iodo-*N,N*-dimethylaniline; 74

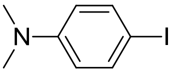

Into a stirred mixture of 4-iodoaniline (**49**) (10 g, 45.6 mmol) and $NaHCO_3$ (9.6 g) in DMF (100 ml), iodomethane (19.4 g, 137 mmol) was added dropwise and stirred for 24 h at rt. The resulting mixture was poured into cold water (100 ml). The precipitate was filtered and recrystallised from MeOH to afford **74** (1.25 g, 55%) as white crystals. mp: 79.0-79.5 °C. ^1H NMR ($CDCl_3$), δ 7.46 (d, *J*=9.2 Hz, 2H), 6.48 (d, *J*=9.2 Hz, 2H), 2.91 (s, 6H). ^{13}C NMR (101 MHz, CDCl$_3$) δ 150.35, 138.14, 115.04, 77.69, 40.96. MS (ES$^+$) *m/z* (%): 248.1 ([M+H]$^+$, 80). The data are consistent with the literature.[166]

***N,N*-Dimethyl-4-((trimethylsilyl)ethynyl)aniline; 75**

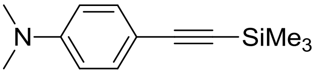

General procedure (I): **74** (2.00 g, 8.09 mmol), [Pd(PPh$_3$)$_4$] (0.284 g), CuI (77 mg), TMSA (0.875 g, 8.90 mmol), (*i*-Pr)$_2$NH, 5 h, rt. Purified by column chromatography using DCM/hexane as eluent (1:1, v/v) to give **75** as a yellow solid (1.74 g, 97%). mp: 52.0 - 53.0 °C. ^{1}H NMR (400 MHz, CDCl$_3$) δ 7.34 (d, *J* = 9.0 Hz, 2H), 6.59 (d, *J* = 9.0 Hz, 2H), 2.96 (s, 6H), 0.22 (s, 9H). ^{13}C NMR (101 MHz, CDCl$_3$) δ 150.40, 133.33, 111.79, 110.08, 106.76, 91.39, 40.39, 0.44. MS (ES$^+$) *m/z* (%): 218.5 ([M+H]$^+$, 40). The data are consistent with the literature.[166]

4-Ethynyl-*N,N*-dimethylaniline; 76

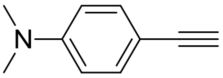

To a solution of **75** (1.50 g, 6.90 mmol) in anhydrous DCM / MeOH (40 ml, 4:1, v/v) mixture, K$_2$CO$_3$ (1.91 g) was added in one portion and the mixture was stirred under argon at rt. When the reaction was complete, as judged by TLC (after 15 h) the solution was passed through a 5 cm silica pad using DCM as eluent and the solvent removed under reduced pressure. The resulting solid was purified by column chromatography using DCM/hexane (1:1, v/v) as eluent to afford **76** as a yellow solid (0.908 g, 90%). mp: 54.0 - 55.0 °C. ^{1}H NMR (400 MHz, CDCl$_3$) δ 7.38 (d, *J* = 9.2 Hz, 2H), 6.62 (d, *J* = 9.2 Hz, 2H), 2.98 (s, 1H), 2.97 (s, 6H). ^{13}C NMR (101 MHz, CDCl$_3$) δ 150.60, 133.42, 111.90, 108.95, 85.09, 75.01, 40.40. MS (ES$^+$) *m/z* (%): 146.2 ([M]$^+$, 100). The data are consistent with the literature.[166]

4,4'-(Ethyne-1,2-diyl)bis(*N,N*-dimethylaniline); 77

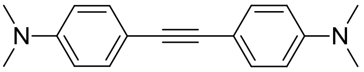

General procedure (I): Compound **74** (0.374 g, 1.52 mmol), [Pd(PPh$_3$)$_4$] (48 mg), CuI (8 mg) and **76** (0.200 g, 1.37 mmol), (*i*-Pr)$_2$NH, 4 h, rt. Purified by column chromatography using EtOAc/hexane (3:7, v/v) as eluent and then recrystallisation from MeOH to afford **4** as yellow needles (0.140 g, 38%). mp: darkened ~198 °C, melted 217-218 °C. ^{1}H NMR (400 MHz, $CDCl_3$) δ 7.38 (d, *J* = 9.0 Hz, 4H), 6.65 (d, *J* = 9.0 Hz, 4H), 2.97 (s, 12H). ^{13}C NMR (101 MHz, $CDCl_3$) δ 149.90, 132.59, 112.16, 111.36, 88.30, 40.53. HR-MS EI$^+$ *m/z* calcd for $C_{18}H_{20}N_2$ $[M+H]^+$ 265.1699, found *m/z* : $[M+H]^+$ 265.1703. Anal. Calcd. For $C_{18}H_{20}N_2$: C, 81.78; H, 7.63; N, 10.60. Found: C, 81.67; H, 7.58, N, 10.46. The data are consistent with the literature.[165]

4,4'-(Buta-1,3-diyne-1,4-diyl)bis(*N,N*-dimethylaniline); 78

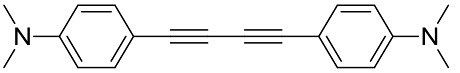

General Procedure (III): **76** (0.200 g, 1.37 mmol), $[PdCl_2(PPh_4)_2]$ (19 mg), CuI (6 mg), 3 h, rt. Purified by column chromatography using hexane/EtOAc (2:8, v/v) as eluent and then recrystallisation from EtOAc to give **78** as yellow needles (0.090 g, 45% yield). mp: darkened ~235 °C, melted 242.0 – 243.5 °C. ^{1}H NMR (400 MHz, $CDCl_3$) δ 7.39 (d, *J* = 8.4 Hz, 4H), 6.61 (d, *J* = 8.4 Hz, 4H), 2.99 (s, 12H). ^{13}C NMR (101 MHz, $CDCl_3$) δ 150.55, 133.84, 111.91, 108.84, 82.58, 72.84, 40.35. HR-MS EI$^+$ *m/z* calcd for $C_{20}H_{20}N_2$ $[M+H]^+$ 288.1699, found *m/z* : $[M+H]^+$ 289.1694. Anal. Calcd. For $C_{20}H_{20}N_2$: C, 83.30; H, 6.99; N, 9.71 Found: C, 83.17; H, 7.01, N, 9.66. The data are consistent with the literature.[165]

***N,N*-Dimethyl-4-((trimethylsilyl)buta-1,3-diyn-1-yl)aniline; 79**

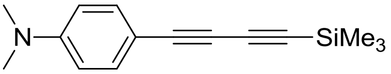

General Procedure (III): **76** (0.250 g, 1.72 mmol), $[PdCl_2(PPh_3)_2]$ (60 mg), CuI (17 mg), TMSA (0.303 g, excess), 5 h, rt. Purified by column chromatography using DCM as eluent to afford **79** as a yellow solid (0.310 g, 74% yield). mp: 69.5 - 70.0 °C. ^{1}H NMR (400 MHz, $CDCl_3$) δ 7.34 (d, *J* = 9.1 Hz, 2H), 6.56 (d, *J* = 9.1 Hz, 2H), 2.96 (s, 6H), 0.21 (s, 9H). ^{13}C NMR (101 MHz, $CDCl_3$) δ 150.86, 134.24, 111.82, 107.45, 89.49, 89.03, 79.02, 72.71, 40.26, 0.01. MS (ES$^+$) *m/z* (%): 242,1 ($[M+H]^+$, 35). The data are consistent with the literature.[155]

4,4'-(Octa-1,3,5,7-tetrayne-1,8-diyl)bis(*N,N*-dimethylaniline); 80

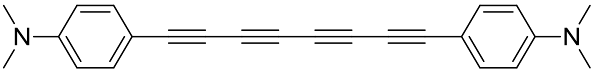

General Procedure (IV): **79** (0.200 g, 0.82 mmol), $Cu(OAc)_2.H_2O$ (0.331 g) , 12 h, rt. Purified by column chromatography using DCM as eluent to afford **80** as a light sensitive, orange solid (0.110 g, 78% yield). ^{1}H NMR (400 MHz, $CDCl_3$) δ 7.34 (d, *J* = 9.0 Hz, 4 H), 6.51 (d, *J* = 9.0 Hz, 4 H), 2.92 (s, 12 H). ^{13}C NMR (101 MHz, $CDCl_3$): δ, 151.58, 135.18, 112.53, 105.12, 79.79, 73.81, 68.26, 65.12, 40.39. HR-MS EI$^+$ *m/z* calcd for $C_{24}H_{20}N_2$ $[M]^+$ 336.1626, found *m/z* : $[M]^+$ 336.1628. The data are consistent with the literature.[155]

4-Iodo-*N*-methylaniline; 81

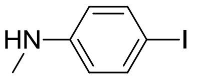

To a solution of 4-iodoaniline (**49**) (3.10 g, 14.2 mmol) and paraformaldehyde (2.12 g, 70 mmol) in dry methanol (50 ml) was added sodium methoxide (3.82 g, 70 mmol) and the mixture was refluxed under argon for 2 h. The mixture was cooled to 0 °C and $NaBH_4$ (2.68 g, 70 mmol) was slowly added. The mixture was refluxed for an additional 2 h then poured into water (400 ml). The basic reaction mixture was neutralized with 5% HCl solution and the mixture was extracted with ether (2 x 100 ml) and purified by column chromatography using DCM/hexane (1:1, v/v) as eluent to afford **81** as a yellow oil (2.00 g, 60%). ^{1}H NMR (400 MHz, $CDCl_3$) δ 7.43 (d, *J*=9.2 Hz, 2H), 6.38 (d, *J*=9.2 Hz, 2H), 3.74 (s, 1H), 2.80 (s, 3H). ^{13}C NMR (101 MHz, $CDCl_3$) δ 149.06, 137.93, 114.84, 77.92, 30.80. MS (ES$^+$) *m/z* (%): 233,9 ($[M+H]^+$, 65). The data are consistent with the literature.[167]

4-Ethynyl-*N*-methylaniline; 82

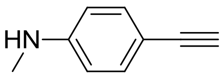

To a stirred mixture of 4-ethynylaniline (**48**) (0.819 g, 7.0 mmol) and paraformaldehyde (1.05 g, 35 mmol) in MeOH (20 mL) was added sodium methoxide (1.89 g, 35 mmol). The reaction mixture was heated to reflux for 2 h and cooled to 0 °C with an ice bath. $NaBH_4$ (1.323 g, 35 mmol) was added slowly. The reaction mixture was heated to reflux again for 1 h and then cooled to rt. Solvents were removed under reduced pressure and the resulting crude product was purified by column chromatography using EtOAc/hexane (3:7, v/v) as eluent to afford **82** as a light yellow clear oil (0.60 g, 65%). ^{1}H NMR (400 MHz, $CDCl_3$) δ 7.28 (dd, *J* = 8.8 Hz, *J* = 2.2 Hz, 2H), 6.52 (dd, *J* = 8.8 Hz, *J* = 2.2 Hz, 2H), 3.90 (s, 1H), 2.96 (s, 1H), 2.86 (s, 3H). ^{13}C NMR (101 MHz, $CDCl_3$) δ 149.77, 133.62, 112.07, 109.91, 85.02, 74.89, 30.57. MS (ES$^+$) *m/z* (%): 132.0 ($[M+H]^+$, 50). The data are consistent with the literature.[167]

4,4'-(Ethyne-1,2-diyl)bis(*N*-methylaniline); 83

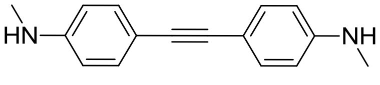

General procedure (I): **81** (0.489 g, 2.10 mmol), [Pd(PPh$_3$)$_4$] (66 mg), CuI (8 mg), **82** (0.250 g, 1.90 mmol), (*i*-Pr)$_2$NH, 3 h, rt. Purified by column chromatography using DCM/hexane (1:1, v/v) as eluent and then recrystallisation from MeOH to afford **83** as yellow crystals (0.280 g, 62%). mp: 140.5 – 141.0 $^{\circ}$C. ^{1}H NMR (400 MHz, CDCl$_3$) δ 7.33 (d, *J* = 8.8 Hz, 4H), 6.55 (d, *J* = 8.8 Hz, 4H), 3.84 (s, 2H), 2.85 (s, 6H). ^{13}C NMR (101 MHz, CDCl$_3$) δ 148.94, 132.80, 112.25, 112.21, 88.07, 30.72. HR-MS EI$^+$ *m/z* calcd for $C_{16}H_{16}N_2$ [M+H]$^+$ 237.1386, found *m/z* : [M+H]$^+$ 237.1391. Anal. Calcd. For $C_{16}H_{16}N_2$: C, 81.32; H, 6.82; N, 11.85. Found: C, 81.27; H, 6.82, N, 11.79.

4,4'-(Buta-1,3-diyne-1,4-diyl)bis(*N*-methylaniline); 84

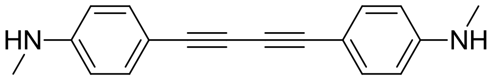

General procedure (III): **82** (0.250 g, 1.906 mmol), [PdCl$_2$(PPh$_3$)$_2$] (27 mg), CuI (7 mg), 12 h, rt. Purified by column chromatography using DCM as eluent to and then recrystallisation from MeOH to afford **84** as yellow crystals (0.220 g, 88% yield). mp: 168.0 – 169.5 $^{\circ}$C. ^{1}H NMR (400 MHz, CDCl$_3$) δ 7.34 (d, *J* = 8.7 Hz, 4H), 6.51 (d, *J* = 8.7 Hz, 4H), 3.96 (s, 2H), 2.84 (s, 6H). ^{13}C NMR (101 MHz, CDCl$_3$) δ 149.85, 134.06, 112.15, 109.82, 82.46, 72.63, 30.52. HR-MS EI$^+$ *m/z* calcd for $C_{18}H_{16}N_2$ [M+H]$^+$ 261.1386, found *m/z* : [M+H]$^+$ 261.1392. Anal. Calcd. For $C_{18}H_{16}N_2$: C, 83.04; H, 6.19; N, 10.76. Found: C, 83.01; H, 6.23, N, 10.69.

***N*-Methyl-4-((trimethylsilyl)buta-1,3-diyn-1-yl)aniline; 85**

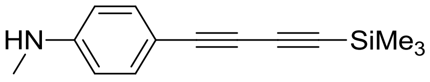

General procedure (I): **81** (0.500 g, 2.1 mmol), BDTMS (0.525, 4.2 mmol), [Pd(PPh$_3$)$_4$] (0.124g), CuI (10 mg), (*i*-Pr)$_2$NH, 3 h, rt. Purified by column chromatography using DCM/PE (1:1, v/v) as eluent to afford **85** as yellow, light sensitive oil (0.445 g, 92% yield). ^{1}H NMR (400 MHz, CDCl$_3$) δ 7.31 (d, *J* = 8.8 Hz, 2H), 6.48 (d, *J* = 8.8 Hz, 2H), 4.01 (s, 2H), 2.83 (s, 6H), 0.22 (s, 9H). ^{13}C NMR (101 MHz, CDCl$_3$) δ 150.24, 134.44, 112.11, 108.54, 89.56, 88.89, 78.86, 72.49, 30.45, -0.01. HR-MS ES$^+$ *m/z* calcd for $C_{14}H_{17}NSi$ [M]$^+$ 227.1125, found *m/z* : [M]$^+$ 227.1140.

4,4'-(Octa-1,3,5,7-tetrayne-1,8-diyl)bis(*N*-methylaniline); 86

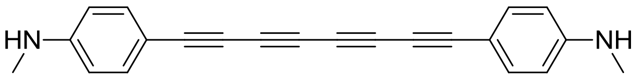

General Procedure (IV): **85** (0.200 g, 0.88 mmol), $Cu(OAc)_2.H_2O$ (0.386 g), 12 h, rt. Purified by column chromatography using DCM/PE (1:1, v/v) as eluent and then recrystallisation from EtOAc to give **86** as yellow needles (0.110, 81%). ^{1}H NMR (400 MHz, $CDCl_3$) δ 7.36 (d, *J* = 8.4 Hz, 4H), 6.49 (d, *J* = 8.4 Hz, 4H), 4.07 (s, 2H), 2.86 (s, 6H). ^{13}C NMR (101 MHz, $CDCl_3$) δ 150.56, 135.11, 112.15, 107.76, 79.79, 73.39, 67.53, 64.67, 30.39. HR-MS EI$^+$ *m/z* calcd for $C_{22}H_{16}N_2$ $[M+H]^+$ 309.1686, found *m/z* : $[M+H]^+$ 309.1692. Crystals for X-ray crystallography were grown by slow evaporation of $CHCl_3$ mixture in an NMR tube.

4-((Trimethylsilyl)buta-1,3-diyn-1-yl)benzonitrile; 87

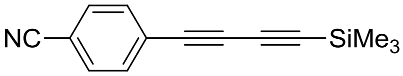

General procedure (III): 4-ethynylbenzonitrile (**51**) (1.00 g, 7.87 mmol), $[PdCl_2(PPh_3)_2]$ (276 mg), CuI (75 mg), TMSA (3.86 g, excess), 5 h, rt. Purified by column chromatography using DCM as eluent to give **87** as a yellow solid (0.70 g, 40 % yield). mp: 82.0 – 83.0 °C. ^{1}H NMR (400 MHz, $CDCl_3$) δ 7.61 (d, *J* = 8.6 Hz, 2H), 7.56 (d, *J* = 8.6 Hz, 2H), 0.25 (s, 9H). ^{13}C NMR (101 MHz, Acetone-d_6) δ 151.07, 134.90, 114.00, 105.73, 80.69, 71.98, 66.56, 64.55, -0.87. HR-MS ASAP$^+$ *m/z* calcd for $C_{14}H_{13}NSi$ $[M+H]^+$ 224.0890, found *m/z* : $[M+H]^+$ 224.0904.

4,4'-(Buta-1,3-diyne-1,4-diyl)dibenzonitrile; 88

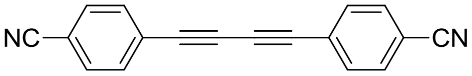

General procedure (III): 4-ethynylbenzonitrile (**51**) (0.500g, 3.9 mmol), $[PdCl_2(PPh_3)_2]$(138 mg) CuI (37 mg), overnight, rt. Yellow precipitate formed in the reaction mixture was filtered and recrystallised from acetic acid to give orange-brown needle crystals of **88** (0.408 g, 82% yield). mp: darkened ~250 °C, melted: 301.0 – 303.0 °C. ^{1}H NMR (500 MHz, CF_3COOD) δ 7.75 (d, *J* = 8.5 Hz, 4H), 7.70 (d, *J* = 8.5 Hz, 4H). ^{13}C NMR (101 MHz, CF_3COOD) δ 134.56, 132.71, 129.07, 117.82, 114.35, 79.23, 76.79. HR-MS EI$^+$ *m/z* calcd for $C_{18}H_8N_2$ $[M+H]^+$ 253.0760, found *m/z* : $[M+H]^+$ 253.0757. Anal. Calcd. for $C_{18}H_8N_2$: C, 85.70; H, 3.20; N, 11.10. Found: C, 85.55; H, 3.22; N, 11.02. The data are consistent with the literature.[242]

4,4'-(Octa-1,3,5,7-tetrayne-1,8-diyl)dibenzonitrile; 89

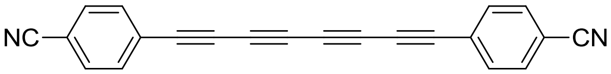

General procedure (IV): **87** (0.250, 1.20 mmol), $Cu(OAc)_2.H_2O$ (0.407 g), overnight, rt. Yellow precipitate formed in the reaction mixture was filtered and recrystallised from acetic acid to afford **89** as shiny yellow crystals (0.105g, 63%). mp: darkened 224 ^oC, **DANGER(!)** exploded at 245 ^oC. ^1H NMR (400 MHz, $CDCl_3$) δ 7.73 (d, *J* = 7.6 Hz, 4H), 7.70 (d, *J* = 7.6 Hz, 4H). ^{13}C NMR (101 MHz, CF_3COOD / $CDCl_3$) δ 133.50, 132.24, 126.75, 110.95, 109.98, 78.03, 75.07, 68.43, 63.31. HR-MS ASAP$^+$ *m/z* calcd for $C_{22}H_8N_2$ $[M+H]^+$ 300.0760, found *m/z* : $[M+H]^+$ 301.0760. Crystals for X-ray crystallography were grown by slow evaporation of CF_3COOD / $CDCl_3$ mixture in an NMR tube.

4-(Buta-1,3-diyn-1-yl)benzonitrile; 90

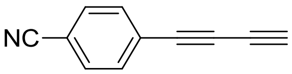

Compound **87** (0.100 g, 0.44 mmol) was dissolved in anhydrous DCM / MeOH (10 mL, 4:1, v/v) mixture, K_2CO_3 (0.13 g) was added in one portion and the mixture was stirred under argon overnight at rt. Then the solution was passed through a 5 cm silica pad and the solvent removed under reduced pressure. The resulting solid was purified by column chromatography using EtOAc / hexane (1:9, v/v) as eluent to afford **90** as a yellow solid (0.057 mg, 85% yield). ^1H NMR (400 MHz, $CDCl_3$) δ 7.63 (d, *J* = 8.4 Hz, 2H), 7.59 (d, *J* = 8.4 Hz, 2H), 2.60 (s, 1H). ^{13}C NMR (101 MHz, $CDCl_3$) δ 133.45, 132.33, 126.20, 118.31, 113.08, 73.80, 73.37, 67.63, 0.23. HR-MS ASAP$^+$ *m/z* calcd for $C_{11}H_5N$ $[M]^+$ 151.0417, found *m/z* : $[M]^+$ 151.0423. Crystals for X-ray crystallography were grown by slow evaporation of $CDCl_3$ in an NMR tube.

2-Methyl-4-(4-nitrophenyl)but-3-yn-2-ol; 92

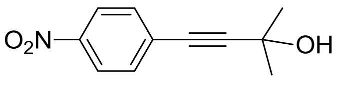

General procedure (I): 4-Iodonitrobenzene (**91**) (3.00 g, 12 mmol), $[Pd(PPh_3)_4]$ (0.254 g), CuI (69 mg), 2-methyl-3-butyn-2-ol (1.22 g, 14.5 mmol), Et_3N, 5 h, rt. Purified by column chromatography using DCM as eluent to afford **92** (2.31 g, 94% yield) as a yellow solid. mp: 101.0 – 102.0 °C. ^1H NMR (400 MHz, Acetone-d_6) δ 8.23 (d, *J* = 9.0 Hz, 2H), 7.66 (d, *J* = 9.0

Hz, 2H), 4.65 (s, 1H), 1.56 (s, 6H). ^{13}C NMR (101 MHz, $CDCl_3$) δ 147.29, 132.60, 129.92, 123.74, 99.28, 80.65, 65.87, 31.46. MS (ASAP$^+$) *m/z* (%): 205.0 ([M]$^+$, 100). The data are consistent with the literature.[243]

1-Ethynyl-4-nitrobenzene; 93

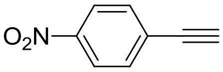

92 (2.00 g, 9.75 mmol) was dissolved in dry toluene (50 ml) and NaOH (1.00 g, excess) was added and the mixture was refluxed under argon for 45 mins. The mixture was poured onto water (100 ml) and the pH was neutralised by adding 5% HCl solution. The organic phase was seperated and washed with brine, dried over $MgSO_4$ and solvents removed. The remaining crude was purified by column chromatography using DCM/PE (1:1, v/v) as eluent to afford **93** (1.00 g, 70% yield). mp: 108.0 - 108.5 °C. ^{1}H NMR (400 MHz, Acetone-d_6) δ 8.13 (d, *J* = 9.0 Hz, 1H), 7.63 (d, *J* = 8.9 Hz, 1H), 3.96 (s, 1H). ^{13}C NMR (101 MHz, Acetone-d_6) δ 205.55, 133.27, 129.09, 123.86, 83.62, 81.69. MS (ASAP$^+$) *m/z* (%): 147.0 ([M]$^+$, 100). The data are consistent with the literature.[243]

1,2-Bis(4-nitrophenyl)ethyne; 94

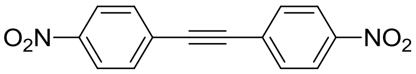

General Procedure (I): 4-Iodonitrobenzene (**91**) (0.231 g, 0.92 mmol), **93** (0.150 g, 1.02 mmol), [$Pd(PPh_3)_4$] (53 mg), CuI (4 mg), (*i*-Pr)$_2$NH, overnight, rt. Purified by column chromatography using DCM/PE (1:1, v/v) as eluent and then recrystallisation from EtOAc to afford **94** as a yellow solid (0.125 g, 50% yield). mp: 198.0 – 200.0 °C. ^{1}H NMR (400 MHz, $CDCl_3$) δ 8.26 (dd, *J* = 5.2, 3.8 Hz, 4H), 7.71 (dd, *J* = 5.2, 3.8 Hz, 4H). ^{13}C NMR (101 MHz, $CDCl_3$) δ 147.84, 132.84, 129.08, 124.01, 92.22. HR-MS ASAP$^+$ *m/z* calcd for $C_{14}H_8N_2O_4$ [M]$^+$ 268.0484, found *m/z* : [M]$^+$ 268.0484. Anal. Calcd. for $C_{14}H_8N_2O_4$: C, 62.69; H, 3.01; N, 10.44. Found: C, 62.45; H, 3.02; N, 10.32. The data are consistent with the literature.[171]

1,4-Bis(4-nitrophenyl)buta-1,3-diyne; 95

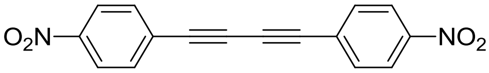

General Procedure (III): **93** (0.150 g, 1.02 mmol), [$PdCl_2(PPh_3)_2$] (21 mg), CuI (6 mg), overnight, rt. Yellow precipitate formed in the reaction mixture was filtered and recrystallised from toluene to afford **95** (0.112 g, 75%) as yellow flakes. mp: 282.0 – 285.0 °C. ^{1}H NMR (500 MHz, $CDCl_3$) δ 8.25 (d, *J* = 8.8 Hz, 4H), 7.71 (d, *J* = 8.8 Hz, 4H). ^{13}C NMR (126 MHz, $CDCl_3$) δ 148.18, 133.59, 128.20, 123.96, 81.71, 78.05.; MS (ES) *m/z* : 292.44 (M^+). HR-MS ASAP$^+$ *m/z* calcd for $C_{16}H_8N_2O_4$ $[M]^+$ 292.0484, found *m/z* : $[M]^+$ 292.0484. Anal. Calcd. for $C_{16}H_8N_2O_4$: C, 65.76; H, 2.76; N, 9.59. Found: C, 65.75; H, 2.62; N, 9.32. The data are consistent with the literature.[172]

Trimethyl((4-nitrophenyl)buta-1,3-diyn-1-yl)silane; 96

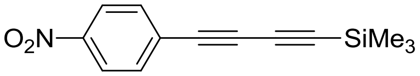

General Procedure (I): 4-iodonitrobenzene (**91**) (0.400g, 1.6 mmol), **58** (0.216 g, 1.77 mmol), [$Pd(PPh_3)_4$] (92 mg), CuI (6 mg), (i-Pr)$_2$NH, overnight, rt. Purified by column chromatography using DCM/Hexane (1:1, v/v) as eluent to afford **96** as a yellow solid (0.30, 77% yield). mp: 110.0 - 111.0 °C. ^{1}H NMR (400 MHz, $CDCl_3$) δ 8.18 (d, *J* = 9.0 Hz, 2H), 7.61 (d, *J* = 9.0 Hz, 2H), 0.24 (s, 9H). ^{13}C NMR (101 MHz, $CDCl_3$) δ 147.75, 133.62, 128.58, 123.87, 94.45, 87.12, 79.19, 74.37, -0.32. MS (ES^+) *m/z* (%): 244.0 ($[M+H]^+$, 100). The data are consistent with the literature.[201]

1,8-Bis(4-nitrophenyl)octa-1,3,5,7-tetrayne; 97

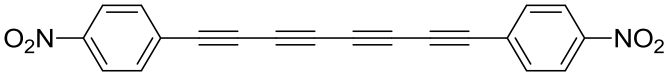

General procedure (IV): **96** (0.200 g, 0.82 mmol) and $Cu(OAc)_2.H_2O$ (0.328 g), overnight, rt. Yellow-green precipitate formed in the reaction mixture was filtered and recrystallised from hot toluene to give **97** (0.12 g, 86%). Due to very low solubility, no clear NMR spectrum was obtained. HR-MS ASAP$^+$ *m/z* calcd for $C_{20}H_8N_2O_4$ $[M]^+$ 340.0479, found *m/z* : $[M]^+$ 340.0466. Crystals for X-ray crystallography were grown in toluene by the slow evaporation of the solvent. [173]

1,4-Bis[4-(2-acetylsulfanyl)-phenyl]-1,3-butadiyne; 99

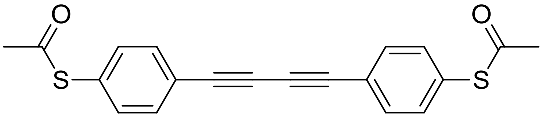

General Procedure (IV): 45 (0.200 g, 0.80 mmol), $Cu(OAc)_2.H_2O$ (0.321 g), overnight, rt. Purified by column chromatography using DCM as eluent and then recrystallisation from EtOAc to give **99** (0.105 g, 76%) as yellow crystals. mp: 144.0 – 145.0 °C. ^1H NMR (400 MHz, $CDCl_3$) δ 7.55 (d, *J* = 8.1 Hz, 4H), 7.39 (d, *J* = 8.1 Hz, 4H), 2.44 (s, 6H). ^{13}C NMR (101 MHz, $CDCl_3$) δ 193.25, 134.44, 133.24, 129.74, 122.95, 81.66, 75.51, 30.60. MS (MALDI-TOF) *m/z* (%): 350.0 ($[M]^+$, 100). Anal. Calcd. for $C_{20}H_{14}O_2S_2$: C, 68.54; H, 4.03; S, 18.30. Found: C, 68.65; H, 4.05; S, 18.04. The data are consistent with the literature.[174]

S-(4-((Trimethylsilyl)buta-1,3-diyn-1-yl)phenyl) ethanethioate; 100

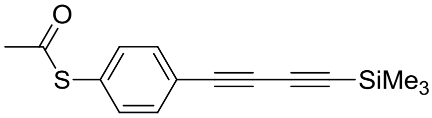

General Procedure (I): **44** (0.250g, 0.9 mmol), $[Pd(PPh_3)_4]$ (52 mg), CuI (4 mg), **58** (52 mg, 0.99 mmol), $(i\text{-}Pr)_2NH$, 3 h, rt. Purified by column chromatography using DCM/PE (1:1, v/v) to give **100** (0.229 g, 94%) as a yellow solid. ^1H NMR (400 MHz, $CDCl_3$) δ 7.50 (d, *J* = 8.1 Hz, 2H), 7.36 (d, *J* = 8.1 Hz, 2H), 2.43 (s, 3H), 0.23 (s, 9H). ^{13}C NMR (101 MHz, $CDCl_3$) δ 193.22, 134.38, 133.37, 129.68, 122.78, 91.93, 87.76, 75.99, 75.87, 30.57, -0.20. MS ($ASAP^+$) *m/z* (%): 272.0 ($[M]^+$, 60). HR-MS $ASAP^+$ *m/z* calcd for $C_{15}H_{16}OSSi$ $[M+H]^+$ 273.0764, found *m/z* : $[M+H]^+$ 273.0778.

5-Bromo-2,3-dihydrobenzo[*b*]thiophene; 104

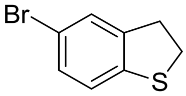

To a solution of compound **113** (1.50 g, 11 mmol) in DCM (25 ml), Br_2 (1.76 g, 11 mmol) in DCM (25 ml) was added dropwise and stirred overnight at rt. A saturated $NaHSO_3$ solution (100 ml) was added to the mixture and the aqueous layer was washed with DCM (2 x 25 ml). The solvent was removed under reduced pressure and the residue was purified by column chromatography using PE as eluent to afford **104** (2.10 g, 89%) as a white solid. mp: 46.5 – 47.0 °C. ^1H NMR (400 MHz, $CDCl_3$) δ 7.29 (s, 1H), 7.21 (d, *J* = 8.2 Hz, 1H), 7.05 (d, *J* = 8.2 Hz, 1H), 3.36 (t, *J* = 7.6 Hz, 2H), 3.26 (t, *J* = 7.6 Hz, 2H). ^{13}C NMR (101 MHz, $CDCl_3$) δ 142.65, 141.07, 130.39, 127.66, 123.55, 117.54, 36.27, 33.91. MS ($ASAP^+$) *m/z* (%): 213.9 ($[M]^+$, 100). The data are consistent with the literature.[244]

5-Iodo-2,3-dihydrobenzo[*b*]thiophene; 105

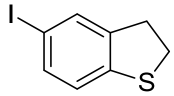

Under argon atmosphere, to a solution of **104** (1.50 g, 7 mmol) in dry THF (10 ml) cooled in a dry-ice-acetone bath was added dropwise *n*-butyllithium solution (2.5 M in hexane) (3.1 ml, 7.6 mmol). The solution was stirred for 2 h at low temperature followed by the addition of iodine (2.12 g, 8.3 mmol). The mixture was stirred for an additional 5 h while the temperature was allowed to rise to rt. The solvents were removed under vacuum and the remaining oily residue was dissolved in Et_2O (15 ml) and the mixture was washed twice with saturated Na_2SO_3 solution (2 x 30 ml). The ether layer was dried over $MgSO_4$ and the solvent removed under reduced pressure. The crude compound was purified by sublimation (55 °C, 0.2 mbar) to afford **105** as a white solid (1.62 g, 89% yield). mp: 45.5 - 46.0 °C. ^{1}H NMR (400 MHz, $CDCl_3$) δ 7.49 (s, 1H), 7.39 (d, *J* = 7.2 Hz, 1H), 6.95 (d, *J* = 7.2 Hz, 1H), 3.34 (t, *J* = 8.4 Hz, 2H), 3.25 (t, *J* = 7.5 Hz, 2H). ^{13}C NMR (101 MHz, $CDCl_3$) δ 142.99, 142.04, 136.30, 133.45, 124.07, 87.98, 36.10, 33.76. HR-MS ASAP$^+$ *m/z* calcd for C_8H_7IS $[M]^+$ 261.9308, found *m/z* : $[M]^+$ 261.9328.

Methyl 2-((4-bromophenyl)thio)acetate; 106a

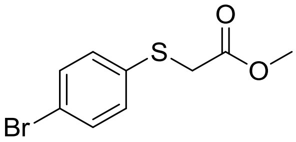

Into a solution of 4-bromothiophenol (**42**) (6.00 g, 31.73 mmol) and methyl bromoacetate (5.10 g, 33.30 mmol, 1.05 equiv) in benzene (120 ml) was added Et_3N (4.64 ml, 33.3 mmol, 1.05 equiv) in benzene (120 ml) in 10 min and the solution was refluxed under argon for 2h. The precipitated salt was filtered, and the filtrate was concentrated under vacuum to yield a light yellow liquid. This crude product was vacuum distilled, (Kugelrohr, 0.5 mbar), yielding **106a** (8.10 g, 97%) as a clear liquid. ^{1}H NMR (400 MHz, $CDCl_3$) δ 7.37 (d, *J* = 8.4 Hz, 2H), 7.22 (d, *J* = 8.4 Hz, 12H), 3.66 (s, 3H), 3.59 (s, 2H). ^{13}C NMR (101 MHz, $CDCl_3$) δ 169.94, 134.48, 132.29, 131.46, 121.10, 52.82, 36.43. The data are consistent with the literature.[177]

2-((4-Bromophenyl)thio)acetic acid; 106b

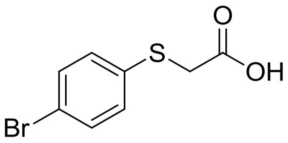

106 (5.00 g, 19.1 mmol) was dissolved in MeOH (100 ml) containing NaOH (0.91 g, 23 mmol, 1.2 equiv) and was stirred at reflux for 2 h. The acid salt was concentrated and dried under vacuum. The resultant solid was dissolved in H_2O and acidified to pH < 1. The white precipitate was filtered and dried (3.85 g, 81%). mp: 118.0 – 119.0 °C. ^1H NMR (400 MHz, $CDCl_3$) δ 10.94 (broad s, 1H), 7.43 (d, *J* = 8.6 Hz, 2H), 7.28 (d, *J* = 8.6 Hz, 2H), 3.64 (s, 2H). ^{13}C NMR (101 MHz, $CDCl_3$) δ 175.98, 133.79, 132.50, 131.90, 121.67, 36.76. The data are consistent with the literature.[177]

((2,3-Dihydrobenzo[*b*]thiophen-5-yl)ethynyl)trimethylsilane; 107a

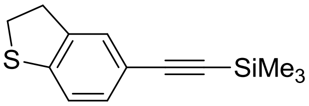

General procedure (I): **104** (0.50 g, 1.90 mmol), TMSA (0.374 g, 3.80 mmol, 2 equiv.), [$Pd(PPh_3)_4$] (110 mg), CuI (8 mg), (i-Pr)$_2$NH, 4 h, rt. Purified by column chromatography using first PE then DCM/PE (1:9, v/v) as eluent to afford **107a** as a white solid (0.42 g, 94% yield). mp: 64.0 - 65.0 °C. ^1H NMR (400 MHz, $CDCl_3$) δ 7.27 (s, 1H), 7.22 (d, *J* = 8.2 Hz, 1H), 7.12 (d, *J* = 8.0 Hz, 1H), 3.35 (t, *J* = 7.5 Hz, 2H), 3.24 (t, *J* = 7.7 Hz, 2H), 0.24 (s, 9H). ^{13}C NMR (101 MHz, $CDCl_3$) δ 143.05, 140.38, 131.37, 127.83, 122.00, 118.88, 105.52, 93.59, 36.01, 33.64, 0.28. HR-MS ASAP$^+$ *m/z* calcd for $C_{13}H_{16}SSi$ $[M]^+$ 232.0736, found *m/z* : $[M]^+$ 232.0736.

5-Ethynyl-2,3-dihydrobenzo[*b*]thiophene; 107b

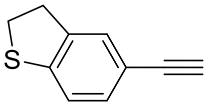

General Procedure (II): 107a (0.150 g, 0.64 mmol), TBAF solution (1M, 1.29 ml), 30 mins, rt. Purified by column chromatography using first PE then DCM/PE (1:9, v/v) as eluent to afford **107b** as white solid (95 mg, 92%). mp: 74.0 – 74.5 °C. ^1H NMR (400 MHz, $CDCl_3$) δ

7.28 (s, 1H), 7.25 (d, *J* = 8.0 Hz, 1H), 7.15 (d, *J* = 8.0 Hz, 1H), 3.34 (m, 2H), 3.24 (m, 2H), 3.05 (s, 1H). ^{13}C NMR (101 MHz, $CDCl_3$) δ 143.52, 140.57, 131.55, 127.99, 122.12, 117.80, 84.10, 76.87, 36.06, 33.68. HR-MS ASAP$^+$ *m/z* calcd for $C_{10}H_8S$ $[M]^+$ 160.0341, found *m/z* : $[M]^+$ 160.0357.

5-Bromobenzo[*b*]thiophen-3(2H)-one; 108

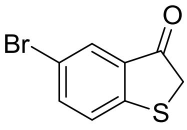

107 (1.76 g, 7.12 mmol) in an excess of $SOCl_2$ (15 ml) was refluxed, under argon for 1 h. The excess $SOCl_2$ was removed under vacuum and the resultant acid chloride was dissolved in $CHCl_3$ (20 ml) and the flask was cooled in a salt ice bath. $AlCl_3$ (1.14 g, 8.55 mmol, 1.2 equiv) was added to the cooled solution whilst stirring vigorously, over 5 min period. The solution was stirred with cooling for another 10 min, then the ice bath was removed, and the solution was stirred at rt for a further 40 min. The reaction was quenched with ice/water, then **108** was extracted with DCM, dried over $MgSO_4$, concentrated, and dried under vacuum. The yellowish solid **108** slowly decomposed and so was used as soon as possible. The product could only be characterised by ^{1}H NMR. ^{1}H NMR (400 MHz, $CDCl_3$) δ 7.86 (d, *J* = 1.8 Hz, 1H), 7.61 (dd, *J* = 8.5, 1.8 Hz, 1H), 7.29 (d, *J* = 8.5 Hz, 1H), 3.81 (s, 2H). The data are consistent with the literature.[177]

Benzo[*b*]thiophene 1,1-dioxide; 111

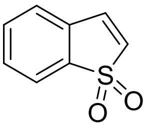

To a solution of benzo[*b*]thiophene (**110**) (11.40 g, 85 mmol) in DCM (500 ml), *m*-chloroperbenzoic acid (mCPBA) (70%, 52.40 g, 0.2 mol, 2.5 eq.) was added portionwise at rt. The mixture was stirred for 16 h then a saturated aqueous solution of $NaHCO_3$ (500 ml) was added and the aqueous layer was extracted with DCM (2x100 ml). The combined organic layers were dried over $MgSO_4$, solvent was removed under vacuum and the crude product was recrystallised from EtOH to afford **111** as white crystals (13.70 g, 98%). mp: 142.0 - 143.0 °C. ^{1}H NMR (400 MHz, $CDCl_3$) δ 7.68 (d, *J* = 6.9 Hz, 1H), 7.52 (m, 2H), 7.34 (dd, *J* = 6.8, 1.2 Hz, 1H), 7.21 (dd, *J* = 6.9, 0.9 Hz, 1H), 6.69 (d, *J* = 6.9 Hz, 1H). ^{13}C NMR (101 MHz,

$CDCl_3$) δ 136.88, 133.93, 132.73, 131.40, 131.02, 130.79, 125.70, 121.54. MS (ES^+) *m/z* (%): 322.2 ([$2M^+$], 100), 167.0 ($[M+H]^+$, 15). The data are consistent with the literature.[178]

2,3-Dihydrobenzo[*b*]thiophene-1,1-dioxide; 112

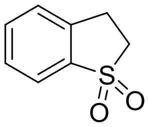

111 (7.30 g, 44 mmol) was dissolved in EtOH and added 0.1 g of 10% Pd on charcoal catalyst. Hydrogen was bubbled through the solution at ambient pressure for 5 h at rt. Solvent removed under reduced pressure and the crude product was filtrated through a 10 cm Celite pad to afford **112** as white crystals (7.25 g, 98%). mp: 87.5 - 88.0 °C. ^{1}H NMR (400 MHz, $CDCl_3$) δ 7.72 (dd, *J* = 7.8, 0.5 Hz, 1H), 7.56 (td, *J* = 7.6, 1.2 Hz, 1H), 7.45 (td, *J* = 7.6, 1.2 Hz, 1H), 7.37 (dd, *J* = 7.8, 0.5 Hz, 1H), 3.48 (t, *J* = 6.4 Hz, 2H), 3.38 (t, *J* = 6.4 Hz, 2H). ^{13}C NMR (101 MHz, $CDCl_3$) δ 139.11, 137.43, 133.67, 129.03, 127.49, 121.67, 50.85, 25.60. MS ($ASAP^+$) *m/z* (%): 169.0 ($[M+H]^+$, 100). The data are consistent with the literature.[178]

2,3-Dihydrobenzo[*b*]thiophene; 113

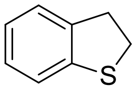

A solution of **112** (4.00 g, 23.8 mmol) in dry diethyl ether (100 ml) was added to a suspension of $LiAlH_4$ (8.12 g, 9 eq.) in dry diethyl ether (150 ml) at 0 °C under argon. After the addition the reaction mixture was stirred for 15 mins then allowed to warm up to rt and refluxed for 2 h, then cooled to 0 °C and the excess $LiAlH_4$ was decomposed by dropwise addition of water (50 ml). The resulting white precipitate was dissolved in 4M aqueous HCl solution (400 ml) and extracted with diethyl ether (2 x 100 ml). The combined organic layers dried over $MgSO_4$ and the crude product was purified by column chromatography using hexane as eluent to afford **113** as a colourless oil (2.55 g, 77% yield). ^{1}H NMR (400 MHz, $CDCl_3$) δ 7.22 (m, 2H), 7.13 (td, *J* = 7.2, 1.2 Hz, 1H), 7.03 (td, *J* = 7.2, 1.2 Hz, 1H), 3.36 (m, 1H), 3.30 (m, 1H). ^{13}C NMR (101 MHz, $CDCl_3$) δ 141.74, 140.27, 127.55, 124.64, 124.32, 122.36, 36.46, 33.56. MS (ES^+) *m/z* (%): 137.0 ($[M+H]^+$ 100), 274.1 ([$2M^+$], 20). The data are consistent with the literature.[178]

1,2-Bis(2,3-dihydrobenzo[*b*]thiophen-5-yl)ethyne; 114

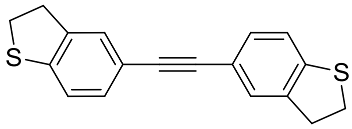

General Procedure (I): 107b (0.100 g, 0.62 mmol), **105** (0.180 g, 0.68 mmol), [Pd(PPh$_3$)$_4$] (36 mg), CuI (3 mg), (*i*-Pr)$_2$NH, overnight, rt. Purified by column chromatography using DCM/PE (1:1, v/v) as eluent and then recrystallisation from EtOAc to afford **114** as white needle crystals (0.120 g, 67%). mp: 227.0 - 228.5 °C. ^{1}H NMR (400 MHz, CDCl$_3$) δ 7.31 (s, 2H), 7.26 (d, *J* = 7.9 Hz, 2H), 7.17 (d, *J* = 7.9 Hz, 2H), 3.38 (m, 4H), 3.28 (t, *J* = 7.7 Hz, 4H). ^{13}C NMR (101 MHz, CDCl$_3$) δ 142.51, 140.54, 130.89, 127.35, 122.15, 119.21, 89.21, 36.09, 33.69. HR-MS ASAP$^+$ *m/z* calcd for $C_{18}H_{14}S_2$ [M]$^+$ 294.0531, found *m/z* : [M]$^+$ 294.0536. Anal. Calcd. for $C_{18}H_{14}S_2$: C, 73.43; H, 4.79; S, 21.78. Found: C, 73.35; H, 4.75; S, 21.54.

1,4-Bis(2,3-dihydrobenzo[*b*]thiophen-5-yl)buta-1,3-diyne; 115

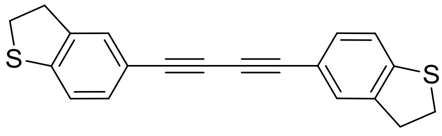

General Procedure (IV): **107a** (0.392 g, 1.68 mmol), Cu(OAc)$_2$.H$_2$O (0.673 g), 12 h, rt. Purified by column chromatography using DCM/PE (1:1, v/v) as eluent and then recrystallisation from EtOAc to give **115** (0.230 g, 86%) as pale yellow needles. mp: 221.5 - 223.0 °C. ^{1}H NMR (400 MHz, CDCl$_3$) δ 7.30 (s, 2H), 7.27 (d, *J* = 8.0 Hz, 2H), 7.15 (d, *J* = 8.0 Hz, 2H), 3.38 (m, 4H), 3.27 (t, *J* = 7.7 Hz, 4H). ^{13}C NMR (101 MHz, CDCl$_3$) δ 144.25, 140.68, 131.96, 128.12, 122.22, 117.51, 82.05, 73.84, 35.99, 33.68. HR-MS ASAP$^+$ *m/z* calcd for $C_{20}H_{14}S_2$ [M+H]$^+$ 319.0610, found *m/z* : [M+H]$^+$ 319.0610. Anal. Calcd. for $C_{20}H_{14}S_2$: C, 75.43; H, 4.43; S, 20.14. Found: C, 75.45; H, 4.48; S, 20.07. Crystals for X-ray crystallography were grown by slow evaporation of CDCl$_3$ mixture in an NMR tube.

((2,3-Dihydrobenzo[*b*]thiophen-5-yl)buta-1,3-diyn-1-yl)trimethylsilane; 116

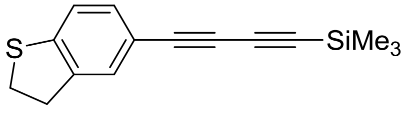

General procedure (I): **105** (0.50, 1.90 mmol), BDTMS (0.280, 2.29 mmol), [Pd(PPh$_3$)$_4$] (110 mg), CuI (8 mg), (*i*-Pr)$_2$NH, 3 h, rt. Purified by column chromatography using DCM/PE (1:3, v/v) to afford **116** as light brown solid (0.380 g, 78% yield). ^{1}H NMR (400 MHz, CDCl$_3$) δ 7.28

(s, 1H), 7.26 (d, *J* = 8.2 Hz, 1H), 7.15 (d, *J* = 8.0 Hz, 1H), 3.38 (t, *J* = 7.7 Hz, 2H), 3.27 (t, *J* = 7.8 Hz, 2H), 0.25 (s, 9H). ^{13}C NMR (101 MHz, $CDCl_3$) δ 144.62, 140.67, 132.21, 128.30, 122.21, 116.90, 90.64, 88.27, 77.40, 73.90, 35.96, 33.66, -0.11. HR-MS ASAP$^+$ *m/z* calcd for $C_{15}H_{16}SSi$ $[M]^+$ 256.0736, found *m/z* : $[M]^+$ 256.0778.

1,8-Bis(2,3-dihydrobenzo[*b*]thiophen-5-yl)octa-1,3,5,7-tetrayne; 117

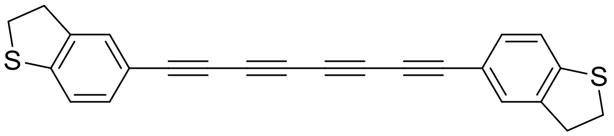

General procedure (IV): 116 (0.100 g, 0.39 mmol), $Cu(OAc)_2.H_2O$ (0.156 g), 12 h, rt. Yellow-green precipitate formed in the reaction mixture was filtered and recrystallised from EtOAc to afford **117** (0.065g, 91% yield) as yellow needle crystals. ^{1}H NMR (400 MHz, $CDCl_3$) δ 7.31 (s, 2H), 7.29 (d, *J* = 8.2 Hz, 2H), 7.15 (d, *J* = 8.0 Hz, 2H), 3.38 (t, *J* = 7.5 Hz, 4H), 3.27 (t, *J* = 7.7 Hz, 4H). ^{13}C NMR (101 MHz, $CDCl_3$) δ 145.72, 140.85, 132.80, 128.73, 122.33, 116.00, 78.50, 74.44, 67.64, 64.24, 35.89, 33.69. HR-MS ASAP$^+$ *m/z* calcd for $C_{24}H_{14}S_2$ $[M+H]^+$ 366.0610, found *m/z* : $[M+H]^+$ 367.06241. X-ray crystals were grown by slow evaporation of $CHCl_3$ from a dilute solution.

4-Iodo-3,5-dimethylbenzenamine; 125

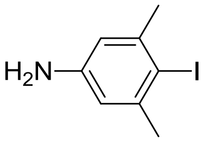

To a solution of 3,5-dimethylaniline (**124**) (5 g, 41 mmol) in acetonitrile (40 ml) was added *N*-iodosuccinimide (9.283 g, 41 mmol). The mixture was stirred overnight at rt, then the solvent was removed under vacuum. The resulting residue was dissolved in ether (100 ml) and washed with 5% $NaHSO_3$ solution (2 x 100 ml) then washed with water (2 x 200 ml), dried over $MgSO_4$ and solvents removed. The resulting solid was first recrystallised from hexane, then THF / water (1:3, v/v) mixture to give **125** as white crystals (6.80 g, 67%). mp: 110.0 – 112.0 °C (lit. 112-113 °C). ^{1}H NMR (400 MHz, $CDCl_3$) δ 6.46 (s, 2H), 3.51 (s, 2H), 2.37 (s, 6H). ^{13}C NMR (101 MHz, $CDCl_3$) δ 146.20, 142.78, 114.41, 94.22, 29.74. MS (ES$^+$) *m/z* (%): 248.0 ($[M+H]^+$, 100). The data are consistent with the literature.[190]

3,5-Dimethyl-4-((trimethylsilyl)buta-1,3-diyn-1-yl)aniline; 126

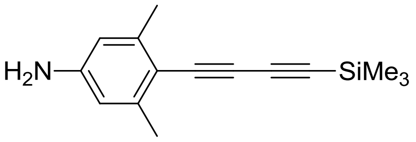

General Procedure (I): **125** (0.300 g, 1.21 mmol), BDTMS (**58**) (0.297g, 2.43 mmol), [Pd(PPh_3)$_4$] (70 mg), (*i*-Pr)$_2$NH, CuI (5 mg), 20 mins, microwave reactor, 100 °C. Purified by column chromatography using DCM/PE (1:1, v/v) as eluent to afford **126** as a brownish oil (40 mg, 13%). ^{1}H NMR (400 MHz, $CDCl_3$) δ 6.32 (s, 2H), 3.76 (s, 2H), 2.34 (s, 6H), 0.23 (s, 9H). ^{13}C NMR (101 MHz, $CDCl_3$) δ 147.17, 144.37, 113.52, 110.84, 90.50, 88.92, 80.05, 76.21, 21.32, 0.03. MS (ES$^+$) *m/z* : 241.1 ([M]$^+$, 40).

4,4'-(Octa-1,3,5,7-tetrayne-1,8-diyl)bis(3,5-dimethylaniline); 127

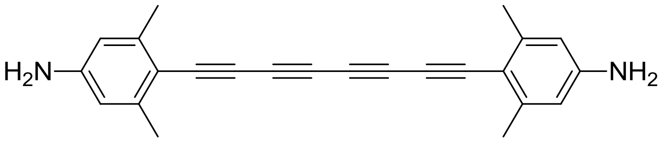

General Procedure (IV): **126** (40 mg, 0.16 mmol), Cu(OAc)$_2$.H_2O (66 mg), overnight, rt. Purified by column chromatography using DCM as eluent to afford **127** as yellow solid (18 mg, 65%). ^{1}H NMR (400 MHz, Acetone-d$_6$) δ 6.41 (s, 4H), 5.27 (s, 4H), 2.29 (s, 12H). ^{13}C NMR (101 MHz, $CDCl_3$) δ 155.72, 150.04, 118.21, 111.92, 84.91, 84.36, 73.54, 70.66, 25.66. HR-MS ASAP$^+$ *m/z* calcd for $C_{24}H_{20}N_2$ [M+H]$^+$ 337.1699, found *m/z* : [M+H]$^+$ 337.1711. X-ray crystals were grown by slow evaporation of acetone from a dilute solution.

3,5-Dimethyl-4-((trimethylsilyl)ethynyl)aniline; 128

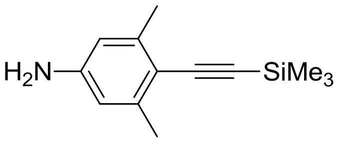

General Procedure (I): 125 (1.00 g, 4.05 mmol), TMSA (0.795 g, 8.09 mmol), [Pd(PPh_3)$_4$] (0.234 g), CuI (15 mg), (*i*-Pr)$_2$NH, 20 mins, microwave reactor, 100 °C. Purified by column chromatography using DCM/PE (1:1, v/v) as eluent to afford **128** as a yellow oil (0.64 g, 72%). ^{1}H NMR (400 MHz, $CDCl_3$) δ 6.33 (s, 2H), 3.68 (s, 2H), 2.36 (s, 6H), 0.27 (s, 9H). ^{13}C

NMR (101 MHz, $CDCl_3$) δ 146.46, 142.44, 113.53, 113.05, 104.02, 100.06, 21.34, 0.62. MS (ES^+) *m/z* (%): 217.1 ($[M]^+$, 100). The data are consistent with the literature.[192]

2,6-Dimethyl-4-nitrophenyl trifluoromethanesulfonate; 133

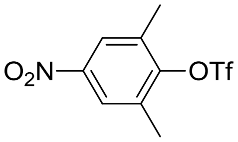

To a solution of 2,5-dimethyl-4-nitrophenol (**132**) (1.00 g, 5.98 mmol) in DCM (10 ml) and pyridine (2 ml), trifilic anhydride (2.03 g, 7.18 mmol) in DCM (5 ml) was added dropwise in 15 min at 0 °C under argon. After the addition the mixture was warmed to rt and stirred for 1 h at ambient temperature. The mixture was diluted with ether (50 ml) and quenched with 10% aqueous HCl solution (50 ml) and washed with $NaHCO_3$ and brine solutions. The solvents were removed and the product was purified by column chromatography using DCM as eluent to afford white crystals of **133** (1.517 g, 85% yield). mp: 148.0 - 149.5 °C. ^{1}H NMR (400 MHz, $CDCl_3$) δ 8.02 (s, 2H), 2.50 (s, 6H). ^{13}C NMR (101 MHz, $CDCl_3$) δ 150.53, 134.00, 125.04, 120.29, 117.11, 17.72. ^{19}F NMR (376 MHz, $CDCl_3$) δ -73.45. MS (ES^+) *m/z* (%): 300.0 ($[M+H]^+$, 100), 299.0 ($[M]^+$, 25).

((2,6-Dimethyl-4-nitrophenyl)ethynyl)trimethylsilane; 134

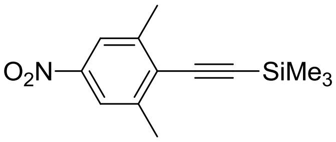

133 (2.50 g, 8.35 mmol), TMSA (0.98 g, 12.5 mmol), $[Pd(PPh_3)_4]$ (0.483 g) and CuI (31 mg) was dissolved in dry DMF (50 ml) and stirred under argon for 4 h at rt. The solvents were removed and the residue was purified by column chromatography using PE then DCM/PE (1:1, v/v) as eluent to afford **134** as a yellow solid (1.04 g, 50% yield). mp: 121 °C. ^{1}H NMR (400 MHz, $CDCl_3$) δ 7.89 (s, 2H), 2.50 (s, 6H), 0.29 (s, 9H). ^{13}C NMR (101 MHz, $CDCl_3$) δ 146.57, 142.33, 129.94, 121.60, 109.20, 100.93, 21.39, 0.11. MS ($ASAP^+$) *m/z* : 248.1 ($[M+H]^+$, 100), 247.1 ($[M]^+$, 10). The data are consistent with the literature.[192]

2-Ethynyl-1,3-dimethyl-5-nitrobenzene; 135

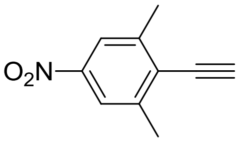

General Procedure (II): 134 (0.900 g, 3.6 mmol), TBAF solution (7.28 ml, 7.2 mmol), 30 mins, rt. Purification by column chromatography using DCM / PE (1:1, v/v) as eluent to afford **135** (0.54 g, 85%) as a yellowish solid. mp: 170 °C. ^{1}H NMR (400 MHz, $CDCl_3$) δ 7.91 (s, 2H), 3.78 (s, 1H), 2.53 (s, 6H). ^{13}C NMR (101 MHz, $CDCl_3$) δ 142.84, 128.91, 121.67, 104.88, 90.46, 79.76, 21.38. MS (ES^+) *m/z* (%)*:* 176.1 $[M]^+$. The data are consistent with the literature.[192]

4-Bromo-3,5-dimethylpyridine; 136

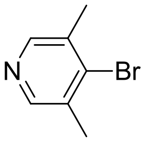

To a $TiCl_4$ (0.465 g, 2.45 mmol, 0.99 equiv.) solution in anhydrous THF (20 ml) was gradually added $LiAlH_4$ (68 mg, 1.78 mmol, 0.72 equiv.) under argon atmosphere. The reaction mixture was stirred 30 mins at rt. Then, cooled to 0 °C by an ice bath and subsequently **144** (0.500 g, 2.47 mmol, 1 equiv.) was gradually added. The mixture was then stirred for 30 min at rt. Hydrolysis was carried out by addition of water (15 ml) and then NH_4OH (33% in water, 15 ml). After dilution, the aqueous layer was extracted three times with Et_2O. The combined etheral layers were dried with $MgSO_4$ and concentrated under vacuum and purified by column chromatography using Et_2O/DCM (1:1, v/v) as eluent to afford **136** as a clear oil (0.30 g, 65%). ^{1}H NMR (400 MHz, $CDCl_3$) δ 8.17 (s, 2H), 2.31 (s, 6H). ^{13}C NMR (101 MHz, $CDCl_3$) δ 148.39, 137.72, 133.94, 20.37. MS (ES^+) *m/z* (%): 184.9 ($[M]^+$, 100); 186.9 (80). The data are consistent with the literature.[193]

3,5-Dimethylpyridine 1-oxide; 142

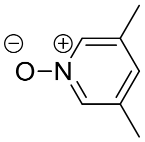

To a solution of 3,5-lutidine (**141**) (5.00 g, 46.7 mmol) in DCM (250 ml), *m*-chloroperbenzoic acid (mCPBA) (70%, 15.70 g, 70 mol, 1.5 eq.) was added portionwise at rt. The mixture was stirred for overnight then a saturated solution of $NaHCO_3$ (100 ml) was added and the aqueous layer was extracted with DCM (2 x 50 ml). The combined organic layers were dried over $MgSO_4$, solvent was removed under vacuum to afford the crude **142** as white crystals (4.20 g, 73%), which were used without further purification. mp: 103.0 - 104.0 °C. ^1H NMR (400 MHz, $CDCl_3$) δ 7.86 (s, 2H), 6.87 (s, 1H), 2.21 (s, 6H). ^{13}C NMR (101 MHz, $CDCl_3$) δ 136.82, 136.16, 128.79, 18.39. MS ($ASAP^+$) *m/z* (%): 124.0 ($[M+H]^+$, 40). The data are consistent with the literature.[193]

3,5-Dimethyl-4-nitropyridine 1-oxide; 143

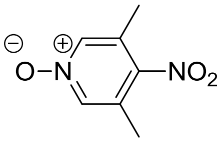

142 (3.00 g, 24.4 mmol) was dissolved in H_2SO_4 (8 ml) and fuming HNO_3 (5 ml) mixture. The temperature was gradually raised to 90 °C. The reaction mixture was stirred for 3 h at this temperature and then allowed to cool down to rt. Crushed ice was added and the aqueous layer was neutralised with solid K_2CO_3. The precipitate was filtered and first washed with water and then with DCM. The organic filtrate was concentrated under vacuum to afford **143** (2.90 g, 71%), which was purified by recrystallisation from EtOAc as pinkish white flakes. mp: 175.0 – 178.5 °C. ^1H NMR (400 MHz, $CDCl_3$) δ 7.98 (s, 1H), 2.31 (s, 6H). ^{13}C NMR (101 MHz, $CDCl_3$) δ 138.94, 137.86, 129.57, 15.69. MS (ES^+) *m/z* (%): 169.0 ($[M+H]^+$, 20). The data are consistent with the literature.[193]

4-Bromo-3,5-dimethylpyridine 1-oxide; 144

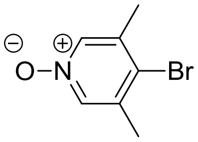

Under an atmosphere of Ar, to a solution of **143** (3.00 g, 17.8 mmol) in AcOH (40 ml) was added dropwise acetyl bromide (22 ml). After stirring 3 h at 80 °C, the reaction mixture was allowed to cool down to rt. The reaction mixture was poured onto crushed ice and then neutralised by the addition of aqueous NaOH (%10) and then solid Na_2CO_3. The aqueous mixture was extracted DCM (2 x 50 ml). The combined extract was dried over $MgSO_4$ and solvents removed under vacuum. The resulting solid was recrystallised from EtOAc to afford **144** as white crystals (3.47 g, 96%). mp: 100.0 - 100.05 °C. ^1H NMR (400 MHz, $CDCl_3$) δ 7.96

(s, 2H), 2.35 (s, 6H). ^{13}C NMR (101 MHz, $CDCl_3$) δ 137.27, 136.70, 125.38, 20.55. MS (ES$^+$) *m/z* (%): 202.0 ([M]$^+$, 100), 204.0 (95). The data are consistent with the literature.[193]

4,4'-((2,5-Dimethoxy-1,4-phenylene)bis(ethyne-2,1-diyl))dianiline; 145

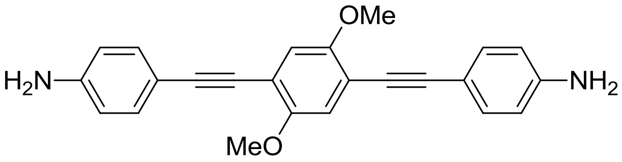

General Procedure (I): **148** (0.200 g, 0.51 mmol), [Pd(PPh_3)$_4$] (30 mg), CuI (2 mg), **48** (0.132 g, 1.13 mmol), (*i*-Pr)$_2$NH, 4 h, rt. Purified by column chromatography using DCM as eluent and then recrystallisation from EtOH to afford **145** (0.140 g, 73%) as orange needle crystals. mp: darkened 207-210 °C, no clear melting point was observed. ^{1}H NMR (400 MHz, $CDCl_3$) δ 7.37 (d, *J* = 8.6 Hz, 4H), 6.99 (s, 2H), 6.63 (d, *J* = 8.6 Hz, 4H), 3.88 (s, 6H), 3.83 (broad s, 4H). ^{13}C NMR (101 MHz, $CDCl_3$) δ 153.83, 146.94, 133.31, 115.60, 114.91, 113.53, 112.83, 95.94, 83.95, 56.67. MS (ASAP$^+$) *m/z* (%): 368.2 ([M]$^+$, 100). Anal. Calcd. for $C_{24}H_{20}N_2O_2$: C, 78.24; H, 5.47; N, 7.60. Found: C, 77.87; H, 5.40; N, 7.07.

1,4-Bis(pyridin-4-ylethynyl)benzene; 146

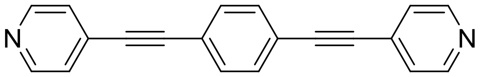

To a solution of **151** (0.200 g, 0.74 mmol) in THF (10 ml) were added Ag_2O (0.685 g, 2.96 mmol, 4 equiv.), **38** (0.333 g, 1.63 mmol) and [Pd(PPh_3)$_4$] (0.171 g, 0.20 equiv.) under an argon atmosphere. The resulting suspension was heated at 60 °C for 36 h. After cooling down to rt, the mixture was passed through a 5 cm Celite pad to remove silver residues. Solvents were removed and the crude was purified by column chromatography using DCM/Acetone (2:1, v/v) as eluent and then recrystallisation to afford **146** as white crystals (0.100 g, 49%). mp: 195.5 – 196.5 °C (Lit. value: 189-191 °C). ^{1}H NMR (400 MHz, $CDCl_3$) δ 8.63 (d, *J* = 5.9 Hz, 4H), 7.56 (s, 4H), 7.39 (d, *J* = 5.9 Hz, 4H). ^{13}C NMR (101 MHz, $CDCl_3$) δ 150.07, 132.13, 131.19, 125.71, 123.06, 93.38, 89.04. HR-MS ASAP$^+$ *m/z* calcd for $C_{20}H_{12}N_2$ [M+H]$^+$ 280.1073, found *m/z* : [M+H]$^+$ 281.1034. The data are consistent with the literature.[245]

1,4-Diiodo-2,5-dimethoxybenzene; 148

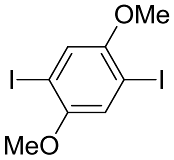

To a solution of dimethoxybenzene **148** (3.138 g, 22.7 mmol) in acetic acid (150 ml), water (15 ml), concentrated H_2SO_4 (1.5 ml), KIO_3 (4.24 g, 19.8 mmol) and I_2 (5.79g) were added. The mixture was stirred at 100 ^{o}C for 18 h. The mixture was then filtered and the solid precipitate was washed with MeOH (100 ml) until the solid became colourless. The solid gave the pure product **148** by recrystallisation from ethyl acetate as white crystals (588 mg, 63% yield); mp: 173.0 - 174.5 °C. ^{1}H NMR (400 MHz, $CDCl_3$): δ 7.19 (s, 2H), 3.83 (s, 6H); ^{13}C NMR ($CDCl_3$, 100 MHz): δ 153.5, 121.8, 85.6, 57.4. MS (ASAP$^+$) *m/z* (%): 390.1 ([M+H]$^+$, 100). The data are consistent with the literature.[246]

4,4'-((Perfluoro-1,4-phenylene)bis(ethyne-2,1-diyl))dianiline; 150

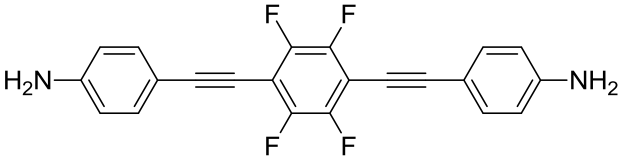

General Procedure (I): **149** (0.480 g, 1.20 mmol), $[Pd(PPh_3)_4]$ (69 mg), CuI (5 mg), 48 (0.308 g, 2.63 mmol), (*i*-Pr)$_2$NH, 4 h, rt. Purified by column chromatography using DCM as eluent and then recrystallisation from EtOH to give **150** as yellow needles (0.256 g, 56%). mp: darkened 280 °C, no clear melting point was observed until 300 °C. ^{1}H NMR (400 MHz, Acetone) δ 7.33 (d, *J* = 8.6 Hz, 4H), 6.73 (d, *J* = 8.6 Hz, 4H), 5.35 (s, 4H). ^{13}C NMR (176 MHz, Acetone-d$_6$) δ 150.58, 146.86, 133.24, 113.94, 107.87, 105.27, 104.30, 72.09. ^{19}F NMR (376 MHz, Acetone-d$_6$) δ -141.05. HR-ASAP$^+$ MS *m/z* calcd for $C_{22}H_{12}N_2F_4$ [M]$^+$ 380.0931, found *m/z* : [M]$^+$ 380.0945. X-ray crystals were grown by slow evaporation of acetone in an NMR tube.

((2,5-Dimethoxy-1,4-phenylene)bis(ethyne-2,1-diyl))bis(trimethylsilane); 151

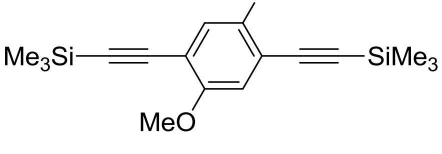

General Procedure (I): **148** (2.0 g, 5.13 mmol), TMSA (1.26 g, 12.8 mmol), [Pd(PPh$_3$)$_4$] (0.296 g), CuI (20 mg), (*i*-Pr)$_2$NH, 4 h, rt. Purified by column chromatography by using DCM/PE (1:4, v/v) and then recrystallisation from hexane to give **151** as white flake crystals (1.61 g, 95%). mp: 164.5 - 166.0 °C. ^{1}H NMR (400 MHz, CDCl$_3$) δ 6.85 (s, 2H), 3.87 (s, 6H), 0.26 (s, 18H). ^{13}C NMR (101 MHz, CDCl$_3$) δ 154.20, 116.26, 113.46, 100.81, 100.40, 56.44, -0.02. The data are consistent with the literature.[247]

1,4-Diethynyl-2,5-dimethoxybenzene; 152

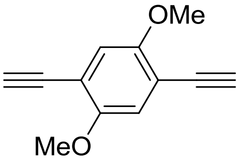

General Procedure (II): **151** (0.50 g, 1.51 mmol), TBAF solution (6.05 ml, 1M in THF), 30 mins, rt. After removing solvents, **152** was obtained as a white solid (0.270 g, 95%), which was used without further purification. ^{1}H NMR (400 MHz, CDCl$_3$) δ 6.96 (s, 2H), 3.94 (s, 6H), 3.37 (s, 2H). ^{13}C NMR (101 MHz, CDCl$_3$) δ 154.14, 117.89, 113.41, 82.61, 79.94, 69.87. The data are consistent with the literature.[247]

S,S'-(((2,5-Dimethoxy-1,4-phenylene)bis(ethyne-2,1-diyl))bis(4,1-phenylene)) diethanethioate; 33

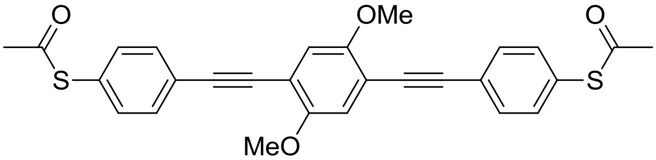

General Procedure (I): **44** (0.329, 1.18 mmol), **152** (0.100, 0.53 mmol), [Pd(PPh$_3$)$_4$] (31 mg), CuI (2 mg), (*i*-Pr)$_2$NH, 4 h, rt. Purified by column chromatography using DCM as eluent and then recrystallisation from EtOAc to afford **33** as yellow crystals (0.245 g, 95%). mp: 170.4 – 171.8 °C. ^{1}H NMR (400 MHz, CDCl$_3$) δ 7.59 (d, J = 8.4 Hz, 4H), 7.40 (d, J = 8.4 Hz, 4H), 7.03 (s, 2H), 3.89 (s, 6H), 2.42 (s, 6H). ^{13}C NMR (101 MHz, CDCl$_3$) δ 193.68, 154.20, 134.41, 132.46, 128.45, 124.63, 115.84, 113.52, 94.59, 87.59, 56.69, 30.54. MS (ASAP$^+$) *m/z* (%): 486.0 ([M]$^+$, 100). Anal. Calcd. for $C_{28}H_{22}O_4S_2$: C, 69.11; H, 4.56; S, 13.18. Found: C, 68.87; H, 4.50; S, 12.76. The data are consistent with the literature.[121]

1,4-Bis((trimethylsilyl)ethynyl)benzene; 158

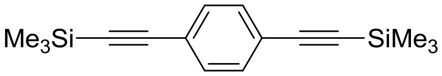

General Procedure (I): **157** (2.00 g, 8.48 mmol), TMSA (2.08 g, 21.2 mmol), [Pd(PPh_3)$_4$] (0.490 g), CuI (32 mg), (*i*-Pr)$_2$NH, 12 h, rt. Purified by column chromatography by using DCM/PE (1:4, v/v) and then recrystallisation from hexane to give **158** as white flake crystals (2.03 g, 88%). ^{1}H NMR (400 MHz, $CDCl_3$) δ 7.39 (s, 4H), 0.25 (s, 18H). ^{13}C NMR (101 MHz, $CDCl_3$) δ 131.96, 123.34, 104.77, 96.51, 0.14. The data are consistent with the literature.[248]

6.3 Crystallographic Data

Compound Number	**86**	**89**	**97**	**117**	**115**	**90**	**127**	**150**
Chemical formula	$C_{22}H_{16}N_2$	$C_{22}H_8N_2$	$C_{20}H_8N_2O_4$	$C_{24}H_{14}S_2$	$C_{20}H_{14}S_2$	$C_{11}H_5N$	$C_{24}H_{20}N_2$	$C_{22}H_{12}N_2F_4$
fw	308.37	300.30	340.28	366.47	318.43	151.16	336.16	438.41
T (K)	120	120	120	120	120	120	120	120
crystal system	monoclinic	triclinic	monoclinic	triclinic	triclinic	triclinic	tricilinic	monoclinic
space group (no.)	P-1 (#2)	P-1 (# 2)	$P2_1/n$ (# 14)	P-1 (# 2)	P-1 (# 2)	P-1 (# 2)	P-1 (#2)	$P2_1/m$ (# 1)
a (Å)	19.3766(8)	3.7768(3)	3.7441(4)	6.3945(5)	6.2320(4)	3.8166(3)	8.9776(10)	5.9340(8)
b (Å)	3.9924(2)	7.2969(6)	7.1001(7)	11.8782(11)	11.0083(7)	8.8887(7)	5.2275(6)	21.935(3)
c (Å)	21.1174(10)	14.1750(12)	29.394(3)	12.3998(10)	16.6103(9)	12.7368(8)	27.790(3)	8.1126(11)
α (deg)	90.00	93.06(3)	90	70.290(3)	90.838(11)	104.002(4)	90.00	90.00
β (deg)	101.083(4)	97.30(2)	93.12(3)	87.216(3)	98.346(11)	97.611(3)	91.488(10)	103.14(2)
γ (deg)	90.00	97.03(3)	90	86.910(3)	93.769(11)	92.025(3)	90.00	90.00
V (Å^3)	1603.16(13)	383.62(5)	780.24(14)	884.90(13)	1124.68(12)	414.54(5)	1303.7(2)	1028.3(3)
Z	4	1	2	2	3	2	2	2
ρ_{calcd} (g cm^{-3})	1.278	1.300	1.448	1.375	1.410	1.211	1.153	1.416
μ (mm^{-1})	0.06	0.08	0.10	0.31	0.35	0.07	0.072	0.112
no. of reflns total	2818	4449	7908	8917	20199	7556	4614	2435
no. of reflns unique	2465	1752	1386	3130	5712	1878	1977	1824
R_{int}	0.066	0.071	0.100	0.063	0.042	0.078	0.078	0.058
R_1 ^{a,b}	0.050	0.039	0.050	0.039	0.039	0.050	0.050	0.037
wR_2 ^{c}	0.126	0.097	0.112	0.078	0.103	0.139	0.136	0.093

^{a} Reflections with $I \geq 2\sigma(I)$; ^{b} $R_1 = \Sigma||F_o| - |F_c||/\Sigma|F_o|$; ^{c} $wR_2 = \{\Sigma[w(F_o^2 - F_c^2)^2]/\Sigma[w(F_o^2)^2]\}^{1/2}$

Conclusions and Outlook

As a result of the rapid growth in the electronics industry for over the past three decades, the demand for more advanced materials has been raised. Therefore, the number of scientific studies to develop new types of electronic materials and new techniques to fabricate denser electronic devices has increased and new fields of research such as nanotechnology and molecular electronics are now established.

The objective of the research presented in this thesis was to synthesise organic conjugated molecular wires and study their electron transport properties by various methods. The single molecule conductance characteristics of several molecular wires were investigated by using STM-BJ and MCBJ techniques. Additionally, some of those molecular wires were also used in QDSSCs as linkers between the nanoparticles to evaluate the effect of the conjugated bridge within the QD networks.

The effect of the anchoring group on the single-molecule conductance of a series of tolanes **41**, **47**, **50** and **53** was investigated by comparing four different anchoring groups (PY, SH, NH_2 and CN) via extensive data analysis of the conductance-distance traces without data selection, DFT calculations and simulations. Our results showed that SH, NH_2 and PY anchoring groups have relatively high conductance, whereas the conductance for CN is significantly lower. Statistically, PY and SH revealed higher junction formation probability and stability than NH_2 and CN. From these findings, we conclude that practically the PY anchoring group is the best candidate among others in terms of reproducibility and high conductance values.

We also have synthesised functional oligoyne molecular wires and explored their electron transport properties in single-molecule junctions. The stability of the tetrayne compounds synthesised was assessed. We observed that nitrobenzene **97** and benzonitrile **89** end-capped tetrayne compounds are the most stable in solution and as crystalline samples. However, due to the weak interaction between nitrile and nitro anchoring groups and gold electrodes, their poor solubility in non-polar solvents which are more suitable for single-molecule conductance measurements, the electron-transport measurements through these molecules are less well defined than other analogues. Additionally, tetraynes end-capped with aniline **67**, *N*,*N*-dimethylaniline **80** and *N*-methylaniline **86** were observed to not be stable enough for single molecule experiments under ambient conditions. Our attempts to synthesise acetothiophenol

101 end-capped tetrayne failed due to its instability. However, we were able to measure the UV-vis absorption spectrum, which supports the formation of the tetrayne.

We developed the synthesis of the key building-block of the DHBT anchoring group for the first time and used it as an end-cap for the oligoyne series. DHBT end-capped tetrayne compound **117** was observed to be stable in ambient conditions. The performance of the DHBT series in single-molecule junctions was excellent where we observed the highest conductance and junction formation probability among others.

It is known that the synthesis of longer oligoynes encounters problems as the stability decreases with the increasing number of the triple bonds in the *sp*-backbone. Therefore, the synthesis of longer derivatives remains as a challenge. Our initial studies showed that introducing methyl substituents adjacent to the oligoyne chains on the head phenyl groups increases the stability. We proved this by synthesising 3,5-dimethylaniline end-capped tetrayne **127**, which was observed to be much more stable than aniline end-capped tetrayne **67**. The synthesis of pyridyl **140** and 3,5-dimethyaniline **131** anchored hexayne compounds are still in progress.

We also investigated the effects of using conjugated molecular wires in QDSSCs. Preliminary results show that introducing amine anchored conjugated cross-linking molecular wires between the QDs improves the performance of a solar cell. Further detailed studies by using pyridyl and thiophenol anchored wires are still in progress.

Appendix 1

List of Seminars Attended

- 23 June 2009: Michael Hon-Wah Lam, Hong Kong, "*Versatile Luminescent Organometallic Pt(II) Systems for Bio-Labelling Applications*"
- 7 July 2009: Tim Swager, MIT, USA, "*Polymer Electronics in the Design of Chemical Sensors*"
- 17 July 2009: Uwe Bunz, Georgia Tech, USA, "*Cruciform Fluorophores*"
- 2 of March 2010: Paul Burn, Uni. Queensland, Australia, "*In Search of Deep Blue Phosphorescence*"
- 11 March 2010: Frieder Jakle, Rutgers Uni., USA, "*Organoborane functionalised conjugated polymers as optoelectronic sensory materials*"
- 10 May 2010: Dan Nocera, MIT, USA, "*The Global Energy Challenge*"
- 11 May 2010: Dan Nocera, MIT, USA, "*The Chemistry of Solar Fuels*"
- 12 May 2010: Dan Nocera, MIT, USA, "*Personalised Energy*"
- 28 September 2010 : Lars-Olof Pålsson, Durham, UK, "*Solvatochromism Through the Eye Piece – Sensing of the Physiologica Environment Inside Cells and other Biological Structures*"
- 28 September 2010: Claude Lapinte, Rennes, France, "*Redox-Active Organometallics. Magnetic and Electronic Couplings through Carbon – Silicon Hybrid Molecular Connectors"*
- 10 November 2010: Martyn Twigg, Johnson Matthey Co., UK, "*Controlling Emissions from Cars*"
- 12 November 2010: Michael Bendikov, Tel-Aviv, Israel, "*Novel Organic Electronic Materials*"
- 23 February 2011: Laura Herz, Oxford, UK, "*Ultrafast Photoexcitation Dynamics in Hybrid Materials*"
- 09 March 2011: N. Champness, Nottingham, UK, "*Molecular Organisation: Working with Molecules on the Nanoscale*"
- 11 May 2011: M. C. Nicasio, Seville, Spain, "*C-Heteroatom Bond Formation Using Ni and Cu*"
- 11 May 2011: Pete Skabara, Strathclyde, UK, "*Complex Conjugated Architectures*"

- 13 May 2011: Henri Doucet, Rennes, France, “*Pd-Catalysed Arylations via C-H Bond Activation*”
- 18 May 2011: Randy Thummel, Houston, USA, “*Heterocyclic Ligands to Capture Sun’s Energy*”
- 12 September 2011: Chihaya Adachi, Kyushu, Japan
- 12 October 2011: S. Koshihara, Tokyo, Japan, “*Ultrafast Dynamics of Cooperative Lattice Charge Coupling Phenomena*”
- 12 October 2011: K. Kiguchi, Tokyo, Japan, “*Characterisation of a Molecular Junction*”.
- 19 October 2011: F. Paul, Rennes, “*Molecular Wires Made from Fe(Cp*)(dppe) end-Groups*”
- 01 November 2011: Igor Larrosa, Queen Mary, “*C-H Activation to C-C Activation*”
- 14 November 2011: J. Sessler, Texas, USA, *“Recent Advances in Calixpyrole Chemistry*”.
- 03-04 April 2012: Durham-Rennes Mini Symposium.

Chapter 7

Bibliography

(1) Kilby, J. S. C. *ChemPhysChem* **2001**, *2*, 482.
(2) Intel 2007 Annual Report. [Online Early Access]. Published Online: 2007. http://media.corporate-ir.net/media_files/irol/10/101302/2007annualReport/common/pdfs/intel_2007ar.pdf.
(3) Moore, G. E. *Electronics* **1965**, *38*, 114.
(4) Moore, G. E. In *Digest of the 1975 International Electron Devices Meeting, IEEE* New York, 1975, p 1113.
(5) Ghosh, A. W.; Damle, P.; Datta, S.; Nitzan, A. *MRS Bull.* **2004**, *29*, 391.
(6) Schwierz, F. *Nature Nanotechnol.* **2010**, *5*, 487.
(7) Weibel, N.; Grunder, S.; Mayor, M. *Org. Biomol. Chem.* **2007**, *5*, 2343.
(8) Feynman, R. *"There's Plenty of Room at the Bottom"*; American Physical Society, 1959.
(9) Aviram, A.; Ratner, M. A. *Chem. Phys. Lett.* **1974**, *29*, 277.
(10) Mann, B.; Kuhn, H. *J. Appl. Phys.* **1971**, *42*, 4398.
(11) Helms, A.; Heiler, D.; McLendon, G. *J. Am. Chem. Soc.* **1992**, *114*, 6227.
(12) Sedghi, G.; Sawada, K.; Esdaile, L. J.; Hoffmann, M.; Anderson, H. L.; Bethell, D.; Haiss, W.; Higgins, S. J.; Nichols, R. J. *J. Am. Chem. Soc.* **2008**, *130*, 8582.
(13) Selzer, Y.; Allara, D. L. *Annu. Rev. Phys. Chem.* **2006**, *57*, 593.
(14) Ulman, A. *Chem. Rev.* **1996**, *96*, 1533.
(15) Nuzzo, R. G.; Allara, D. L. *J. Am. Chem. Soc.* **1983**, *105*, 4481.
(16) Bain, C. D.; Troughton, E. B.; Tao, Y. T.; Evall, J.; Whitesides, G. M.; Nuzzo, R. G. *J. Am. Chem. Soc.* **1989**, *111*, 321.
(17) Moreno-Garcia, P.; Wandlowski, T., Unpublished Results.
(18) Hong, W.; Manrique, D. Z.; Moreno-Garcia, P.; Gulcur, M.; Mishchenko, A.; Lambert, C. J.; Bryce, M. R.; Wandlowski, T. *J. Am. Chem. Soc.* **2012**, *134*, 2292.
(19) Moreland, J.; Ekin, J. W. *J. Appl. Phys.* **1985**, *58*, 3888.
(20) Muller, C. J.; van Ruitenbeek, J. M.; Dejongh, L. J. *Physica C* **1992**, *191*, 485.
(21) Huber, R.; Gonzalez, M. T.; Wu, S.; Langer, M.; Grunder, S.; Horhoiu, V.; Mayor, M.; Bryce, M. R.; Wang, C.; Jitchati, R.; Schonenberger, C.; Calame, M. *J. Am. Chem. Soc.* **2008**, *130*, 1080.
(22) Gonzalez, M. T.; Wu, S.; Huber, R.; van der Molen, S. J.; Schonenberger, C.; Calame, M. *Nano Lett.* **2006**, *6*, 2238.
(23) Reed, M. A.; Zhou, C.; Muller, C. J.; Burgin, T. P.; Tour, J. M. *Science* **1997**, *278*, 252.
(24) Dulic, D.; van der Molen, S. J.; Kudernac, T.; Jonkman, H. T.; de Jong, J. J. D.; Bowden, T. N.; van Esch, J.; Feringa, B. L.; van Wees, B. J. *Phys. Rev. Lett.* **2003**, *91*, 207402.
(25) Smit, R. H. M.; Noat, Y.; Untiedt, C.; Lang, N. D.; van Hemert, M. C.; van Ruitenbeek, J. M. *Nature* **2002**, *419*, 906.
(26) Song, H.; Reed, M. A.; Lee, T. *Adv. Mat.* **2011**, *23*, 1583.

(27) Mazur, U.; Hipps, K. W. *J. Phys. Chem. B* **1999**, *103*, 9721.
(28) Stipe, B. C.; Rezaei, M. A.; Ho, W. *Science* **1998**, *279*, 1907.
(29) Moresco, F. *Phys. Rep.-Rev. Sec. Phys. Lett.* **2004**, *399*, 175.
(30) *Procedures in Scanning Probe Microscopies*; 1st edition ed.; Colton, R. J.; Ebeling, W.; Frommer, J. E.; Gaub, H. E.; Gewirth, A. A.; Guckenberger, R.; Rabe, J.; Heckl, W. M.; Parkinson, B., Eds.; John Wiley & Sons, 1998.
(31) Cui, X. D.; Primak, A.; Zarate, X.; Tomfohr, J.; Sankey, O. F.; Moore, A. L.; Moore, T. A.; Gust, D.; Harris, G.; Lindsay, S. M. *Science* **2001**, *294*, 571.
(32) Xu, B. Q.; Xiao, X. Y.; Tao, N. J. *J. Am. Chem. Soc.* **2003**, *125*, 16164.
(33) Xu, B. Q.; Li, X. L.; Xiao, X. Y.; Sakaguchi, H.; Tao, N. J. *Nano Lett.* **2005**, *5*, 1491.
(34) Xu, B.; Tao, N. J. *Science* **2003**, *301*, 1221.
(35) Li, C.; Pobelov, I.; Wandlowski, T.; Bagrets, A.; Arnold, A.; Evers, F. *J. Am. Chem. Soc.* **2008**, *130*, 318.
(36) Cunha, F.; Tao, N. J.; Wang, X. W.; Jin, Q.; Duong, B.; D'Agnese, J. *Langmuir* **1996**, *12*, 6410.
(37) Krans, J. M.; van Ruitenbeek, J. M.; Fisun, V. V.; Yanson, I. K.; de Jongh, L. J. *Nature* **1995**, *375*, 767.
(38) Pascual, J. I.; Méndez, J.; Gómez-Herrero, J.; Baró, A. M.; García, N.; Binh, V. T. *Phys. Rev. Lett.* **1993**, *71*, 1852.
(39) Haiss, W.; van Zalinge, H.; Higgins, S. J.; Bethell, D.; Hobenreich, H.; Schiffrin, D. J.; Nichols, R. J. *J. Am. Chem. Soc.* **2003**, *125*, 15294.
(40) Haiss, W.; Nichols, R. J.; van Zalinge, H.; Higgins, S. J.; Bethell, D.; Schiffrin, D. J. *Phys. Chem. Chem. Phys.* **2004**, *6*, 4330.
(41) Holmlin, R. E.; Haag, R.; Chabinyc, M. L.; Ismagilov, R. F.; Cohen, A. E.; Terfort, A.; Rampi, M. A.; Whitesides, G. M. *J. Amer. Chem. Soc.* **2001**, *123*, 5075.
(42) Rampi, M. A.; Whitesides, G. M. *Chem. Phys.* **2002**, *281*, 373.
(43) Kushmerick, J. G.; Pollack, S. K.; Yang, J. C.; Naciri, J.; Holt, D. B.; Ratner, M. A.; Shashidhar, R. In *Molecular Electronics III*; New York Acad Sciences: New York, 2003; Vol. 1006, p 277.
(44) Park, H.; Lim, A. K. L.; Alivisatos, A. P.; Park, J.; McEuen, P. L. *Appl. Phys. Lett.* **1999**, *75*, 301.
(45) Liang, W. J.; Shores, M. P.; Bockrath, M.; Long, J. R.; Park, H. *Nature* **2002**, *417*, 725.
(46) Li, C. Z.; Bogozi, A.; Huang, W.; Tao, N. J. *Nanotechnology* **1999**, *10*, 221.
(47) Amlani, I.; Rawlett, A. M.; Nagahara, L. A.; Tsui, R. K. *Appl. Phys. Lett.* **2002**, *80*, 2761.
(48) Blum, A. S.; Kushmerick, J. G.; Long, D. P.; Patterson, C. H.; Yang, J. C.; Henderson, J. C.; Yao, Y. X.; Tour, J. M.; Shashidhar, R.; Ratna, B. R. *Nat. Mater.* **2005**, *4*, 167.
(49) Dadosh, T.; Gordin, Y.; Krahne, R.; Khivrich, I.; Mahalu, D.; Frydman, V.; Sperling, J.; Yacoby, A.; Bar-Joseph, I. *Nature* **2005**, *436*, 677.
(50) Chen, F.; Hihath, J.; Huang, Z.; Li, X.; Tao, N. J. *Annu. Rev. Phys. Chem.* **2007**, *58*, 535.
(51) Ashwell, G. J.; Phillips, L. J.; Robinson, B. J.; Urasinska-Wojcik, B.; Lambert, C. J.; Grace, I. M.; Bryce, M. R.; Jitchati, R.; Tavasli, M.; Cox, T. I.; Sage, I. C.; Tuffin, R. P.; Ray, S. *ACS Nano* **2010**, *4*, 7401.
(52) Metzger, R. M. *Chem. Rev.* **2003**, *103*, 3803.
(53) Perepichka, D. F.; Bryce, M. R.; Pearson, C.; Petty, M. C.; McInnes, E. J. L.; Zhao, J. P. *Angew. Chem. Int. Ed.* **2003**, *42*, 4636.
(54) Perepichka, D. F.; Bryce, M. R.; Batsanov, A. S.; McInnes, E. J. L.; Zhao, J. P.; Farley, R. D. *Chem. Eur. J.* **2002**, *8*, 4656.
(55) Perepichka, D. F.; Bryce, M. R.; McInnes, E. J. L.; Zhao, J. P. *Org. Lett.* **2001**, *3*, 1431.
(56) Ho, G.; Heath, J. R.; Kondratenko, M.; Perepichka, D. F.; Arseneault, K.; Pezolet, M.; Bryce, M. R. *Chem. Eur. J.* **2005**, *11*, 2914.

(57) Metzger, R. M.; Chen, B.; Höpfner, U.; Lakshmikantham, M. V.; Vuillaume, D.; Kawai, T.; Wu, X.; Tachibana, H.; Hughes, T. V.; Sakurai, H.; Baldwin, J. W.; Hosch, C.; Cava, M. P.; Brehmer, L.; Ashwell, G. J. *J. Am. Chem. Soc.* **1997**, *119*, 10455.

(58) Kushmerick, J. G.; Whitaker, C. M.; Pollack, S. K.; Schull, T. L.; Shashidhar, R. *Nanotechnology* **2004**, *15*, S489.

(59) van der Molen, S. J.; Liljeroth, P. *J. Phys.: Condens. Matter* **2010**, *22*, 133001.

(60) Irie, M.; Mohri, M. *J. Org. Chem.* **1988**, *53*, 803.

(61) van der Molen, S. J.; Liao, J. H.; Kudernac, T.; Agustsson, J. S.; Bernard, L.; Calame, M.; van Wees, B. J.; Feringa, B. L.; Schonenberger, C. *Nano Lett.* **2009**, *9*, 76.

(62) Gittins, D. I.; Bethell, D.; Schiffrin, D. J.; Nichols, R. J. *Nature* **2000**, *408*, 67.

(63) Leary, E.; Higgins, S. J.; van Zalinge, H.; Haiss, W.; Nichols, R. J.; Nygaard, S.; Jeppesen, J. O.; Ulstrup, J. *J. Am. Chem. Soc.* **2008**, *130*, 12204.

(64) van Dijk, E. H.; Myles, D. J. T.; van der Veen, M. H.; Hummelen, J. C. *Org. Lett.* **2006**, *8*, 2333.

(65) Garcia, P. M.; Wandlowski, T. In *FUNMOLS Workshop* Data presented at Zurich, January 2012.

(66) Low, P. J. *Dalton Trans.* **2005**, 2821.

(67) Robertson, N.; McGowan, C. A. *Chem. Soc. Rev.* **2003**, *32*, 96.

(68) Launay, J. P. *Chem. Soc. Rev.* **2001**, *30*, 386.

(69) Schumm, J. S.; Pearson, D. L.; Jones, L.; Hara, R.; Tour, J. M. *Nanotechnology* **1996**, *7*, 430.

(70) Venkataraman, L.; Klare, J. E.; Tam, I. W.; Nuckolls, C.; Hybertsen, M. S.; Steigerwald, M. L. *Nano Lett.* **2006**, *6*, 458.

(71) Wang, W. Y.; Lee, T.; Reed, M. A. *Phys. Rev. B* **2003**, *68*, 035416.

(72) Parameswaran, R.; Widawsky, J. R.; Vazquez, H.; Park, Y. S.; Boardman, B. M.; Nuckolls, C.; Steigerwald, M. L.; Hybertsen, M. S.; Venkataraman, L. *J. Phys. Chem. Lett* **2010**, *1*, 2114.

(73) Pauly, F.; Viljas, J. K.; Cuevas, J. C.; Schön, G. *Phys. Rev. B* **2008**, *77*, 155312.

(74) Lortscher, E.; Elbing, M.; Tschudy, M.; von Hanisch, C.; Weber, H. B.; Mayor, M.; Riel, H. *ChemPhysChem* **2008**, *9*, 2252.

(75) Mishchenko, A.; Vonlanthen, D.; Meded, V.; Burkle, M.; Li, C.; Pobelov, I. V.; Bagrets, A.; Viljas, J. K.; Pauly, F.; Evers, F.; Mayor, M.; Wandlowski, T. *Nano Lett.* **2010**, *10*, 156.

(76) Tour, J. M. *Acc. Chem. Res.* **2000**, *33*, 791.

(77) James, P. V.; Sudeep, P. K.; Suresh, C. H.; Thomas, K. G. *J. Phys. Chem. A* **2006**, *110*, 4329.

(78) Wu, S.; Gonzalez, M. T.; Huber, R.; Grunder, S.; Mayor, M.; Schoenenberger, C.; Calame, M. *Nat. Nanotechnol.* **2008**, *3*, 569.

(79) Martin, S.; Grace, I.; Bryce, M. R.; Wang, C.; Jitchati, R.; Batsanov, A. S.; Higgins, S. J.; Lambert, C. J.; Nichols, R. J. *J. Am. Chem. Soc.* **2010**, *132*, 9157.

(80) Lörtscher, E.; Ciszek, J. W.; Tour, J.; Riel, H. *Small* **2006**, *2*, 973.

(81) Zotti, L. A.; Kirchner, T.; Cuevas, J. C.; Pauly, F.; Huhn, T.; Scheer, E.; Erbe, A. *Small* **2010**, *6*, 1529.

(82) Cai, L. T.; Skulason, H.; Kushmerick, J. G.; Pollack, S. K.; Naciri, J.; Shashidhar, R.; Allara, D. L.; Mallouk, T. E.; Mayer, T. S. *J. Phys. Chem. B* **2004**, *108*, 2827.

(83) Kushmerick, J. G.; Holt, D. B.; Pollack, S. K.; Ratner, M. A.; Yang, J. C.; Schull, T. L.; Naciri, J.; Moore, M. H.; Shashidhar, R. *J. Am. Chem. Soc.* **2002**, *124*, 10654.

(84) Mayor, M.; Weber, H. B.; Reichert, J.; Elbing, M.; von Hänisch, C.; Beckmann, D.; Fischer, M. *Angew. Chem. Int. Ed.* **2003**, *42*, 5834.

(85) Tour, J. M.; Rawlett, A. M.; Kozaki, M.; Yao, Y. X.; Jagessar, R. C.; Dirk, S. M.; Price, D. W.; Reed, M. A.; Zhou, C. W.; Chen, J.; Wang, W. Y.; Campbell, I. *Chem. Eur. J.* **2001**, *7*, 5118.

(86) Wang, C. S.; Batsanov, A. S.; Bryce, M. R.; Martin, S.; Nichols, R. J.; Higgins, S. J.; Garcia-Suarez, V. M.; Lambert, C. J. *J. Am. Chem. Soc.* **2009**, *131*, 15647.

(87) Widawsky, J. R.; Kamenetska, M.; Klare, J.; Nuckolls, C.; Steigerwald, M. L.; Hybertsen, M. S.; Venkataraman, L. *Nanotechnology* **2009**, *20*, 434009.
(88) Bunz, U. H. F. *Chem. Rev.* **2000**, *100*, 1605.
(89) Taylor, J.; Brandbyge, M.; Stokbro, K. *Phys. Rev. B* **2003**, *68*, 121101.
(90) Ulrich, J.; Esrail, D.; Pontius, W.; Venkataraman, L.; Millar, D.; Doerrer, L. H. *J. Phys. Chem. B* **2006**, *110*, 2462.
(91) Jones, D. R.; Troisi, A. *J. Phys. Chem. C* **2007**, *111*, 14567.
(92) Roper, M. G.; Skegg, M. P.; Fisher, C. J.; Lee, J. J.; Dhanak, V. R.; Woodruff, D. P.; Jones, R. G. *Chem. Phys. Lett.* **2004**, *389*, 87.
(93) Quek, S. Y.; Venkataraman, L.; Choi, H. J.; Louie, S. G.; Hybertsen, M. S.; Neaton, J. B. *Nano Lett.* **2007**, *7*, 3477.
(94) Dell'Angela, M.; Kladnik, G.; Cossaro, A.; Verdini, A.; Kamenetska, M.; Tamblyn, I.; Quek, S. Y.; Neaton, J. B.; Cvetko, D.; Morgante, A.; Venkataraman, L. *Nano Lett.* **2010**, *10*, 2470.
(95) Quek, S. Y.; Kamenetska, M.; Steigerwald, M. L.; Choi, H. J.; Louie, S. G.; Hybertsen, M. S.; Neaton, J. B.; Venkataraman, L. *Nat. Nanotechnol.* **2009**, *4*, 230.
(96) Bagrets, A.; Arnold, A.; Evers, F. *J. Am. Chem. Soc.* **2008**, *130*, 9013.
(97) Mishchenko, A.; Zotti, L. A.; Vonlanthen, D.; Burkle, M.; Pauly, F.; Cuevas, J. C.; Mayor, M.; Wandlowski, T. *J. Am. Chem. Soc.* **2011**, *133*, 184.
(98) Kim, B.; Beebe, J. M.; Jun, Y.; Zhu, X. Y.; Frisbie, C. D. *J. Am. Chem. Soc.* **2006**, *128*, 4970.
(99) Chen, F.; Li, X.; Hihath, J.; Huang, Z.; Tao, N. *J. Am. Chem. Soc.* **2006**, *128*, 15874.
(100) Cheng, Z. L.; Skouta, R.; Vazquez, H.; Widawsky, J. R.; Schneebeli, S.; Chen, W.; Hybertsen, M. S.; Breslow, R.; Venkataraman, L. *Nat. Nanotechnol.* **2011**, *6*, 353.
(101) Martin, C. A.; Ding, D.; Sorensen, J. K.; Bjornholm, T.; van, R. J. M.; van, d. Z. H. S. J. *J. Am. Chem. Soc.* **2008**, *130*, 13198.
(102) Schull, G.; Frederiksen, T.; Arnau, A.; Sanchez-Portal, D.; Berndt, R. *Nat. Nanotechnol.* **2011**, *6*, 23.
(103) Cuevas, J. C.; Scheer, E. *Molecular electronics: An Introduction to Theory and Experiment*; World Scientific: Singapore, 2010.
(104) Noy, A. *Handbook of Molecular Force Spectroscopy*; Springer: New York, 2008.
(105) Kamenetska, M.; Koentopp, M.; Whalley, A. C.; Park, Y. S.; Steigerwald, M. L.; Nuckolls, C.; Hybertsen, M. S.; Venkataraman, L. *Phys. Rev. Lett.* **2009**, *102*, 126803.
(106) Park, Y. S.; Whalley, A. C.; Kamenetska, M.; Steigerwald, M. L.; Hybertsen, M. S.; Nuckolls, C.; Venkataraman, L. *J. Am. Chem. Soc.* **2007**, *129*, 15768.
(107) Krüger, D.; Rousseau, R.; Fuchs, H.; Marx, D. *Angew. Chem. Int. Ed.* **2003**, *42*, 2251.
(108) Paulsson, M.; Krag, C.; Frederiksen, T.; Brandbyge, M. *Nano Lett.* **2009**, *9*, 117.
(109) Wang, G. M.; Sandberg, W. C.; Kenny, S. D. *Nanotechnology* **2006**, *17*, 4819.
(110) Konopka, M.; Turansky, R.; Reichert, J.; Fuchs, H.; Marx, D.; Stich, I. *Phys. Rev. Lett.* **2008**, *100*, 115503.
(111) Kim, Y.; Hellmuth, T. J.; Burkle, M.; Pauly, F.; Scheer, E. *ACS Nano* **2011**, *5*, 4104.
(112) Champness, N. R.; Khlobystov, A. N.; Majuga, A. G.; Schroder, M.; Zyk, N. V. *Tetrahedron Lett.* **1999**, *40*, 5413.
(113) Wang, C.; Batsanov, A. S.; Bryce, M. R.; Sage, I. *Org. Lett.* **2004**, *6*, 2181.
(114) Nishimura, D.; Oshikiri, T.; Takashima, Y.; Hashidzume, A.; Yamaguchi, H.; Harada, A. *J. Org. Chem.* **2008**, *73*, 2496.
(115) Dixon, S.; Whitby, R. J. *Tetrahedron Lett.* **2006**, *47*, 8147.
(116) Venkataraman, L.; Klare, J. E.; Nuckolls, C.; Hybertsen, M. S.; Steigerwald, M. L. *Nature* **2006**, *442*, 904.
(117) Yanson, A. I.; Bollinger, G. R.; van den Brom, H. E.; Agrait, N.; van Ruitenbeek, J. M. *Nature* **1998**, *395*, 783.
(118) Velizhanin, K. A.; Zeidan, T. A.; Alabugin, I. V.; Smirnov, S. *J. Phys. Chem. B* **2010**, *114*, 14189.

(119) Xing, Y.; Park, T.-H.; Venkatramani, R.; Keinan, S.; Beratan, D. N.; Therien, M. J.; Borguet, E. *J. Am. Chem. Soc.* **2010**, *132*, 7946.
(120) Hybertsen, M. S.; Venkataraman, L.; Klare, J. E.; Cwhalley, A.; Steigerwald, M. L.; Nuckolls, C. *J. Phys.: Condens. Matter* **2008**, *20*.
(121) Haiss, W.; Wang, C.; Grace, I.; Batsanov, A. S.; Schiffrin, D. J.; Higgins, S. J.; Bryce, M. R.; Lambert, C. J.; Nichols, R. J. *Nat. Mater.* **2006**, *5*, 995.
(122) Agrait, N.; Yeyati, A. L.; van, R. J. M. *Phys. Rep.* **2003**, *377*, 81.
(123) Valkenier, H.; Huisman, E. H.; van, H. P. A.; de, L. D. M.; Chiechi, R. C.; Hummelen, J. C. *J. Am. Chem. Soc.* **2011**, *133*, 4930.
(124) Jacob, J. A.; Naumov, S.; Biswas, N.; Mukherjee, T.; Kapoor, S. *J. Phys. Chem. C* **2007**, *111*, 18397.
(125) Oldfield, L. F.; Bockris, J. O. M. *J. Phys. Colloid Chem.* **1951**, *55*, 1255.
(126) *Acetylene Chemistry: Chemistry, Biology and Material Science*; Diederich, F.; Stang, P. J.; Tykwinski, R. R., Eds.; Wiley-VCH: Weinheim, Germany, 2005.
(127) Gholami, M.; Tykwinski, R. R. *Chem. Rev.* **2006**, *106*, 4997.
(128) Nielsen, M. B.; Diederich, F. *Chem. Rev.* **2005**, *105*, 1837.
(129) Haley, M. M.; Tykwinski, R. R.; Wiley-VCH: Weinheim: Germany, 2006.
(130) Szafert, S.; Gladysz, J. A. *Chem. Rev.* **2003**, *103*, 4175.
(131) Cornil, J.; Beljonne, D.; Calbert, J. P.; Brédas, J. L. *Adv. Mat.* **2001**, *13*, 1053.
(132) Slepkov, A. D.; Hegmann, F. A.; Eisler, S.; Elliott, E.; Tykwinski, R. R. *J. Chem. Phys.* **2004**, *120*, 6807.
(133) Crljen, Ž.; Baranović, G. *Phys. Rev. Lett.* **2007**, *98*, 116801.
(134) Garcia-Suarez, V. M.; Lambert, C. J. *Nanotechnology* **2008**, *19*, 455203.
(135) Gibtner, T.; Hampel, F.; Gisselbrecht, J.-P.; Hirsch, A. *Chem. Eur. J.* **2002**, *8*, 408.
(136) Luu, T.; Elliott, E.; Slepkov, A. D.; Eisler, S.; McDonald, R.; Hegmann, F. A.; Tykwinski, R. R. *Org. Lett.* **2004**, *7*, 51.
(137) Mohr, W.; Stahl, J.; Hampel, F.; Gladysz, J. A. *Chem. Eur. J.* **2003**, *9*, 3324.
(138) Wang, C.; Batsanov, A. S.; West, K.; Bryce, M. R. *Org. Lett.* **2008**, *10*, 3069.
(139) Klinger, C.; Vostirowsky, O.; Hirsch, A. *Eur. J. Org. Chem.* **2006**, 1508.
(140) Sugiyama, J.; Tomita, I. *Eur. J. Org. Chem.* **2007**, 4651.
(141) Johnson, T. R.; Walton, D. R. M. *Tetrahedron* **1972**, *28*, 5221.
(142) Simpkins, S. M. E.; Weller, M. D.; Cox, L. R. *Chem. Commun.* **2007**, 4035.
(143) Carroll, R. L.; Gorman, C. B. *Angew. Chem. Int. Ed.* **2002**, *41*, 4379.
(144) Maruccio, G.; Cingolani, R.; Rinaldi, R. *J. Mater. Chem.* **2004**, *14*, 542.
(145) Troisi, A.; Ratner, M. A. *Small* **2006**, *2*, 172.
(146) Kamenetska, M.; Quek, S. Y.; Whalley, A. C.; Steigerwald, M. L.; Choi, H. J.; Louie, S. G.; Nuckolls, C.; Hybertsen, M. S.; Neaton, J. B.; Venkataraman, L. *J. Am. Chem. Soc.* **2010**, *132*, 6817.
(147) Ziessel, R.; Suffert, J.; Youinou, M. T. *J. Org. Chem.* **1996**, *61*, 6535.
(148) Beck, W.; Niemer, B.; Wieser, M. *Angew. Chem. Int. Ed.* **1993**, *32*, 923.
(149) Schumm, J. S.; Pearson, D. L.; Tour, J. M. *Angew. Chem. Int. Ed.* **1994**, *33*, 1360.
(150) Lang, N. D.; Avouris, P. *Phys. Rev. Lett.* **1998**, *81*, 3515.
(151) Jin, C.; Lan, H.; Peng, L.; Suenaga, K.; Iijima, S. *Phys. Rev. Lett.* **2009**, *102*, 205501.
(152) Meyer, J. C.; Girit, C. O.; Crommie, M. F.; Zettl, A. *Nature* **2008**, *454*, 319.
(153) Ballmann, S.; Hieringer, W.; Secker, D.; Zheng, Q.; Gladysz, J. A.; Goerling, A.; Weber, H. B. *ChemPhysChem* **2010**, *11*, 2256.
(154) Fiandanese, V.; Bottalico, D.; Marchese, G.; Punzi, A. *Tetrahedron* **2008**, *64*, 53.
(155) Kivala, M.; Boudon, C.; Gisselbrecht, J. P.; Seiler, P.; Gross, M.; Diederich, F. *Angew. Chem. Int. Ed.* **2007**, *46*, 6357.
(156) Frank, B. B.; Kivala, M.; Blanco, B. C.; Breiten, B.; Schweizer, W. B.; Laporta, P. R.; Biaggio, I.; Jahnke, E.; Tykwinski, R. R.; Boudon, C.; Gisselbrecht, J. P.; Diederich, F. *Eur. J. Org. Chem.* **2010**, 2487.

(157) Lee, C. K. Y.; Groneman, J. L.; Turner, P.; Rendina, L. M.; Harding, M. M. *Tetrahedron* **2006**, *62*, 4870.

(158) Bruce, M. I.; Low, P. J.; Werth, A.; Skelton, B. W.; White, A. H. *J. Chem. Soc., Dalton Trans.* **1996**, 1551.

(159) Hoshi, M.; Shirakawa, K. *Synlett* **2002**, *7*, 1101.

(160) Degraaf, W.; Smits, A.; Boersma, J.; Vankoten, G.; Hoekstra, W. P. M. *Tetrahedron* **1988**, *44*, 6699.

(161) Holmes, A. B.; Jones, G. E. *Tetrahedron Lett.* **1980**, *21*, 3111.

(162) Yamaguchi, I.; Higashi, H.; Kimura, S.; Sato, M. *Helv. Chim. Acta* **2010**, *93*, 819

(163) West, K.; Hayward, L. N.; Batsanov, A. S.; Bryce, M. R. *Eur. J. Org. Chem.* **2008**, 5093.

(164) West, K.; Wang, C.; Batsanov, A. S.; Bryce, M. R. *J. Org. Chem.* **2006**, *71*, 8541.

(165) Umezawa, H.; Okada, S.; Oikawa, H.; Matsuda, H.; Nakanishi, H. *J. Phys. Org. Chem.* **2005**, *18*, 468.

(166) Leonard, K. A.; Nelen, M. I.; Anderson, L. T.; Gibson, S. L.; Hilf, R.; Detty, M. R. *J. Med. Chem.* **1999**, *42*, 3942.

(167) Qu, W.; Kung, M.-P.; Hou, C.; Oya, S.; Kung, H. F. *J. Med. Chem.* **2007**, *50*, 3380.

(168) Batsanov, A. S.; Collings, J. C.; Fairlamb, I. J. S.; Holland, J. P.; Howard, J. A. K.; Lin, Z.; Marder, T. B.; Parsons, A. C.; Ward, R. M.; Zhu, J. *J. Org. Chem.* **2004**, *70*, 703.

(169) Hudson, C. M.; Shenoy, R. A.; Neubert, M. E.; Petschek, R. G. *Liquid Crystals* **1999**, *26*, 241.

(170) Coates, G. W.; Dunn, A. R.; Henling, L. M.; Dougherty, D. A.; Grubbs, R. H. *Angew. Chem. Int. Ed.* **1997**, *36*, 248.

(171) Ravera, M.; D'Amato, R.; Guerri, A. *J. Organomet. Chem.* **2005**, *690*, 2376

(172) Serwinski, P. R.; Lahti, P. M. *Org. Lett.* **2003**, *5*, 2099

(173) Andrievskii, V. N.; Kotlyarevskii, I. L.; Shvartsberg, M. S. *Russ. Chem. Bull.* **1966**, *15*, 844.

(174) Muesmann, T. W. T.; Wickleder, M. S.; Christoffers, J. *Synthesis* **2011**, 2775

(175) Park, Y. S.; Widawsky, J. R.; Kamenetska, M.; Steigerwald, M. L.; Hybertsen, M. S.; Nuckolls, C.; Venkataraman, L. *J. Am. Chem. Soc.* **2009**, *131*, 10820.

(176) Yamagishi, F. G.; Rayner, D. R.; Zwicker, E. T.; Cram, D. J. *J. Am. Chem. Soc.* **1973**, *95*, 1916.

(177) Eggers, K.; Fyles, T. M.; Montoya-Pelaez, P. J. *J. Org. Chem.* **2001**, *66*, 2966.

(178) Madec, D.; Mingoia, F.; Macovei, C.; Maitro, G.; Giambastiani, G.; Poli, G. *Eur. J. Org. Chem.* **2005**, 552.

(179) Szafert, S.; Gladysz, J. A. *Chem. Rev.* **2006**, *106*, PR1.

(180) Kaliginedi, V.; Moreno-Garcia, P.; Valkenier, H.; Hong, W.; Garcia-Suarez, V. M.; Buiter, P.; Otten, J. L. H.; Hummelen, J. C.; Lambert, C. J.; Wandlowski, T. *J. Am. Chem. Soc.* **2012**, *134*, 5262.

(181) Liu, K.; Li, G.; Wang, X.; Wang, F. *J. Phys. Chem. C* **2008**, *112*, 4342.

(182) Lu, Q.; Liu, K.; Zhang, H. M.; Du, Z. B.; Wang, X. H.; Wang, F. S. *ACS Nano* **2009**, *3*, 3861.

(183) Hybertsen, M. S.; Venkataraman, L.; Klare, J. E.; Whalley, A. C.; Steigerwald, M. L.; Nuckolls, C. *J. Phys.: Condens. Matter* **2008**, *20*, 374115.

(184) Sedghi, G.; Sawada, K.; Esdaile, L. J.; Hoffmann, M.; Anderson, H. L.; Bethell, D.; Haiss, W.; Higgins, S. J.; Nichols, R. J. *J. Am. Chem. Soc.* **2008**, *130*, 8582.

(185) Choi, S. H.; Kim, B.; Frisbie, C. D. *Science* **2008**, *320*, 1482.

(186) Kroto, H. W.; Heath, J. R.; Obrien, S. C.; Curl, R. F.; Smalley, R. E. *Nature* **1985**, *318*, 162.

(187) Lambert, C. J., Unpublished results.

(188) Chalifoux, W. A.; Tykwinski, R. R. *Nature Chem.* **2010**, *2*, 967.

(189) Chalifoux, W. A.; McDonald, R.; Ferguson, M. J.; Tykwinski, R. R. *Angew. Chem. Int. Ed.* **2009**, *48*, 7915.

(190) Kajigaeshi, S.; Kakinami, T.; Yamasaki, H.; Fujisaki, S.; Okamoto, T. *Bull. Chem. Soc. Jap.* **1988**, *61*, 600.
(191) Zysman-Colman, E.; Arias, K.; Siegel, J. S. *Can. J. Chem.* **2009**, *87*, 440.
(192) Broman, S. L.; Petersen, M. A.; Tortzen, C. G.; Kadziola, A.; Kilsa, K.; Nielsen, M. B. *J. Am. Chem. Soc.* **2010**, *132*, 9165.
(193) Diemer, V.; Chaumeil, H.; Defoin, A.; Fort, A.; Boeglin, A.; Carre, C. *Eur. J. Org. Chem.* **2008**, 1767.
(194) Saito, H.; Hamana, M. *Heterocycles* **1979**, *12*, 475.
(195) Steigerwald, M. L.; Brus, L. E. *Annu. Rev. Mater. Sci.* **1989**, *19*, 471.
(196) *Colloids and Colloid Assemblies*; Caruso, F., Ed.; Wiley-VCH: Weinheim, 2004.
(197) Nozik, A. J.; Beard, M. C.; Luther, J. M.; Law, M.; Ellingson, R. J.; Johnson, J. C. *Chem. Rev.* **2010**, *110*, 6873.
(198) Talapin, D. V.; Lee, J.-S.; Kovalenko, M. V.; Shevchenko, E. V. *Chem. Rev.* **2010**, *110*, 389.
(199) Yu, W. W.; Qu, L. H.; Guo, W. Z.; Peng, X. G. *Chem. Mat.* **2003**, *15*, 2854.
(200) *Organic Semiconductors in Sensor Applications*; 1st Ed. ed.; Bernards, D. A.; Owens, R. M.; Malliaras, G. G., Eds.; Springer: Heidelberg, 2008.
(201) Kwon, S. G.; Piao, Y.; Park, J.; Angappane, S.; Jo, Y.; Hwang, N.-M.; Park, J.-G.; Hyeon, T. *J. Am. Chem. Soc.* **2007**, *129*, 12571.
(202) Murray, C. B.; Norris, D. J.; Bawendi, M. G. *J. Am. Chem. Soc.* **1993**, *115*, 8706.
(203) De Mello Donega, C. D.; Liljeroth, P.; Vanmaekelbergh, D. *Small* **2005**, *1*, 1152.
(204) Shevchenko, E. V.; Talapin, D. V.; Schnablegger, H.; Kornowski, A.; Festin, O.; Svedlindh, P.; Haase, M.; Weller, H. *J. Am. Chem. Soc.* **2003**, *125*, 9090.
(205) Talapin, D. V.; Rogach, A. L.; Kornowski, A.; Haase, M.; Weller, H. *Nano Lett.* **2001**, *1*, 207.
(206) Boettcher, S. W.; Fan, J.; Tsung, C.-K.; Shi, Q.; Stucky, G. D. *Acc. Chem. Res.* **2007**, *40*, 784.
(207) Niederberger, M. *Acc. Chem. Res.* **2007**, *40*, 793.
(208) Yao, H. H.; Lu, T. C.; Huang, G. S.; Chen, C. Y.; Liang, W. D.; Kuo, H. C.; Wang, S. C. *Nanotechnology* **2006**, *17*, 1713.
(209) Chang, C.-H.; Lee, Y.-L. *Appl. Phys. Lett.* **2007**, *91*, 053503.
(210) Yin, Y.; Alivisatos, A. P. *Nature* **2005**, *437*, 664.
(211) Burda, C.; Chen, X. B.; Narayanan, R.; El-Sayed, M. A. *Chem. Rev.* **2005**, *105*, 1025.
(212) Cushing, B. L.; Kolesnichenko, V. L.; O'Connor, C. J. *Chem. Rev.* **2004**, *104*, 3893.
(213) Gaponik, N.; Talapin, D. V.; Rogach, A. L.; Hoppe, K.; Shevchenko, E. V.; Kornowski, A.; Eychmuller, A.; Weller, H. *J. Phys. Chem. B* **2002**, *106*, 7177.
(214) Wuister, S. F.; Donega, C. D.; Meijerink, A. *J. Phys. Chem. B* **2004**, *108*, 17393.
(215) Kuno, M.; Lee, J. K.; Dabbousi, B. O.; Mikulec, F. V.; Bawendi, M. G. *J. Chem. Phys.* **1997**, *106*, 9869.
(216) Murray, C. B.; Kagan, C. R.; Bawendi, M. G. *Annu. Rev. Mater. Sci.* **2000**, *30*, 545.
(217) Yu, D.; Wang, C. J.; Guyot-Sionnest, P. *Science* **2003**, *300*, 1277.
(218) Yang, Z.; Chen, C.-Y.; Roy, P.; Chang, H.-T. *Chem. Commun.* **2011**, *47*, 9561.
(219) Nozik, A. J. *Physica E.* **2002**, *14*, 115.
(220) Hanna, M. C.; Nozik, A. J. *J. Appl. Phys.* **2006**, *100*, 074510.
(221) Lin, S. C.; Lee, Y. L.; Chang, C. H.; Shen, Y. J.; Yang, Y. M. *Appl. Phys. Lett.* **2007**, *90*, 143517.
(222) Salant, A.; Shalom, M.; Hod, I.; Faust, A.; Zaban, A.; Banin, U. *ACS Nano* **2010**, *4*, 5962.
(223) Guijarro, N.; Lana-Villarreal, T.; Mora-Sero, I.; Bisquert, J.; Gomez, R. *J. Phys. Chem. C* **2009**, *113*, 4208.
(224) Kongkanand, A.; Dominguez, R. M.; Kamat, P. V. *Nano Lett.* **2007**, *7*, 676.
(225) Robel, I.; Kuno, M.; Kamat, P. V. *J. Am. Chem. Soc.* **2007**, *129*, 4136.
(226) Robel, I.; Subramanian, V.; Kuno, M.; Kamat, P. V. *J. Am. Chem. Soc.* **2006**, *128*, 2385.

(227) Lee, Y. L.; Lo, Y. S. *Adv. Funct. Mat.* **2009**, *19*, 604.
(228) Niitsoo, O.; Sarkar, S. K.; Pejoux, C.; Ruhle, S.; Cahen, D.; Hodes, G. *J. Photochem. Photobiol. A-Chem.* **2006**, *181*, 306.
(229) Barea, E. M.; Shalom, M.; Gimenez, S.; Hod, I.; Mora-Sero, I.; Zaban, A.; Bisquert, J. *J. Am. Chem. Soc.* **2010**, *132*, 6834.
(230) Mora-Sero, I.; Gimenez, S.; Fabregat-Santiago, F.; Gomez, R.; Shen, Q.; Toyoda, T.; Bisquert, J. *Acc. Chem. Res.* **2009**, *42*, 1848.
(231) Shen, Q.; Kobayashi, J.; Diguna, L. J.; Toyoda, T. *J. Appl. Phys.* **2008**, *103*, 084304.
(232) Mori, A.; Kondo, T.; Kato, T.; Nishihara, Y. *Chem. Lett.* **2001**, 286.
(233) Bullen, C. R.; Mulvaney, P. *Nano Lett.* **2004**, *4*, 2303.
(234) Ito, S.; Murakami, T. N.; Comte, P.; Liska, P.; Graetzel, C.; Nazeeruddin, M. K.; Graetzel, M. *Thin Solid Films* **2008**, *516*, 4613.
(235) Munro, A. M.; Jen-La Plante, I.; Ng, M. S.; Ginger, D. S. *J. Phys. Chem. C* **2007**, *111*, 6220.
(236) Knowles, K. E.; Tice, D. B.; McArthur, E. A.; Solomon, G. C.; Weiss, E. A. *J. Am. Chem. Soc.* **2010**, *132*, 1041.
(237) Liu, I. S.; Lo, H.-H.; Chien, C.-T.; Lin, Y.-Y.; Chen, C.-W.; Chen, Y.-F.; Su, W.-F.; Liou, S.-C. *J. Mater. Chem.* **2008**, *18*, 675.
(238) Talgorn, E.; Moysidou, E.; Abellon, R. D.; Savenije, T. J.; Goossens, A.; Houtepen, A. J.; Siebbeles, L. D. A. *J. Phys. Chem. C* **2010**, *114*, 3441.
(239) Zeidan, T. A.; Kovalenko, S. V.; Manoharan, M.; Clark, R. J.; Ghiviriga, I.; Alabugin, I. V. *J. Am. Chem. Soc.* **2005**, *127*, 4270.
(240) Krüger, C.; Agarwal, S.; Greiner, A. *J. Am. Chem. Soc.* **2008**, *130*, 2710.
(241) Pearson, D. L.; Tour, J. M. *J. Org. Chem.* **1997**, *62*, 1376.
(242) Merkul, E.; Urselmann, D.; Müller, T. J. J. *Eur. J. Org. Chem.* **2011**, 238.
(243) Watanabe, J.-i.; Yokoyama, H.; Okada, S.; Takaragi, S.; Matsuda, H.; Nakanishi, H. *Mol. Cryst. Liq. Cryst.* **2009**, *505*, 203.
(244) Yamagishi, F. G.; Rayner, D. R.; Zwicker, E. T.; Cram, D. J. *J. Am. Chem. Soc.* **1973**, *95*, 1916.
(245) Grunder, S.; Huber, R.; Horhoiu, V.; González, M. T.; Schönenberger, C.; Calame, M.; Mayor, M. *J. Org. Chem.* **2007**, *72*, 8337.
(246) Hubig, S. M.; Jung, W.; Kochi, J. K. *J. Org. Chem.* **1994**, *59*, 6233.
(247) Yi, C.; Blum, C.; Lehmann, M.; Keller, S.; Liu, S.-X.; Frei, G.; Neels, A.; Hauser, J. r.; Schürch, S.; Decurtins, S. *J. Org. Chem.* **2010**, *75*, 3350.
(248) Matsumi, N.; Naka, K.; Chujo, Y. *J. Am. Chem. Soc.* **1998**, *120*, 5112.